CHEMICAL REVIEWS

Review

Cite This: *Chem. Rev.* XXXX, XXX, XXX–XXX

pubs.acs.org/CR

One-Dimensional Metal Nanostructures: From Colloidal Syntheses to Applications

Da Huo,[†,#] Myung Jun Kim,[§,#] Zhiheng Lyu,[¥,#] Yifeng Shi,[‡,#] Benjamin J. Wiley,[*,§] and Younan Xia[*,†,¥,‡]

[†]The Wallace H. Coulter Department of Biomedical Engineering, Georgia Institute of Technology and Emory University, Atlanta, Georgia 30332, United States

[§]Department of Chemistry, Duke University, Durham, North Carolina 27708, United States

[¥]School of Chemistry and Biochemistry, Georgia Institute of Technology, Atlanta, Georgia 30332, United States

[‡]School of Chemical and Biomolecular Engineering, Georgia Institute of Technology, Atlanta, Georgia 30332, United States

ABSTRACT: This Review offers a comprehensive review of the colloidal synthesis, mechanistic understanding, physicochemical properties, and applications of one-dimensional (1D) metal nanostructures. After a brief introduction to the different types of 1D nanostructures, we discuss major concepts and methods typically involved in a colloidal synthesis of 1D metal nanostructures, as well as the current mechanistic understanding of how the nanostructures are formed. We then highlight how experimental studies and computational simulations have expanded our knowledge of how and why 1D metal nanostructures grow. Following specific examples of syntheses for monometallic, multimetallic, and heterostructured systems, we showcase how the unique structure–property relationships of 1D metal nanostructures have enabled a broad spectrum of applications, including sensing, imaging, plasmonics, photonics, display, thermal management, and catalysis. Throughout our discussion, we also offer perspectives with regard to the future directions of development for this class of nanomaterials.

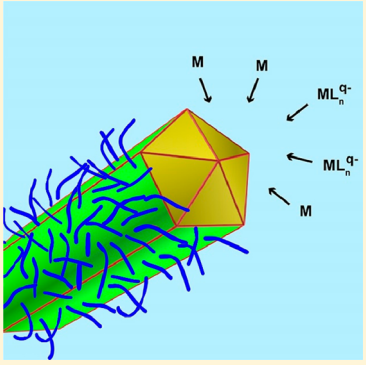

CONTENTS

Special Issue: 1D Nanomaterials/Nanowires

Received: December 4, 2018

DOI: 10.1021/acs.chemrev.8b00745
Chem. Rev. XXXX, XXX, XXX–XXX

1. INTRODUCTION

One-dimensional (1D) metal nanostructures refer to those structures made of metals with two of the three dimensions between 1−100 nm.[1] Different from their zero-dimensional (0D) and two-dimensional (2D) counterparts (i.e., nanoparticles and nanosheets, respectively), 1D nanostructures offer a unique platform for tailoring and utilizing the electronic, plasmonic, magnetic, electrical, mechanical, and thermal properties of metals to suit or enable various types of applications. For example, by simply adjusting the aspect ratio (AR) of Au nanorods (NRs), one can tune their longitudinal localized surface plasmon resonance (LSPR) peaks from visible to near-infrared wavelengths, enabling biomedical applications related to sensing, optical imaging, and cancer treatment.[2,3] For Ag nanowires (NWs), they can be mixed with a polymer and cast as thin films with high optical transparency, excellent electrical conductivity, and good mechanical flexibility to allow for the fabrication of touchscreens and flexible solar cells.[4,5] For both NRs and NWs comprised of Fe, Co, or Ni, their magnetic anisotropy is expected to bring new capabilities for applications related to actuation and information storage.[6,7]

It has been 15 years since the first publication of a comprehensive review article on the subject of 1D nanostructures.[1] At that time, the entire research field, including semiconductors and metals, both top-down and bottom-up approaches to their production, their properties, their assembly into complex architectures, and their use in device fabrication, could be covered in about 30 pages and 200 citations. The research on 1D nanostructures has since exploded to encompass over 100 000 articles, and now requires an entire issue of *Chemical Reviews* to cover different aspects of this class of nanomaterials.

Our own research has focused on metal nanostructures that can be obtained by controlling the assembly of atoms in the solution phase, an approach that is often referred to as solution-phase or colloidal synthesis. At the time of the 2003 review,[1] 1D nanostructures could only be synthesized from two metals: Au[8] and Ag.[9] The synthesis required the use of appropriate capping agents to induce anisotropic growth. Since then, colloidal synthesis of NRs and NWs have been reported for 23 different metals (Figure 1), most of which still rely on capping agents to achieve anisotropic growth. Researchers can now not only control the AR of a variety of 1D metal nanostructures but also produce them with various types of cross sections. In addition, colloidal syntheses have been further developed to produce bimetallic and trimetallic nanostructures, as well as heterostructured systems consisting of a metal and a dielectric or semiconductor.

In tandem with the expansion of the scope of colloidal synthesis, 1D metal nanostructures have found widespread use in various applications. Studies of the AR-dependent colors of AuNRs have evolved into exploration of their use as optical sensors, contrast agents for biomedical imaging, and therapeutic agents for cancer treatment.[2,3,10] A variety of metal NWs have been examined as highly active electrocatalysts.[11−13] Large-scale syntheses of metal NWs have also enabled their use in the fabrication of electrically and thermally conductive composites, as well as wearable electronics.[4,5,14−17] As one of the success stories, several companies have started to

DOI: 10.1021/acs.chemrev.8b00745
Chem. Rev. XXXX, XXX, XXX−XXX

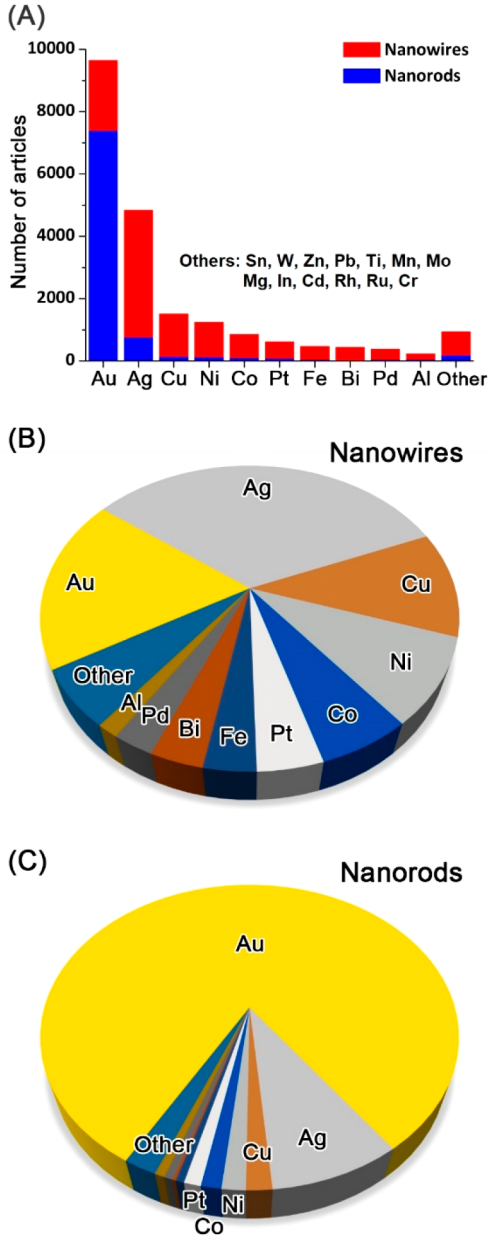

Figure 1. (A) Number of articles about 1D metal nanostructures retrieved from the Web of Science database. (B, C) Relative distributions of articles about NWs and NRs made of different metals.

commercialize the use of AgNWs in the fabrication of transparent, conductive films for use in touchscreens, organic light-emitting diodes (OLEDs), and photovoltaics.[17]

The demand for improved dimensional control, purity, and reproducibility has motivated further study of how and why metals grow into 1D nanostructures. Although researchers have undertaken exhaustive studies of how reaction temperature, reactant concentration, as well as the presence of different types of capping agents or halides affect the morphology of a metal nanostructure, the precise mechanism of how and why the 1D morphology is attained largely remains a matter of debate. New tools and experimental methods that enable in situ measurements, as well as computational simulations, are shedding light on the mystery of 1D nanostructure growth and may eventually settle some of the debates. For example, in situ visualization of nanostructure growth has enabled researchers to quantify the growth kinetics and differentiate between growth mechanisms such as atomic addition and oriented attachment.[18,19] Single-crystal electrochemistry can provide clear experimental tests of the hypotheses for the roles of capping agents and halides in directing anisotropic growth.[20] Computational simulations are increasingly used to scrutinize the driving forces for anisotropic growth, illustrate the types of surface structures preferred by various capping agents, and test hypotheses that still cannot be examined experimentally at the current stage of development.[21−23]

This Review is an attempt to provide a comprehensive review of the synthesis, mechanistic understanding, properties, and applications of 1D metal nanostructures. We start with a brief introduction to the different types of 1D metal nanostructures in section 2. Section 3 provides an overview of the different methods that have been developed for producing 1D metal nanostructures, as well as the current mechanistic understanding of the formation process. Section 4 reviews the experimental tools, methods, and computational simulations that are expanding our understandings of how and why 1D metal nanostructures grow. Specific examples of syntheses for different monometallic, multimetallic, and heterogeneously structured systems are covered in sections 5−7, respectively. In section 8, we highlight how the unique structure−property relationships of various 1D metal nanostructures have enabled a multitude of applications. We hope this Review will provide the broader context for new students entering the field who are seeking to not only learn what was done previously on this research topic but also how their work fits into this large and rapidly growing body of knowledge. We also hope this Review will help update veteran nanomaterial researchers on the most current synthetic methods, new tools for exploring the growth mechanisms, as well as the most recent ways researchers are using 1D metal nanostructures to solve problems.

2. DIFFERENT TYPES OF 1D METAL NANOSTRUCTURES

As shown in Figure 2A−C, 1D metal nanostructures can be classified into different types or subgroups according to their AR, internal twin structure, and cross section, respectively. In addition, nanostructures can be straight, wavy (worm-like), or branched (dendritic); solid or hollow; monometallic, bimetallic, or multimetallic; as well as homogeneously mixed or spatially segregated in terms of elemental distributions. All these parameters can be used as handles to tailor the properties of 1D nanostructures, as illustrated in Figure 2D−F. Here, we provide a brief account of the common practice in classifying 1D nanostructures so the readers will be able to quickly grasp the terminology used in literature.

2.1. Aspect Ratio

The AR (defined as the ratio of length to diameter) of a 1D metal nanostructure not only determines the location of its longitudinal plasmon resonance peak[2,10,24−29] but also the minimum loading of nanostructures needed to obtain electrical or thermal conduction in both thin films and bulk composites.[4,5,29−32] In our discussion, 1D nanostructures with low and high ARs are typically referred to as NRs and NWs, respectively. There is no widely accepted cutoff to define the line between these two types of nanostructures, but in practice, NRs usually refer to 1D nanostructures with ARs

DOI: 10.1021/acs.chemrev.8b00745
Chem. Rev. XXXX, XXX, XXX−XXX

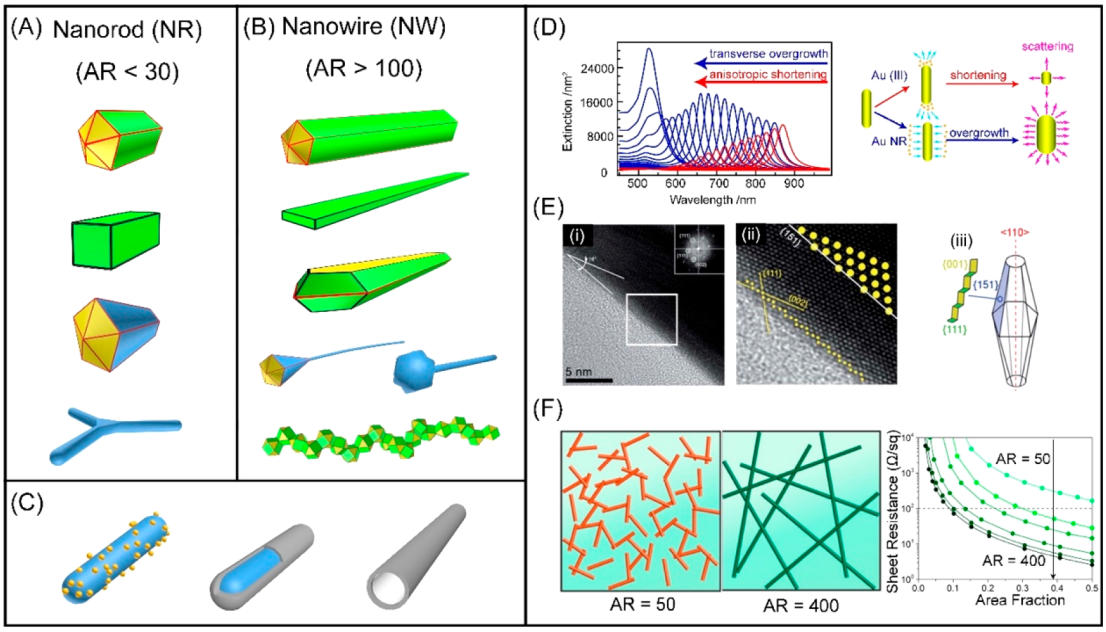

Figure 2. Schematic illustrations of different types of 1D metal nanostructures and how to tailor their properties. (A–C) Typical examples of 1D nanostructures, including (A) NRs, (B) NWs, and (C) their derivative structures. (D–F) Structure–property relationships of 1D nanostructures: (D) simulated extinction spectra of AuNRs with different ARs, (E) high-index facets on the side surface of a tapered NR, and (F) simulated sheet resistance for thin films comprised of AgNWs with different ARs. Reprinted with permission from ref 24. Copyright 2008 American Chemical Society. (E) Reprinted with permission from ref 25. Copyright 2012 The Royal Society of Chemistry. (F) Reprinted with permission from ref 29. Copyright 2013 American Chemical Society.

below 30, whereas NWs typically have ARs over 100. The specific term that should be used in the region of 30–100 is probably best left to the discretion of the researcher as different names can make sense for the same structure depending on the context and conventions of the field. For simplicity and convenience, we only use NRs and NWs in our discussion. For those 1D nanostructures originally reported under the names, such as nanobars, nanobeams, or nanobelts in literature, we simply call them NRs or NWs depending on their AR, together with the specification of the geometric shape of the cross section. Although most NRs and NWs have the same cross-sectional area along the long axis, some of them may develop a tapered morphology during the growth process, generating cross sections with increasingly smaller areas.[25,33,34] Whenever this happens, the side surface will be covered by high-index facets featuring a high density of atomic steps (see Figure 2E).

2.2. Internal Twin Structure

A 1D metal nanostructure can be monocrystalline, with the same crystal lattice extending over the entire dimensions of the structure; it can contain one or five twin planes running parallel to its long axis; and it can be polycrystalline, comprising multiple monocrystalline domains arranged along its long axis. The internal twin structure is a manifestation of the type of seed involved in the growth, as well as the growth pathway. At very small sizes, there is enough thermal energy for a nucleus to fluctuate among different shapes and crystal structures.[35] The fluctuation will cease once the nucleus has grown to reach a certain size, generating a minuscule structure commonly referred to as a seed. Within a certain size range, twinned structures can be energetically more favorable than the monocrystalline counterpart due to the requirement to minimize the total free energy. As a result, seeds with different numbers of twin planes, including monocrystalline (no twin plane), singly twinned (one twin plane), and multiply twinned (typically, five twin planes), can all be formed in the early stage of a colloidal synthesis. The exact populations of these different types of seeds are determined by the experimental conditions, in particular, the initial reaction rate involved in the nucleation step.[36] By optimizing the experimental parameters, it is feasible to obtain a pure sample of seeds characterized by a single type of internal twin structure. As illustrated in the top panel of Figure 3, the internal twin structure of the seed will be preserved when the seed grows anisotropically to evolve into a 1D nanostructure through atomic addition.

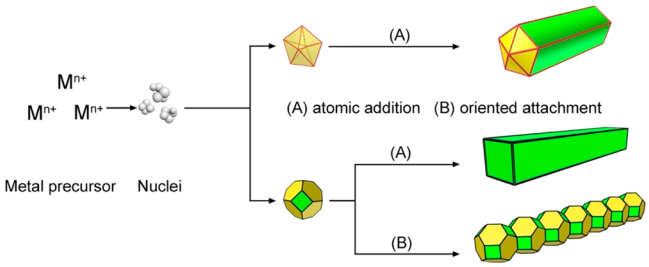

Figure 3. Schematic illustration showing the growth of 1D nanostructures through two different pathways: (A) atomic addition and (B) oriented attachment.

For a face-centered cubic (*fcc*) metal, monocrystalline seeds (typically, in a cuboctahedral shape and covered by a mix of {111} and {100} facets) can grow to evolve into NRs with a square, rectangular, or octagonal cross section.[37] Monocrystalline NRs with a square or rectangular cross section are also referred to as nanobars in the literature.[38–40] They can be considered as nanocubes elongated along one or two of the three axes of an *fcc* lattice, so their surface is still enclosed by {100} facets, together with some truncations at the corners and edges, just like those of a nanocube. When the edges are

DOI: 10.1021/acs.chemrev.8b00745
Chem. Rev. XXXX, XXX, XXX–XXX

significantly truncated, the 1D nanostructures become NRs with an octagonal cross section.[38,41−44] Truncation at edges may also lead to the formation of high-index facets on the surface, rather than just {110} facets. In early reports, it was claimed that the side surface of a AuNR was covered by alternating four {100} and four {110} facets while their caps were thought to be enclosed by four {111} and four {110} facets, together with {100} facets at the ends.[41,42] Later studies revealed that the side surface of a AuNR could be encased by {520} facets, alternating {520} and {110} facets, or {0512} facets.[43,44] Upon further growth along the long axis, NRs with a rectangular cross section will evolve into nanobelts, a morphology more commonly observed for 1D nanostructures made of metal oxides rather than metals.[45] In our discussion, nanobelts are referred to as NWs with a rectangular cross section.

For the seeds featuring a singly or multiply twinned structure, they can grow to evolve into nanobeams and penta-twinned NRs (or NWs), respectively. The nanobeam contains a single twin plane running parallel to the long axis, and will be called a NW in our discussion.[46] The penta-twinned NRs and NWs are supposed to evolve from decahedral seeds whose surface is covered by 10 {111} facets and five twin boundaries. During growth, it is hypothesized that atoms are preferentially deposited onto the twin boundaries, followed by their diffusion to the {111} facets.[9,47−56] Penta-twinned NRs and NWs contain five twin planes running parallel to the long axis, while their side surface is covered by five {100} facets and their ends are capped by a pentagonal pyramid consisting of five {111} planes and five twin boundaries.

As an alternative growth pathway to atomic addition, the seeds can also self-assemble into 1D nanostructures through random aggregation or oriented attachment (Figure 3, bottom panel).[18,57−66] As a signature of this growth pathway, there are multiple planar defects, including twin boundaries and stacking faults, oriented perpendicular to the long axis as a result of imperfect alignment between the seed particles during their aggregation or attachment process. This growth pathway can also lead to the production of NWs with a wavy morphology due to the presence of grooves at the interfaces among the constituent seed particles. Surface diffusion after the assembly process can help smooth out these grooves, improving the mechanical strength of the NWs.[18] This growth route can be validated by following the growth process through in situ transmission electron microscopy (TEM) (see section 4).

2.3. Branched, Segmented, Core−Sheath, Core−Satellite, and Hollow 1D Nanostructures

Additional variations to 1D nanostructures include branched (or dendritic) morphologies, as well as the formation of a hollow, core−sheath, core−satellite, alloyed, or spatially segmented structure. Branched or dendritic nanostructures can be obtained through additional growth of NRs or even NWs from the surface of presynthesized 1D nanostructures.[67−72] In particular, site-selective overgrowth of the second metal on the ends of 1D metal nanostructures can lead to the formation of structures with a segmented[73−78] or dogbone-like (or tadpole)[79−83] morphology. When the second metal is applied uniformly to the entire surface of a 1D nanostructure, the resultant structure is often referred to as either core−shell or core−sheath depending on the AR.[84−90] Seed-mediated growth represents the most versatile route to the fabrication of such nanostructures. The shell or sheath can be leveraged to modify the properties of the 1D nanostructures. If the 1D nanostructures have a hollow interior, one will obtain nanotubes when the AR is relatively large. The hollow interior is often generated through the use of a sacrificial template.[91−93]

3. COLLOIDAL SYNTHESIS OF 1D METAL NANOSTRUCTURES

Over the past two decades, a wide variety of strategies for the colloidal syntheses of 1D metal nanostructures have been demonstrated and refined, with notable examples including one-pot synthesis, seed-mediated growth, oriented attachment, and template-assisted growth. In this section, we focus our discussion on the methods and mechanistic insights associated with the production of 1D metal nanostructures. We also cover the fundamentals of nucleation and growth, as well as other general concepts typically involved in the colloidal synthesis of metal nanostructures.

3.1. Challenges in Creating and Preserving 1D Metal Nanostructures

Despite the remarkable progress, it remains a challenging task to produce 1D metal nanostructures in a predictable, controlled, and deterministic fashion. Because of the high symmetry associated with the cubic lattice taken by most metals, it is not an easy matter to force the seed to evolve into an anisotropic shape during a colloidal synthesis.[94] For example, we have to overcome the strong tendency of a monocrystalline nanostructure made of an *fcc* metal to reduce its total surface energy by taking a highly symmetric shape in the form of cube, cuboctahedron, or octahedron. In addition, the lack of an external driving force for initiating and sustaining anisotropic growth in an isotropic medium in the absence of a template also makes it very difficult to create the 1D morphology. In general, to initiate and sustain anisotropic growth from a highly symmetric seed, the synthesis has to be placed under a kinetic control, which can be achieved by manipulating the generation or deposition rate of metal atoms, as well as the surface diffusion rate of adatoms.[95] For example, anisotropic growth will naturally occur when the number of atoms available for heterogeneous nucleation is fewer than the number of equivalent growth sites on the surface of a seed. At the same time, the use of a relatively low temperature can suppress the surface diffusion of adatoms and thus help retain the anisotropic growth pattern in the course of a colloidal synthesis.

In addition to the difficulty in generating anisotropic nanostructures, the intrinsic instability of a 1D nanostructure also presents a major challenge. Because of the high surface-to-volume ratio, it is difficult to preserve the 1D morphology in the presence of an oxidant (e.g., O_2 from the air) for the metal and a coordination ligand for the corresponding metal ion because of oxidative etching. Taking PdNWs as a typical example, when they were dispersed in diethylene glycol (DEG, a polyol used for the synthesis) and aged at 160 °C for 4 h in the presence of poly(vinylpyrrolidone) (PVP), the 1D morphology could be preserved (Figure 4A).[96] When the aging time was extended to 12 h, however, the NWs were transformed into NRs with rough surfaces and varying diameters (Figure 4B). In comparison, most of the PdNWs were quickly fragmented to form nanoparticles after aging in DEG-containing PVP, NaI, and HCl for just 10 min (Figure

DOI: 10.1021/acs.chemrev.8b00745
Chem. Rev. XXXX, XXX, XXX−XXX

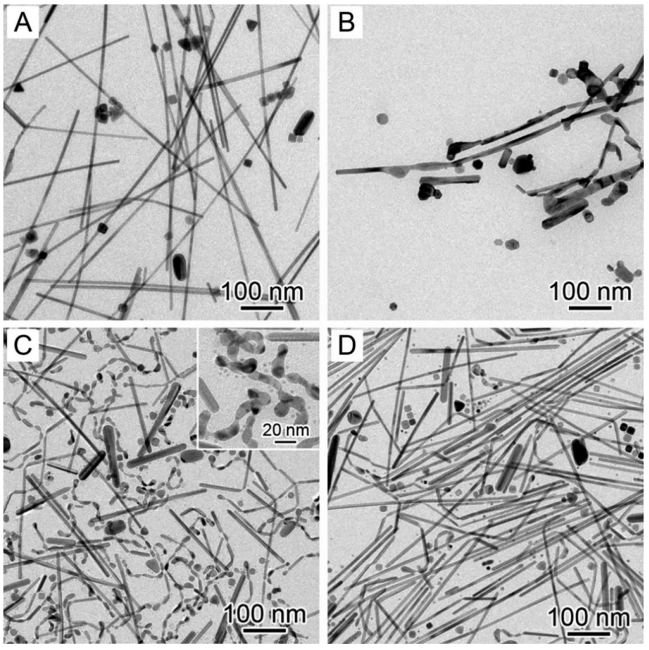

Figure 4. TEM images of the products obtained by aging the PdNWs at 160 °C. The NWs were dispersed in (A, B) DEG-containing PVP for 4 and 12 h, respectively; (C) DEG-containing NaI, PVP, and HCl for 10 min; and (D) DEG-containing NaI, PVP, and HCl for 60 min, while argon was bubbled through the solution. Reprinted with permission from ref 96. Copyright 2017 American Chemical Society.

4C). The presence of a coordination ligand such as I^- and Cl^- resulted in the oxidative etching of PdNWs by promoting the formation of $PdCl_4^{2-}$ or PdI_4^{2-}. The O_2 from the air also played an important role in accelerating the destruction of PdNWs. When argon was bubbled through a similar DEG solution containing PVP, NaI, and HCl, most of the PdNWs can be retained after aging at 160 °C for 60 min (Figure 4D). Taken together, it is clear that 1D metal nanostructures, especially those containing twin defects, are vulnerable to corrosion caused by oxidative etching. This intrinsic instability further contributes to the difficulty in generating, storing, and utilizing 1D metal nanostructures.

3.2. Homogeneous Nucleation versus Heterogeneous Nucleation

In a one-pot synthesis of metal nanostructures, a precursor compound is either decomposed or reduced to generate zerovalent atoms—the basic building blocks of the nanostructures. The atoms then undergo homogeneous nucleation (or self-nucleation) to generate nuclei, followed by growth to evolve into seeds and then nanostructures. This process is expected to follow the LaMer model established in the 1950s to account for the chemical synthesis of sulfur hydrosols with uniform sizes by reacting $Na_2S_2O_3$ with HCl in an aqueous solution (Figure 5A).[97] When applied to the colloidal synthesis of metal nanostructures,[37] the concentration of metal atoms is supposed to increase steadily with reaction time as the precursor is reduced or decomposed. Once the concentration of atoms reaches the minimum level of supersaturation, the atoms will start to aggregate to generate nuclei (i.e., small clusters consisting of atoms and ions) and then seeds (i.e., nanocrystallites with well-defined internal twin structures) in a process commonly referred to as homogeneous nucleation. The seeds will then grow in an accelerated manner because of autocatalysis so the concentration of metal atoms in the solution will drop quickly. Once the concentration has dropped below the minimum level of supersaturation, no additional nucleation event will be able to occur. With a continuous supply of atoms because of the reduction or decomposition of the remaining precursor, the seeds will grow into nanostructures with increasing sizes until the synthesis is terminated or an equilibrium state is reached between the atoms on the surface of the nanostructures and those in the reaction solution. Although this simple model is only qualitative in terms of description, the fundamental concept is still useful in understanding the mechanistic details of a colloidal synthesis of metal nanostructures.

Preformed seeds with a well-defined internal twin structure and facets can also be introduced into a synthesis to serve as primary sites for nucleation and growth (Figure 5B).[98] In this

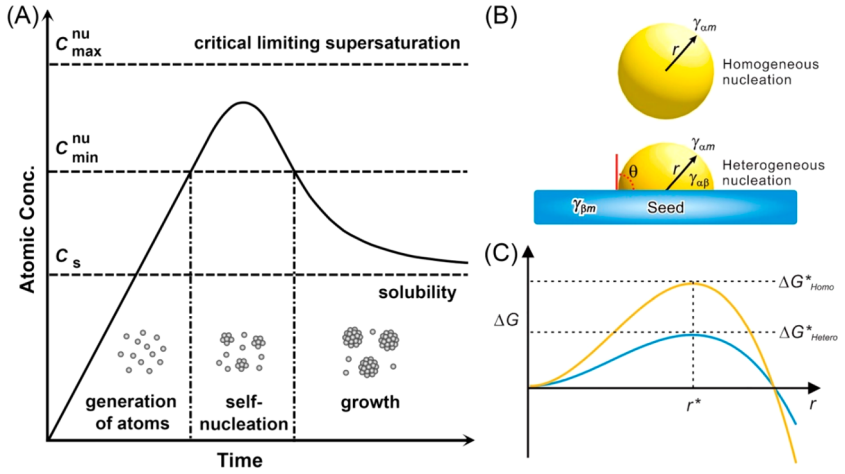

Figure 5. (A) Plot of the concentration of atoms as a function of time, illustrating the processes of atom generation, self-nucleation, and growth. (B) Illustration of two different nucleation modes: (top) homogeneous nucleation in the reaction solution and (bottom) heterogeneous nucleation on the surface of a seed. (C) Plot showing the change in Gibbs free energy as a function of particle size for homogeneous (yellow line) and heterogeneous nucleation (blue line). (A) Modified with permission from ref 97. Copyright 1950 American Chemical Society. (B, C) Reprinted with permission from ref 98. Copyright 2016 Wiley-VCH.

DOI: 10.1021/acs.chemrev.8b00745
Chem. Rev. XXXX, XXX, XXX−XXX

case, the newly formed atoms can nucleate on the surface of the introduced seeds at a concentration well below the minimum level of supersaturation in a process usually referred to as heterogeneous nucleation. If the incoming atoms and those on the seeds have the same chemical identity, the atoms newly formed in the reaction solution will be deposited on the seeds through an epitaxial process, in which the deposited atoms will take a crystal structure identical to that of the seed. When two different metals are involved, a large mismatch in lattice constant may exist, often resulting in the formation of planar defects. Relative to homogeneous nucleation, a much smaller driving force (i.e., with the requirement of a lower concentration of atoms or a lower reaction temperature) is needed for heterogeneous nucleation (Figure 5C), making seed-mediated growth favorable in most cases. In general, when we want to avoid homogeneous nucleation and thus the formation of undesired nanoparticles during seed-mediated growth, the minimum level of supersaturation should be treated as the upper limit for the concentration of atoms in the reaction solution to ensure that all the newly formed atoms will be deposited on the added seeds.

3.3. Different Routes to the Formation of 1D Metal Nanostructures

As discussed above, the atoms generated from the reduction and/or decomposition of a precursor will either aggregate to form nuclei/seeds or be deposited onto the preformed seeds. To achieve anisotropic growth for the formation of 1D metal nanostructures, symmetry breaking has to occur during the deposition of atoms.[94] Alternatively, the seeds (or even larger nanoparticles) can assemble through random aggregation or orientated attachment for the generation of 1D nanostructures.[18] In both cases, templates featuring a 1D morphology can also be introduced to help guide the deposition and assembly processes.

3.3.1. Atomic Addition. *3.3.1.1. Reduction Pathways.* As demonstrated in a series of recent studies, the reduction of a metal precursor may take two completely different pathways during the synthesis of metal nanostructures: solution reduction versus surface reduction.[99−101] When a precursor is introduced into the reaction solution containing a reductant, it can be directly reduced in the solution phase through collision and electron transfer with the reductant, in a process referred to as solution reduction (Figure 6A). The resultant atoms then undergo homogeneous or heterogeneous nucleation, with the latter being more favorable due to its lower activation energy barrier. In the presence of seeds, formed in situ through homogeneous nucleation or preformed and introduced into the reaction solution, the precursor can undertake an alternative pathway known as surface reduction (Figure 6B). In this case, the precursor adsorbs onto the surface of a seed or growing nanostructure, followed by reduction to the elemental form for incorporation into the surface of the nanostructure.

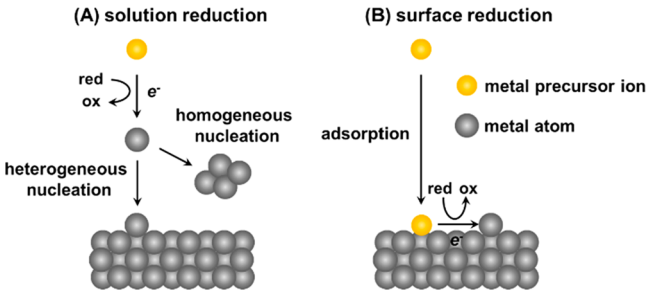

Figure 6. Schematic illustrations of the two different reduction pathways: (A) solution reduction and (B) surface reduction. Modified with permission from ref 99. Copyright 2017 American Chemical Society.

At the beginning of a one-pot synthesis, the solution-phase reduction should be the only option for the metal precursor. However, once seeds have been formed (or in the case of seed-mediated growth with the introduction of preformed seeds), the reduction of the precursor may take either of the two pathways. On the basis of quantitative analysis, it was demonstrated that the precursor would be reduced on the surface of a seed through an autocatalytic process when the rate of reduction is slow, whereas it would be reduced in the solution phase when the rate of reduction is fast.[99] In the case of Pd, for example, small particles generated through homogeneous nucleation were observed in the products when $PdCl_4^{2-}$ was used as a precursor while nearly all the atoms were deposited on the introduced seeds when using $PdBr_4^{2-}$ as a precursor. Because the reduction potential of $PdCl_4^{2-}$/Pd is more positive than $PdBr_4^{2-}$/Pd, $PdCl_4^{2-}$ prefers to be reduced in the solution phase because of the fast reduction kinetics, while $PdBr_4^{2-}$ tends to be reduced on the surface of a seed because of the slow reduction kinetics. Interestingly, for the same pair of precursor and reducing agent, it was demonstrated that the reduction pathway could be switched from one to another depending on the reaction temperature which can affect the reduction kinetics. For example, when $PdBr_4^{2-}$ was reduced in the presence of Pd seeds, a transition from surface reduction to solution reduction was observed as the reaction temperature was increased.[99] This quantitative understanding of reduction pathway can serve as a guideline for the rational synthesis of 1D metal nanostructures with desired properties. However, since all the observations and analyses with regard to the reduction pathway were made in the past few years, we are unable to deliberately elaborate on this subject when discussing most of the synthetic methods.

3.3.1.2. Site Selectivity. During the growth of a nanostructure, the incoming atom (or precursor in the case of surface reduction) always needs to decide onto which site it will land in order to be incorporated into the nanostructure. To minimize the total surface free energy, the atom prefers to land on the site with the greatest energy. As a result, only those sites with the lowest energy will be exposed on the surface of the final nanostructures. For example, the reduction of a Ag(I) precursor in the presence of Ag spheres or cubes will lead to the formation of Ag octahedra enclosed by {111} facets in the absence of a capping agent such as PVP, which blocks the growth on {100} facets.[102] Because of the intrinsically lower energy of {111} facets relative to {100} facets for an *fcc* crystal, the deposition of Ag atoms favors {100} facets in the absence of PVP, leaving behind {111} facets on the surface for the formation of nanocrystals with an octahedral shape.

Although atomic deposition on high-energy facets is thermodynamically preferred because it lowers the total surface free energy, the actual deposition pattern of atoms is affected by many other parameters. In general, the final location of the deposited atom is governed by a combination of intrinsic and extrinsic experimental parameters, including the extent of lattice mismatch, type and coverage density of the capping agent, reduction potentials of the metal precursor, type

DOI: 10.1021/acs.chemrev.8b00745
Chem. Rev. XXXX, XXX, XXX−XXX

of reducing agent, solvent, and reaction temperature, among others. For example, monocrystalline Ag nanocubes mainly covered by {100} facets would be obtained when reducing $AgNO_3$ with ethylene glycol (EG) in the presence of PVP.[103] Further investigations confirmed that PVP interacted more strongly with Ag atoms on the {100} facets than those on the {111} facets and the strong interaction greatly reduced the growth rate on Ag(100) surface.[104] If PVP was not present, the Ag atoms generated from the reduction of $AgNO_3$ would nucleate and grow into octahedra bounded by the most stable {111} facets. A similar strategy was also involved in the synthesis of AgNWs where the capping effect from PVP greatly stabilized the {100} facets on Ag nanostructures for the formation of penta-twinned NWs covered by {100} side faces.[47]

3.3.1.3. Symmetry Breaking. Constrained by the inherent *fcc* lattice, most of the shapes taken by noble-metal nanostructures are highly symmetric in terms of spatial arrangements of atoms. The products usually exhibit a monocrystalline structure such as cube, cuboctahedron, or octahedron, as well as a multiple-twinned structure like decahedron or icosahedron. At the fundamental level, symmetry breaking involves the inhibition (or promotion) of growth for some of the equivalent sites on the surface of a growing seed, resulting in a nanostructure with reduced symmetry relative to the initial seed.[94,105] This process is dictated by both kinetic and thermodynamic parameters and can be controlled by carefully manipulating the experimental conditions. A number of strategies have been developed for breaking/reducing the symmetry of a seed particle (Figure 7), including the manipulation of reduction or decomposition kinetics to limit the supply of atoms, formation of internal twin defects, involvement of different metals with a large lattice mismatch, selective capping (or asymmetric passivation) of the surface of a seed, and participation of oxidative etching. In the following discussion, we will provide a brief account of each strategy.

3.3.1.3.1. Manipulation of Reaction Kinetics. Limiting the supply of precursor or atom will inevitably result in their uneven nucleation and deposition on the multiple equivalent sites present on the surface of a seed.[105−108] As shown in Figure 7A, once a few atoms have landed at one site on a seed, continued growth will be favored at this activated location owing to a relatively higher surface energy relative to other sites. When the supply of precursor molecules or the resultant atoms is limited, it will be impossible for the growth to occur at all the equivalent sites on the surface of a seed, leading to an asymmetric pattern for the nucleation and deposition and thus the generation of anisotropic shapes.

By manipulating the reduction rate at which the atoms are produced from a precursor, the supply of atoms can be conveniently managed. In general, the reduction rate of a precursor is determined by a set of parameters, including the type and concentration (related to the injection rate) of the precursor, the type and concentration of the reducing agent, temperature, and pH value of the reaction solution. For example, one can finely control the deposition pattern of Ag atoms on the surface of a Au decahedral seed by tuning the reduction kinetics of the Ag(I) precursor with ammonia.[75] It was demonstrated that, although the complexation of Ag(I) ions with ammonia might slow down the reduction kinetics, increasing the concentration of ammonia led to an increase in the alkalinity of the solution and thus a stronger reducing

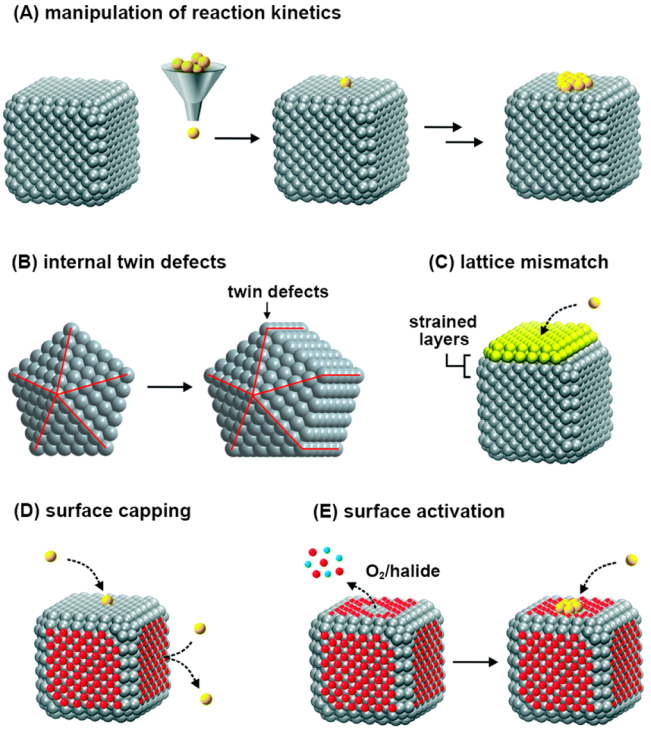

Figure 7. Schematic illustrations showing the asymmetric growth enabled by (A) manipulation of reduction kinetics, (B) twin defect, (C) lattice mismatch, (D) surface capping, and (E) surface activation. For clarity, the atoms added to the surface of a seed and the metal ions released from the etching take golden and blue colors, respectively. The twin defects in (B) are marked by red lines and the multiply twinned structure has an icosahedral shape. The red spheres in (D and E) correspond to the capping agent chemisorbed on the surface of the seed. Modified with permission from ref 94. Copyright 2017 Royal Society of Chemistry.

power for the polyol, which in turn accelerated the reduction of Ag(I). When a relatively low concentration of ammonia was used, the slow reaction rate favored asymmetrical growth to generate Au-tipped AgNRs, in which the Au seed was located at one of the two ends of each NR. In the case of a fast reduction rate at a high concentration of ammonia, symmetrical growth dominated, leading to the formation of Ag−Au−Ag NRs, in which the Au seed was located at the midpoint of each NR. When Pd or Ag cubic seeds were used for the deposition of Ag atoms, it was demonstrated that the deposition could be confined to one to six side faces by carefully manipulating the reduction kinetics.[106−108] Specifically, the deposition or growth could be confined to one of the six side faces at an extremely slow reduction rate, resulting in the formation of Pd−Ag nanobars with a Janus configuration or Ag nanobars.

3.3.1.3.2. Internal Twin Defects. When seeds with twin defects are used for growth, a thermodynamic driving force may be responsible for their asymmetric growth into 1D nanostructures (Figure 7B). Notable examples include the formation of penta-twinned NRs or NWs from decahedral seeds.[47] As the decahedron is not a space-filling structure, it is hypothesized that atoms located farther away from the central axis of a decahedron will experience a larger lattice strain and thus a higher energy. The strain energy will increase if the decahedral seed grows laterally while, in contrast, elongation of a decahedral seed along the axial direction parallel to the twin

DOI: 10.1021/acs.chemrev.8b00745
Chem. Rev. XXXX, XXX, XXX−XXX

planes will not experience additional penalty in terms of strain energy.[109] As a result, the decahedral seed would preferentially grow along the axial direction to evolve into a penta-twinned NR and then NW instead of growing laterally into a decahedron with a larger size. As some of the popular examples of 1D nanostructures, penta-twinned Au, Ag, and Cu NRs have all been successfully synthesized using decahedral seeds generated in the initial stage of a synthesis, or preformed and introduced into the reaction solutions.[47−56] In another report on the growth of penta-twinned AgNWs, it was proposed that the NW could be considered as a combination of a heavily strained core and a less-strained sheath. The crystalline defects in the core provided active sites for the growth of an NW along the longitudinal axis, while the less-strained side faces of the NW are lower in reactivity toward the deposition of atoms to make them thicker. The difference in reactivity between the ends and side faces could serve as a driving force for the anisotropic growth of a penta-twinned NW.[110]

3.3.1.3.3. Lattice Mismatch. Lattice mismatch refers to the situation in which two solid materials with different lattice constants share a common interface. When the deposited material is similar in terms of both structure and lattice constant to the substrate material, a strain-free, uniform layer can be formed over the entire surface of the substrate. In contrast, if the lattice mismatch between the two materials is too large (e.g., equal to or exceeding 5%), the strain energy arising from the lattice distortion at the interface will alter the growth pattern (Figure 7C). Once the second metal has nucleated on the surface of a seed, subsequent deposition will be favored at the lattice-matched location (i.e., the sites covered by the same material) to minimize the interfacial strain. The seeds can only be completely covered after a sufficiently large number of atoms has been deposited and spread out across the surface. When the lattice mismatch between two materials is excessive, failure to achieve epitaxial growth will lead to the generation of defects, providing another route to symmetry breaking.

A notable example can be found in the synthesis of Au@Cu NRs using monocrystalline Au spheres as seeds.[111] Because of the large (12%) lattice mismatch between Au and Cu, the freshly reduced Cu atoms tended to land onto the sites at which the previously formed Cu atoms had already been deposited. In this case, Au−Cu Janus structures were formed in the initial stage of a synthesis. The strain energy associated with a large lattice mismatch could effectively induce the formation of twin planes on the monocrystalline Au seed and led to the formation of a penta-twinned Cu shell. As the reaction proceeded, the twinned structure slowly evolved into CuNRs with the Au seeds completely encased in each NR.

3.3.1.3.4. Surface Capping. Surface capping also plays an important role in the synthesis of 1D metal nanostructures. Capping agents are molecular species with relatively strong binding affinity toward specific crystallographic facets on a nanostructure.[37,112] Typical examples include monatomic ions (e.g., halides such as Cl^- and Br^-), small gas molecules (e.g., CO, O_2, and H_2S), coordination ligands (e.g., thiols and amines), surfactants, and polymers (Figure 7D). By selectively binding to the surface of a seed, a capping agent can markedly impede the deposition of atoms, and serve as a barrier to the surface diffusion of adatoms. In this way, the growth rate of the capped region will be greatly retarded, and the capped facets will be preferentially exposed on the surface of the resultant nanostructures. In general, the coverage density of a capping agent on a seed should be more or less the same for equivalent facets related by symmetry. However, if the capping agent is partially removed or its concentration in the solution is too low to ensure a complete coverage, the deposition will occur preferentially on the less capped region, resulting in the formation of asymmetric nanostructures.[94]

Through the deactivation of certain facets, a capping agent can help initiate and direct the growth of nanostructures into shapes not favored in terms of minimization of surface energy. For example, when Cu atoms were deposited onto a Pd decahedral seed in the presence of hexadecylamine (HDA) and Cl^- ions, a penta-twinned CuNR was obtained with a Pd seed located at one of the two ends of each NR.[113] Because of the strong binding of HDA to Cu(100), the side faces covered by {100} facets were stabilized and a penta-twinned shape was favored. Another example is the synthesis of penta-twinned AgNWs in the presence of PVP.[47] It was proposed that multiply twinned Ag particles were formed in the initial stage, which then grow into NWs due to the selective coverage of the {100} facets on side faces with PVP while leaving the {111} facets at two ends largely uncovered and thus reactive for continuous growth. In addition to capping agents, the deposition of atoms onto the surface of a seed can also be inhibited by selective depositing an inert material (e.g., SiO_2) on certain regions of a seed.

Underpotential deposition (UPD) of metal atoms is one of the most widely used methods for guiding the shape evolution of metal nanostructures.[114] Underpotential deposition refers to the electrodeposition of one metal as a monolayer on another metal at potentials significantly less negative than what is required for the deposition on the surface of the first metal. This process allows for a precise control of the surface coverage caused by the selective capping of metal atoms, leading to the formation of nanostructures with well-defined shapes. A notable example is the use of Ag(I) ions in the synthesis of Au nanostructures.[115] It was proposed that up to one monolayer of Ag atoms could be deposited onto an existing Au surface through the UPD process, stabilizing certain facets of Au and thus directing the evolution of 1D Au nanostructures. When different concentrations of Ag(I) was used, high-index facets such as {110}, {310}, or {720} could be stabilized, leading to the formation of Au nanostructures in the shape of a rhombic dodecahedron, rod, truncated ditetragonal prism, and concave cube, respectively.

3.3.1.3.5. Surface Activation. Site-selective surface activation is another strategy commonly used for the synthesis of anisotropic nanostructures, and oxidative etching is often involved in this process. In the presence of an oxidant/ligand pair (e.g., O_2/halide), corrosion will be initiated from a limited number of sites rather than the entire surface. The corrosion can subsequently accelerate the deposition on these sites by means such as removing the capping agents or increasing the surface roughness, and the resultant anisotropic growth can lead to the formation of asymmetric structures (Figure 7E). A notable example can be found in the synthesis of Pd nanobars through surface activation with oxidative etching.[38] In the synthesis of Pd nanocubes, the addition of Br^- at a sufficiently high concentration could lead to the coverage of the entire surface of Pd cubes with Br^- ions because of the strong binding to {100} facets. The chemisorbed Br^- layer retarded further addition of Pd atoms from solution to the surface, inhibiting the growth. However, when oxidative etching was initiated on

DOI: 10.1021/acs.chemrev.8b00745
Chem. Rev. XXXX, XXX, XXX−XXX

one of the six side faces of a cubic seed, with the dissolved oxygen and Br^- ions acting as the oxidant/ligand pair, some of the Pd atoms could be dissolved from the surface. The etching activated the side face because of desorption of Br^- anions from the surface, and then the newly formed Pd atoms were selectively and continuously deposited onto the activated side face, resulting in the formation of Pd nanobars. The same mechanism might also be involved in the synthesis of monocrystalline Au@Ag NRs.[76]

3.3.1.3.6. Surface Diffusion. In addition to deposition, the diffusion of adatoms plays an important role in the shape-controlled synthesis of metal nanostructures. It was demonstrated that it is the relative rate (V) of atom deposition over surface diffusion that determines the growth pathway of a seed and thus the shape or morphology taken by the final product.[116] Using the overgrowth of Pd cubic seeds as a model system, it was shown that when $V_{deposition}/V_{diffusion} \gg 1$, surface diffusion could be ignored and thereby the growth will be largely confined to the corner sites, resulting in the formation of Pd octopods. In contrast, when $V_{deposition}/V_{diffusion} \ll 1$, growth was dominated by surface diffusion and most of the atoms at the corners migrated to edges and side faces of the cubic seed, leading to the formation of a cuboctahedron to minimize the total surface energy. As a result, to generate 1D nanostructures through symmetry breaking from the initially formed seeds, the ratio of the deposition rate to the diffusion rate has to be properly controlled.[95] When the diffusion rate exceeds that of deposition, the resultant nanostructures often adopt a symmetric shape favored by thermodynamics. Only when the deposition rate exceeds that of surface diffusion, the deposited atoms will be able to land and stay at the sites of deposition, facilitating the site-selective, kinetically controlled growth mode. A detailed discussion on surface diffusion is presented in section 3.4.2.

3.3.2. Random Aggregation and Oriented Attachment. Aggregation-based growth, which involves coalescence of nanoparticles rather than atomic addition, has been widely observed in the synthesis of nanostructures.[57−66,117,118] Typically, the nanoparticles can be attached to each other in a random or oriented manner (Figure 8A and B). Compared to random aggregation, which does not involve the orientation of crystal lattices, oriented attachment can be more favored thermodynamically for the growth of 1D metal nanostructures. Segmented 1D nanostructures can also be obtained through an oriented attachment mechanism. It should be pointed out that, because the existence of Brownian motion for the nanoparticles in a solution, random aggregation or disordered attachment may also be involved. In addition, misorientation or imperfectly oriented attachment is frequently observed, leading to the inclusion of planar defects.[119]

Oriented attachment could be described as a self-directed arrangement of neighboring nanoparticles that have identical or similar crystallographic structures. These nanoparticles merge together when a favorable crystallographic orientation is encountered. This process can reduce the overall surface energy due to the elimination of energy associated with unsatisfied bonds, and is thus favored thermodynamically. A good understanding of oriented attachment can be achieved using the Derjaguin, Landau, Verwey, and Overbeek (DLVO) theory.[120] In principle, aggregation can be triggered when the repulsion is reduced below a critical level. As an extension to this theory, other non-DLVO forces such as solvation have been taken into consideration.[121] Different from random

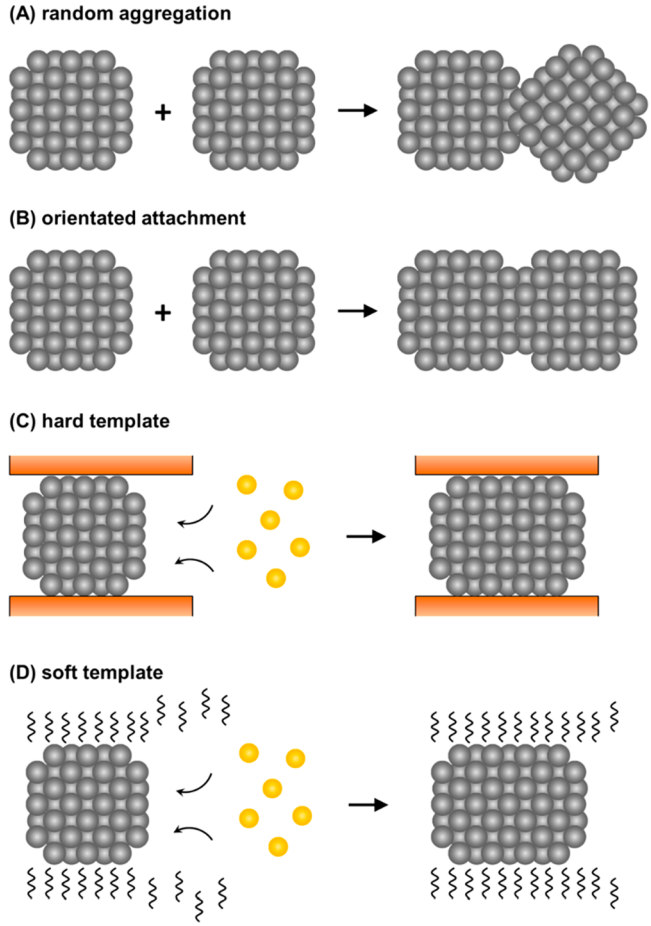

Figure 8. Schematic illustrations of four different strategies for generating 1D nanostructures: (A) random aggregation, (B) oriented attachment, and template-directed growth with the use of (C) hard and (D) soft templates, respectively. The orange spheres, gray spheres, brown blocks, and wavy lines represent metal ions, atoms, hard templates, and surfactants, respectively.

attachment, for inorganic nanoparticles in close proximity, Coulombic forces dominate over van der Waals interactions and random Brownian forces in guiding the interacting particles to find energetically favorable crystallographic orientations for attachment.

The aggregation-based growth mechanism was proposed in 1998 to account for the growth of TiO_2 nanocrystallites under hydrothermal conditions.[122] Perfect single crystals were formed if the adjacent nanoparticles adopted parallel crystallographic orientations, whereas slight misorientation between them would lead to the formation of dislocations. A similar phenomenon was also observed in some natural minerals, such as iron oxyhydroxide,[123] where it was found that the adjacent 2- to 3 nm particles could spontaneously aggregate and further grow into bulk crystals. In recent years, efforts have been directed to a systematic investigation of oriented attachment and this process has been applied to the synthesis of several kinds of nanostructures, including 1D metal nanostructures, such as NRs, NWs, and dendrites, among others.[119,124,125]

3.3.3. Template-Directed Synthesis. Template-directed synthesis offers a straightforward route to the generation of 1D nanostructures. As we mentioned in the previous sections, the growth of 1D nanostructures could proceed through an atomic addition or particle aggregation pathway, with atoms or

DOI: 10.1021/acs.chemrev.8b00745
Chem. Rev. XXXX, XXX, XXX−XXX

particles serving as the building blocks. In both cases, templates can be introduced to help direct the assembly of these building blocks into 1D nanostructures. In this approach, the template can simply serve as a scaffold within (or around) which a different material is generated in situ and shaped into a nanostructure with its morphology similar to that of the template. A variety of templates have been reported, with notable examples including step edges present on the surface of a solid substrate,[126] channels within a porous material,[127] mesostructures assembled from surfactants or polymers,[128] biological macromolecules, such as proteins, DNA, or viruses,[129] and existing nanostructures with various shapes.[130] When the template is only involved physically, it is necessary to selectively remove the template using postsynthesis treatment (such as chemical etching or calcination) to obtain pure products. In a chemical process, the template is usually consumed as the reaction proceeds and it is possible to directly obtain the products. Although template-directed synthesis offers a simple and straightforward route with good reproducibility, the quantity of the structures that can be produced in each batch is rather limited and polycrystalline products are often obtained. Here, we focus on three major types of templates that are widely used in the synthesis of 1D metal nanostructures, including both hard and soft templates, as well as existing nanostructures.

3.3.3.1. Channels in Porous Materials (Hard Templates). Channels in porous materials provide a class of straightforward templates for use in the synthesis of 1D nanostructures. Typically, three steps are involved in this process: (i) infiltration of the channels with an appropriate precursor via a solution-based approach; (ii) conversion of the precursor to the desired element under the physical confinement of the channels; and (iii) recovery of the nanostructures by selectively removing the template (Figure 8C). Porous materials with different pore sizes, including macroporous (>50 nm in diameter) and mesoporous (1.5−30 nm) have been explored.[131] For example, Pt and PtRu NWs with a uniform diameter of 30 nm were synthesized by templating with an anodic aluminum oxide (AAO) membrane.[132] In a typical synthesis, an AAO film with a pore diameter of 40 nm was fabricated on a Ti/Si substrate and then used as a template for the electrodeposition of Pt or PtRu NWs using H_2PtCl_6 or H_2PtCl_6 and $RuCl_3$ as the precursors. The electrodeposition was continued until the deposited NWs overflowed from the channels in the template. The sample was then immersed in NaOH solution to remove the AAO template and obtain an array of metal NWs on the Ti/Si substrate.

In addition to the macroporous templates, 1D nanostructures with smaller diameters can be produced using mesoporous templates. For example, AgNWs with uniform diameters of 5−6 nm and large ARs between 100−1000 were obtained through impregnation of $AgNO_3$ solution into mesoporous silica SBA-15 template, followed by the thermal decomposition of $AgNO_3$ at 300 °C.[127] Carbon nanotubes (CNTs) represent another class of templates that can be used to direct the formation of 1D nanostructures.[133] With at least one open end, CNTs could be filled with a salt solution through capillary action. After the reduction of the metal precursor and removal of the tubular templates, 1D nanostructures were obtained. In this way, metal NWs, including Au, Ag, Pt, Pd, and Ru, have all been successfully produced by templating with single-walled CNTs.

3.3.3.2. Self-Assembled Molecular Structures (Soft Templates). Structures self-assembled from surfactants provide another class of simple and versatile templates for the fabrication of 1D nanostructures in relatively large quantities. The surfactant molecules can spontaneously organize into rod- or wire-shaped micelles (or inverse micelles) when their concentration reaches a critical value. The micelles comprised of surfactants can be immediately used as soft templates to promote the formation of 1D nanostructures when coupled with an appropriate chemical reaction. When the reaction is completed, the surfactant molecules need to be selectively removed by dissolution or ligand exchange to collect the nanostructures as pure samples (Figure 8D). By leveraging this procedure, a variety of 1D metal nanostructures have been produced.[1] For example, PtNW networks with a diameter of 2.2 nm were synthesized by reducing K_2PtCl_4 with $NaBH_4$ in the presence of a soft template formed from cetyltrimethylammonium bromide (CTAB) in a two-phase system containing water and chloroform.[128] It was demonstrated that a network of swollen, worm-like micelles was initially generated within the chloroform droplet, with the CTAB molecules residing at the interface between chloroform and water. The K_2PtCl_4, confined within the inverse micellar network, was then reduced by $NaBH_4$ to generate PtNWs that replicated the structure of the template. Using the same protocol, substitution of a Pd(II) complex for the Pt(II) precursor gave PdNW networks, demonstrating the generality of this method. Although metal NWs can be synthesized in relatively large quantities using this method, the preparation and removal of the micelles is often difficult and tedious, which is one of the major drawbacks of a method involving soft templates.

Metal nanostructures with a controllable thickness and AR can be produced from preformed seeds with the help of soft templates. Notable examples include Au and Ag NRs.[134] In a typical synthesis, Au or Ag nanoparticles (3−5 nm in diameter) were added as seeds into a solution containing rod-like micelles assembled from CTAB and a metal precursor, such as $HAuCl_4$ or $AgNO_3$. When a weak reducing agent (e.g., ascorbic acid) was added, the seeds served as nucleation sites for the growth of NRs within the confinement of the micelle structure. The lateral dimensions and ARs of these NRs could be controlled by varying the amount of the metal precursors relative to the seeds.

Block copolymers—polymers comprising two or more chemically distinct segments (i.e., blocks) that are linked by covalent bonds—have also been exploited as soft templates to direct the growth of 1D nanostructures.[135−137] When the chemically distinct segments are immiscible, the polymer chains will separate into different phases. Under appropriate conditions (e.g., a proper ratio between the molecular weights of different segments), arrays of cylinders could be formed from these polymers, with a structure similar to those self-assembled from surfactants. Different regions in such an arrayed structure can be selectively decorated with metal atoms or filled with a precursor that will later be reduced to the elemental form, making block copolymers a class of versatile templates for the synthesis of 1D nanostructures. To this end, AgNWs have been synthesized using different types of block copolymers as templates, including those made of carbosilane dendrimers and polyisocyanopeptides, or double-hydrophilic poly(ethylene oxide)-*block*-poly(methacrylic acid).[135,136]

DOI: 10.1021/acs.chemrev.8b00745
Chem. Rev. XXXX, XXX, XXX−XXX

3.3.3.3. Existing 1D Nanostructures. Existing 1D nanostructures can also serve as templates to generate 1D nanostructures made of various metals, some of which may be difficult directly synthesize as uniform samples. Taking Cu or Ag NWs as an example, their surface could be directly coated with a conformal sheath made of a different material to form core−sheath NWs. In this case, nanotubes will be obtained after subsequent removal of the original NWs. For example, it was demonstrated that a conformal, ultrathin Au shell with a thickness of 1−2 nm can be deposited onto the surface of Cu (or Ag) NWs by modifying the ligand in the Au(III) precursor complex.[90] The introduction of a phosphine ligand could reduce the reduction potential to a level that the galvanic replacement between Au ions and Cu is no longer favored, favoring the formation of a core−sheath structure. On the other hand, hollow NWs or nanotubes can be directly produced from existing 1D nanostructures using methods, such as galvanic replacement or oxidative etching.[91] Metal nanotubes, including those based on Au, Pd, Pt, and their alloys, have been synthesized using Ag or Cu NWs as templates.[130] See sections 3.4.3 and 3.4.4. for a detailed discussion of galvanic replacement and oxidative etching.

3.4. Chemistry Involved in the Synthesis of 1D Metal Nanostructures

3.4.1. Reduction versus Decomposition. In a colloidal synthesis of metal nanostructures, a precursor is either reduced or decomposed to generate zerovalent atoms, followed by nucleation and growth. The majority of the protocols reported for the synthesis of metal nanostructures are based on reduction, which can be conducted in a variety of media under different conditions, including aqueous, organic, polyol, hydrothermal, and solvothermal. The reduction route is most effective for the monometallic system because it is often very difficult to match the reduction rates of different precursors when more than one metal is involved. In the case of decomposition, it is commonly conducted in an organic medium with the assistance of heating and/or ultrasonication. As an example, monocrystalline PbNWs were prepared via thermal decomposition of $Pb(OAc)_2$ in EG (see section 5.3).[138] The decomposition route is particularly effective for bimetallic and even multimetallic systems as the different metals can be incorporated into the same precursor compound at the right atomic ratio and then generated at that particular ratio during decomposition. In comparison, it is more challenging to precisely control the elemental composition of bi- and multimetallic nanostructures for the reduction route.

3.4.2. Thermodynamics versus Kinetics. When their concentration reaches the minimum level of supersaturation, the atoms derived from reduction or decomposition will nucleate to generate clusters and then seeds with single-crystal or internal twin structures. In general, the formation of seeds with a specific type of internal twin structure is controlled by both thermodynamics and kinetics.[139,140] In addition, the population of different types of seeds can be altered in the presence of other processes, such as oxidative etching and galvanic replacement. Here we provide a brief account of the thermodynamic and kinetic aspects of a typical synthesis of metal nanostructures.

3.4.2.1. Thermodynamics. The thermodynamically controlled product exhibits a global minimum in total free energy, at which point the sum of the surface and volume free energies, internal defects, and strain energies are collectively minimized. For noble metals with an *fcc* structure, the surface energies of the low-index crystallographic facets increase in the order of {111} < {100} < {110}. This sequence implies that a single-crystal seed would take either an octahedral or a tetrahedral shape in order to maximize the expression of {111} facets and thus minimize the total surface free energy.[139] However, both octahedra and tetrahedra have a higher surface area to volume ratio relative to a cube. As a compromise, the seed is supposed to exist as a truncated octahedron (the so-called Wulff polyhedron) enclosed by a mixture of {111} and {100} facets. This shape has a nearly spherical profile and thus the smallest surface area to volume ratio, minimizing the total surface free energy. Similar to a single-crystal seed, the surface of a twinned seed also tends to be covered by a mixture of {111} and {100} facets to lower the total surface free energy. Although twin boundaries can cause internal strain that increases the internal bond energy, the overall free energy of a nanostructure can still be lowered by enabling a larger coverage of {111} planes.

One effective way to drive a nanostructure to adopt a shape or morphology different from the Wulff polyhedron is through the introduction of a capping agent.[37,112] As discussed in section 3.3.1 and summarized in Table 1, capping agents are ionic species, small molecules, or macromolecules that can selectively bind to different types of facets on a nanostructure to alter the surface free energies and therefore their proportions in the final product. When a capping agent is introduced into a reaction mixture, the facets preferentially stabilized by the capping agent will exhibit a lower surface free energy, leading to the formation of nanostructures with a shape that maximizes the surface area of the capped facet. From a kinetic perspective, the capping agent chemisorbed on a facet will serve as a physical barrier to hinder or even prohibit the deposition of atoms on this facet and eventually lead to the formation of a shape with that particular facet being preferentially exposed.

Table 1. Capping Agents Commonly Used for Stabilizing Various Facets on Metal Nanostructures

metals	facets	capping Agents
Cu	{100}	tetradecylamine (TDA)
		HDA
		octadecylamine (ODA)
		oleylamine (OLA)
Ag	{100}	PVP
		Br^-
		cetyltrimethylammonium chloride (CTAC)
	{111}	citric acid
	{110}	Cu(II)
Au	{100}	Br^-
	{111}	citric acid
	{110}	Ag(I)
Pd	{100}	Cl^-
		Br^-
		I^-
	{111}	citric acid
Pt	{100}	CO

A notable example is Br^- ions, which can serve as a capping agent that binds strongly to the {100} facets on Ag and Pd nanostructures.[141,142] This preferential capping will lead to a slower growth rate on the {100} facets and drive the addition of metal atoms to other facets. For single-crystal seeds

DOI: 10.1021/acs.chemrev.8b00745
Chem. Rev. XXXX, XXX, XXX−XXX

terminated with a mixture of {111} and {100} facets, metal atoms will add preferentially to the poorly passivated {111} facets. As a result, a single-crystal cuboctahedral seed will evolve into a cube in the case of symmetric growth, or a NR with a square or rectangular cross section in the case of asymmetric growth.[38] Similarly, for multiply twinned seeds with a decahedral profile, NRs or NWs with a pentagonal cross-section and side surfaces covered by {100} facets will be produced.[47−56]

3.4.2.2. Kinetics. Although thermodynamics provides useful information with regard to the most favored structure at a given size for the seed, accumulating evidence from experimental studies indicate that nanostructures rarely grow in a way that minimizes the total free energy of the final structure. In most cases, the nanostructures would rather settle into locally stable positions, a propensity determined by the interplay of thermodynamics and kinetics.[139] To this end, the exact shape or morphology taken by the nanostructure will be largely determined by the relative ratio of the rates corresponding to atom deposition ($V_{deposition}$) and surface diffusion ($V_{diffusion}$), as discussed in section 3.3.1.[116] Both rates can be manipulated by changing the experimental conditions related to a nanostructure synthesis.

In general, $V_{deposition}$ is directly correlated to the rate at which the newly formed metal atoms are supplied and it is largely determined by the reduction rate (V) of a metal precursor A by a reductant B. In general, R can be expressed as eq 1[139]

$$V = k[A]^x[B]^y \quad (1)$$

where [A] and [B] are the molar concentrations of A and B, respectively, the exponents x and y are the reaction orders with respect to A and B, and k is the rate constant of the reduction reaction, which is strongly dependent on temperature, as well as the nature of the precursor and reductant. As a result, $V_{deposition}$ can be manipulated in a number of different ways, including variations of reagent concentration and reaction temperature, the choice of reductant or precursor, and the type of coordination ligand for the metal ion.

Surface diffusion is a thermally activated process that involves the motion of atoms on a solid surface through a jumping or hopping mechanism.[139] The diffusion rate, $V_{diffusion}$, is largely determined by the diffusion coefficient D, which measures the rate of jumping of an atom across a surface. An Arrhenius-type equation can be used to express the coefficient

$$D = D_0 \exp(-E_{diff}/RT) \quad (2)$$

where D_0 is the diffusion pre-exponential factor, E_{diff} is the potential energy barrier to diffusion, R is the ideal gas constant, and T is the absolute temperature. Clearly, for surface diffusion of adatoms across the surface of a growing seed, D and the corresponding $V_{diffusion}$ are mainly determined by the reaction temperature (T) and E_{diff}. In general, E_{diff} is dependent on a number of factors, including the strength of the bond between the surface atom and the adatom, the crystallographic plane of the surface, the accessibility of the surface (e.g., passivation by a capping agent), and the chemical potential gradient. To conclude, both surface deposition and diffusion play an important role in the growth of nanostructures and the relative ratio of their rates can be finely tuned by controlling the experimental conditions.[116]

In addition to controlling the overgrowth of nanostructures from seeds, kinetics also provides us with a powerful means for understanding and maneuvering the crystal structure of seeds at the initial stage of a synthesis.[143] The initial reduction rate of a precursor can serve as a quantitative knob for manipulating the number of twin defects developed in a seed. For example, Pd seeds changed their structures from stacking-fault-lined to multiply twinned and then single-crystal as the initial reduction rate was increased from 10^{-8} to 10^{-6} and then 10^{-4} M s^{-1}.[143] Though more efforts are required to investigate the generality of this result, it provides us with a quantitative relationship between the initial reduction rate and the structure of the seeds, as well as an effective approach to controlling the twin structure and thus the shape taken by metal nanostructures.

It should be pointed out that, in addition to reducing agent, temperature, and capping agents which are often discussed in manipulating the reduction kinetics, we should also pay special attention to the coordination ligands. The addition of chemical additives that strongly coordinate with metal ions may have great influence on the stability and reduction potential of the metal precursor, and thus its reduction kinetics. For example, the introduction of HDA, whose amine group was expected to coordinate with Au(III) and Cu(II) ions, would lower the reduction potentials of these metal precursors.[144] The standard reduction potentials of $AuCl_4^-$/Au and Cu^{2+}/Cu pairs are 1.00 and 0.34 V versus standard hydrogen electrode (SHE), but the reduction potentials would decrease after coordination with HDA. For example, the reduction potentials of $[Au(NH_3)_4]^{3+}$/Au and $[Cu(NH_3)_4]^{2+}$/Cu pairs are only 0.33 and 0 V, respectively. The drop in reduction rate would lead to the formation of AuCu alloy shell instead of a phase-separated Au−Cu shell on a Pd cubic seed.[144]

Taken together, it is critical to consider the roles of both thermodynamic and kinetic parameters in defining the pathways for the nucleation and growth of nanostructures. The essence of thermodynamic control is to minimize the total free energy of a system. With the help of capping agents and surface diffusion, shapes with the lowest energy can be reached. In reality, however, the shape of the nanostructure can be easily trapped in a thermodynamically unstable, but kinetically enabled, state. Activity involving the manipulation of the rate for either surface diffusion or atom deposition should be considered as a kinetic control, which can be most conveniently achieved by controlling the temperature used for a synthesis. As the hallmark of a kinetically controlled process, the products are no longer confined to global minima, allowing for the formation of nanostructures with highly anisotropic shapes, like NRs and NWs. We believe a combination of thermodynamic and kinetic control can help us better understand the formation mechanism and give rise to the synthesis of a wider variety of nanostructures.

3.4.3. Oxidative Etching. Oxidative etching is a common phenomenon in our everyday life, with familiar examples including corrosion of steels. When steel is exposed to both air and water, rust will begin to form at specific sites and then eventually spread to cover the entire surface. In addition to rust formation, corrosion can take many other forms such as pitting, crevice etching, galvanic replacement, and dealloying, among others. When applied to the synthesis of metal nanostructures, oxidative etching can affect the reduction rate of a precursor and thus the shape of resultant nanostructures.[35,145−147] When a synthesis is conducted in air, together with the presence of a proper coordination ligand for the metal ions such as halide ions, the zerovalent species (including atoms, clusters, seeds, and nanostructures) can be oxidized back to the ionic forms during both the nucleation

DOI: 10.1021/acs.chemrev.8b00745
Chem. Rev. XXXX, XXX, XXX−XXX

and growth stages of a synthesis. The situation becomes even more complicated when the product has twin defects on the surface as etching tends to selectively start from the defect sites rather than a single-crystal region because of the high energy of defects.[145] For example, during the synthesis of Ag nanostructures that involved the reduction of $AgNO_3$ by a polyol, the presence of Cl^- ions, together with O_2 from the air, had great influence on the nucleation and growth processes.[35] In particular, the reaction solution turned from light yellow to nearly colorless and then back to light yellow, indicating the sequential formation of Ag nanoparticles, removal of the twinned nanoparticles due to oxidative etching, and the subsequent growth of the single-crystal species.

The combination of oxidative etching and reduction, which is supposed to coexist throughout a synthesis of metal nanostructures, can have a major impact on the outcome. In one demonstration, monocrystalline AuNRs were synthesized with the help of an Fe-based etchant.[148] The synthesis involved the room-temperature aging of a mixture of [AuCl(OLA)] complex with amorphous Fe nanoparticles in chloroform. Analysis of the growth mechanism indicated that Au nanostructures with a high density of defects were formed in the early stage. The unstable defect regions in the particles were preferentially oxidized back to Au(I) or Au(III) at a late stage of the synthesis. These Au cations were reduced again by Fe(0) or Fe(II) and the newly formed zerovalent Au atoms were deposited epitaxially onto the defect-free regions of the Au nanostructures. Continuous etching and deposition eventually reshaped the nanostructures into monocrystalline NRs, which were more stable than the twinned counterparts due to a lower defect density. A similar mechanism was also proposed for the synthesis of AuNWs, in which AuCl was reduced by OLA.[149] In the presence of oxidative etching, the OLA molecules adsorbed on the low-energy {111} facets and the highly reactive twin defects were selectively removed, inducing anisotropic growth for the Au nanostructures. Continuous etching of Au atoms from defect sites and their reduction and deposition onto other sites at a faster rate eventually reshaped and elongated the nanostructures into ultrathin NWs. Such observations further confirm the crucial role of oxidative etching in controlling the shape or morphology of metal nanostructures.

The involvement of oxidative etching often lowers the growth rate of a metal nanostructure by oxidizing atoms back to ions while the precursor is being reduced.[145] Oxidative etching thereby enables control over the nucleation kinetics and growth mode. For example, it has been reported that Ag atoms could be deposited asymmetrically onto a Ag cubic seed by taking advantage of oxidative etching.[105] In the presence of O_2 from the air, some Ag atoms were oxidized back to Ag(I) prior to redeposition onto the cubic seed, making the concentration of Ag atoms too low to nucleate on all six side faces of the seed. In this case, rather than being added evenly to all six side faces of the cube, the Ag atoms were deposited on three adjacent {100} faces more rapidly than the other three {100} faces, leading to the generation of an anisotropically truncated Ag octahedron. In comparison, when the reaction was conducted under the protection of argon, oxidative etching was suppressed and Ag nanocube with a larger size was obtained from a conformal growth of Ag atoms onto the cubic seed.

3.4.4. Galvanic Replacement. When metal ions are employed as an oxidative etchant, it is possible to generate zerovalent species during the oxidation of preformed metal nanostructures in a process commonly referred to as galvanic replacement. This process offers a simple and versatile approach to the fabrication of metal (as well as metal oxide) nanostructures with controlled compositions, structures, and morphologies.[150] In principle, galvanic replacement is an electrochemical process that involves the oxidation of one metal (the sacrificial template) by the ions of another metal with a higher reduction potential. Upon contact in a solution phase, the template will be oxidized and dissolved into the solution while the ions of the second metal will be reduced and plated right on the outer surface of the template.

For example, when aqueous $HAuCl_4$ solution is added into an aqueous suspension of Ag nanostructures, because of the difference in standard reduction potentials (1.52 and 0.80 V versus SHE for Au^{3+}/Au and Ag^+/Ag pairs, respectively), galvanic replacement will be initiated at the sites with high surface energies (e.g., defect regions, stacking faults, and/or steps).[130,151] As a result, Ag atoms will be oxidized to ions and dissolved into the solution, generating small holes on the surface of the nanostructure. At the same time, the electrons migrating to the surface of the nanostructure were captured by $AuCl_4^-$ to generate Au atoms for deposition, resulting in the formation of a thin and incomplete layer of Au on the surface of each nanostructure, which helps prevent the underlying Ag from reacting with $AuCl_4^-$. In this case, the small holes serve as the primary sites for continuous dissolution of Ag, and the opening will allow all the species involved in the reaction, including Ag(I) and Au(III) ions, to diffuse in and out of the cavity. Accompanying the deposition of Au, alloying will occur with the underlying Ag because a homogeneous alloy is thermodynamically more stable than phase-segregated Au and Ag. At the end, dissolution of Ag leaves a void inside the nanostructure while an alloyed sheath comprised of Au and Ag is generated.

The wall thickness and void size depend not only on the size of the template but also on the stoichiometric ratio between the two metals involved. For example, in comparison with Au(III), the reaction between a Ag nanostructure and the same amount of Au(I) ions will generate a Au−Ag alloy sheath with a thicker wall since every three Ag atoms dissolved will result in the reduction of three Au(I) ions rather than one Au(III) ion.[152] If a larger amount of $HAuCl_4$ is added into the reaction system, the $AuCl_4^-$ will cause dealloying for the Au−Ag sheath by selectively removing Ag atoms from the alloyed walls. During this process, many lattice vacancies will be generated as the Ag atoms are extracted by $AuCl_4^-$, leading to an increase in surface free energy. To lower the total energy, the vacancies coalesce to generate small holes in the wall. Further dealloying enlarges the holes, generating hollow nanostructures with porous walls. Complete dealloying will cause the hollow nanostructure to collapse into small fragments when an excess amount of $HAuCl_4$ is added.

The simple reaction of galvanic replacement can be employed to generate a wide variety of metal nanostructures, and is limited by no more than the requirement of a favorable difference in the reduction potentials of the two metals. To this end, metals with relatively lower reduction potentials, such as Cu, Ag, and Pd, are most commonly used as templates. For example, AuCu alloy nanotubes have been synthesized by injecting a Au(III) precursor, such as $HAuCl_4$, into a suspension of CuNWs in EG.[54] Because of the large difference between their reduction potentials (1.52 and 0.34 V versus

DOI: 10.1021/acs.chemrev.8b00745
Chem. Rev. XXXX, XXX, XXX−XXX

SHE for Au(III)/Au and Cu(II)/Cu pairs, respectively), galvanic replacement could happen even at room temperature, leading to partial removal of Cu. At the same time, Au atoms were produced for the formation of an alloy with the remaining Cu, leading to the creation of AuCu alloy nanotubes. Other examples include PdPt and PdAu alloy nanotubes derived from TeNWs.[153] By repeating the replacement reaction, multiwalled nanotubes have also been produced,[91,154] including Au/Ag alloy nanotubes containing two or three coaxial walls (see section 6.1).

4. INVESTIGATION OF THE GROWTH MECHANISM

4.1. General Concepts

Understanding the mechanism by which 1D metal nanostructures grow anisotropically and how the growth pathway is affected by a multitude of parameters remains incomplete. A nonexhaustive list of experimental parameters that can impact how nanostructures grow include the reaction temperature, the concentrations of the primary reaction constituents (reducing agent, metal precursor, and capping agents), the presence of secondary additives (e.g., halides), the presence of trace contaminants (often, unknown), the stirring rate, and even the presence of light.[37,115,155−158] Fundamental factors that influence growth and should be considered in computational simulations include what facets and/or defects are present on the growing nanostructure, facet dependence of surface energy, facet-dependent diffusion rates of adatoms, the facet-dependent electrochemical potential at which reduction occurs, the facet-dependent rate of metal addition (or deposition), the facet-dependent binding energies of various species, as well as how the binding of one species might influence the binding of another. Deconvoluting the roles played by all these parameters or factors is obviously a daunting task and remains an active area of research.

Most early investigations of the growth mechanism of 1D metal nanostructures in a solution relied on the analysis of dry samples by TEM or scanning electron microscopy (SEM). Electron microscopy provides information on the size, shape, crystal structure, and purity of the nanostructures produced in a given synthesis. Identification of the twin structure provided clues as to the growth mechanism, as well as the seeds from which the structures grow. For example, the presence of planar defects perpendicular to the growth direction suggests that the NWs likely grew via attachment.[18] Revealing the 5-fold twinned structure and a pentagonal cross-section of NWs indicate that they grew from penta-twinned, decahedral seeds.[47] Further exploration of the internal twin structure of seeds (e.g., single-crystal or multiply twinned) also help pinpoint its explicit role in dictating the evolution of the 1D morphology.[37,46,159−161]

Despite the insights gained from ex situ imaging techniques, many details of the mechanisms by which nanostructures grow remain unclear. For example, ex situ imaging techniques could not tell whether the species being added onto a nanostructure was an ion, a cluster, or a nanoparticle. In addition, ex situ techniques could not reveal what was the rate-limiting step for 1D nanostructure growth, and they could not adequately validate the hypotheses on the roles of capping agents and additives in driving anisotropic growth. Answering these questions is important as it shows how nanostructure synthesis fits into our current understanding of related chemical processes, and thereby connects to the fields of physical chemistry, surface science, and electrochemistry. A deeper understanding of the growth mechanisms also allows us to more effectively search the vast, multidimensional variable space when optimizing or scaling-up a colloidal synthesis of 1D nanostructures for a given application.

Motivated by the many unsolved mysteries of nanomaterial synthesis, researchers have developed a variety of analytical methods to gain new insights into the processes by which 1D nanostructures form. Notable examples include in situ TEM,[18,58,64,162−165] dark-field optical microscopy (DFOM),[19,166−168] and transmission X-ray microscopy (TXM).[169−171] All these techniques have been used to observe the growth of 1D metal nanostructures in real time, quantify their growth kinetics, and distinguish between atomic addition and oriented attachment. In addition, single-crystal electrochemistry has provided new insights into the roles played by halides and capping agents during anisotropic growth.[172−179] Computational simulations have also been used to evaluate different hypotheses pertaining to how anisotropic growth occurs, offering additional insights into atomic-level processes that determine the rates of anisotropic growth, as well as why anisotropic growth occurs.[21−23,64,180−190] This section focuses on the contributions made by these new analytical methods, each of which can contribute a different perspective on the development and testing of models to account for 1D growth.

4.2. Liquid−Cell Transmission Electron Microscopy

4.2.1. Liquid Cells. Recent developments in liquid-cell TEM have enabled the real-time visualization of anisotropic growth,[18,58,62,64] the evolution of nanostructures containing defects,[18,62,163] as well as changes to the distributions of different elements within a nanostructure.[18] Liquid-cell TEM involves the use of a specialized cell that has a very thin window that is transparent to electrons but is robust enough so that the liquid does not leak into the high vacuum of the microscope. Newer liquid-cell holders from Hummingbird Scientific and Protochips also enable the user to apply heating to the liquid cell and add reagents via a pump to conduct a synthesis in the liquid cell. The cost of the equipment for performing liquid-cell TEM is around $200 000. The experiments are also much more time-consuming than imaging of dry samples, which further increases the cost of the TEM and personnel time involved in the experiments. For these reasons, liquid-cell TEM has not yet become a routine technique, such as conventional TEM, that is accessible to essentially every researcher in the field. It is still a specialized technique used by a relatively small number of groups that are willing to dedicate significant resources to these experiments, but the situation is changing as more user facilities are acquiring the necessary equipment.

The liquid cell typically consists of silicon nitride windows with a thickness of 10−100 nm.[62,162,191,192] The spacing between the windows in a liquid cell is around 150 nm, which limits their use to relatively small nanostructures. The mechanical stiffness and strength of these cells allow for the incorporation of various elements for electrochemical measurement,[193] temperature control,[194] and liquid flow.[195] The silicon nitride causes electron scattering, making it difficult to achieve atomic resolution with liquid cells based on this material. For this reason, methods were developed to perform a synthesis in the liquid confined between two graphene sheets (<1 nm in thickness).[165,196] Owing to their higher electron transparency, the graphene-based liquid cells allow in situ

DOI: 10.1021/acs.chemrev.8b00745
Chem. Rev. XXXX, XXX, XXX−XXX

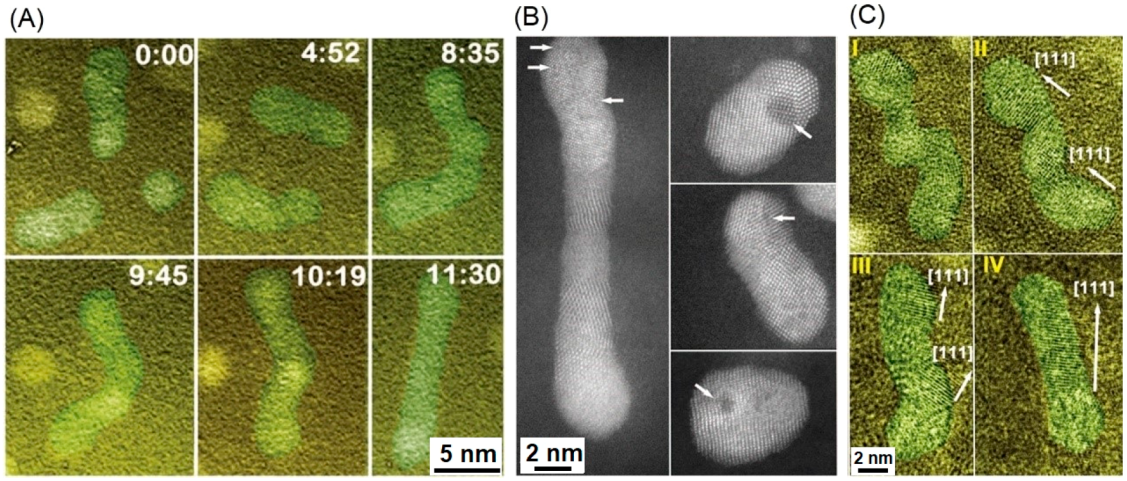

Figure 9. (A) Attachment-based growth of Pt_3Fe NRs and a subsequent straightening process. (B) Images of polycrystalline chains of Pt_3Fe nanoparticles (white arrows indicate Fe-rich regions). (C) The structural evolution of a polycrystalline trimer of Pt_3Fe nanoparticles into a single-crystal NR via lattice rotation and straightening. Reprinted with permission from ref 18. Copyright 2012 AAAS.

TEM to achieve atomic resolution. At the current stage of development, the graphene-based liquid cells are not available commercially, limiting their use to a few research groups only.

Even when atomic resolution is achieved, the mechanistic understanding that can be achieved using liquid cells is limited by the fact that the electron beam itself can cause reactions in the solution that otherwise would not occur in a conventional synthesis. For example, the electron beam can easily reduce metal ions without any reducing agent present in the reaction solution.[197] Procedures for quantifying the effect of electron dose, imaging mode, and acceleration voltage on beam-induced solution chemistry have been reported.[198] In the case of an aqueous reaction medium, the high-energy electrons decomposed water molecules, producing a variety of reactive chemicals and radicals, such as $H^{\bullet}$, $OH^{\bullet}$, H_2, H_2O_2, H^+, and OH^-. These chemical species can possibly cause undesired reactions. Adjustment of irradiation dose rate[198] and addition of radical scavengers into the reaction solutions[199] can reduce the impact of such species. Minimizing the effects of the electron beam on the outcome of a synthesis while obtaining high-quality images in the highly dynamic liquid environment remains a challenging task and an area of active research. It is important to consider and plan for beam-induced reactions if one wishes to obtain results that are relevant to the syntheses conducted in flasks.

4.2.2. Anisotropic Growth via the Attachment of Nanoparticles. Real-time visualization of 1D nanostructure growth by liquid-cell TEM has produced new insights into how the structures could grow via particle attachment rather than atomic addition, revealing mechanistic details with regard to neck formation/elimination, straightening, and defect formation/elimination, as well as the attachment frequency as a function of alignment angles.

In the liquid-cell TEM study of Pt_3Fe NRs,[18] several stages of growth were observed. Initially, Pt_3Fe nanoparticles were formed in the liquid cell under electron beam-induced reduction. This was followed by the attachment of the nanoparticles to form short NRs. Additional attachment to the ends of the rods led to the formation of longer NRs. The chains of nanoparticles were initially wavy and flexible, and planar defects were present at the attachment interfaces. Some of the chains became straighter over time, presumably due to surface diffusion of atoms to the necks in order to lower the total surface energy. The TEM images in Figure 9A show the formation of wavy chains of Pt_3Fe nanoparticles and the subsequent straightening process. The addition of a surfactant into the growth solution facilitated the formation of straight, stiff chains of nanoparticles. In the absence of surfactant, the chains did not straighten but instead remained wavy.

After the straightening process, additional structural relaxation occurred, eliminating the planar defects and resulting in the formation of single-crystal NRs. The rate of the straightening process was not affected by the length of the nanoparticle chain whereas the kinetics of the single-crystal NR formation process decreased as the length of the nanoparticle chain increased. Figure 9B indicates that the NR was still polycrystalline after the straightening process. In addition, variations in composition were observed, with the Fe-enriched regions highlighted by white arrows. The size of Fe-enriched regions was much smaller than the size of the attached nanoparticles, indicating that Pt and Fe atoms were redistributed in the nanostructure during the relaxation process. Lattice rotation that resulted in the formation of a single-crystal NR was also observed, as shown in Figure 9C. Taken together, it can be concluded that a polycrystalline chain of nanoparticles was initially formed because of the misalignment between the attaching particles. A subsequent lattice rotation and straightening process led to the formation of the straight, single-crystal NRs.

Tracking of the attachment process by liquid-cell TEM suggests that the attachment angle could affect the removal of planar defects at the interfaces between the attached nanoparticles.[62] When the angles between the {111} facets of the two attaching particles were below 20°, the attachment resulted in bonding without defects, presumably due to prealignment prior to attachment. When the attachment angles were over 20°, planar defects were observed at the interfaces. In a separate study, the attachment between AgNRs was investigated using liquid-cell TEM.[64] End-to-end attachment was found to be most favorable, with over 85% of the attachments taking place with the rod−rod orientation angles below 45°. This experimental observation was supported by molecular dynamic simulations, which indicated that a higher activation energy was required for the side-to-side attachment

DOI: 10.1021/acs.chemrev.8b00745
Chem. Rev. XXXX, XXX, XXX−XXX

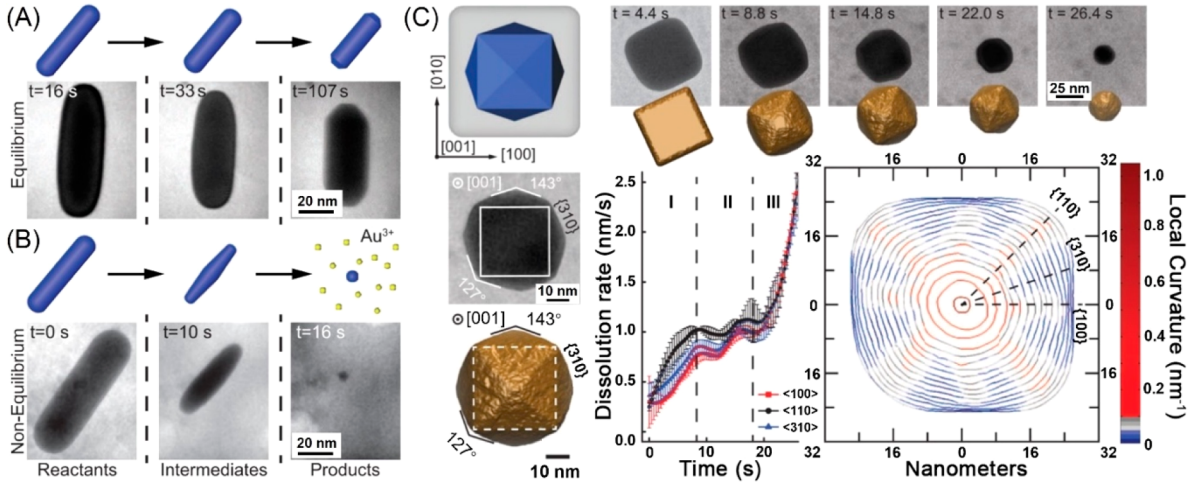

Figure 10. (A, B) Oxidative etching of AuNRs results in the formation of (A) an equilibrium shape at a low etching rate and (B) a nonequilibrium shape at a higher etching rate. (C) Kinetically controlled oxidative etching of Au nanocubes and the formation of tetrahexahedron with high-index {310} facets. Reprinted with permission from ref 165. Copyright 2016 AAAS.

relative to end-to-end attachment because of the solvation energy.

4.2.3. Oxidative Etching. As discussed in section 3.4.3, oxidative etching plays an important role in controlling the internal defect structure of seeds, and thereby the final shape or morphology of nanostructures.[145−147] Oxidative etching can also be used in conjunction with liquid-cell TEM to provide information on surface diffusion rates, as well as which facets on a nanostructure are most susceptible to oxidation. To this end, the degree of oxidative etching of AuNRs was found to affect the dissolution rate as well as the intermediate structures involved.[165] When the etching of AuNRs was slow, there was enough time for surface diffusion to reconstruct the shape of the nanostructure so as to minimize its total surface free energy (Figure 10A). When the etching process was accelerated with an additional etchant, a nonequilibrium ellipsoidal shape with sharp tips was observed. The etching rate at the ends of the AuNRs was also faster than the side faces, presumably due to the presence of a lower coverage density for the adsorbed CTAB (Figure 10B).

The formation of nonequilibrium nanostructures was also observed for the oxidative etching of Au nanocubes and rhombic dodecahedra.[165] Figure 10C shows images taken at different stages of the oxidative etching of a Au rhombic dodecahedron bounded by {100} facets. A nanostructure with high-index {310} facets was observed as the intermediate when the etching was relatively fast. At lower etching rates, truncated octahedra covered by a lower total surface energy was observed. These results illustrate how nanostructures with nonequilibrium shapes can be produced through the control of reaction kinetics.

4.3. In Situ Dark-Field Optical Microscopy

In a set of studies, DFOM was explored to measure the anisotropic growth kinetics of 1D metal nanostructures.[19,166−168] DFOM cannot provide any information about the internal defect structure, but this method is much more cost-effective than liquid-cell TEM. The liquid cell can be readily constructed from glass coverslips and double-sided tape (Figure 11A).[19] The reaction solution can also be heated with a transparent indium tin oxide (ITO) heater and an integrated temperature controller. Altogether, the material cost should be below $100, while the optical microscope costs another $15,000. DFOM can easily resolve NWs with diameters as thin as 20 nm because they scatter much more light than the background solution.

DFOM was first applied to the syntheses of CuNWs with ethylenediamine (EDA) in a NaOH solution.[19,167] Figure 11B shows typical images for the growth of CuNWs acquired using DFOM.[19] Although the complete conversion of Cu in this synthesis required at least 30 min, individual NWs grew to their full length within ∼2 min. For example, the average growth rate of CuNWs at 70 °C in a solution containing 14.3 M NaOH, 4.7 mM $Cu(NO_3)$, 25 mM N_2H_4, and 110 mM EDA was 86 nm/s (Figure 11C). Changing the concentration of $Cu(NO_3)_2$ revealed that the growth rate of CuNWs increased with the $Cu(NO_3)_2$ concentration at a rate of 24 nm s^{-1} mM^{-1} (Figure 11D). In contrast, the reducing agent (hydrazine, N_2H_4) had no effect on the NW growth rate (Figure 11E). The temperature dependence of the growth rate shown in Figure 11F revealed that the activation energy for NW growth (11.5 kJ mol^{-1}) was lower than the activation energy for water self-diffusion (18−20 kJ mol^{-1}).[200] These results suggested that the growth of CuNWs was diffusion-limited in such a synthesis. This hypothesis was tested by modeling the rate of NW growth based on the diffused-limited steady-state current at an ultramicroelectrode and by measuring the diffusion rate of $Cu(OH)_2^-$ in the reaction solution. This simple model produced a $Cu(NO_3)_2$-dependent growth rate of 25 nm s^{-1} mM^{-1}, which almost perfectly matched the experimentally measured growth rate of 24 nm s^{-1} mM^{-1}. These results provided strong evidence that the NW growth was limited by the rate of diffusion of $Cu(OH)_2^-$ complex to the ends of CuNWs.[19]

In another example, DFOM was used to show that CuNW growth in an alkylamine-mediated synthesis is charge-transfer limited.[168] Although the concentration of Cu(II) precursor for the alkylamine-based synthesis was 3.5 times higher than what was used for the EDA-based synthesis (16.4 mM versus 4.7 mM), the growth of CuNWs with TDA (69 nm/s) and ODA (5 nm/s) were slower than that with EDA (120 nm/s) at the same temperature of 90 °C.[19,168] Based on electrochemical measurements of the diffusion rate of Cu(II)-alkylamine complexes, the diffusion-limited growth rates were calculated

DOI: 10.1021/acs.chemrev.8b00745
Chem. Rev. XXXX, XXX, XXX−XXX

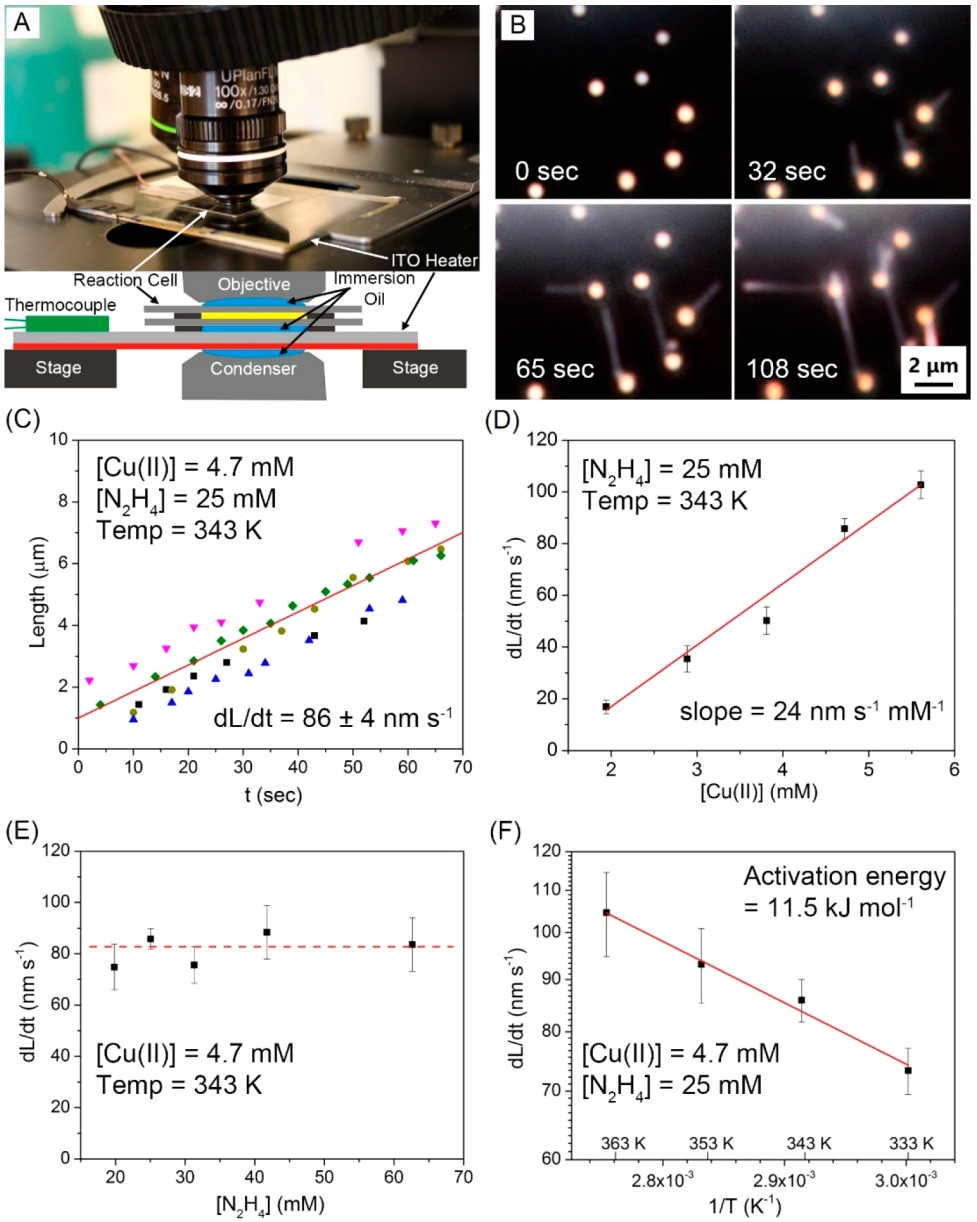

Figure 11. (A) Photograph and schematic of the setup used for DFOM. (B) Real-time visualization of CuNW growth. (C) Changes in length as a function of time when measured by DFOM from five individual NWs. The CuNW growth rate as a function of the concentrations of (D) Cu(II) ions, (E) N_2H_4, and (F) reaction temperature. Reprinted with permission from ref 19. Copyright 2014 American Chemical Society.

to be 31 400 and 5260 nm/s for the TDA- and ODA-based systems, respectively.[168] The fact that the growth rates measured by DFOM are 450−1000 times slower than the calculated diffusion-limited growth rates indicates that the growth of CuNWs in the presence of alkylamines is limited by charge transfer. These studies demonstrate that DFOM can provide insights into the rate-limiting step for NW growth.

4.4. In Situ Transmission X-ray Microscopy

In situ TXM offers a resolution of 25 nm, which is worse than TEM but obviously better than DFOM.[169−171] The advantage of TXM relative to TEM is that the depth of focus is on the order of tens of micrometers, allowing this technique for syntheses involving relatively thick metal NWs. In contrast, the need for electron transparency in TEM limits the cell thickness to less than 200 nm due to the electron scattering, making it difficult to study the growth of long, thick NWs. Another advantage of TXM over TEM is that the cell sits under atmospheric pressure rather than vacuum, so one can more easily develop custom-made flow cells without worrying as much about leakage. Most importantly, with TXM, it is possible to map the distributions of elements by tuning the X-ray energy across their absorption edges, as well as to determine their oxidation or coordination states by examining their X-ray absorption near-edge structure (XANES). Related to 1D nanostructures, TXM has been used to monitor the chemical transformation from AgNWs to Au nanotubes via galvanic displacement, as well as the conversion of AgNWs to nanotubes made of silver oxide.[169,171]

Figure 12A shows a schematic diagram of TXM, integrated with a flow cell.[171] To study galvanic replacement, AgNWs were transferred onto a Si_3N_4 membrane, and a liquid cell was assembled and placed in the TXM system.[169] A reaction solution containing $HAuCl_4$ was injected into the liquid cell to

DOI: 10.1021/acs.chemrev.8b00745
Chem. Rev. XXXX, XXX, XXX−XXX

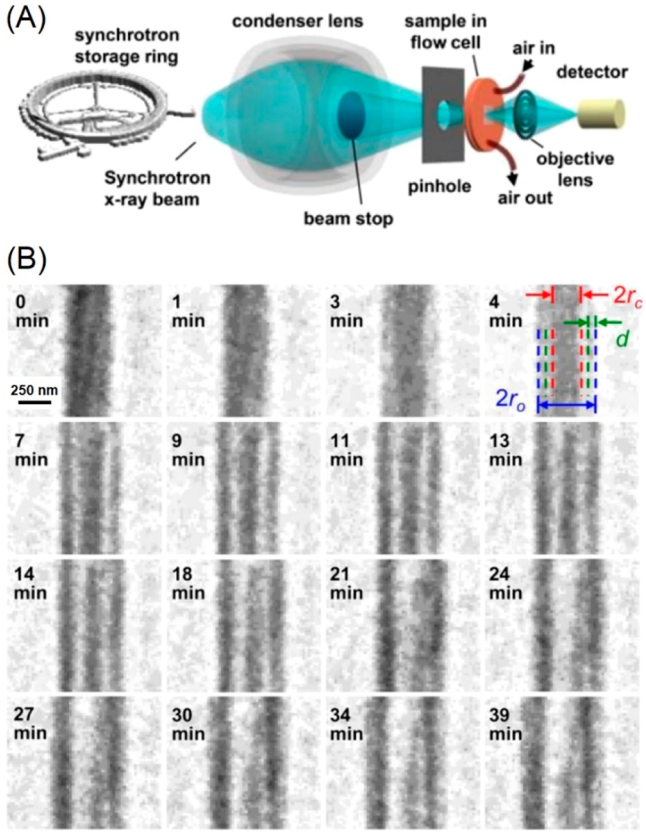

Figure 12. (A) Schematic diagram of the TXM system. (B) TXM images of a AgNW undergoing oxidation for the generation of Ag_2O nanotubes. Reprinted with permission from ref 171. Copyright 2016 American Chemical Society.

initiate the galvanic replacement reaction with AgNWs. A number of stages of the galvanic displacement reaction could be clearly resolved using TXM. First, random pits formed on the AgNW in the initial stages of galvanic replacement, but the deposition of the Au shell was relatively uniform. After the AgNW had been dissolved, the porous Au wall evolved into a continuous shell via Ostwald ripening, finally producing Au-based nanotubes. For AgNWs with a diameter below 80 nm, galvanic replacement resulted in the formation of fragmented nanotubes, whereas thicker NWs were converted to nanotubes without fragmentation.[169]

The Kirkendall effect during the oxidation of AgNWs was also investigated by TXM.[171] Air was injected into the cell, and the radiolysis of air by X-rays generated a strong oxidant for converting the NWs to Ag_2O nanotubes. The oxidation process of a AgNW is presented in Figure 12B. A thin oxide layer (i.e., the lighter gray region) formed in the first 3 min. The diffusion of oxygen into the core was slower than the diffusion of Ag to the surface of the NW, resulting in the accumulation of Kirkendall voids at the interface between the oxide shell and the Ag core. As the oxidation progressed, the thickness of the Ag_2O shell increased whereas the diameter of the Ag core decreased. Finally, the Ag core and the oxide shell were completely separated from each other by the Kirkendall voids.

4.5. Electrochemical Methods

The growth of 1D metal nanostructures via atomic addition is the result of spontaneous oxidation of a reducing agent and the simultaneous reduction of a metal precursor. After the nucleation stage, the electron transfer that occurs in both of these reactions is likely mediated by the metal surface in an autocatalytic fashion. The formation of anisotropic nanostructures has largely been attributed to the modulation of the atomic addition rate on specific crystal facets by the adsorption of shape-directing (i.e., capping) agents. Measurements of the surface reactivity as a function of crystal orientation and the concentration of adsorbate can test this hypothesis and offer a deep understanding of the facet-dependent chemistry that causes anisotropic growth of 1D metal nanostructures. To this end, single-crystal electrochemical measurements have been demonstrated as a powerful analytical tool for obtaining such information in the fields of electrocatalysts,[201−204] electrochemical deposition,[114,205−208] and corrosion.[209−212] To date, single-crystal electrochemistry has been used to test the hypothesis of capping agent for AuNR and CuNW growth.[172−179] There remain many additional nanostructure syntheses in which single-crystal electrochemistry can be applied to provide a deeper understanding of the facet-selective chemistry.

The first application of single-crystal electrochemistry to nanostructure synthesis was a test of the hypothesis that surfactants such as CTAB selectively adsorb on Au(100) over Au(111).[173,174] Such facet-selective adsorption has been hypothesized to be responsible for the anisotropic growth of AuNRs. Using chronocoulometry to study the adsorption of octyltrimethylammonium onto Au(100) and Au(111), it was found that although the presence of bromide promoted the adsorption of the surfactant, there was no preferential adsorption of octyltrimethylammonium onto Au(100) in the presence of bromide. It was concluded that the preferential adsorption of CTAB onto Au(100) was, therefore, unlikely to be the cause of anisotropic growth of AuNRs. The authors did not explore whether there was any difference in the kinetics (i.e., charge transfer resistance) of ascorbic acid (H_2Asc) oxidation or $HAuCl_4$ reduction between Au(111) and Au(100) surfaces. In a separate study with a polycrystalline Au electrode, it was found that the adsorption of CTAB onto Au decreased the rate of H_2Asc oxidation, and that having a Ag layer on the Au in combination with CTAB decreased it even further.[213] Since this work was done with a polycrystalline electrode, it is not clear whether the H_2Asc oxidation kinetics differ between the {100} facets on the side surface of a AuNR and the {111} facets on the ends.

Most previous experiments with single-crystal electrodes have been performed separately with different crystals, such that the crystals are electrically disconnected. This situation differs from the solution-phase synthesis, in which the two crystal facets are in electrical contact, and therefore will presumably be at the same potential. To address this issue, researchers used single-crystal Au bead electrodes consisting of four Au(111) surfaces and one Au(100) surface.[178] These electrodes are made by flame annealing the end of a gold wire. Since all the surfaces were connected, it was impossible to measure the currents on different facets in a single measurement when fluorescent, single-stranded DNA was employed as an indicator of the facet-selective adsorption of capping agents. A typical experiment involved the formation of self-assembled monolayers (SAMs) of mercaptoundecanoic acid on all the Au surfaces, followed by the electrochemical or chemical desorption of the monolayers at different potentials. The surfaces were then exposed to fluorescent, single-stranded DNA to compare the facet-dependent desorption of

DOI: 10.1021/acs.chemrev.8b00745
Chem. Rev. XXXX, XXX, XXX−XXX

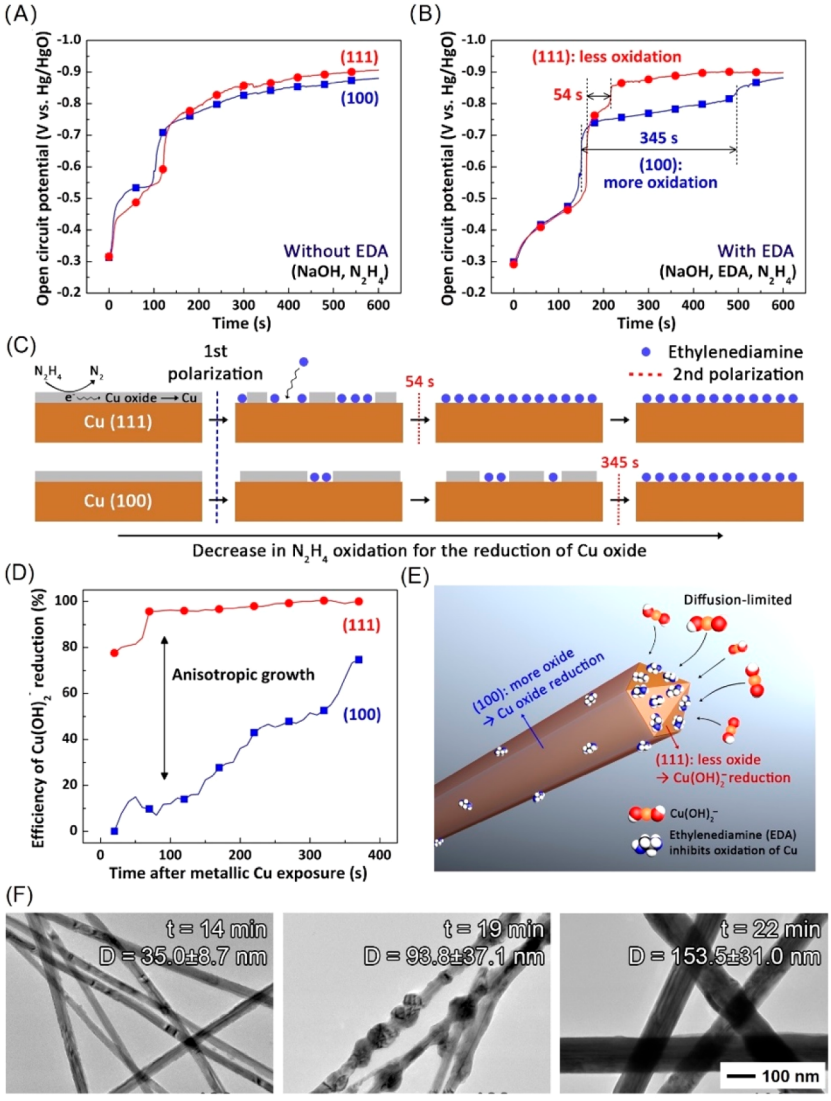

Figure 13. Changes in the open circuit potential in a solution containing NaOH and N_2H_4 (A) without and (B) with EDA. (C) Schematic diagrams showing the facet-dependent effect of EDA on surface oxidation. (D) Current efficiencies of $Cu(OH)_2^-$ reduction to metallic Cu on Cu(111) and Cu(100) surfaces, respectively. (E) Growth mechanism of CuNWs in NaOH solution with EDA as a facet-dependent promoter. (F) TEM images confirming that the time scale for the lateral growth of CuNWs in the reaction solution matches the time scale for facet-selective Cu(II) reduction on single crystals. (A–E) Reprinted with permission from ref 177. Copyright 2017 American Chemical Society. (F) Reprinted with permission from ref 167. Copyright 2014 Royal Society of Chemistry.

monolayers on Au(111) and Au(100). Depending on the electrochemical potential, the detachment of the monolayer from Au(111) was up to 20 times greater than that from Au(100). At no potential was the fluorescence intensity greater on Au(100) than on Au(111). The same results were obtained by changing the potential at the electrode with the use of $NaBH_4$ in place of an applied electrical potential. Facet-dependent adsorption of CTAB on Au surfaces was also investigated in the same manner, but the results were less conclusive because of nonspecific adsorption of the DNA. Fluorescent images indicate single-stranded DNA adsorbed onto the Au(111) surface to a greater extent than Au(100) in the presence of CTAB, suggesting that the Au(100) surface was blocked by CTAB. This result supported the hypothesis that CTAB preferentially adsorbs onto Au{100} facets during the growth of AuNRs.[178]

Single-crystal electrodes were also used to test the hypothesis of capping agent for the growth of penta-twinned CuNWs in a highly basic solution (15 M NaOH) containing EDA.[177] It has been hypothesized that EDA acted as a capping agent that preferentially adsorbed onto the side faces of NWs, the {100} facets, while less EDA adsorbed at the ends of the growing NWs terminated in the {111} facets, leading to the selective addition of Cu to the ends of the NWs. This study showed that, rather than acting as a capping agent, EDA was a facet-selective promoter for CuNW growth under the experimental conditions used. Since the rate of Cu(II) reduction in this synthesis is diffusion-limited, electrochemical quartz crystal microbalance (EQCM) and chronocoulometry measurements were used to determine the rate of Cu(II) reduction and the mixed potential at which such reduction occurred in the reaction solution. Surprisingly, 73% of the electrons from hydrazine oxidation went to the reduction of surface oxide on the Cu, with only 27% going to the reduction of $Cu(OH_2)^-$ to elemental Cu. Such a high fraction of electrons going to the reduction of oxide was due to the highly

DOI: 10.1021/acs.chemrev.8b00745
Chem. Rev. XXXX, XXX, XXX−XXX

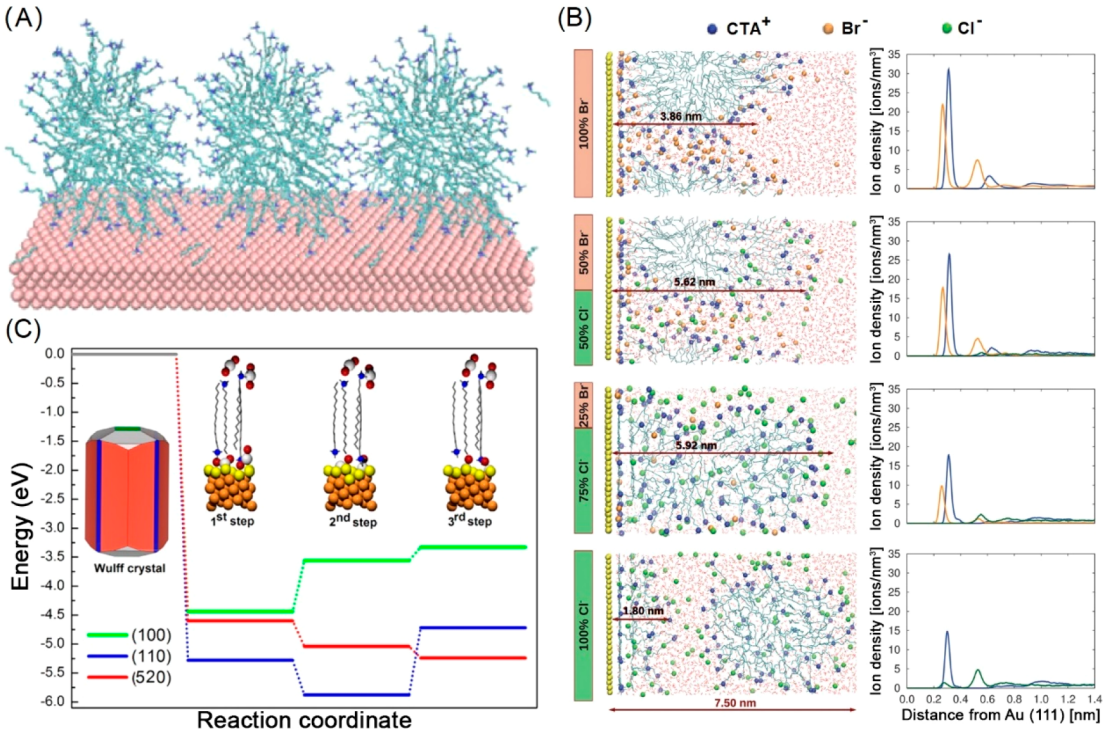

Figure 14. (A) Illustration of the CTA^+ micelles formed on Au(111) surface. (B) Changes in the adsorption of CTA^+ micelles according to the halides. (C) Changes in the energies during Au atomic addition onto (100), (110), and (520) surfaces covered by the CTAB−AgBr complex. (A) Reprinted with permission from ref 22. Copyright 2013 American Chemical Society. (B) Reprinted with permission from ref 23. Copyright 2016 Royal Society of Chemistry. (C) Reprinted with permission from ref 21. Copyright 2014 American Chemical Society.

basic reaction environment. Single-crystal electrochemical measurements further revealed that EDA was more effective in preventing the oxidation of Cu(111) than Cu(100) (Figure 13A−C), suggesting that EDA specifically adsorbed on the Cu(111) surface.[177]

Rather than acting as a capping agent, it was found that increasing the concentration of EDA increased the current from hydrazine oxidation for both surfaces, but to a greater extent on Cu(111) than Cu(100).[177] By comparing the mixed potentials in the reaction solution with and without Cu(II) ions, and using those potentials to oxidize hydrazine, the time-dependent efficiency of $Cu(OH_2)^-$ reduction on Cu(111) or Cu(100) surface was determined (Figure 13D). The results indicated that EDA actually acted as a facet-dependent promoter for CuNW growth by keeping the Cu(111) surface at the ends of the NWs free from surface oxidation for the first 5 min into a synthesis (Figure 13E). The capping agent in this synthesis is actually surface oxide on the {100} side faces on the NW. This result demonstrates that single-crystal electrochemistry can reveal the actual role of an organic additive as a facet-selective promoter, which is the opposite to what is generally hypothesized.[177]

The time-dependent facet-selective chemistry with single-crystal electrodes was similar to the time-dependent growth of CuNWs in a solution-phase synthesis.[167] Stopping the reaction at 14 min showed that NWs of 35 nm in diameter were produced, but 5 min later Cu started to plate onto the side faces of the NWs, leading to the increase of their diameters to 154 nm. The fact that the time-dependent facet-selective electrochemical results generally match with what is observed for the time-dependent NW growth process suggests a good correspondence between the chemistry occurring on the single-crystal electrodes and what is occurring on the NW facets in a solution-phase synthesis.[167,177]

4.6. Computational Simulation

Electrochemical methods can reveal what species in the reaction solution are responsible for the facet-selective chemistry that causes anisotropic growth, but they cannot reveal why these species behave in a facet-selective manner. To this end, computational simulations are helpful in using energy landscapes to test hypotheses that are not easily tested experimentally, revealing potential new mechanisms and elucidating what types of surface structures may be responsible for anisotropic growth. For these reasons, extensive simulations have been performed to help clarify the roles of shape-directing agents in the growth of Au, Ag, and Cu NRs/NWs.

Early reports on AuNR growth suggested that the adsorbed CTAB existed as a bilayer on the side surface of a AuNR. In contrast, molecular dynamics (MD) simulations revealed that such a bilayer is not stable, and instead CTAB forms cylindrical micelles on the Au surface within 1 ns (Figure 14A).[22] The thickness of micelles on Au(111), (100), and (110) surfaces was similar (3.7−3.9 nm), but the area per CTAB molecule was slightly greater (0.76 nm^2) on Au(111) than on Au(110) and Au(100) (0.67 and 0.67 nm^2, respectively). Due to the cylindrical shape of the adsorbed micelles, the researchers observed water−ion channels at the interfaces between micelles. This water−ion channel allowed Au(III) ions (or complexes) to diffuse toward the Au surface, which would presumably allow them to be reduced and add to the surface, although these steps were not simulated. The widths of the ion channels were 0.94, 0.71, and 0.73 nm for (111), (110), and (100) surfaces, respectively. These widths implied that 23.10%, 17.40%, and 17.80% of (111), (110), and (100) surfaces were

DOI: 10.1021/acs.chemrev.8b00745
Chem. Rev. XXXX, XXX, XXX−XXX

accessible to the diffusion of Au(III) ions. These results suggested that the lower packing density of CTAB on Au(111) would facilitate a greater rate for atomic addition.

Motivated by the work showing that AuNRs and NWs grew in the presence of bromide but not chloride,[115,214,215] researchers have studied the effects of different halide ions on the adsorption of cetyltrimethylammonium ion (CTA^+) by MD simulations.[23] The simulations were performed with the same amount of CTA^+ but different ratios of Br^- and Cl^- ions. It was found that the most compact CTA^+ layer was observed when only Br^- ions were used as the counteranion (Figure 14B), indicating that Br^- ions enhanced the adsorption of CTA^+. The surface densities of Br^- and CTA^+ on Au(111) were 23% and 13% lower than those on (110) and (100) surfaces. When Cl^- ions coadsorbed with Br^- ions on Au surfaces, less compact and more stretched micelles were observed on all Au surfaces (Figure 14B), and the difference in the surface density of CTA^+ between the different crystal surfaces became negligible. This result suggested that surface adsorption of Cl^- ions impeded the facet-selective growth of Au nanostructures. The simulated results were confirmed by experimental results in that NRs were formed when the Br^- to Cl^- ratio was above 0.75, but Au nanostructures lost their shape anisotropy with a ratio less than 0.2. The combination of simulation and experimental studies suggested that both Br^- ions and CTA^+ were important in inducing the anisotropic growth of AuNRs. It is not clear why the simulated results reported in this paper differ from experimental measurements of surface adsorption performed with single-crystal chronocoulometry.[173,174]

The process by which highly symmetric *fcc* metals break their symmetry to form single-crystal NRs is one that is difficult to explore experimentally, but for which computational simulations can be used to scrutinize potential mechanisms. To this end, density functional theory (DFT) simulations have been used to study the symmetry breaking process of Au cuboctahedra in the presence of Ag(I) and CTAB.[21] This work highlighted the potential role of a CTAB–AgBr complex in causing symmetry breaking. The energy gained by the adsorption of this complex was more than 3 eV, and was preferential for {100} facets because AgBr can grow epitaxially on {100} but not {111} facets. The researchers indicate that the structures of the nanoparticle and the adsorbed CTAB–AgBr complexes are such that only 4 out of 6 {100} surfaces can be simultaneously blocked, leading to the formation of a tube due to dispersion interactions between the alkyl chains, which will, in turn, cause anisotropic growth along the [100] direction. Unfortunately, this paper did not provide any detailed images or schematics of the proposed tube structure and did not report any tests of whether the formation of such a tube structure would be energetically favorable.

The same authors also explored the energetics of formation of different side faces on single-crystal AuNRs.[21] To do so, they broke the atomic addition process into three steps that include (i) adsorption of a CTAB–AgBr complex, (ii) the desorption and loss of a Br atom from the complex, and (iii) the addition of Au to the crystal. It is not exactly clear how the energetics of these steps were determined, especially for step iii, which would involve electron transfer (Figure 14C). It was shown that atomic addition to the {520} facet was more energetically favorable than the {100} and {110} surfaces. The authors further demonstrated that the adsorption energy of a CTAB–AgBr complex was most favorable for the {520} facet because such adsorption gave this facet the lowest surface energy. On the basis of the calculated surface energies, Wulff construction was used to draw a NR dominated by {520} facets. Such a construction agrees with some experimental observations with regard to the NR's surface structure.[43,44]

Computational simulations also offered insights into the growth mechanism of penta-twinned Ag and Cu NWs. Since penta-twinned NWs consisted of 10 {111} facets at the ends and five {100} facets on the side surface, the simulations mainly compared the binding energies of organic capping agents toward {111} and {100} surfaces.[188−190] The simulation results for Cu and Ag NWs generally support the hypothesis of surface capping for NW growth, in which anisotropic addition is caused by the stronger binding of a capping agent to {100} rather than {111} facets.

Poly(vinylpyrrolidone) is a general shape-directing agent for the synthesis of penta-twinned AgNWs.[104,216−218] Since DFT calculations of the binding of an entire polymer chain would be too costly, researchers explored the potential for facet-selective binding of PVP by considering the binding of segments of a PVP chain: 2-pyrrolidone and ethane.[188] Ethane did not bind to the Ag surface, but 2-pyrrolidone could bind to Ag surface via the O atom. The total binding energy of 2-pyrrolidone on Ag(100) was 0.08 eV greater than that on Ag(111). This difference was attributed to the hybridization of the 2-pyrrolidone orbitals with the *d*-band of Ag(100) but not Ag(111). Although the difference in binding energy for one repeat unit was rather small, the researchers estimated that the probability for binding of a chain with nine PVP segments was 10^9 times greater for Ag(100) than Ag(111). In a separate study, simulations suggested that the selectivity of PVP binding toward Ag(100) was 10^7 times greater than poly(ethylene oxide) (PEO). These simulation results are consistent with experimental data, demonstrating that the growth of penta-twinned AgNWs was more effectively promoted by PVP than by PEO.[219]

For the case of penta-twinned CuNW growth, simulations revealed that alkylamines could form SAMs on Cu surface when the alkyl chain contained more than 10 carbons.[185] In comparison, experimental data showed that the minimum carbon chain length was 12 to obtain CuNWs with alkylamines. Nanoparticles were obtained with shorter alkylamines.[168] These calculated and experimental results suggest that the formation of alkylamine monolayers is necessary for the anisotropic growth of CuNWs with long-chain alkylamines. Simulations also indicated that the binding energy of alkylamines on Cu(100) was slightly higher (by 0.12 eV) than that on Cu(111) surface.[186] The energy required to remove TDA (14 carbons) from a monolayer on a Cu surface was 2.06 eV versus 3.59 eV for ODA (18 carbons).[168] This difference in the binding energy may explain why CuNWs grow 13.8 times faster with TDA compared to ODA.[168]

4.7. Single-Crystal Electrochemistry Integrated with Computational Simulations

Although each method discussed above can provide pieces of the puzzle for how and why nanostructures grow anisotropically, one must fit these pieces together to get the whole picture. For example, in situ visualization can give information about the growth rate of anisotropic nanostructures but not the chemistry that drives anisotropic growth. Single-crystal electrochemistry can reveal what species are responsible for facet-selective metal deposition, but the surface of a bulk single

DOI: 10.1021/acs.chemrev.8b00745
Chem. Rev. XXXX, XXX, XXX−XXX

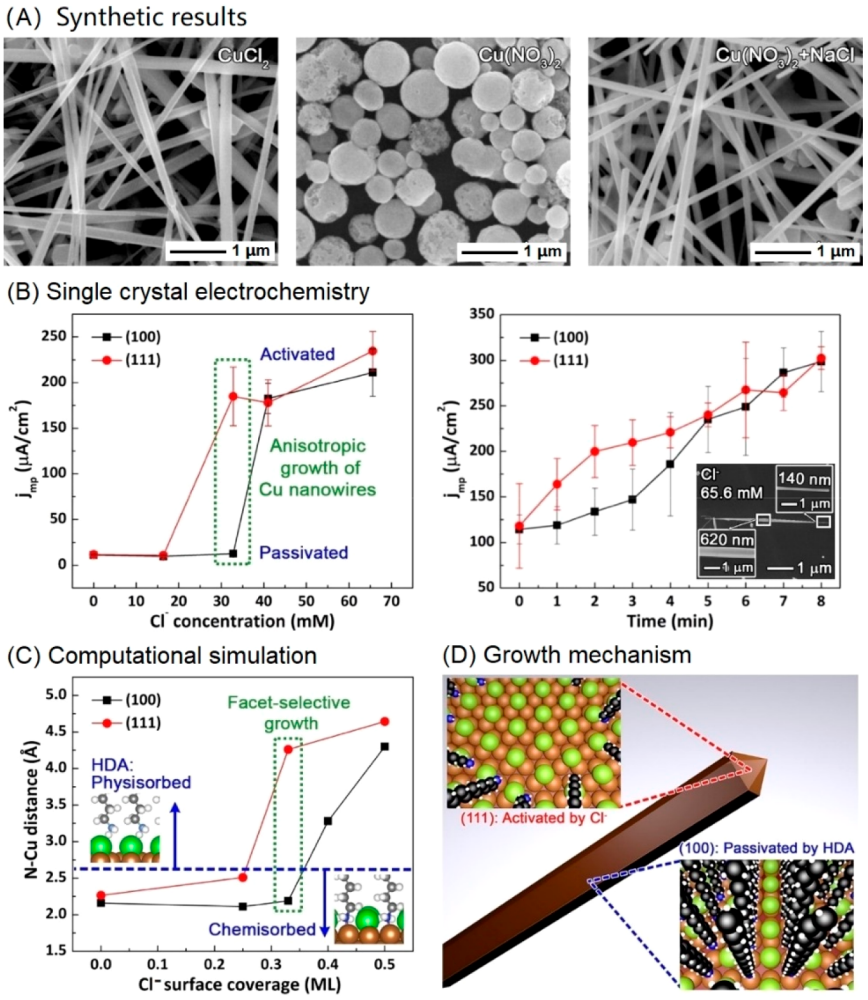

Figure 15. (A) Synthetic results with and without Cl^- in the presence of HDA. (B) Current at the mixed potential, where the oxidation rate of the reducing agent matches that of Cu(II) reduction, as a function of Cl^- concentration and time for Cu(111) and Cu(100) single-crystal electrodes. Relatively high concentrations of Cl^- resulted in a higher current on Cu(111) within the first few minutes, a condition which corresponded to the formation of javelin-shaped CuNWs (inset image). (C) DFT results for competitive adsorption of HDA and Cl^- on Cu(100) and Cu(111). (D) A schematic diagram showing the proposed growth mechanism of CuNWs in the presence of HDA and Cl^-. Reprinted with permission from ref 20. Copyright 2018 American Chemical Society.

crystal differs in scale and defect structure from a growing nanostructure. Computer simulations can explore part of the thermodynamic landscape but usually involve approximations and exclude solvent to reduce the computational cost, which may lead to results that differ from experimental observations. In principle, a combination of all these methods can allow one to compensate for the shortcomings of any one method. Establishing a robust theory of 1D metal nanostructure growth will thus require collaboration between synthetic chemists, electron microscopists, electrochemists, and theoreticians.

One recent report that examines the growth of CuNWs in the presence of HDA provides an example of such a collaboration (Figure 15).[20] It has been hypothesized that HDA selectively binds to the {100} facets on the side surface of NWs and thereby inhibits Cu deposition while leaving the {111} facets at the end of the NWs open for Cu addition. However, this mechanism cannot explain the fact that Cl^- is necessary for the anisotropic growth of CuNWs (Figure 15A). On the basis of the synthetic results, one could propose two hypotheses: (i) Cl^- selectively enhances the adsorption of HDA on {100} facets or (ii) Cl^- selectively removes the HDA monolayer from {111} facets. These hypotheses could be tested with single-crystal electrochemistry (Figure 15B), which clearly showed that the first hypothesis was false because Cl^- disrupted the ability of the HDA monolayer to passivate the Cu(111) surface at lower concentrations than for the Cu(100) surface. The concentration at which the difference in the charge transfer resistance between the Cu(111) and Cu(100) was the greatest exactly matches the concentration that produced the CuNWs with the highest AR. In addition, single-crystal electrochemistry helped explain why javelin-shape CuNWs rather than spheres formed at relatively high Cl^- concentrations when the HDA monolayer was disrupted on both Cu(111) and Cu(100). Figure 15B shows the disruption of the HDA monolayer by Cl^- on Cu(111) was faster than Cu(100), but after 5 min both surfaces were activated by Cl^- to an equivalent extent. As a result of this time-dependent facet-selective activation, and the fact that the CuNWs grew from the middle out over a similar time scale, javelin-shape CuNWs formed with a diameter in the middle that was larger than the diameter at the ends.

DOI: 10.1021/acs.chemrev.8b00745
Chem. Rev. XXXX, XXX, XXX−XXX

The facet-dependent displacement of HDA by Cl^- was corroborated by DFT calculations (Figure 15C). Both surfaces exhibited similar N−Cu bond distances (and thus similar bond strengths), in the absence of Cl^-, which agrees with the lack of facet-dependent electrochemical activation, as well as the formation of spherical particles, in the absence of Cl^-. At a Cl^- coverage of 0.25 monolayer, the Cu−N interaction was nearly doubled in strength for Cu(100), but weakened for Cu(111). Increasing the Cl^- coverage to 0.33 monolayer resulted in weak physisorption of HDA on Cu(111) surface because of short-range repulsion between Cl^- and HDA, whereas the structure of the Cu(100) surface accommodated strong chemisorption of both Cl^- and HDA. At the 0.5 monolayer coverage of Cl^-, short-range repulsion between Cl^- and HDA resulted in HDA being weakly physisorbed on both surfaces.

The corroboration between the results from the synthesis of CuNWs, single-crystal electrochemistry, and DFT calculations provided strong support for the proposed growth mechanism illustrated in Figure 15D. An intermediate concentration of Cl^- led to selective desorption of HDA from the {111} facets at the end of the CuNW, thereby causing anisotropic growth. This result illustrates that the simple picture of HDA acting as a facet-selective capping agent was incomplete. Instead, the presence of both Cl^- and HDA was necessary to obtain facet-selective atomic addition. Since the presence of both capping agents and halides is necessary for AuNRs, AgNWs, and a variety of other metal nanostructures, this work provides a template for uncovering the synergistic role that capping agents and halides might play in driving anisotropic growth.

5. MONOMETALLIC SYSTEMS

5.1. Noble Metals

Five metals, including copper (Cu), silver (Ag), gold (Au), palladium (Pd), and platinum (Pt), will be discussed in this subsection. These metals all have standard reduction potentials that are positive relative to hydrogen, making it relatively easy to reduce their respective ions.

5.1.1. Copper (Cu). Copper and Cu-based nanostructures have received steadily growing interest in various applications related to catalysis, electronics, and plasmonics because of the high abundance and low cost of Cu.[220] Compared to those with a 0D or 2D morphology, 1D Cu nanostructures are advantageous in terms of a larger area for the desired surface, faster electron transportation, and better flexibility. Taking penta-twinned CuNWs as an example, their large area of {100} facets on the side surface give them greatly improved activity and selectivity in catalyzing the electrochemical reduction of CO_2 to multicarbon products, such as ethylene.[221,222] Relative to ITO, a CuNW network offers the comparable conductivity, transparency, and flexibility but at a much lower cost.[4,223] The LSPR effect also makes 1D Cu nanostructures a promising candidate in plasmonic applications such as surface-enhanced Raman scattering (SERS) detection.[56,224] Compared to other noble metals, such as Au or Ag, however, there are only a limited number of reports on the colloidal syntheses of 1D Cu nanostructures. This shortage can be largely attributed to the difficulty in reducing a Cu(II) or Cu(I) precursor, lack of effective capping agents for shape control, limited choice of solvents, and poor stability of Cu under ambient conditions.[113] Among the reports on 1D Cu nanostructures, the majority of them were focused on CuNWs, with a few on NRs and other types of 1D nanostructures, such as tadpole-like NWs.

5.1.1.1. Nanowires. In general, methods for the production of CuNWs can be divided into three major categories: one-pot, seed-mediated, and template-directed. In this following discussion, we will introduce them in this sequence, together with the inclusion of some typical examples.

In a one-pot synthesis, Cu atoms are first formed via chemical reduction, followed by their aggregation into nuclei and then further growth into seeds and nanostructures. Surface capping agents are typically involved in the growth process, with notable examples including long-chain alkyl amines.[225] The slow reduction rate of a Cu(II) precursor, together with the use of a proper capping agent, can result in the formation of decahedral seeds, which further grow into penta-twinned NWs with high ARs. The NWs are covered by {100} facets on the side surface, together with {111} facets at the ends. It was reported that CuNWs with an average diameter of 24 nm could be produced in high purity of 95% and with a high conversion yield of 93% for Cu(II) in an aqueous solution heated at 100 °C (Figure 16A and B).[53] The lengths of the NWs varied in the range from several micrometers to millimeters. In a typical synthesis, the Cu(II) precursor based on $CuCl_2$ was reduced by glucose in the presence of HDA, which was hypothesized to act as a facet-selective capping agent for the {100} facets on the side surface of CuNWs. The capping agent not only directed the growth of nanostructures but also protected the surface from being oxidized in air. When reducing the amount of HDA by half, Cu nanocubes were generated due to the selective removal of multiply twinned, decahedral seeds via oxidative etching. Interestingly, using a similar protocol, tadpole-like NWs could be obtained by increasing the amount of glucose (Figure 16C and D). Increasing the concentration of the reducing agent led to an accelerated reduction rate for the Cu(II) precursor and thus the formation of decahedral seeds with a relatively large size. As the synthesis proceeded, glucose was consumed and the reduction rate would be decreased. The anisotropic growth on the decahedral seeds finally resulted in the formation of pentagonal bipyramids, which further evolved into tadpole-like NWs.

More recent work has demonstrated that CuNWs only formed in the presence of HDA when $CuCl_2$ rather than $Cu(NO_3)_2$ was used as a precursor to Cu.[20] This observation suggested that HDA by itself did not act as a facet-selective capping agent. Electrochemical measurements confirmed this hypothesis by showing that, in a solution of HDA and $Cu(NO_3)_2$, there is no difference in the charge transfer resistance between Cu(111) or Cu(100) for the reduction of Cu(II). However, if Cl^- is added into the reaction solution, the charge transfer resistance was 14.7 times lower on Cu(111) than on Cu(100), resulting in a 14.7 times greater reduction rate. The concentration of Cl^- that resulted in the lowest charge transfer resistance on Cu(111) relative to Cu(100) matched with the production of CuNWs with the highest AR. DFT calculations further showed that a coverage of 0.33 monolayer of Cl^- could selectively displace HDA from Cu(111), while allowing HDA to remain strongly bound to Cu(100), corroborating the synthetic and electrochemical results.

Under certain reaction conditions, alkylamines can also serve as both reducing agents and capping agents. For example, penta-twinned CuNWs were produced by heating CuCl in OLA at 170 °C.[55] In the initial stage of the synthesis, a Cu(I)-OLA complex was reduced to generate Cu atoms and then

DOI: 10.1021/acs.chemrev.8b00745
Chem. Rev. XXXX, XXX, XXX−XXX

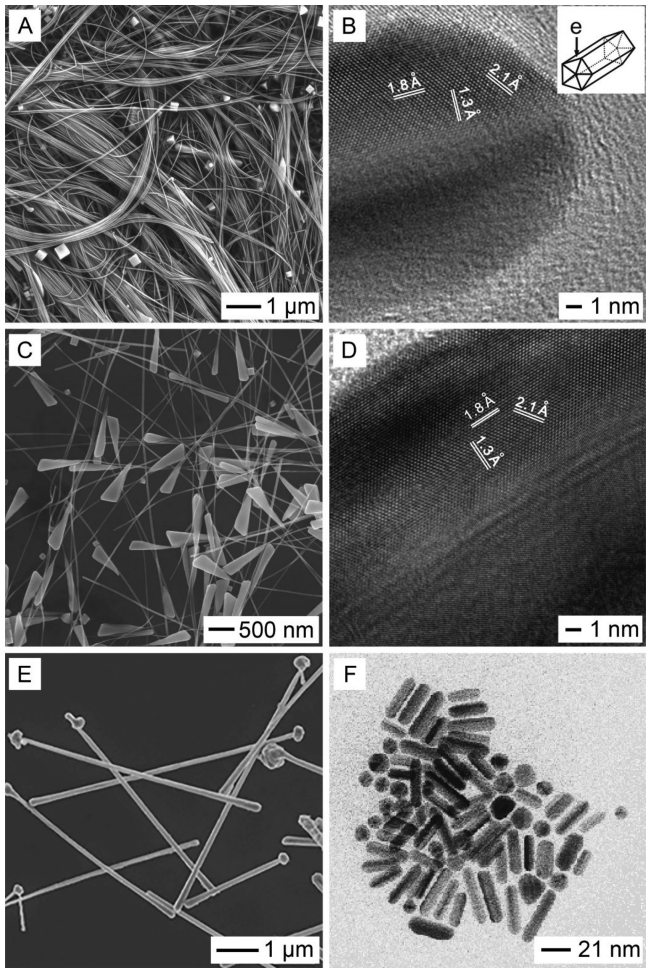

Figure 16. (A) SEM image of CuNWs synthesized in an aqueous solution in the presence of HDA and Cl^- ions. (B) High-resolution TEM (HRTEM) image taken from a CuNW oriented with one of its side faces parallel to the e-beam. (C) SEM image of tadpole-like CuNWs. (D) HRTEM image of a tadpole-like CuNW, revealing the twinned structure of the NW. (E) SEM image of CuNWs with Cu nanoparticles attached to one end. (F) TEM image of CuNRs synthesized from cylindrical templates assembled from surfactants (water content = 34). (A–D) Reprinted with permission from ref 53. Copyright 2011 Wiley-VCH. (E) Reprinted with permission from ref 229. Copyright 2010 Wiley-VCH. (F) Reprinted with permission from ref 238. Copyright 1997 American Chemical Society.

decahedral seeds through homogeneous nucleation. Due to the high energy of twin boundary and the capping of Cu{100} facets by OLA, the decahedral seeds then grew into penta-twinned NWs with an average diameter of 63 nm and lengths around 30 μm. In such a synthesis, OLA played multiple roles as a solvent, a coordination ligand, a reducing agent, as well as a capping agent.

The introduction of other metal ions may sometimes help the generation of CuNWs through galvanic replacement. For example, it was reported that CuNWs with a diameter of 15 nm and lengths up to 10 μm could be produced by reducing $CuCl_2$ in the presence of $Ni(acac)_2$ and OLA.[226] It was hypothesized that Ni(II) ions were first reduced to zerovalent atoms by OLA at a relatively low temperature, at which Cu(II) cannot be reduced to Cu(0) due to the stable complex between Cu(II) and ligands, such as OLA and Cl^-. The Ni atoms with high chemical activity would then rapidly reduce Cu(II) to Cu(0) atoms due to the synergy between the reduction by OLA and the galvanic replacement reaction, while the Ni(0) atoms were oxidized back to Ni(II). Eventually, nuclei made of Cu(0) atoms were formed, followed by their growth into decahedral seeds and penta-twinned NWs. Other additives such as $RuCl_3$ and $FeCl_2$ were shown to be able to protect the twinned seeds from oxidative etching, ensuring the evolution of NRs and then NWs from the decahedral seeds.[227]

Organic radicals have also been explored as reducing agents for the formation of uniform CuNWs with diameters ranging from 18–36 nm and lengths up to 20 μm.[228] It was demonstrated that, upon heating, benzoin decomposed into two radical segments, benzoyl radical and α-hydroxybenzyl radical, and the resulting radicals can act as efficient electron donors to reduce Cu(II) species to Cu(I) and then to Cu atoms. With the aid of OLA, Cu atoms nucleated to produce penta-twinned NWs with the side surface being covered by {100} facets. The reducing power of benzoin can be readily tuned by symmetrically adding different functional groups to the aromatic rings, with the introduction of electron-donating and electron-withdrawing groups to increase and decrease the reducing power, respectively.

Copper NWs have also been observed to grow from relatively large (200–300 nm), polycrystalline Cu nanoparticles that formed at the early stages of a synthesis (Figure 16E).[229] The synthesis involved the reduction of $Cu(NO_3)_2$ in an aqueous solution containing NaOH, EDA, and hydrazine. The as-synthesized CuNWs have a diameter of 90 nm and a length around 10 μm. Examination of the products formed in the early stages indicated that polycrystalline Cu nanoparticles were generated from the reduction of Cu_2O nanoparticles, which, in turn, formed from the precipitation of Cu(I).[230] In the absence of EDA, nearly all the Cu(I) precipitated out to form Cu_2O octahedra within the first few minutes, thereby depleting the Cu(I) precursor. This result shows that one of the major roles played by EDA in this synthesis is to suppress Cu(I) precipitation. It was initially hypothesized that EDA was a capping agent that selectively blocked the {100} facets on the side surface of a NW, enabling selective atomic addition to the {111} facets on the ends of a NW. Single-crystal electrochemistry experiments later revealed that this hypothesis was false.[177] Rather than acting as a capping agent, EDA acted as a facet-selective promoter for NW growth by keeping the {111} facets free from oxidation within the first few minutes of the reaction. Removal of the surface oxide from the side surface of the CuNWs in the later stages of the reaction resulted in an increase in their diameter from 35 to 153 nm.[167]

Various types of templates have also been used to direct the growth of CuNWs.[129,201,231–233] The templates can be selectively removed after the synthesis by calcination or dissolution to obtain free-standing nanostructures. For example, it was reported that CuNWs could be produced in a CTAB–amine–water–cyclohexane system, with $CuCl_2$ serving as a precursor and glucose as a reducing agent.[201] The best result was obtained when tetramethylenediamine (TMEDA) was used in the formation of CuNWs with diameters of 200–1000 nm and lengths up to 50 μm. It was believed that the assembly of CTAB, which lay at the interface between an aqueous solution and a nonpolar solvent, acted as a soft template to direct the growth of NWs. Biological entities with well-defined sizes and structures, such as DNA and viruses, have also been explored as templates for the

DOI: 10.1021/acs.chemrev.8b00745
Chem. Rev. XXXX, XXX, XXX–XXX

production of 1D Cu nanostructures, with notable examples including λ-DNA and tobacco mosaic virus (TMV).[129,233]

5.1.1.2. Nanorods. There are only a few reports on the synthesis of CuNRs, which might be related to the difficulty in avoiding oxidative etching and the tendency for the NRs to quickly grow into NWs. Similar to NWs, the one-pot synthesis of CuNRs often involves the reduction of a Cu(II) or Cu(I) precursor in the presence of capping agents.[234,235] For example, by reducing $Cu(acac)_2$ in octyl ether, CuNRs with an AR around 7 (~100 nm in width and ~700 nm in length) were obtained, albeit in low purity and quality.[235] In a typical protocol, 1,2-hexadecanediol was used as a reducing agent, with oleic acid (OA) and OLA both serving as capping agents. The proposed mechanism involved the initial formation of decahedral seeds and the preferential adsorption of capping agents on {100} facets, which led to the faster growth rate on {111} facets and thus the formation of NRs. In some cases, organic surfactants were not needed and CuNRs could be synthesized in the absence of a surfactant. As an example, the reduction of $CuSO_4$ by glucose in the presence of NaOH could generate CuNRs with an average diameter of 46 nm and a length of about 116 nm.[236] It was believed that the $Cu(OH)_2$ formed under the alkaline condition was responsible for nucleation and continuous growth. The formation of NRs may also be ascribed to the chelate stabilization between Cu(II) and the OH groups of glucose (at a particular concentration). The chelates might self-assemble into cylindrical shapes with voids inside them and, thus, act as templates for the growth of NRs.

In addition to one-pot synthesis, CuNRs were synthesized using a seed-mediated approach. Preformed metal nanocrystals with well-defined shapes, including Pd decahedra and Au spheres, have been used as seeds.[111,113] This will be discussed in section 6.2 because of the involvement of a different metal. In addition to seeds made of another metal, Cu nanocrystals can also serve as seeds to generate CuNRs. In a typical protocol, Cu nanocrystals to be used as seeds were first synthesized by reducing $CuCl_2$ with hydrazine in ethanol, with PVP serving as both capping agent and stabilizer.[237] These nanocrystals were then collected by centrifugation and added into an ethanol solution containing $CuCl_2$, PVP, and hydrazine for the growth of CuNRs. The as-prepared CuNRs had a diameter ranging from 50 to 70 nm and a length from 480 to 600 nm. According to the UV−vis spectrum, there was a strong extinction peak at 586 nm, which was red-shifted relative to that of Cu seeds. The redshift could be attributed to the increase in the AR for the products, indicating the formation of NRs.

Template-directed synthesis has also been applied to the production of CuNRs.[238−240] It was reported that cylindrical CuNRs could be prepared by reducing copper(II) bis(2-ethylhexyl) sulfosuccinate ($Cu(AOT)_2$) in an isooctane-water system with hydrazine serving as a reducing agent (Figure 16F).[238] Cylindrical water-in-oil droplets could be obtained when a certain ratio of water and $Cu(AOT)_2$ was used (water content, which was defined as the ratio of $[H_2O]/[AOT]$, located at 5.5−11 and 30−35), and these droplets then served as templates for the formation of cylindrical CuNRs. The CuNRs showed a diameter of around 6.5 nm and a length of around 20 nm. It was also reported that a self-assembled structure of long-chain, saturated fatty acid, lauric acid ($C_{12}H_{24}O_2$), could serve as a template for the synthesis of CuNRs with a diameter of 14 nm and lengths ranging from 100 to 235 nm.[241] In a standard protocol, a basic aqueous solution (with pH up to 12−13), containing $CuCl_2$, lauric acid, $AlCl_3$, NaOH, and EDA, was heated at 170 °C for 24 h. In this process, lauric acid acted as the reducing agent and template for the formation of CuNRs. In addition to organic templates, biotemplates including DNA and rod-like virus have also been exploited for the production of CuNRs.[233,242]

5.1.1.3. Summary. Among the various protocols for the synthesis of 1D Cu nanostructures, amine-based organic compounds, such as HDA, ODA, EDA, and OLA, are most commonly used as the shape-directing agents. Although it was initially thought that these additives acted as facet-selective capping agents, single-crystal electrochemical measurements revealed that the hypothesis needs to be modified.[20,177] For example, HDA passivates both Cu {111} and {100} facets to an equivalent extent, but can be selectively displaced from {111} facets by Cl^- for the initiation of anisotropic growth. The passivation by long-chain alkyl amines can protect the Cu surface from being oxidized in air, instrumental to the formation of nanostructures that are vulnerable to etching or corrosion due to their high surface areas and the presence of twin defects.[186] The coordination of amine groups to Cu(I) or Cu(II) ions could slow down the reduction kinetics of the precursor, and the relatively slow reduction rate is beneficial to the generation of multitwinned seeds, which will further grow into penta-twinned NWs.[243] Reducing agents such as hydrazine, H_2Asc, and glucose are typically used for aqueous systems. The use of radicals as reducing agents opens the door to a broad range of syntheses for Cu nanostructures, and it is hoped that more robust protocols will be developed in this regard. In addition to the synthetic methods, how to disperse and store 1D Cu nanostructures has emerged as a major concern because of the intrinsic instability of elemental Cu under ambient conditions. Methods including ligand exchange, introduction of reducing agents, involvement of oxygen scavengers, and application of metal coating can all be used to improve the stability of Cu nanostructures.[89]

5.1.2. Silver (Ag). Silver NWs have received considerable interest in the manufacturing of conductive, transparent, and flexible electrodes, which are key to a variety of applications such as touchscreens, flexible electronics, solar cells, and surface-enhanced infrared absorption device.[159,244] In this subsection, we highlight the major accomplishments in the syntheses of both Ag NWs and NRs, with an emphasis on NWs because they have already been incorporated into commercial products. Generally, the vast majority of the reported AgNWs are penta-twinned, so their internal structure will not be discussed in detail unless necessary.

5.1.2.1. Synthesis of NRs. The Br^--mediated polyol method was also modified for the synthesis of AgNRs (originally known as nanobars) with a single-crystal structure and a rectangular cross section. In a typical synthesis,[39] two solutions, one containing $AgNO_3$ in EG and the other containing PVP and NaBr in EG, were added dropwise via a two-channel syringe pump into EG held at 155 °C. The solid products obtained at 1 h into the synthesis contained a mixture of nanocubes and NRs with a range of ARs. Ionic bromides were also found to perform much more efficiently than the covalent compounds in inducing and promoting anisotropic growth.[40] In a typical synthesis with ionic bromides, the products contained a mixture of Ag nanocubes and NRs with square and rectangular cross sections, implying that the growth

DOI: 10.1021/acs.chemrev.8b00745
Chem. Rev. XXXX, XXX, XXX−XXX

rates along the three orthogonal ⟨100⟩ directions were different because of the presence of bromide.

In a most recent study,[245,246] similar AgNRs were also synthesized in an aqueous protocol that sharpened the corners and edges of truncated Ag nanocubes with sizes down to 18 nm, followed by their elongation into NRs with ARs up to 2. The key to the success of this synthesis is the site-selective deposition at corners and edges, as enabled by CTAC. In particular, Cl^- can react with Ag(I) to generate AgCl precipitates, slowing down the reduction kinetics. In addition, Cl^- can serve as a facet-selective capping agent toward the {100} side faces and thereby confine the growth mainly to corners and edges. Interestingly, once all the corners and edges had been sharpened, the growth was switched to an asymmetric mode that favored deposition on one of the six side faces only for the production of AgNRs with controllable ARs. The symmetry reduction was believed to take place as a result of the limited supply of Ag atoms, the strong capping of Cl^- ions toward the {100} facets, and the possible involvement of localized oxidative etching and thus activation for growth as caused by Cl^-/O_2.

5.1.2.2. Polyol Synthesis of NWs. Polyol reduction has long been the most popular approach to the production of uniform AgNWs.[247] Syntheses that fall within this category are conducted in a polyol (e.g., EG),[9,32,219] which plays dual roles as the reducing agent and solvent under heating. To stabilize or passivate specific facets on the nanostructures, it is also necessary to introduce various types of capping agents.

The initially reported polyol synthesis of AgNWs involved the use of preformed seeds. In one example,[9,248] the seeds were produced by reducing $PtCl_2$ or $AgNO_3$ with EG at 160 °C. Shortly after the emergence of seeds, an EG solution containing $AgNO_3$ and PVP was added dropwise. The close match in crystal structure and lattice constant between Pt and Ag is favorable for the heterogeneous nucleation and subsequent deposition of Ag atoms on Pt seeds. During the synthesis, the newly added $AgNO_3$ precursor could also undergo homogeneous nucleation, proceeding competitively with heterogeneous nucleation for the formation of Ag nanoparticles as a typical byproduct. These Ag nanoparticles could be consumed through Ostwald ripening to serve as a source of Ag atoms for the formation of relatively large nanostructures. In general, the AR of the resultant AgNWs (Figure 17A) can be tuned by varying a number of parameters, including the ratio of PVP to metal precursor, the reaction temperature, and the seeding conditions. Aspect ratios as high as 1000 could be easily and routinely achieved. Later, this protocol involving two steps condensed into one step. In the modified protocol,[219] an EG solution containing both $AgNO_3$ and PVP was titrated into EG heated at 160 °C with a syringe pump. By controlling the rate at which the metal precursor was introduced, the Ag atoms nucleated at the very beginning of a synthesis could serve as the seeds for growth. The seeds produced in situ were almost identical to the aforementioned Pt seeds in terms of function. Again, it was found that both the molecular weight of PVP and the molar ratio of PVP to $AgNO_3$ were critically associated with the purity and AR of the AgNWs.

The synthesis of AgNWs was also optimized by introducing various inorganic additives. In one demonstration,[49] AgNWs were synthesized by reducing $AgNO_3$ with EG at 148 °C in the presence of PVP and a trace amount of NaCl. In this case, Ag decahedral nanocrystals served as seeds for the growth of sub-

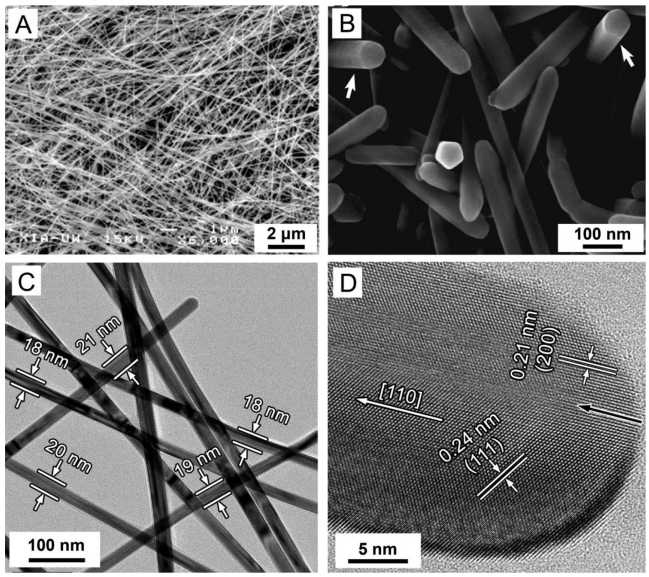

Figure 17. Silver NWs synthesized via a polyol process. (A) SEM image of a typical sample of AgNWs. (B) SEM image showing the characteristic pentagonal cross section of the AgNWs as marked by the arrows. (C) TEM and (D) HRTEM images of AgNWs with diameters controlled below 20 nm. (A) Reprinted with permission from ref 9. Copyright 2002 American Chemical Society. (B) Reprinted with permission from ref 47 Copyright 2003 American Chemical Society. (C, D) Reprinted with permission from ref 49 Copyright 2016 American Chemical Society.

20-nm AgNWs. It has now been well-documented that PVP has a stronger binding toward the Ag{100} facets over Ag{111} facets in EG.[47,112] This leads to the passivation of {100} facets that ultimately become the side faces of penta-twined AgNWs featuring a pentagonal cross section (Figure 17B). However, the formation of AgNWs was impeded by the presence of oxygen from air as it could work with Cl^- ions to dissolve the decahedral seeds through oxidative etching. To address this issue, Fe(II) was added to scavenge the dissolved O_2, eliminating oxidative etching and facilitating the formation of AgNWs.[218] Specifically, Fe(II) could be oxidized by O_2 to generate Fe(III), which could be recycled back to Fe(II) through reduction by EG. Likewise, the addition of other oxygen scavengers, such as Cu(I), also exert a similar effect.[249] In this case, it is interesting to note that the syringe pump was no longer necessary as the slow reduction kinetics could effectively mitigate the supersaturation problem that is detrimental to sample uniformity. In this case, the Cl^- ions from the additives were able to form poorly soluble compounds with Ag(I) ions, through which the availability of Ag atoms in the growth solution was reduced substantially. The poorly soluble species can act as a "sponge" to slowly but continuously release Ag(I) ions, which essentially serves the role of a syringe pump. Additionally, the Cl^- ions can also facilitate the growth of uniform AgNWs by stabilizing the Ag seeds via electrostatic interactions. In a third demonstration,[250] the goal of depleting O_2 was realized in the absence of any oxygen scavenger. Specifically, the EG being used as solvent or growth solution was preheated at 170 °C for 1 h prior to the introduction of NaCl, PVP, and $AgNO_3$. During the heating process, the O_2 in the reaction system was consumed by oxidizing EG to aldehyde, the actual reducing agent responsible for polyol reduction. Compared to the initial

DOI: 10.1021/acs.chemrev.8b00745
Chem. Rev. XXXX, XXX, XXX−XXX

attempt, such an approach was able to increase the volume of production by a factor of 10 while allowing for the synthesis of AgNWs with different diameters.

To reduce the diameter of AgNWs, the deposition of atoms on side faces should be minimized, halide species, such as Br^- ions, whose interaction with Ag{100} facets are relatively stronger than other facets, have been shown to be more effective than PVP alone in inhibiting atomic addition to Ag{100} facets,[49,159] enabling the synthesis of AgNWs featuring narrow diameters. It should be noted that the presence of Br^- ions can behave in a way similar to that of Cl^- ions by forming poorly soluble species (AgBr), in addition to its role in oxidative etching. Therefore, it is necessary to remove O_2 from the growth solution through either the addition of O_2 scavenger or preheating treatment. Furthermore, it was found that increasing the molecular weight of PVP could also help reduce the diameter of AgNWs.[49] In a typical synthesis, an EG solution of PVP ($M_w \approx 1.3$ MDa) was heated at 160 °C for 1 h, followed by the addition of NaBr that was dissolved in EG. An EG solution of $AgNO_3$ was then titrated into the mixture at a rate of 0.15 mL/min. The reaction could be finished within 35 min after initiation, and the products contained AgNWs (>85% in purity) with a mean diameter below 20 nm (Figure 17C and D). In this case, the passivation of side faces by both PVP and Br^- ions contributed to the inhibition of lateral growth, only allowing for the deposition of Ag atoms along the longitudinal direction. In another study,[248] it was found that a high reaction temperature promoted lateral growth. As such, it is essential to reduce the temperature to minimize the diameter of the AgNWs. However, a lower temperature will weaken the reducing power of polyol, leading to the production of fewer Ag atoms. A recent study addressed this issue through the introduction of benzoin, a precursor to reductive radicals, into the growth solution. In a typical synthesis, $AgNO_3$, PVP ($M_w \approx 1.3$ MDa), NaCl, and NaBr were mixed together in EG, followed by the addition of benzoin.[217] The reaction was conducted at 150 °C for 1 h under the protection of N_2. Specifically, the presence of both Cl^- and Br^- ions resulted in the production of AgNWs with diameters down to 16 nm, whereas the participation of Br^- ions alone could further reduce the mean diameter to 13 nm. Possibly, it was the replacement of Cl^- ions absorbed on Ag{100} facets by Br^- ions that contributed to an enhanced passivation effect.

Polyol synthesis has also been conducted by heating with a microwave system.[251−253] In this case, almost all reagents involved in the synthesis are the same as what were used in a traditional polyol synthesis except for the heating method. Recent studies suggested that dissolved oxygen can also play a key role in inducing 1D growth under microwave irradiation. One study reported that AgNWs could be produced with a purity as high as 90% without any purification under continuous bubbling of air.[251] By contrast, if the synthesis was conducted under the protection of N_2, a mixture of byproducts including cubes and bipyramids emerged, and the yield of AgNWs dropped to 20%. No explanation was provided to account for the exact role played by oxygen in this system.

5.1.2.3. Other Methods for NWs. In addition to the polyol method, it is possible to produce AgNWs in an aqueous system.[48,254,255] In one study,[254] AgNWs were obtained at a relatively large scale through the direction by a soft template based on CTAB. In this case, a two-step protocol was used. Silver nanoparticles 4 nm in diameter were prepared by the reduction of $AgNO_3$ with $NaBH_4$ in the presence of trisodium citrate (Na_3CA). Next, the nanocrystals were used as seeds for the deposition of Ag atoms in a growth solution containing $AgNO_3$, H_2Asc, CTAB, and NaOH. Upon reaching a critical concentration, the CTAB molecules can spontaneously assemble into tubular micelles. Thanks to the strong interaction between Br^- ions and Ag{100} facets, the CTAB micelles could effectively guide the 1D growth necessary for the formation of AgNWs. By increasing the pH of the growth solution to a value slightly greater than 11.8 (p*K*a of the second proton of H_2Asc), the length of the resultant AgNWs could be reduced for the production of rod-like nanostructures. Though feasible to some extent, the limited ARs of the AgNWs (typically, below 50) offered by this method cannot satisfy the requirements of many applications.

In the absence of preformed seeds, AgNWs can only be produced as a consequence of self-nucleation. The purity and uniformity of the resultant AgNWs tend to be compromised unless the synthesis is conducted under extreme conditions such as hydrothermal or solvothermal heating. In one study,[48] $AgNO_3$ precursor was reduced by glucose, Na_3CA or sodium hypophosphite in water at different temperatures. Regardless of the reducing agent, short AgNWs and irregularly shaped Ag nanoparticles were produced. Through the introduction of sodium dodecylsulfonate as a surfactant, another group reported the preparation of high-quality 1D Ag nanostructures under similar conditions.[256] In this case, the AR of the resultant 1D nanostructures increased as the concentration of Na_3CA was decreased, making it feasible to produce both NRs and NWs.

Solvothermal conditions have also been used to produce uniform AgNWs. In one study,[257] both $AgNO_3$ and PVP ($M_w \approx 360$ kDa) were dissolved in ethanol, followed by the addition of an ethanol solution containing NaCl. The mixture was transferred into an autoclave and heated at 150 °C. The dominant products were AgNWs (length = 5−20 μm; diameter = 70 nm). Here, the PVP molecule played the dual roles as both the reducing agent and capping agent. The concentration of NaCl was found to be crucial to the evolution into NWs, with abundant byproducts emerging in the case of inadequate NaCl. In another study,[258] a solvothermal condition based on polyol was used to produce ultralong AgNWs. Specifically, $AgNO_3$ and PVP ($M_w \approx 1.3$ MDa) were dissolved in EG before the introduction of $FeCl_3$. The mixture was sealed in an autoclave and heated at 130 °C. Silver NWs with lengths up to 400 μm, together with a diameter of about 55 nm (AR > 4000) were obtained, which were much longer than those produced using the conventional polyol method (typically, 1000−2000). It was proposed that the extreme condition, most importantly, the high pressure, favored stronger passivation of Ag{100} facets by both Cl^- ions and PVP with a high molecular weight. Despite these demonstrations, concern still exists with regard to the reproducibility, as well as the cost-effectiveness of a hydrothermal or solvothermal method.

5.1.2.4. Summary. For the colloidal synthesis of AgNWs, the polyol method has been the most versatile and most successful one. Initial attempts involved the use of seeds that were prepared separately. With a better understanding of how the 1D nanostructures are formed, AgNWs can now be prepared in one pot and in a single step by controlling the experimental conditions so that the Ag nanoparticles that emerge during the early stage of reduction can serve as the

DOI: 10.1021/acs.chemrev.8b00745
Chem. Rev. XXXX, XXX, XXX−XXX

seeds for further growth. An optimized polyol method would only allow homogeneous nucleation to take place at the very beginning of the reaction, helping mitigate the size and morphology variations for the final products. Aside from their role in manipulating the reduction kinetics, inorganic additives such as halide ions can also selectively bind to the {100} facets on both NWs and NRs to help initiate and direct 1D growth. On the other hand, the formation of less soluble species between Ag(I) and halides ions can reduce the availability of Ag atoms and modify the reaction kinetics, both are vital to the reduction of symmetry and thus the formation of 1D nanostructures. If there is anything to be said as a major drawback of the polyol synthesis, it should be the relatively high reaction temperature and the high sensitivity of a synthesis toward the impurities, including Cl^- and iron species, commonly associated with commercial polyols. It is still not feasible to produce high-quality 1D Ag nanostructures in an aqueous system and at room temperature.

5.1.3. Gold (Au). Gold is the most extensively investigated noble metal for the synthesis and exploration of 1D metal nanostructures. Like Cu and Ag, 1D Au nanostructures feature highly tunable LSPR peaks in the visible and near-infrared regions, but Au is much more resistant to oxidation. The combination of plasmonic activity and stability makes 1D Au nanostructures a versatile platform material for a wide variety of applications, including sensing, SERS, and catalysis.[259−263] Gold is also biocompatible and can be conjugated to a library of molecules, such as drugs, DNA or siRNA, targeting ligands, as well as fluorescent or radioactive labels through the well-established Au−S chemistry. These features have been instrumental in applying Au-based nanostructures to the diagnosis and treatment of various types of malignancies like cancer, inflammation, infection, and Alzheimer's Disease.[2,3,264]

5.1.3.1. Nanorods. The most popular form of 1D Au nanostructure is the NR. When we conducted a search on the Web site of Google Scholar using the keyword "gold nanorod", as many as 59,900 publications were found (dated 08/02/2018), which is certainly beyond the capacity of a single review article. In this subsection, we would like to highlight the key concepts with regard to the colloidal synthesis of AuNRs.

In 2001, the first wet chemical synthesis of AuNR was reported on the basis of seed-mediated growth.[8] In a typical experiment, 3.5 nm Au seeds, whose surface was capped by citrate, were prepared through the reduction of $HAuCl_4$ by $NaBH_4$ in the presence of citrate. The seeds were subsequently introduced into a growth solution containing $HAuCl_4$, CTAB, and H_2Asc, w/wo $AgNO_3$, in a mixture of cyclohexane and acetone. Next, part of this growth solution was extracted and used as the seeds for a second-round of reduction in another growth solution. Although it was not resolved in the original study, now it is clear that the AuNRs obtained using this protocol were penta-twinned, featuring ARs tunable in the range of 6−20 and lengths up to 400 nm. Afterward, many studies were carried out to optimize this protocol in an effort to improve the purity (initially, it was as low as 5%) and uniformity of AuNRs. One of the breakthroughs was made two years later.[265] In that work, a new protocol was reported by switching to CTAB-capped Au nanoparticles (1.5 nm in diameter) as the seeds. Specifically, the seeds were synthesized by reducing an aqueous solution containing CTAB and $HAuCl_4$ with $NaBH_4$. Different from the multiply twinned seeds prepared in the presence of citrate, the seeds synthesized using this new protocol were single crystalline, featuring a cuboctahedral shape. Using these seeds, short AuNRs with ARs in the range of 2−5 were obtained through Ag(I)-assisted growth in a way similar to what was used in the three-step method. One of the marked developments is the substantial improvement in the purity (>95%) of AuNRs.

On the basis of this new development, a library of wet chemical methods has been reported for the preparation of AuNRs differing in length, diameter, AR, and crystallinity.[266−272] Despite the differences in synthetic procedures to a minor or even moderate content, essentially all the vast majority of approaches available so far are based on seed-mediated growth. Collectively, putting the details of chemicals aside, the synthesis of AuNRs can be simply described as a two-stage process: initially, surface-capped, tiny Au seeds ranging from 1−3 nm are prepared through the reduction with a strong reducing agent. The freshly prepared seeds are then introduced into a growth medium containing metal precursor, capping agents that stabilize or direct the growth of NRs, a reducing agent with moderate reducing power that promotes heterogeneous atomic addition, or some inorganic or organic additives that promote the formation of AuNRs featuring with a high purity. To this end, many studies sought to improve the understanding of the roles of many parameters in the preparation of AuNRs, consequently leading to the emergence of numerous hypotheses on the basis of experimental observations or computational modeling.[21−23,273−275] Though informative to some extent, there is still no consensus as to how AuNRs grow asymmetrically from highly symmetric seeds, or the relative importance of different parameters for this process. Here we focus on the roles of several key parameters that govern the formation of AuNRs.

5.1.3.2. The Role of Seeds. As discussed in section 3, the crystallinity, size, and shape of seeds are crucial to the evolution of nanostructures. This has been validated in the case of AuNRs. Generally, two classes of AuNRs that differ in crystal structure have been prepared: (i) penta-twinned AuNRs with a pentagonal cross section (Figure 18A) and (ii) single-crystal AuNRs with an octagonal cross section (Figure 18B). For the later one, its truncated tip is enclosed by a mix of {100}, {111}, and possibly {110} facets. Initially, the lateral facets enclosing the single-crystal AuNRs were believed to be {011}, but more recent results suggest the side surface of

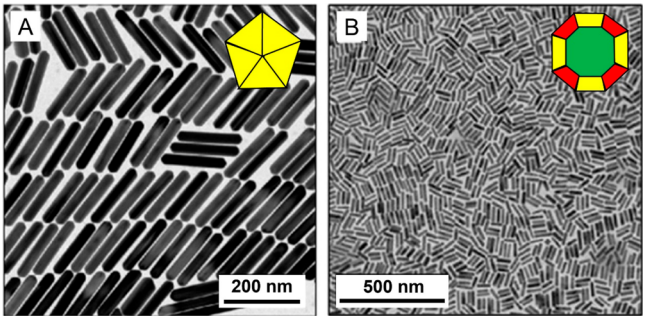

Figure 18. (A) TEM image of penta-twinned AuNRs with a pentagonal cross section (see the inset for a projection along the long axis). (B) TEM image of single-crystal AuNRs with an octagonal cross section (see the inset for a projection along the long axis). (A, B) Reprinted with permission from ref 277. Copyright 2015 American Chemical Society. (Inset A) Reprinted from ref 279. Copyright 2014 American Chemical Society. (Inset B) Reprinted from ref 43. Copyright 2010 Wiley-VCH.

DOI: 10.1021/acs.chemrev.8b00745
Chem. Rev. XXXX, XXX, XXX−XXX

AuNRs consists of high-index {011 + $\sqrt{2}$} facets.[276] To produce single-crystal AuNRs, one must first produce Au cuboctahedral seeds enclosed by {100} and {111}. In a typical synthesis,[265] an aqueous solution containing $HAuCl_4$ is mixed with that of CTAB at a concentration above its critical micelle concentration (CMC), resulting in the formation of CTAB micelles. The mixture will immediately change to a blond color, which is much brighter than that of the original metal precursor. This observation reveals the ligand exchange between the counterion (Br^-) of CTAB and the Cl^- of $HAuCl_4$. Next, $NaBH_4$, a potent reducing agent that is dissolved in iced water (in an effort to slow down its decomposition) is introduced, and the reaction will be completed almost immediately as reflected by the swift change in color. Specifically, starting from a brownish seed suspension, AuNRs can be produced that feature better monodispersity than the reddish colored seed solution does, presumably owing to the abundance of Au nanospheres with sizes beyond 4 nm.[277] It is now well established that a combination of CTAB and $NaBH_4$ favorably produces single-crystal Au nanoparticles with sizes below 4 nm. When these seeds are introduced into a growth solution containing $HAuCl_4$, H_2Asc, and CTAB, w/wo additives such as Ag(I), aromatic compounds, or sialic acid. The Au atoms derived from the reduction of Au(I)-Br^--CTA^+ complex will be deposited onto the seeds. As mediated by several components that will be detailed later in this subsection, the atom deposition under such condition can break the original symmetry of seeds, a criterion for growing essentially all types of 1D nanostructures, leading to (i) the elongation of the seeds, (ii) the formation of dog-bone-like intermediate, and (iii) the transient evolution into NRs that feature flat, lateral surfaces.[278] Essentially all AuNRs prepared using this protocol are single crystalline, featuring an octagonal cross section.[276]

Alternatively, the agent used to stabilize the seeds can be switched to either citrate or PVP. Without changing other parameters, the as-prepared AuNRs will be changed from single-crystal to penta-twinned.[277] Further investigations revealed that the presence of citrate or PVP favors the production of multiply twinned nanostructures such as decahedra or icosahedra with sizes in the sub-10 nm range.[109,280,281] Since these nanostructures are enclosed by {111} facets, they are thermodynamically stable when containing some portions of truncation in the intersection of {111} facets.[282] When the seeds are introduced into the growth solution, these truncations parallel to ⟨110⟩ direction will be passivated by the surfactant and/or additives, only allowing for the deposition of atoms onto {111} facets for the production of penta-twinned AuNRs

From the perspective of symmetry breaking,[282] the size of seeds is crucial to the successful preparation of AuNRs. Specifically, it has been observed that the symmetry of a nanostructure can only be broken when its size is within a relatively narrow range (typically, 4−6 nm). As such, large Au nanostructures cannot serve as the seeds for the growth of AuNRs in high purity, independent of their surface properties. For the ultrasmall counterparts, their poorly faceted structures abrogate the emergence of {011} or {100} facets in the nascent nanostructures, thereby either totally preventing the production of AuNRs or resulting in the massive production of byproducts such as bipyramids, cubes, and spheres. Within a moderate range, the increase in seed size reduced the AR of the resultant AuNRs by increasing their width. Besides, it is also reported that the surface potential/charge of seeds can influence the purity as well as the AR of the resultant AuNRs. Specially, the variation in these parameters is susceptible to negatively charged seeds, rather than these positive counterparts.[283] However, it should be mentioned that such a study was conducted in the absence of Ag(I),[283] which is now routinely leveraged as an important additive to control the AR and purity of AuNRs. As such, the role of the surface potential of seeds in the growth of AuNRs still needs to revisited under conditions more relevant to what is used currently.

Another important aspect of the seed-mediated growth is the time interval between the seed preparation and their introduction into the growth solution. In the case of $NaBH_4$ reduction, though the seeds are believed to be produced almost immediately upon the initiation of reduction, they have to be aged to get rid of the excess reducing agent. During this period, two processes occur: the decomposition of excess $NaBH_4$ and the ripening of Au seeds. Generally, the resultant Au seeds can be used after storage for a couple of hours at 27 °C.[277] Further aging of the seeds results in the increased formation of nanoparticles instead of NRs in the growth solution.[284] As mentioned earlier, Ostwald ripening increases the size of the initially generated Au seeds at the expense of smaller seeds, increasing the size of the seeds to values beyond what is allowed for symmetry breaking.[285] Altogether, these findings demonstrate that the structure and size of the Au seeds, as governed by many parameters, affect the structure and quality of the resultant AuNRs.

5.1.3.3. The Role of Surfactant. CTAB is the most commonly used surfactant for the growth of AuNRs. Here we only give a brief discussion on the many roles played by CTAB in directing the growth of AuNRs. Starting from the stage of seed preparation, CTAB is critical to the emergence of {100} facets on the cuboctahedral seeds.[282] As we have mentioned above, for sub-10-nm nanoparticles, the thermodynamically favored structures are decahedra or icosahedra with surfaces covered primarily by {111} facets. Chemisorption of CTAB may result in a substantial reduction in the free energy for {100} facets, leading to the production of cuboctahedral seeds. For the anisotropic growth from cuboctahedral seeds to rod-like structures, it was initially proposed to be guided by the worm-like micelles formed by CTAB.[286] In principle, it is possible for CTAB molecules to undergo a spheroid-to-rod change in the micelle structure at a high concentration (typically, ∼0.5 M).[287] However, a simple switch from CTAB to CTAC featuring similar micelles failed to replicate the rod-like structure,[288] suggesting that other roles played by CTAB promote the formation of NRs.

A set of experiments were designed to elucidate the explicit role played by CTAB in anisotropic growth.[214,288−291] It is now believed that the Br^- counterion of CTAB contributes more to the anisotropic growth than the CTA^+.[291] The rapid ligand exchange between Br^- and Cl^- in $AuCl_4^-$ results in a reduced redox potential ($AuBr_4^-$/Au = 0.854 versus SHE; $AuCl_4^-$/Au = 1.002 versus SHE), thus preventing homogeneous nucleation in the presence of a weak reducing agent such as H_2Asc. Furthermore, the Br^-, possibly in tandem with CTA^+, enables symmetry breaking through the selective passivation of facets other than {111}. As one can imagine, for cuboctahedral seeds, the passivation of either {100} or {111} facets will only lead to the production of cubic or octahedral nanocrystals, respectively. Experimental evidence

DOI: 10.1021/acs.chemrev.8b00745
Chem. Rev. XXXX, XXX, XXX−XXX

confirmed the emergence of {110} facets that cover the side surfaces of the resultant nanostructures.[282] The presence of {110} facets can be explained as an attempt of the cuboctahedral seeds to reduce the under-coordinated atoms located at the junction linking two {111} facets. The preservation of these metastable facets, however, has long been poorly understood. Recent computational modeling suggests that the coverage density of CTA^+ on {110} (1.49 molecules/nm^2) is identical to that on {100} (1.49 molecules/nm^2) and higher than that on {111} (1.31 molecules/nm^2).[292] As such, stabilizing these facets may have led to the extension of {110} facets on side surfaces of AuNRs. This simulation was conducted under Ag(I)-free conditions, which is essential to the production of octagonal AuNRs. The authors also studied the case of Ag(I)-assisted growth, and interestingly, it was found that the introduction of Ag(I) reduced the selectivity of CTAB toward {110} facets over {111} and {100}.

Another important parameter that governs the growth of AuNRs is the backbone of the surfactants.[214,290] In one study,[214] the C_{16}TAB was replaced by several analogues (C_nTAB, n = 10, 12, 14, 16, and 18). It was shown that the production of AuNRs differing in AR could also be achieved via fine-tuning of surfactant tail length, with a longer chain favoring the growth of AuNRs with a greater AR. On this basis, the authors proposed a "Zipping" mechanism, in which the intermediate AuNRs were capped by a bilayer of surfactants similar to the cell membrane, with polar groups facing the AuNRs and aqueous solution. In this case, the longer the chain length is, the stronger the van der Waals attracting force between them will be, supporting a more stable surfactant bilayer. On this basis, new approaches leveraging binary/gemini surfactants were proposed in an effort to tune the structure of surfactant micelles.[293] It was found that any choice other than quaternary ammonium surfactant would prevent the formation of NRs,[291] thereby highlighting the significance of the headgroup of a surfactant in guiding the symmetry breaking process. Changes were also made to the headgroup, in which the replacement of methyl with ethyl group could greatly extend the AR of the resultant AuNRs.

In 2008, an interesting observation emerged, in which the quality or even the reproducibility of AuNRs synthesis was linked to an impurity in CTAB.[288,294−296] Initially, the authors noticed that there existed huge differences in the performance of CTAB obtained from different manufacturers or even the same vendor but with different lot numbers.[288] Later, inductively coupled plasma mass spectrometry (ICP-MS) was used by the same group to show that a tiny amount of iodide contaminating some samples could prevent the growth of AuNRs.[294] Paradoxically, some subsequent studies reported that iodide is essential to AuNR synthesis,[295] and others used iodide as an additive to finely tune the structure of AuNRs.[296] Though the exact roles of impurities in CTAB are still under debate, it raised a good point about a previously overlooked parameter that might explain reproducibility issues.

5.1.3.4. The Role of Silver. It is generally accepted that the presence of Ag(I) ions is crucial controlling the AR of single-crystal AuNRs that evolved from CTAB-capped seeds, whereas it prevents anisotropic growth of penta-twinned AuNRs.[277] Although penta-twined AuNRs can still be produced in the presence of Ag(I) ions, their purity and uniformity are relatively poor. It was suggested that the complexation between Ag(I) and surfactant micelles reduce the passivation of specific facets, eventually leading to the formation of less isotropic structures like spheroids.[277] Given this, the following discussion is confined to the roles of Ag(I) ion in the growth of single-crystal AuNRs. Specifically, three different mechanisms have been proposed to account for the influence of Ag(I) ions: (i) the formation of a silver-bromide complex (in the form of either $Ag(I)-Br^--CTA^+$ or simply as $AgBr_2^-$) that acts as a capping agent toward lateral facets of the evolving AuNRs; (ii) the deposition of a thin layer (down to the subnanometer range) of Ag atoms through UPD, resulting in passivation of specific facets of intermediate nanocrystals and thus symmetry breaking; and (iii) the remodeling of spherical CTAB micelles into a cylindrical shape to serve as a soft template to guide the growth. All three types explanations are individually supported by a variety of facts, both experimental and computational.[277] However, a considerable portion of these findings conflicts with one another. For instance, if Ag(I) ions actively participate in the growth of AuNRs through either the formation of a silver-bromide complex or by harnessing the UPD mechanism, the presence of Ag may be found on specific facets.[109] However, energy dispersive X-ray spectroscopy (EDX) maps of Ag on AuNRs synthesized in the presence of Ag(I) ions showed that Ag was concentrated at the surface of AuNRs but had no preference for a particular facet.[297] X-ray photoelectron spectroscopy analysis indicated that the Ag(I) ions were bound in a complex between silver bromide and CTAB.[298] Thus, the role of the Ag(I) additive in symmetry breaking and controlling the AR of single-crystal AuNRs has not yet been resolved.

5.1.3.5. Influence of Other Parameters. During the modification of the experimental procedure, it was noted that several other parameters, including the additives (both organic and inorganic), the pH value, the reaction temperature, and the nature of the reducing agent could all affect the purity and AR of the resultant AuNRs.[299−303]

5.1.3.6. Post-Synthesis Treatment. As we have discussed, during a typical Ag(I)-assisted synthesis, the conversion rate of precursor-to-product is typically lower than 30%.[304] Under this condition, two species, Au(0) in the AuNRs and the Au(III) metal precursor coexists and can react through a disproportionation reaction (Au(III) + Au(0) → Au(I)). Such a reaction, though not favored under normal condition ($K \approx 1.9 \times 10^{-8}$), was drastically promoted through the complexation of $AuCl_4^-$ with CTAB micelles.[305] Specifically, CTAB capping is less dense on the curved tips of a NR, making the atoms vulnerable to etching by Au(III) and a reduction in NR length. This assumption was supported by UV−vis spectra that showed the absorption peak of AuNRs suspended in the growth solution was blue-shifted over time.[161] Since the width of the AuNRs is more or less fixed, the oxidation of AuNRs along the longitudinal direction offers a way to fine-tune the AR postsynthesis.[305]

The AuNRs can also be elongated by leveraging the excess metal precursor in the reaction solution.[304] During a typical synthesis of AuNRs, the reducing agent, H_2Asc, is depleted prior to the metal precursor. The choice of introducing an inadequate amount of reducing agent is built upon the consideration that a too strong a reducing power can lead to isotropic growth. A second addition of H_2Asc, however, can induce a second-round of growth on the pre-existing AuNRs. Depending on the amount of H_2Asc, a set of structures from dog-bone-like to slightly concave rods have can be synthesized.[304]

DOI: 10.1021/acs.chemrev.8b00745
Chem. Rev. XXXX, XXX, XXX−XXX

5.1.3.7. Gram-Scale Production. To fully explore the translational potential of AuNRs in various applications, AuNRs must be produced at the gram-scale or large, but such a scale cannot be achieved with the aforementioned protocols.[8,265] Given this, a different method was proposed and validated.[306] In this study, a one-pot synthesis in the absence of seeds was reported. Specifically, CTAB powder and an aqueous solution of $AgNO_3$ and $HAuCl_4$ were mixed together, followed by the introduction of NaCl in order to narrow the size distribution of AuNRs. Next, two different reducing agents, H_2Asc and $NaBH_4$ were sequentially introduced into the growth solution, and the reduction was allowed to proceed for several minutes under ambient conditions. In this case, the AR of the resultant AuNRs could be tuned, by varying the amount of $NaBH_4$, to a maximal value of 5.6. The AuNRs prepared via seedless growth had ARs similar to those prepared using seed-mediated growth, but had smaller lengths and widths. This one-step strategy is, in principle, similar to that of two-step, seed-mediated growth, but the generation of seeds was executed in situ rather than ex situ. Indeed, the authors demonstrated that the size of the seeds that were generated in situ had a dramatic effect on the resulting nanostructure morphology.

5.1.3.8. Tapered Gold Nanorod. During the evolution of decahedral seeds into penta-twinned NRs, the diameter may keep decreasing, leading to the formation of NRs with a tapered cross-sectional area and enclosed by high-index facets. In one study,[33] it was demonstrated that the hydroxyl group in tetra(ethylene glycol) (TTEG) could also serve as a ligand to stabilize Au(I) ions. When the TTEG-stabilized Au(I) was used as a precursor to elemental Au, the rice-like final products were covered by ten {611} facets their sides and ten {111} facets at the two ends (Figure 19). In a typical synthesis, the

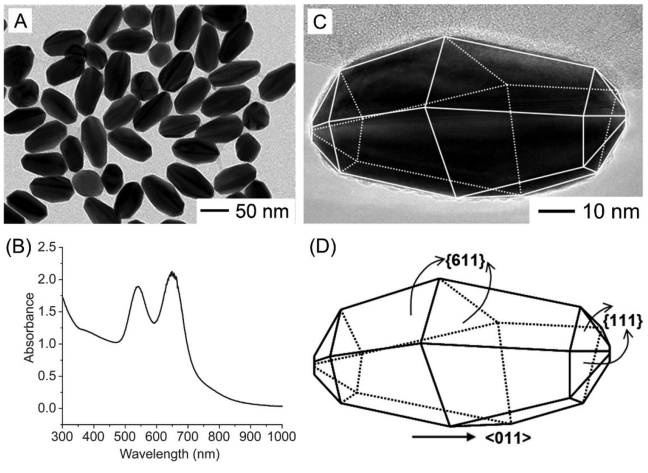

Figure 19. (A) TEM images of tapered AuNRs. (B) UV−vis spectrum recorded from an aqueous suspension of the tapered AuNRs. (C) TEM image of an individual tapered AuNR and (D) the corresponding model. Reprinted with permission from ref 33. Copyright 2011, Wiley-VCH.

freshly prepared Au(I)-TTEG solution was mixed with a freshly prepared aqueous solution of $AgNO_3$ in a vial and heated at 130 °C for 5 h. The molar ratio of Au to Ag was set to 20:1. A trace amount of $AgNO_3$ had to be introduced into the reaction solution to induce the formation of the tapered NRs. Because of the existence of high-index facets on the surface, the tapered AuNRs exhibited better catalytic performance toward CO oxidation reaction than Au nanoparticles with similar dimensions but enclosed by low-index facets.

5.1.3.9. Nanowires. As a promising candidate for flexible electronics, it has been demonstrated that AuNWs outperformed the bulk material over 100 times in terms of mechanical strength.[307] Several strategies, including template-directed synthesis[308] and oriented attachment,[124] have been explored for the production of AuNWs. In one report,[124] $HAuCl_4$ was mixed with OLA and OA in toluene, followed by refluxing at 120 °C. An intermediate composed of Au(I) that was chelated with OLA emerged, as indicated by the faded color of the growth solution. Next, 2 nm Au nanoparticles synthesized by $NaBH_4$-mediated reduction were introduced along with H_2Asc as a reducing agent. The reduction of Au(I)-OLA to Au(0) was allowed to proceed under ambient conditions for a few days, and AuNWs with an average diameter of 2 nm were produced. The main byproduct of this synthesis was poorly defined nanoparticles with sizes below 20 nm. The AuNWs were believed to evolve through orientated attachment of single-crystal, small Au nanoparticles along the ⟨111⟩ direction. The presence of some twin-defects and stacking faults indicated that the fusion of {111} facets of adjacent Au nanocrystals was incomplete. Here, the production of wire-like structures due to oriented attachment was explained by the selective capping of {100} facets of Au nanoparticles, which left the {111} facets exposed and thereby vulnerable to attachment. Both low concentrations of metal precursor and surfactant favored the production of 1D nanostructures by harnessing such a mechanism.

Ultrathin AuNWs have also been synthesized using alternative methods. In one study,[309] AuCl was used as a metal precursor, and reacted with OLA in hexane to form the Au(I)-OLA complex, an intermediate similar to that emerged during the synthesis discussed above. Next, Ag nanoparticles were introduced into the growth solution after it had been heated to 60 °C, and the reaction was allowed to proceed at this temperature for 24−100 h. It was found that the as-synthesized AuNWs had a mean diameter of 1.8 nm (AR > 1000) and they grew along the ⟨111⟩ direction (Figure 20A and B). The polymeric Au(I)−OLA complex was formed due to the aurophilic binding between AuCl and OLA. There, the chain-like complexes were proposed to serve as the backbone of the resultant AuNWs. The exact role of Ag nanoparticles in this synthesis is yet to be elucidated. It is thought that they acted as a reducing agent in addition to OLA in this synthesis. Likewise, AuNWs with a narrower diameter could be produced by slightly changing the reaction temperature and time.[310] Gold NWs featuring a thicker diameter have also been synthesized. As described in one study,[311] OLA and OA were mixed with $HAuCl_4$, and heated at 80 °C for 5 h. The diameters of the resultant AuNWs were 9 and 3 nm in the presence and absence of OA, respectively. The growth of both types of AuNWs took place along the ⟨111⟩ direction. The only crucial component during the synthesis of AuNWs is OLA. Proposed roles for OLA include the formation of structure-guiding micelles, chelation with metal precursor, and serving as a capping agent.[311]

Several synthetic methods have been developed to control the number of planar defects in Au NWs. In one study,[312] it was demonstrated that mechanical forces from stirring rate increased the production of planar defects. In another study,[313] it was shown that the kinked AuNWs composed with many planar defects could be prepared through kinetic control. In

DOI: 10.1021/acs.chemrev.8b00745
Chem. Rev. XXXX, XXX, XXX−XXX

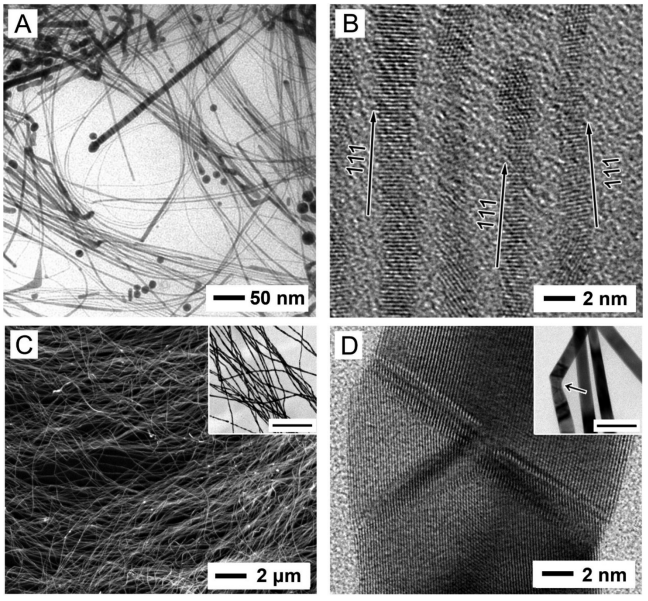

Figure 20. (A) TEM image of the as-synthesized AuNWs and (B) HRTEM images of AuNWs aligned along the ⟨111⟩ direction. (C) SEM images of wavy AuNWs. (Inset: TEM image taken from the same batch of wavy AuNWs.) (D) HRTEM image showing the stacking faults, which was enlarged from the region highlighted by a black arrow in the inset. Inset scale bar: 50 nm. (A, B) Reprinted with permission from ref 309. Copyright 2008 American Chemical Society. (C, D) Reprinted with permission from ref 60. Copyright 2012 American Chemical Society.

this case, different amounts of $CuCl_2$ and ethanol were sequentially introduced into the solution containing $HAuCl_4$ to help tune the rate at which the Au nanoparticles were produced. These nanoparticles were then elongated, and attached with adjacent counterparts to create the kinked structures. Likewise, in the presence of CTAB, wavy AuNWs can also be obtained through the reduction of $HAuCl_4$ with H_2Asc (Figure 20C).[60] Unexpectedly, the AuNW product segregated to the air/water interface, facilitating their purification. The presence twin boundaries perpendicular to the NW growth direction (Figure 20D) suggests the NWs grew through oriented attachment.

All the above-mentioned AuNWs, though differing in the manner of synthesis, share one thing in common: their *fcc* structure. In contrast, a recent demonstration showed that tadpole-shaped AuNWs composed alternating segments in *hcp* and *fcc* phases could be synthesized.[314] $HAuCl_4$ and OLA were heated at 55 °C for 36 h along with graphene oxide (GO) sheets. Tadpole-shaped structures were produced, with the tapering section composed of alternating segments of *hcp* and *fcc* phases, whereas the so-called "head" segment was only *fcc*. Since no special component other than GO was involved, it was proposed that the presence of this substrate helped to stabilize the *hcp*-domains whose emergence is otherwise less favored energetically.

5.1.3.10. Summary. Seed-mediated growth under ambient conditions is the most successful and popular method for synthesizing AuNRs. In this approach, Au nanoparticles are prepared and then introduced into the growth solution as seeds, along with various organic and/or inorganic additives, such as Ag(I) ions and surfactants. The amounts and types of additives, as well as the type of seed, can be used to control the AR, shape, and crystal structure of the resultant AuNRs. For example, the seeds prepared using the $NaBH_4$/CTAB and

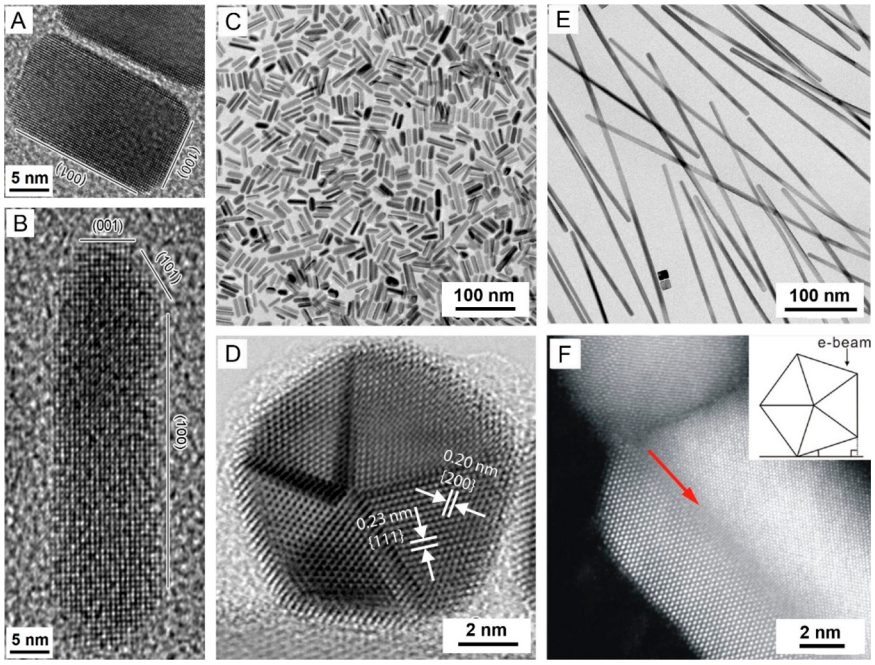

Figure 21. (A, B) HRTEM images showing the single-crystal PdNRs with an AR of (A) 2 and (B) 4, respectively. (C) TEM image of penta-twinned PdNRs. (D) HRTEM image showing the characteristic, penta-twinned structure of such a rod when the electron beam was aligned parallel to the long axis. (E) TEM images of PdNWs synthesized via the polyol method. (F) HRTEM image taken from the end of an individual PdNW, whose projection is illustrated in the inset. (A, B) Reprinted with permission from ref 38. Copyright 2007 American Chemical Society. (C, D) Reprinted with permission from ref 320. Copyright 2015, Wiley-VCH. (E, F) Reprinted with permission from ref 96. Copyright 2017 American Chemical Society.

DOI: 10.1021/acs.chemrev.8b00745
Chem. Rev. XXXX, XXX, XXX−XXX

citrate-mediated reduction routes produce single-crystal and penta-twinned AuNRs, respectively. Extensive experimental efforts have clarified the roles played by various additives to certain extents, but many questions and controversies still remain. Rapidly developing characterization techniques, such as in situ TEM and single-crystal electrochemistry, may help to address some of the outstanding questions. In contrast to the aqueous conditions used for the synthesis of AuNRs, their wire-like counterparts are normally prepared in organic solvents. In a typical process, Au (I or III) chelated with organic ligands serve as the metal precursor, and a large number of nanoparticles are produced shortly after the initiation of the reaction. Next, wire-like nanostructures with planar defects emerge as a result of oriented attachment of the nanoparticles. In this case, the environment as mediated by the dissolved O_2 plays a crucial role in shaping the final products. In addition to AuNWs that adopt an *fcc* structure, Au nanostructures containing the *hcp* crystal domains have been prepared using GO as a template.[314] As an interesting note, there are way more reports on AuNRs than on AuNWs. This disparity can probably be attributed to the easiness in synthesizing AuNRs in high quality. In contrast, it is still very difficult and challenging to generate AuNWs with quality equivalent to that of AuNRs.

5.1.4. Palladium (Pd). Palladium nanostructures have been extensively explored for a range of applications, including the catalysis of organic coupling reactions (e.g., Heck and Suzuki), detection and storage of hydrogen, and electro-oxidation of fuels such as formic acid and ethanol.[315−317] In addition to the shape-dependent catalytic activities, computational studies indicate that 1D Pd nanostructures, such as NRs and NWs, may feature ferromagnetism at room temperature, while bulk Pd is known to be paramagnetic.[318] These and other intriguing findings have motivated the development of protocols for generating 1D Pd nanostructures. Depending on the exact conditions, the methods can be divided into different categories, including solvothermal, polyol, mesophase-templated, galvanic replacement, and phase transfer, among others.

5.1.4.1. Nanorods. There are around 10 publications on the colloidal synthesis of PdNRs, and the methods fall into three general categories: one-pot synthesis, seed-mediated overgrowth, and template-directed growth.

For the one-pot synthesis, one of the protocols involved the introduction of Na_2PdCl_4 into a mixture of KBr, PVP, and different amounts of water in EG held at 100 °C.[38] In this case, both EG and PVP could serve as reducing agents while Br^- ions acted as a capping agent toward the {100} facets. The reaction starts with the formation of single-crystal seeds, followed by their evolution into NRs through anisotropic growth (Figure 21A and B). The NRs took a single-crystal structure (diameter = 6 nm; AR = 2−4). It was proposed that oxidation etching, caused by the Br^- ions and the dissolved oxygen, played an important role in initiating the anisotropic growth. Depending on the exact shape or morphology of the seeds, the final products exhibited different cross sections. Specifically, cubic seeds resulted in the formation of PdNRs with a square (or rectangular) cross section, while cuboctahedral seeds produced PdNRs with an octagonal cross section. A one-pot synthesis of PdNRs could also be conducted in an aqueous system by reducing Na_2PdCl_4 with H_2Asc in the presence of KBr and PVP (a coreductant and a colloidal stabilizer).[319] After heating at 80 °C for 3 h, penta-twinned PdNRs were obtained. In this case, it was believed that Pd decahedral seeds were formed in the early stage of the synthesis due to the slower reduction kinetics relative to the polyol synthesis based on EG. Assisted by the Br^- ions and PVP, the decahedral seeds grew to form penta-twinned NRs covered by {100} on the five side faces and {111} facets on the two ends. The seeds formed in the nucleation stage could also adopt single-crystal and singly twinned structures, leading to the formation of cubes and right bipyramids as byproducts.

Compared to one-pot synthesis, seed-mediated growth offers better control of product purity. Both Pd decahedral nanoparticles[320] and Pd clusters[321] have been explored as the seeds. In the case of Pd clusters, the seeds were obtained by reducing K_2PdCl_4 with $NaBH_4$ in the presence of CTAB as a stabilizer, in a manner similar to the preparation of Au clusters for the growth of AuNRs. The clusters were then added into the growth solution containing K_2PdCl_4, CTAB, and sodium ascorbate. The TEM images of samples from reaction solution at different time points revealed that two populations of nanoparticles were formed at the very beginning of a synthesis, including the added Pd seeds (7−8 nm in size) and smaller Pd nanoparticles (2−3 nm in size) that formed due to homogeneous nucleation.[321] The authors proposed that growth of penta-twinned NRs from the mixture of seeds and smaller particles was due to the assembly of the smaller particles onto one side of the seed with a 5-fold symmetry.

Uniform, high purity PdNRs can be obtained via Pd seed-mediated growth as assisted by Cu(II)-mediated UPD.[322] Palladium seeds were prepared by reducing $PdCl_4^{2-}$ with $NaBH_4$ in the presence of CTAB. The seeds were added to a growth solution containing Na_2PdCl_4, H_2Asc, and CTAB for 2 h, and some of this solution was then added to a second growth solution containing $Cu(OAc)_2$ and H_2Asc. The second growth solution was left undisturbed at 30 °C for 20 h. Addition of increasing amounts of Cu(II) to the second growth solution resulted in the formation of longer NRs (length = 200−300 nm; AR = 10−15), and eventually branched nanostructures. The effect of Cu(II) on the PdNR AR was attributed to the periodic deposition and oxidation of Cu atoms on the ends of PdNRs, but exactly how Cu facilitated anisotropic deposition of Pd was unclear. It was also proposed that higher concentrations of Cu ions activated sites for Pd deposition on the side facets as well as the ends, leading to the branched morphology. Other ions, such as Ni(II), Zn(II), or Ag(I) did not promote anisotropic growth. However, reduction with $NaBH_4$ normally produces seeds with a variety of crystal structures and shapes.[321] Another report improved the purity of NRs through substitution of the seeds.[320] In this protocol, decahedral seeds were prepared using the polyol method. These seeds were mixed with a DEG solution containing PVP, H_2Asc, and NaI, followed by the addition of Na_2PdCl_4 dissolved in DEG. After heating at 160 °C for 1 h, uniform penta-twinned PdNRs with diameters in the range of 6−16 nm and lengths up to 81 nm were obtained (Figure 21C and D). Although I^- and Br^- chemosorb onto the {100} facets of Pd nanostructures in a similar way, the replacement of I^- with Br^- led to the formation of twinned bipyramids only, suggesting that the greater size of I^- was of paramount significance in preserving the penta-twinned structure. Furthermore, control over the diameter and length of PdNRs can be realized by increasing the size of the dodecahedral seeds and the amount of metal precursor, respectively. Although the introduction of seeds can make the reaction less convenient than one-pot syntheses, can enable the

DOI: 10.1021/acs.chemrev.8b00745
Chem. Rev. XXXX, XXX, XXX−XXX

production of a much more uniform NR product with improved shape control.

For template-directed growth, CTAB is broadly exploited either alone or in combination with PVP as a cosurfactant. In one study,[323] PVP, an aqueous solution of CTAB, and H_2PdCl_4 were added sequentially into EG that was heated to 150 °C under the protection of argon gas. By tuning the ratio of CTAB to PVP, the AR of the resultant PdNRs could be adjusted from 2.5 to 7.8. Without the assistance of CTAB, PVP alone cannot guide 1D growth, and polyhedral nanoparticles are produced. The presence of too much CTAB, however, can presumably passivate the NR ends, as well as the side, thereby reducing the anisotropy of the final products. Similar results have also been reported in another study based on microwave synthesis.[324] Alternatively, CTAB alone could support the confined growth in 1D as long as the reduction rate was slow enough.[325] In this case, $Pd(NO_3)_2$ was added into an aqueous solution containing a mixture of CTAB and H_2Asc, and the reaction was allowed to proceed at 50 °C for 2 min. An aqueous solution of sodium ascorbate was then added, followed by another 5 min of reduction at the same temperature. Through the two-stage reduction, penta-twinned, concave PdNRs were synthesized. The key to the success of creating such structures was the interval allowed for the reductions mediated by H_2Asc and sodium ascorbate. It is critical to realize a moderate nucleation rate so that the penta-twinned PdNRs would be favorably formed through the timely migration of deposited atoms to side faces. Subsequently, the introduction of sodium ascorbate markedly accelerates the rate of atom deposition, causing the evolution of concave facets on the PdNRs. The major drawback of this protocol is the unsatisfactory purity of the resultant PdNRs. Because of poor control over nucleation, three types of nanostructures differing in shape emerged, including rods, bipyramids, and cubes, with the PdNRs only accounting for ca. 24% of the final solid products. Nevertheless, the strategy of stepwise reduction is still of practical value in developing rational syntheses of nanostructures with concaved faces.

As in the case of AuNRs, the introduction of metal ions can remodel the growth of PdNRs. To assess the role of Ag(I), H_2PdCl_4 was thoroughly mixed with CTAB, followed by the sequential addition of KI, $AgNO_3$, and H_2Asc.[326] The reduction was allowed to proceed at 90 °C for 1 h. By changing the stage at which $AgNO_3$ was added, the authors found that Ag(I) was associated with the formation of multiply twinned seeds, rather than the subsequent growth. Possibly, either Ag or AgI clusters served as the templates for the further production of Pd twinned nanoparticles. The length of the resultant PdNRs could be tuned in the range of 100−500 nm by decreasing the pH of the growth solution, with the diameter of the resultant nanostructures largely fixed at 20 nm. This control over shape was believed to be associated with the pH-sensitive reducing power of H_2Asc, where slow reduction mediated by H_2Asc under an acidic condition was beneficial to the elongation of NRs.

5.1.4.2. Nanowires. Palladium NWs are generally penta-twinned, with the side surface and ends enclosed by {100} and {111} facets, respectively.[96] In one study,[327] penta-twinned PdNWs were synthesized using a hydrothermal method. Specifically, $PdCl_2$ was used as a metal precursor and added into an aqueous solution containing PVP and NaI. The mixture was sealed in Teflon-lined stainless-steel autoclave and the reaction was allowed to proceed at 200 °C for 2 h. The resultant PdNWs were uniform in size with a mean diameter of 9.0 ± 1.0 nm and a length of about 3 μm. Characterization by HRTEM revealed that the as-synthesized NWs had a penta-twinned structure and grew along the ⟨110⟩ direction. Their lengths could be controlled by varying the reaction time, with an extended time favoring a shorter length and a larger diameter. Given the thermodynamic instability of the {100} facets, prolonged heating is believed to reduce their presence on the surface, leading to the morphological change from NWs to NRs. The amount of PVP was also critical in determining the morphology of the final products, and was believed to serve as a reductant in addition to its role as a stabilizer. Halving or doubling the amount of PVP resulted in the production of cubic, triangular, tetrahedral, or spherical nanostructures, rather than NWs. The presence of I^- was also crucial to the production of PdNWs. In the absence of I^-, a network of interconnected nanoparticles was produced instead of the penta-twinned PdNWs.

Using a hydrothermal method,[328] PdNWs comprised of nanoparticles bounded by high-index facets such as {443}, {331}, and {221} could be synthesized. In this case, the same metal precursor ($PdCl_2$) and stabilizer (PVP) were utilized, whereas the halide ion was switched to F^- through the introduction of NaF. Sodium dodecyl sulfate (SDS) was also used as a cosurfactant. All the reactants were mixed under ambient conditions prior to transferring into an autoclave. After heating at 220 °C for 6 h, wavy NWs comprised of Pd particles (mean diameter = 4.0 ± 0.7 nm) with grain boundaries were obtained. As confirmed by HRTEM, the Pd nanoparticles were oriented along the ⟨110⟩ direction, in line with the growth direction of penta-twinned PdNWs. By reducing the duration of heating to 2 h, bent NRs emerged as the major intermediate. As such, the particle-to-wire shape-evolution is believed to be a consequence of oriented attachment in an effort to minimize the surface energy, followed by the end-to-end attachment of rod-like intermediates that contributed to the extension along the ⟨110⟩ direction. The absence of either SDS or NaF prevented the production of wire-like structures, leading to the production of short rods together with some poorly defined nanoparticles. As a strong interaction between either the sulfate group of SDS or F^- and Pd atoms is not expected, the exact roles played by these two components are unknown.

Through the electrostatic interaction with the metal precursor, the surfactant can also direct the growth of PdNWs in a role other than just the passivation of specific facets. In an early study,[329] poly(methacryloyloxyethyl dimethylbenzylammonium chloride (PMB-Cl), a positively charged, brush-like polymer, was synthesized via free radical polymerization to act as the template. Next, a clean Si wafer was immersed into a solution containing PMB-Cl for 1 min, followed by dipping into an acidic solution of $Pd(OAc)_2$ for another 1 min. The Pd(II) ions absorbed on PMB-Cl were reduced by dimethylamine borane (DMAB) in the same solution. Atomic force microscopy (AFM) analysis revealed that the PMB-Cl molecules deposited on the Si wafer exhibited a worm-like structure, consistent with the morphology of the as-synthesized PdNWs with a mean diameter of 5 nm and lengths up to 1 μm. The length of the resultant PdNWs was governed by the polymer-based substrate. Specifically, when an extremely long polymer ($M_w \approx 6.3$ MDa) was introduced, PdNWs with lengths up to 1 μm were obtained. By contrast, if the PMB-Cl polymer was added freely into an aqueous

DOI: 10.1021/acs.chemrev.8b00745
Chem. Rev. XXXX, XXX, XXX−XXX

solution, their interaction with the metal precursor would make the Coulomb repulsion less favorable, resulting in a substantial change to the polymer conformation. As such, the "freezing" of PMB-Cl on the Si wafer was believed to be crucial to the preservation of wire-like structures.

Alternatively, biotemplates such as DNA molecules can also be harnessed to direct the growth of PdNWs.[330] In a typical experiment, K_2PdCl_4, λ-DNA, and Na_3CA were mixed thoroughly. The strong binding of Pd(II) with the N7 and N3 atoms of guanine/adenine and thymine/cytosine bases, respectively, can be used to immobilize the metal precursor, as confirmed by Fourier-transform infrared spectroscopy (FT-IR) and UV−vis spectra. After the introduction of DMAB or $NaBH_4$ as a reducing agent, the reaction was allowed to proceed for 2−24 h under ambient conditions. The difference in reducing power between these two reducing agents did not change the morphology of the product. The diameters of the resultant PdNWs could be controlled in the range of 5−45 nm as confirmed by AFM analysis, which was greater than what was calculated (1.6 nm) on the basis of X-ray diffraction (XRD) peak width using the Scherrer equation. A bead-on-necklace structure was proposed, in which ultrafine Pd particles (with sizes down to 1.6 nm) crystallized and then arranged along the longitudinal axis of the DNA template.

The surfactant micelles formed by CTAB above the CMC were also proposed to serve as a template for growth of PdNWs. In one example, CTAB was added into the brine to obtain a viscous micellar solution, followed by the addition of a toluene solution of tris(dibenzylideneacetone)dipalladium or $Pd_2(DBA)_3$.[331] The mixture was then gelled as triggered by a tiny amount of 1-pentanol to finalize the formation of the mesophase. Upon reduction with hydrazine vapor, PdNWs were obtained. Small-angle X-ray scattering (SAXS) analysis revealed that the metal precursor-doped surfactant mesophase featured a hexagonal symmetry, in agreement with the three characteristic Bragg peaks in the ratio of $1:3^{1/2}:2$ as confirmed by XRD. Since the reduction of $Pd_2(DBA)_3$ was driven by hydrazine in the vapor phase, the reaction required 48 h for the reducing agent to diffuse through the mixture. Notably, the Pd atoms in $Pd_2(DBA)_3$ are zero in valence, which is substantially different from the conventionally used Pd(II) precursors. Upon the reduction of DBA by hydrazine, the interaction of these ligands with Pd(0) would weaken, leading to the release of Pd(0) atoms and their aggregation into clusters. The resultant clusters are then subjected to orientation and coalesce along the longitudinal axis of CTAB micelles. Though disoriented to a minor content, the selected area electron diffraction (SAED) pattern of the cross section of an individual PdNW confirmed the presence of {111} facets and the growth along the ⟨111⟩ direction. Such an observation, along with the presence of single-crystal domains featuring lengths over 30 nm, rules out the possibility that the PdNWs are penta-twinned. Replacement of CTAB with either SDS or cetylpyridinium chloride (CPC) only led to the production of spherical particles. The authors proposed that Br^-, as assisted by CTA^+ from CTAB, passivated the {100} facets of Pd particles, leading to the orientation-driven growth along ⟨111⟩ direction. Similarly, PdNWs were synthesized using dioctadecyldimethylammonium chloride (DODAC) as a surfactant.[332] The soft template composed of DODAC also features a hexagonal symmetry (*p6mm*) as indicated by SAXS measurements. Upon reduction H_2Asc at 95 °C, a temperature proven to be crucial to the stabilization of worm-like micelles, PdNWs were prepared. Specifically, when the heating temperature was lowered to 65 and 45 °C, helical and ring-like structures were obtained because of the changes in the structure of the DODAC micelles.

The role of oxygen in PdNW growth has also been explored. In one study,[333] *n*-dodecyltrimethylammonium bromide (DTAB) was introduced to bind with $Pd(NO_3)_2$ or $PdCl_2$, and facilitate phase-transfer into a mixture of ODA and toluene. The mixture was then reduced by $NaBH_4$ to produce metastable, elongated nanostructures. These intermediates then underwent secondary growth and resulted in the formation of thread-like PdNWs. Since Br^- was involved in this case, the orientation of intermediates proceeded in a fashion similar to what was mentioned above, in which the passivation of {100} facets presumably led to growth along the ⟨111⟩ direction. Many twin boundaries and stacking faults were observed between the interconnected Pd nanoparticles, making them vulnerable to oxidative etching as mediated by the Br^- and oxygen. This was confirmed by exposing the PdNWs to air, after which the length of NWs was reduced until they split into spherical particles after 12 h. In another study,[96] PVP, H_2Asc, NaI, and a tiny amount of HCl were mixed in DEG before addition of Na_2PdCl_4. When the mixture was heated at 160 °C for 1 h, and PdNWs with diameters below 8 nm and ARs up to 100 were obtained. Extending the reaction time to 1.5 h resulted in the formation of particles at the ends of the PdNW, resulting in a tadpole-like morphology. At 4 h, all the NWs disappeared and only irregularly shaped particles remained. Control experiments showed that the NWs broke up into nanoparticles in DEG solutions containing PVP, NaI, and HCl in just 10 min, but the extent of etching was greatly reduced if argon was bubbled through the reaction solution. These results suggested that oxidative etching was responsible for the conversion of penta-twinned PdNWs into nanoparticles.

Sacrificial templates, such as TeNWs, can also be used to direct the growth of PdNWs.[334] In a typical experiment, the TeNWs were added into EG under ambient conditions. After the introduction of $PdCl_2$, the mixture was heated at 50 °C for 13 h to facilitate the galvanic replacement between Pd(II) and Te. According to the stoichiometry, the removal of 1 Te atom should correspond to the deposition of 2 Pd atoms that were about the same in volume as one Te atom, resulting in the production of solid PdNWs with ARs beyond 10 000. Given the fairly low temperature involved, EG was likely not acting as a reducing agent, but its high viscosity was beneficial for slowing the galvanic replacement reaction to produce a smooth NW surface. This study also highlights the significance of the valence of metal precursor in regulating the morphology of the final products. If the volume of the deposited metal atoms is inadequate to compensate for the loss caused by the removal of atoms from the template, hollow structures will emerge instead of solid ones.

The aforementioned approaches were all seedless in nature, whereas seeded growth can enable the production of nanostructures with more uniform in size and shape. Seed-mediated synthesis was exploited to fabricate PdNWs as a catalyst for Sonogashira-coupling reaction.[335] A thiol-functionalized ionic liquid, (1-methyl-3-(2-mercaptoacetoxyethyl) imidazolium chloride, was first added into an aqueous solution containing $HAuCl_4$ at room temperature, followed by reduction with $NaBH_4$. Next, Au clusters capped by ionic liquid molecules were introduced into an aqueous solution

DOI: 10.1021/acs.chemrev.8b00745
Chem. Rev. XXXX, XXX, XXX−XXX

containing H_2PdCl_4, and the mixture was once again reduced by $NaBH_4$ under ambient conditions. This approach produced worm-like PdNWs with an average diameter of 3.1 nm. The emergence of PdNWs, rather than spherical nanoparticles as normally observed in the case involving $NaBH_4$ as a reducing agent, was attributed to the strong interaction between the thiol group of the ionic liquid and the nanocrystals. XRD results suggested the facets passivated by ionic liquid were {111} facets on the basis of their considerable abundance in the resultant-PdNWs, thereby offering an approach to preserve facets other than {100}, which can be achieved by Br^- or I^-.

Template-free syntheses of PdNWs can offer a less laborious approach compared to template-based methods to producing sufficient quantities of PdNWs to explore and use their properties in applications. In one template-free method, injection of $Pd(OAc)_2$ into PVP solution (in DEG) was carried out at 140 °C, and the reaction was allowed to proceed for 3 h.[63] Wavy PdNWs with a diameter as thin as 2 nm were produced, which were morphologically similar to that of the wavy AuNWs discussed in section 5.1.3. The TEM images at different stages of the reaction demonstrated that the formation of wavy PdNWs involved three steps: (i) ultrafine Pd nanoparticles emerged due to a burst of homogeneous nucleation; (ii) the metastable Pd nanoparticles then aggregated to create intermediate structures such as short NRs; and (iii) the NRs attach end-to-end to form wavy NWs. Increasing the temperatures seemed to result in greater consumption of the metal precursor during nucleation, thereby leading to the production of a greater number of NWs featuring a lower AR than those obtained at a lower temperature. When the precursor was switched to less active Na_2PdCl_4, the reduction rate was substantially decreased, resulting in ongoing nucleation events over the course of the reaction. In this case, only well-dispersed, large Pd polyhedral nanocrystals were obtained, again highlighting the importance of the reduction rate in controlling the produce morphology. Similarly, the vulnerability of the resultant PdNWs to oxidative etching was confirmed by the production of polyhedral nanocrystals after extended heating in air.

5.1.4.3. Summary. Most of the reported Pd NRs and NWs have a penta-twinned structure. Halide ions are usually necessary for the formation of such NRs and NWs, and they can play multiple roles. Ligand exchange can take place between the introduced halide ions and that of the metal precursor, leading to a slower reaction kinetics for the initiation of anisotropic growth. The strong binding of halides toward Pd(100) surface also favors the formation of Pd 1D nanostructures enclosed by {100} facets, including Pd nanobars with a rectangular cross section and penta-twinned NRs and NWs with a pentagonal cross section. By fine-tuning the reaction kinetics, Pd decahedral nanoparticles can be generated in situ. With halide ions passivating the newly formed {100} facets, the Pd decahedral seeds favor growth along ⟨110⟩ direction to evolve into penta-twinned NRs and then NWs. The 1D Pd nanostructures can also be formed as a consequence of random or oriented attachment of nanoparticles, but they are vulnerable to oxidative etching due to the abundance of planar defects located at the intersections between domains. In this case, experimental conditions such as heating temperature and the number of halide ions must be carefully controlled to mitigate the adverse impacts of oxidative etching.

5.1.5. Platinum (Pt). Platinum plays critical roles in an array of applications.[336−340] For instance, it can serve as an excellent catalyst for CO/NOx oxidation in converters, production of nitric acid, as well as many types of organic reactions (e.g., hydrogenation). There have been extensive studies of the use of Pt as an electrocatalyst for the oxygen reduction reaction (ORR), as well as for the oxidation of fuels including hydrogen, methanol, and ethanol.[336] The strong worldwide demand for Pt has resulted in a steady increase in price, motivating researchers to engineer Pt-based catalysts with increased activity, selectivity, and durability. To this end, 1D Pt nanostructures featuring high surface-to-volume ratios, together with well-defined facets, have been actively explored. In this subsection, we focus on the syntheses of PtNWs, the most popular form of 1D Pt nanostructures. The synthetic strategy can be generally divided into three categories: substrate-based, template-directed, and template-free synthesis.

5.1.5.1. Substrate-Assisted Growth. Various types of solid substrates have been explored to guide the growth of PtNWs. PtNWs were grown directly from the surface of a Pt or W gauze, as well as from a Si substrate.[340−342] The selection of Pt or W gauze was made based on the consideration of downstream catalytic applications. Normally, for those PtNWs deposited on commercially available substrates like carbon black, their life span is limited due to corrosion of the underlying carbon. The introduction of Pt gauzes can readily address the issue of corrosion, in addition to other contributions to the catalytic performance. Likewise, the W gauze can also act as a cocatalyst in conjunction with the deposited PtNWs. In a typical experiment, either Pt or W gauze was added into EG that was preheated at 110 °C for 30 min, along with the addition of either Fe(III) or Fe(II) species. Another 30 min of heating was conducted to remove remaining water before the simultaneous introduction of PVP and H_2PtCl_6 that were predissolved in EG. The reaction was proceeded for 18 h in air, with the metal precursor being reduced by EG as mediated by the Fe(III) or Fe(II) species. The final products were collected as black aggregates on the gauze. It was found that the PtNWs (diameter: 5 nm; length: 100 nm) grew along the ⟨111⟩ axis. The addition iron species, either Fe(III) or Fe(II), could slow down the rate of H_2PtCl_6 reduction, which favored the formation of the PtNWs. Since both Pt and W gauzes can serve as substrates for the growth of PtNWs, it is not unreasonable to suggest that such a strategy can be extended to gauzes other than those made of Pt or W, or more broadly speaking, other classes of substrates as long as they are stable in hot polyol.

Besides this, substrate-free, polyol synthesis of PtNWs has also been reported. In one study,[343] and intermediate composed of Pt(II) formed during the reduction of either H_2PtCl_6 or K_2PtCl_6 metal precursor with EG in the presence of PVP. These intermediates, though stable under ambient conditions, can react to form tiny Pt nanocrystals after heating at 110 °C. Furthermore, the authors showed that the introduction of a small amount of either $FeCl_3$ or $FeCl_2$ would slow down the rate at which small Pt nanocrystals were produced, leading to their assembly into sea urchin-like structure (Figure 22A−D). By virtue of the fact that the absence of either air or iron species could prevent the production of PtNWs, the following mechanism underlying their formation was proposed: During the reaction, the reduction of Pt(II) to Pt(0) is autocatalytic, that is, the enlargement of the Pt nanocrystals which emerged at the very

DOI: 10.1021/acs.chemrev.8b00745
Chem. Rev. XXXX, XXX, XXX−XXX

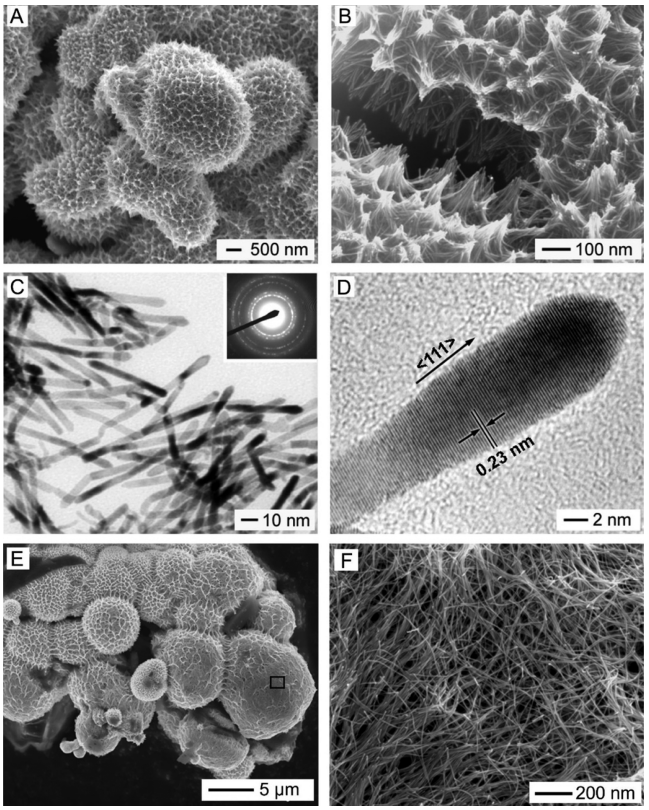

Figure 22. Electron micrographs of PtNWs synthesized via polyol reduction in the presence of Fe(III) species: (A) SEM image of the hierarchically structured Pt agglomerates, (B) SEM image of the PtNWs anchored to the surface of the agglomerates, (C) TEM image of PtNWs harvested from the agglomerates through sonication, (D) HRTEM image showing an individual PtNW grown along the ⟨111⟩ direction, (E) SEM image of the Pt hierarchical structures synthesized using the same protocol except that the Pt nanoparticles were assembled into agglomerates through the introduction of SDS, and (F) SEM image of the PtNWs marked by the box in panel E. (A–D) Reprinted with permission from ref 343. Copyright 2004 American Chemical Society. (E, F) Reprinted with permission from ref 344. Copyright 2006, Wiley-VCH.

beginning would accelerate, which is unfavorable for anisotropic crystal growth. Although oxygen itself is not adequate to slow down the reduction rate, it can be done with the assistance of iron species through oxidative etching. Alternatively, PtNWs can be produced in a seed-mediated fashion.[344] In this case, assemblies of small Pt nanocrystals were prepared at first using polyol methods in the presence of SDS. Tuning the ratio of SDS to metal precursor resulting in nanocrystals could with different shapes (from well-dispersed individuals to submicrometer-sized spherical aggregates). Through the introduction of such aggregates into growth medium, PtNWs can be grown directly from the small Pt nanocrystals making up of the aggregate (Figure 22, E and F). The large size of the aggregate makes it easier to gather the PtNWs from the solution. The NWs can also be separated from the aggregate through sonication.

In addition to the polyol method, solvothermal reactions have also been applied to prepare PtNWs on substrates. In one study,[345] $Ni(OH)_2$ was synthesized and then used as the 2D substrates. During a typical experiment, the aqueous solutions of K_2PtCl_4 and KOH were mixed with a suspension of $Ni(OH)_2$ in formamide. The mixture was sealed in an autoclave and subjected to heating at 120 °C for 4 h. In this case, the formamide played dual roles as reducing agent and solvent for $Ni(OH)_2$. Both HRTEM and XRD analyses confirmed that the NWs with a diameter of about 1.8 nm were made of Pt rather than a Pt–Ni alloy. Increasing the pH through the introduction of KOH could slow down the reduction rate, thereby promoting anisotropic growth. One of the major concerns associated with the extreme conditions is the stability of the substrates. The substrates used in this work were stable up to 4 h, but they were decomposed thereafter, inevitably producing aggregated or bundle-like PtNWs.

In another study,[346] sulfur-doped graphene was leveraged as a substrate for the growth of PtNWs. Briefly, an EG suspension of sulfur-doped graphene, dimethylformamide (DMF), and H_2PtCl_6 were mixed before the addition of KOH. This mixture was transferred into an autoclave and heated at 170 °C for 8 h. A variety of NWs featuring diameters in the range of 3–25 nm, together with lengths greater than 1 μm, were produced. HRTEM analysis revealed that the PtNWs grew along the ⟨111⟩ direction and they were comprised of numerous single-crystal domains. A time-lapse study was also conducted to better understand the growth mechanism. The authors found that single-crystal Pt nanoparticles emerged after several minutes of reaction, and they were then attached in an oriented fashion along the ⟨111⟩ direction. In particular, PtNWs with a rough surface could be observed at 4 h post heating, and they further grew into NWs with a smooth surface during the upcoming 2 h.

5.1.5.2. Template-Directed Growth. The feasibility of both hard and soft templates in guiding the growth of PtNWs have been validated. As one of the most versatile hard templates, metal organic frameworks (MOF) have been harnessed to synthesize PtNWs. In one study,[347] MOF-545 was prepared and added into a mixture of H_2PtCl_4 and formic acid in EG. The suspension was sonicated briefly prior to incubation at 30 °C for 14 h. The PtNW-embedded MOF-545 was precipitated out using a mixture of water and acetone. The PtNWs had an average diameter of less than 3 nm. Brunauer–Emmet–Teller (BET) measurements demonstrated that the original surface area of MOF-545 (2200 m^2/g) was reduced by 75–93% after the growth of PtNWs, indicating that the vast majority of pores in the MOF could serve as a hard template for the deposition of Pt atoms. Alternatively, CTAB micelles were explored as soft template to guide the anisotropic growth of Pt. In a typical experiment,[128] an aged aqueous solution of K_2PtCl_4 was mixed with chloroform containing CTAB. It was proposed that $PtCl_4^{2-}$ could bind with CTA^+, and be reduced by $NaBH_4$ in the worm-like, interconnected CTAB micelles in chloroform, resulting in a network of polycrystalline PtNWs with a mean diameter of 2.2 nm. Furthermore, the authors proved that the fine-tuning of the network structure, such as the intersections, could be realized by simply changing the stirring rate. Specifically, the higher the stirring rate was (up to 1000 rpm), the less significant the intersection would be. It is believed that rapid mass transfer could be realized under a high rate of stirring to enable uniform atom deposition along the interior of the template, producing a smooth surface. Since the as-obtained nanostructures faithfully replicated the structures of micelles, the key to the success of using a soft template in guiding 1D growth is to control the structure of the micelles. As tested by the authors, once the concentration of CTAB was reduced to a certain value (e.g., several mM), the micelles would adopt a spherical shape, rather than a worm-like

DOI: 10.1021/acs.chemrev.8b00745
Chem. Rev. XXXX, XXX, XXX–XXX

morphology, preventing the production of NWs. In addition, how the soft template interacts with the metal precursor also plays a critical role in determining the morphology and structure of the final products, which has been discussed in detail in section 3.

5.1.5.3. Template-Free Synthesis. Though template-directed growth offers an attractive route for the preparation of PtNWs, their downstream applications, especially as catalysts for electrochemical reactions like ORR, has stringent requirements for their surface cleanness. Most of the templates, both hard and soft, are difficult to remove. Thus, there was a need to develop a template-free method for the growth of PtNWs. The early work was based on polyol synthesis in the presence of iron species.[343] In a typical polyol process, H_2PtCl_6 was mixed with PVP in EG at 110 °C. After the system had been exposed to air for 2 h, a Pt(II)-based intermediate emerged, whose stability could enable its storage at room temperature for several months. Extended heating to 4 h would produce numerous tiny, spherical Pt nanoparticles (~5 nm) though reduction of the Pt(II) intermediate. Since such a reduction is autocatalytic, the growth of Pt nanoparticles accelerated with time. Once a critical size was reached for the intermediate Pt nanoparticles, the growth mode switched from isotropic to anisotropic, producing a sea-urchin-like structure with numerous PtNWs exposed on the surface of a micrometer-sized agglomerate of Pt nanoparticles. As mentioned above, it is believed that oxidative etching contributes to the change of growth mode. Furthermore, since the atoms associated with defects such as twin boundaries or dislocations are most vulnerable to oxidative etching, their favorable removal produced single-crystal PtNWs, with a growth direction along the ⟨111⟩ axis. The detrimental influence of oxidative etching on the preparation of polycrystalline PtNWs was validated by another study,[333] in which $PtCl_2$ was phase-transferred into a mixture of ODA and toluene using DTAB. Polycrystalline PtNWs (diameter = 2.4 nm; length = 30 nm) with multiple twin planes and stacking faults were produced from the oriented attachment of intermediates in the form of rod-like nanoparticles. Oxidative etching leads to the breakup of the PtNWs into PtNRs. As discussed in section 5.1.4, the same processes were observed for PdNWs.

In general, anisotropic growth of 1D Pt nanostructures is linked to a slow reduction rate, thereby requiring a fairly long period of time to accomplish the synthesis. To address this issue, efforts have been paid to speed up the synthesis of PtNWs without compromising their uniformity. One of such studies leveraged a modified, $NaBH_4$-mediated reduction. In a typical experiment,[348] H_2PtCl_6 was first reduced by $NaBH_4$ dissolved in a mixture of DMF and toluene. The amount of $NaBH_4$ used was far beyond the value required to convert all the metal precursor to Pt(0). After 3 h, single-crystal PtNWs with a mean diameter of 2.0 ± 0.5 nm were obtained. Regarding the growth mechanism, the authors proposed that the low polarity of the solvent favors the production of Pd(0) nuclei whose surface was protected by the excess $NaBH_4$. These Pt nuclei underwent oriented attachment as a consequence of oxidation as mediated by dissolved oxygen. Their preferential growth along one direction can be explained by the selective passivation of their {111} facets with DMF. Such a hypothesis was supported by the results of ^{1}H NMR with a focus on the intermediates. With respect to the precursor, several newly emerged peaks could be assigned to DMF molecules. The absence of peaks associated with Na^+ and Cl^- ions rules out the possibility for these species to act as capping agents.

To increase the performance of PtNW-based catalysts, it is necessary to narrow their diameters down to several nanometers. To this end, progress has been made through biomimetic synthesis, solvothermal reaction, and CO-mediated reduction. For biomimetic synthesis,[349] a Pt-binding peptide with a sequence of Ac-TLHVSSY-$CONH_2$ (BP7A) was identified with phage display. For the synthesis, H_2PtCl_6 was allowed to form a complex with BP7A peptide prior to the introduction of H_2Asc and $NaBH_4$ as reducing agents, and more metal precursor were sequentially added. The wavy PtNWs synthesized using this method were around 2 nm in diameter and they typically grew along one or more ⟨111⟩ directions, resulting in a wavy morphology. The authors confirmed the presence of defects, including twin boundaries, edges, and adatoms, in addition to high-index facets. The wavy morphology of the resultant PtNWs suggested that they were likely formed as a consequence of oriented attachment. During the attachment, both lattice-matched and lattice-mismatched processes occur, which produced single-crystal and polycrystalline domains, respectively. It is believed that the oriented attachment that occurred in the reaction resulted in a lattice-mismatch and, thus, an alternating growth direction. After the attachment, the newly formed twin boundaries were stabilized by the BP7A peptide. The authors demonstrated that only spherical nanoparticles were produced at low concentrations of peptide.

Ultrathin PtNWs with a diameter of 1.1 nm, or only 6 Pt atoms wide, were prepared through CO-mediated growth.[350] In a typical process, Pt(II) acetylacetonate and EDA were mixed in DMF. Next, the mixture was transferred into a glass pressure vessel, followed by the charging with CO gas. This vessel was heated to 150 °C in 0.5 h and the reduction was allowed to proceed at this temperature for another 5 h. HRTEM analysis confirmed that all the resultant PtNWs were single-crystal and they grew along the ⟨110⟩ axis. The capping effect of CO was crucial to the formation of long, wire-like nanostructures that otherwise shrunk to short segments in the absence of CO.

In addition to their diameter, the length of PtNWs can also be adjusted using a solvothermal method. In one study,[351] H_2PtCl_6 and KOH were added into a mixture of DMF and EG. After thorough mixing at room temperature, the solution was transferred into an autoclave and heated at 170 °C for 8 h. Thin (3 nm) and ultralong (10 μm) PtNWs were synthesized in the form of bundles. HRTEM analysis revealed the PtNWs had a single-crystal structure; they grew along the ⟨111⟩ direction and were enclosed by high-index facets. Imaging of the intermediate products indicated that the PtNWs formed as a result of oriented attachment. As we have discussed above, given the single-crystal nature of the final products, the attachment of facets was believed to occur between matched lattices. The authors proposed that recrystallization and rearrangement of the intersecting atoms could result in the single-crystal structure after oriented attachment. The concentration of KOH, also affected the production of PtNWs. It was proposed that hydroxide could adsorb on the intermediate Pt nanoparticles, affecting their evolution into wire-like structures and the subsequent assembly into bundles.

5.1.5.4. Summary. The polyol method has been widely used to produced PtNWs in solution and on substrates. A slow reduction process mediated by oxidative etching with additives

DOI: 10.1021/acs.chemrev.8b00745
Chem. Rev. XXXX, XXX, XXX−XXX

such as Fe(III) promoted 1D growth. As an alternative, various types of templates, either soft or hard in nature, were used to generate PtNWs featuring multiple planar defects along the long axis. In this case, it may be difficult to remove the template without destroying the NWs. Ideally, one would like to synthesize PtNWs in the absence of any capping agent to keep their surfaces clean for catalytic reactions, but such a synthesis remains to be developed.

5.2. Magnetic Metals

Nanostructures based on magnetic metals have been used for applications related to high-density data storage,[352] as well as heterogeneous catalysis[353] and magnetic separation.[6,7] Some of their physical properties, especially those associated with magnetism, are highly dependent on their morphology. Specifically, it has been shown that anisotropic nanostructures of magnetic metals, including NRs and NWs, exhibit markedly enhanced magnetic properties, such as a larger coercivity or higher blocking temperature.[6,7] In the following subsections, we discuss recent progress in the colloidal syntheses of NRs and NWs made of Fe, Co, and Ni.

5.2.1. Iron (Fe). The only solution-phase synthesis of FeNRs is based on polyol reduction (Figure 23A),[354] in which

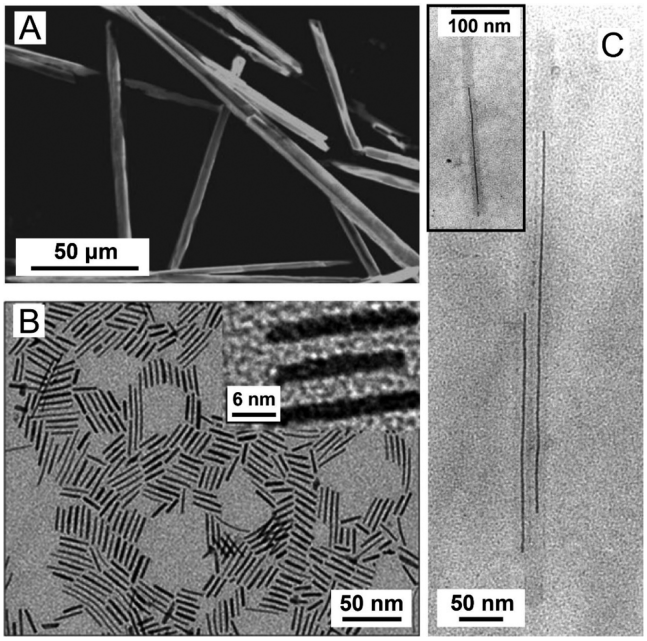

Figure 23. (A) SEM image of FeNRs synthesized using a microwave-based polyol method. (B) TEM image of CoNRs prepared via one-pot synthesis. (Inset: TEM image of the CoNRs at a higher magnification.) (C) TEM image of NiNWs synthesized with TMVs serving as the templates. (Inset: Single virion filled with a 200 nm long NiNW with a diameter of 3 nm.) (A) Reprinted with permission from ref 354. Copyright 2008 American Chemical Society. (B) Reprinted with permission from ref 361. Copyright 2016 The Royal Society of Chemistry. (C) Reprinted with permission from ref 364. Copyright 2003 American Chemical Society.

a given amount of $Fe(NO_3)_3$ dissolved in water was added into liquid poly(ethylene glycol) ($M_w \approx 300$ Da). The mixture was then irradiated in a microwave system at 100 °C for 5 min. The PEG used here has a lower reducing power along with a larger viscosity with respect to EG or DEG. Since the vast majority of the efforts in this study were devoted to the synthesis of AgNRs, there was no discussion on the crystal structure of the FeNRs, as well as its correlation with the experimental conditions.

5.2.2. Cobalt (Co). Cobalt could exist in three different phases, including *hcp*, *fcc*, and ε, with *hcp* being thermodynamically most favorable at room temperature. Such a unique feature makes Co nanostructures ideal templates for the overgrowth of metals that do not favor the *hcp* phase, such as Au and Pt, if the galvanic replacement reaction between the metal precursors and Co can be suppressed. Taking CoNRs as an example, they have been prepared via electrochemical deposition with the assistance of hard templates, such as porous AAO.[355] Although this approach is straightforward and robust, the NRs had large diameters (typically, 380−420 nm) and a polycrystalline structure, resulting in unpredictable magnetic properties.

5.2.2.1. Solvothermal Synthesis. Given the difficulty of reduction associated with the relatively low redox potential of Co (Co^{2+}/Co, −0.28 versus SHE), polyol-based solvothermal synthesis can be used to produce Co NRs and NWs. In one study,[356] $Co(OAc)_2$ and NaOH were mixed together in 1,2-propanediol prior to the introduction of steric acid and a solution of $RuCl_3$ in 1,2-propanediol. Next, the mixture was transferred into an autoclave and heated at 150 °C for 10 h. The products included CoNRs with a mean diameter of 10 nm (Figure 23B). In this case, tiny Ru nanocrystals emerged at the very beginning of the synthesis. Since Ru nanocrystals are typically crystallized in the *hcp* phase, they could serve as seeds for the overgrowth of *hcp*-Co nanostructures. During the reduction, stearic acid acted as a ligand to form a complex with Co(II) ions in addition to its role as a surfactant to direct the anisotropic growth of CoNRs. The addition of NaOH to form solid $Co(OH)_2$, along with the chelation of free Co(II) ions with stearic acid, was used to adjust the reduction kinetics and produce CoNRs. However, if too much NaOH was introduced, plate-like nanocrystals, instead of NRs, were obtained. Likewise, reaction temperatures that were either too high or too low, which correspond to a strong or weak reducing power, respectively, caused the morphology of the resultant Co nanostructures to change.

Using a similar approach, CoNRs with diameters and lengths in the range of 10−30 nm and 100−250 nm, respectively, were also synthesized.[357] In this case, the metal precursor was cobalt carboxylate ($C_nH_{2n+1}COO^-$, n = 7, 9, 11), while the polyol was 1,2-butanediol. Co nanostructures with both *fcc* and *hcp* phases could be obtained depending on the reduction rate, which was determined by both the length of the carboxylate and the concentration of NaOH. A slower reduction caused by a longer carboxylate chain or an increased amount of NaOH favored the formation of *fcc*-Co over *hcp*-Co. Within a narrow range, the AR of the resultant CoNRs could be adjusted without changing the crystal phase. A subsequent computational study revealed that it was the carboxylate that behaved like a ligand to passivate the lateral facets of the NRs.

In addition to NRs and NWs, Co multipods were prepared using the solvothermal method. In a typical synthesis,[358] dodecylsulfate intercalated α-cobalt hydroxide was dispersed in 1-butanol with sonication, followed by the introduction of OLA, before the mixture was transferred into an autoclave. After heating at 220 °C for 24 h, single-crystal, *hcp*-Co multipods with a mean diameter and length of 130 and 320 nm, respectively, were obtained. Notably, the tips of these multipods were terminated in a flat surface that features a 6-fold symmetry, together with a diameter of 190 nm. In addition

DOI: 10.1021/acs.chemrev.8b00745
Chem. Rev. XXXX, XXX, XXX−XXX

to its role as a reducing agent, OLA, as a base, transiently converted the metastable cobalt hydroxide nanosheets from the α- to β-phase. The absence of OLA prevented the formation of any Co nanostructures. The β-cobalt hydroxide contributed to the production of *fcc*-CoO nanospheres, which ultimately grew into Co multipods with an *hcp* phase. The authors proposed that the abundant {111} facets on the intermediate CoO nanocrystals served as sites for additional Co deposition. Since the [111] and [0001] axes correspond to the densest packing direction for both *fcc*- and *hcp*-phases, it is not unreasonable to assume that these CoO nanocrystals could facilitate the growth of a CoNR along the ⟨0001⟩ axis, as confirmed by the HRTEM analysis.

5.2.2.2. Hydrothermal Synthesis. Hydrothermal condition has also been used to synthesize 1D Co nanostructures, including NWs[359] and dendrites.[360] For NWs, a typical synthesis involved a mixture of Na_3CA, $CoCl_2$, and water, along with sodium hypophosphite (NaH_2PO_2) and NaOH.[359] This mixture was transferred into an autoclave before heating at 160 °C for 20 h. In this case, the citrate formed a complex with Co(II) soon after its introduction into the growth solution, which was then reduced by $H_2PO_2^-$. As revealed by XRD analysis, the production of *hcp*-Co nanocrystals began after 6 h. Over the following 12 h, Ostwald ripening contributed to the overgrowth of large intermediates along the ⟨0001⟩ direction by sacrificing smaller particles, resulting in the intensification of scattering from {0002} in XRD patterns. The absence of citrate resulted in the production of spherical Co nanoparticles. FT-IR results confirmed the presence of carbonyl groups of citrate ions on the intermediate nanostructures, suggesting citrate ions passivated the lateral facets on the NWs. Similar to the solvothermal synthesis, the concentration of NaOH determined the morphology of the final product, too low and too high a concentration of NaOH corresponding to the production of bamboo- and dendrite-like Co nanostructures, respectively.

5.2.2.3. Other Methods. In a recent study, uniform CoNRs were prepared using an organometallic Co(I) compound as the metal precursor. In this study,[361] the Co(I) complex, $Co(PPh_3)_3Cl$, was dissolved in degassed OLA in a glovebox under the protection of N_2. The mixture was heated to 190 °C at a rate of 5 °C per minute, and then held at 190 °C for 9 h. Cobalt NRs featuring a mean diameter of 6 nm and ARs in the range of 4−10 were obtained. The XRD pattern recorded from the NRs suggested that they were composed a mixture of both *fcc*- and *hcp*-phases although the crystal orientation could not be resolved.

5.2.3. Nickel (Ni). Anisotropic Ni nanostructures have received interest for their potential use in the fabrication of magnetic sensors as well as data storage and memory devices.[362] Like the case of Co, electrochemical deposition is the most commonly used method for the preparation of 1D Ni nanostructures.[6] This method suffers from drawbacks such as thick diameters and the tedious postsynthetic treatment for removing the template. As a metal that is even harder to be reduced than Co, it is not surprising to see only a very limited number of reports on the solution-phase synthesis of 1D Ni nanostructures. Here, we focus on the methods involving hydrothermal conditions and the use of a soft template.

Nickel NWs can be prepared using a hydrothermal method under conditions similar to what was used for CoNWs, except $CoCl_2$ is replaced with $NiCl_2$, and an additional surfactant, sodium dodecyl benzenesulfonate (SDBS), is added.[363] The reaction was carried out at 110 °C for 24 h. Nanowires with diameters ranging from 0.5 to 1 μm and lengths up to 50 μm were obtained. The SAED pattern confirmed that 1D Ni nanostructures had an *fcc*-crystal structure, and grew along the ⟨011⟩ axis. The reduction of citrate−Ni(II) complex by $H_2PO_2^-$ was proposed to facilitate the formation of 1D nanostructures through an Ostwald ripening mechanism. The presence of SDBS was thought to promote the growth of NiNWs by passivating the {111} facets, thus explaining why the growth was favored along the ⟨011⟩ direction.

Another interesting study reported the synthesis of ultrathin NiNWs by templating with the central channel in TMV (Figure 23C). In this case,[364] TMV was selected for its stable structure and tubular shape to supply the desired template. Tobacco mosaic virus has an inner diameter of 4 nm that limits the maximum diameter of the NWs obtained using this method. An individual TMV is around 300 nm in length, and through the head-to-tail orientation and attachment of TMVs, oligomer-based templates with lengths reaching multiples of 300 nm (e.g., 600 and 900 nm) were obtained. Specifically, a two-step synthesis was conducted. First, Pt(II) or Pd(II) ions were incubated with TMVs to modify their nonconductive inner surface. The as-prepared templates were then immersed in a growth solution containing Ni(II) ions and DMAB ($(CH_3)_2NHBH_3$, a reducing agent). During growth, the inner surface of a TMV is negatively charged, making it unfavorable for the binding of $PtCl_4^{2-}$ or $PdCl_4^{2-}$. However, amine groups in the channel may complex with Pd(II) or Pt(II). The outer surface of the TMV did not have amine groups, thus explaining the selectivity for binding of metal ions to the interior of the TMV. After activation of the channel with Pt(II) or Pt(II), Ni could be deposited within the TMV channel in an electroless plating bath. The crystal structure of the resulting NW was not analyzed. Although the successful use of TMV as a template for NW growth is an important scientific accomplishment, the limited availability of TMV (20 plants yield 1 g) makes this approach impractical for commercial production.

5.3. Other Metals

5.3.1. Aluminum (Al). Aluminum is one of the most abundant elements in the Earth's crust. Despite its relatively low cost, it has been rarely explored in the form of nanostructures primarily because of the difficulty of preparation. Recent studies demonstrate that Al exhibits plasmonic features comparable to those of Au and Ag, if not better. In principle, the plasmon resonance peak of Al nanostructures can be tuned from the ultraviolet to the infrared region, making them viable plasmonic nanomaterials. Given the extremely low reduction potential of Al^{3+}/Al (−1.662 V versus SHE), it was originally believed that it is not feasible to fabricate Al nanostructures using methods other than lithography and atomic deposition.[365] A recent study completely changed this believing by demonstrating a solution-phase method for the synthesis of AlNRs. In this work,[366] anhydrous trioctylamine and triisobutyl aluminum were sequentially introduced into a flask under the protection of N_2. The solution was next heated to 250 °C, with the appearance of opaque gray color indicative of the formation of Al nanostructures. Another 10 min of heating, the reaction was terminated through natural cooling to 80 °C. Afterward, a mixture of 2-[2-(2methoxyethoxy)ethoxy]-acetic acid and cyclohexane was added into the suspension to destabilize the resultant nanostructures so they became collectible by centrifugation. Characterization by HRTEM

DOI: 10.1021/acs.chemrev.8b00745
Chem. Rev. XXXX, XXX, XXX−XXX

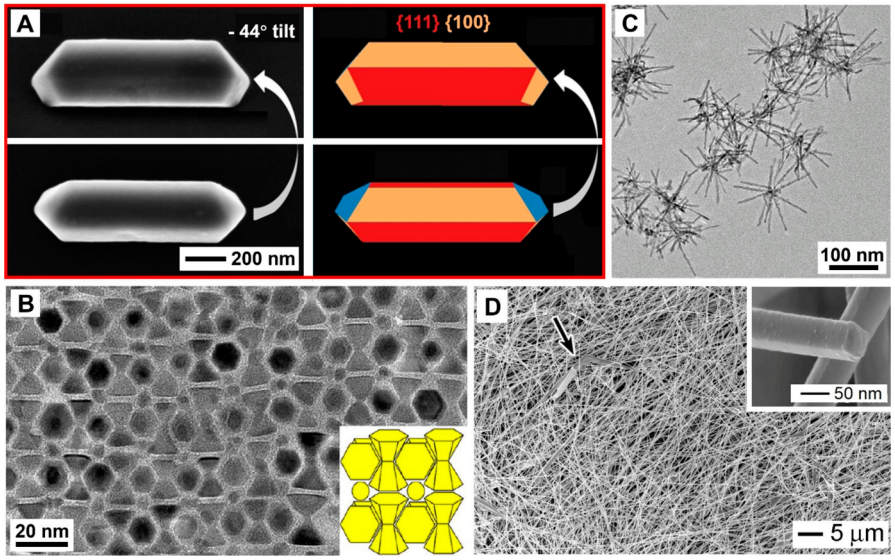

Figure 24. (A) TEM image of AlNRs. (B) TEM image of hourglass-like Ru nanostructures. (C) TEM image of Rh nanodendrites (D) SEM image showing PbNWs synthesized using a polyol process. The inset shows the cross section of a fractured NW. (A–D) Reprinted with permission from refs 366, 373, 375, and 382, respectively. Copyrights 2018, 2013, 2018, and 2004 American Chemical Society, respectively.

suggested that the AlNRs were elongated along the ⟨110⟩ direction to give a diameter and a length of 275 ± 71 and 992 ± 287 nm, respectively (Figure 24A). Unlike the conventional NRs for Au or Ag, the AlNRs showed a distorted, hexagonal cross section. The top and bottom surfaces were enclosed by {100} facets, with all other surfaces terminated in {111} facets when the NR was horizontally placed. The surfactant played a key role in enabling anisotropic growth. The authors believed that the surfactants employed to direct the crystal growth were not proper in all early attempts, highlighting the paramount significance of trioctylamine, which was also proven to serve the synthesis by inhibiting supersaturation in addition to its role as a capping agent. The major problem associated with this synthesis was the low purity of the products. Only 15% of the resultant nanostructures adopted a rod shape, regardless of their difference in length or AR, making the products of limited use, at least in the present form. A better understanding of the shape evolution, starting from the very beginning, is still missing.

5.3.2. Ruthenium (Ru). Ruthenium, a much less expensive noble metal compared to Au, Pt, and Rh, is well-known for its outstanding catalytic performance in a variety of reactions, including selective hydrogenation and CO oxidation,[367] as well as hydrogenation.[368] Although solution-phase methods have been developed for the synthesis of Ru nanostructures,[369] very few of them showed 1D morphology. Only four attempts have been reported with claimed success of creating Ru 1D nanostructures in dendrite-[370−372] or hourglass-like morphology.[373]

One of the attempts involved solvothermal heating.[370] In a typical synthesis, $Ru(acac)_3$ was dissolved in *n*-octylamine and transferred into an autoclave and then heated at 320 °C for 6 h. After they were repeatedly washed with acetone, the products were found to contain short NRs (diameter = 15 nm; length = 50 nm). The authors found that alkylamine played a crucial role in the formation of NRs. When the *n*-octylamine was replaced by hydrocarbons such as decalin or toluene, Ru tiny nanoparticles featuring irregular shapes emerged. In this report, no further characterization with regard to the crystal structure of the RuNRs was provided so it is hard to say what exact role the *n*-octylamine played. Presumably, the RuNRs were formed as a result of the passivation of side faces by *n*-octylamine.

The other two attempts were sort of similar because they both leveraged the thermal decomposition of $Ru_3(CO)_{12}$ to produce Ru dendritic nanostructures. In the earlier attempt,[371] a mixture of $Ru_3(CO)_{12}$ and HDA was prepared, and introduced into tri(*n*-octyl)amine heated at 175 °C. The reaction was allowed to proceed for 1 h before it was terminated through the addition of toluene. As expected, the Ru dendritic nanostructures obtained here favorably crystallized in the *hcp* phase. Powder XRD analysis indicated that such nanostructures were likely made of tiny Ru nanocrystallites with a mean diameter of 1.6 nm. Comparing to the XRD pattern of bulk Ru, the enhanced (0002) diffraction revealed the preferred growth along ⟨0001⟩ direction. The presence of alkylamine, again, was believed to be of paramount importance. When the synthesis was conducted in the absence of an amine species, the decomposition of $Ru_3(CO)_{12}$ took place quickly, leading to the formation of precipitation. On the other hand, the HDA could be replaced by ODA, suggesting the less significance of alkyl chain length once it was beyond a certain value. The temperature also played an important role. When it was elevated to 275 °C, the high supersaturation favored isotropic, rather than anisotropic, growth. In the other study,[372] star-shaped Ru nanostructures were first prepared through thermal decomposition of $Ru_3(CO)_{12}$ in toluene at 160 °C for 6 h under the guidance of HDA and hexadecanoic acid in the presence of hydrogen gas. Afterward, the nanostructures were enriched through centrifugation and employed as the seeds for the next round of growth under identical condition to give rise to Ru dendrites. Their XRD pattern confirmed the dominance of *hcp* phase, but it is hard to tell exactly the dimensions of the nanostructures as they varied dramatically. Again, alkylamine was proposed to serve as a capping agent to direct the anisotropic growth. Regarding the fatty acid, the authors believed that it was involved in slowing

DOI: 10.1021/acs.chemrev.8b00745
Chem. Rev. XXXX, XXX, XXX−XXX

down the reaction rate, making the kinetics more favorable toward anisotropic growth.

Similarly, using hydrogen as a reducing agent, another class of Ru nanostructure featuring a hourglass-like morphology was prepared.[373] In a typical synthesis, $Ru(acac)_2$ and dodecylamine were dissolved in mesitylene and sealed in a Fischer−Porter bottle, with the remaining space filled with hydrogen. Next, the bottle was placed in an oven and heated at 160 °C for 70 h, followed by cooling naturally to room temperature. Characterization with TEM revealed that the nanostructures adopted a hourglass-like morphology, which could be periodically deposited on a substrate to form a superlattice (Figure 24B). A closer look at an individual nanostructure revealed that it was enclosed by {0001} and $\{10\bar{1}1\}$ facets with a mean length of 18 ± 3 nm and widths of 11 ± 2 and 4 ± 1 nm, respectively, for the bottom and neck. The authors also conducted a time-lapse study to better understand the process of shape evolution. It was found that the growth could be divided into three stages: (i) the coalescence of nuclei that gave rise to a rod-like intermediate; (ii) the remodeling of rod-like nanostructures into single-crystal, dumbbell-shaped structures; and (iii) the emergence of well-defined facets as {0001} and $\{10\bar{1}1\}$ in a thermodynamically controlled process. The authors proposed that it was the dense packing of dodecylamine on these two facets that helped preserve them during growth. Introduction of double bonds into the amine, even just one, could weaken the interaction between amine and Ru, leading to the emergence of poorly defined structures.

5.3.3. Rhodium (Rh). In industry, Rh serves as an important catalyst for the oxidation of various toxic species, including CO, NO, and hydrocarbons.[374] With respect to the Pt-based catalyst toward a similar end, the Rh-based counterpart is more appreciated for its superior activity and durability. Although it is not clear about their promise in this catalytic application, there are a number of reports on the chemical synthesis of 1D Rh nanostructures.

An early attempt was made by harnessing the power of polyol reduction.[376] In this work, small Rh nanocrystals were prepared by reducing $RhCl_3$ with EG, along with PVP as the capping agent, at a temperature in the range of 90−190 °C. These nanocrystals could then serve as the seeds for the second-round growth at 90 °C to obtained multipods. In this case, extra $RhCl_3$ was introduced together with DI water. The temperature was found to be critically associated with the shape of the Rh nanocrystals, with anisotropic growth only being favored at temperatures above 90 °C. The XRD pattern recorded from Rh multipods revealed an increased population of {111} planes with respect to their cubic counterpart. The EG was essential as reducing agent for the development of multipods. If EG was replaced by other polyols such as DEG, tri(ethylene glycol) (TEG), and TTEG, tetrahedral nanocrystals emerged instead.[377] It was suggested that the interplay between polyol-mediated reduction and chloride-induced oxidative etching governed the shape of the resultant nanostructures.[376] If the power of oxidative etching overwhelmed that of reduction, multipods could not be formed.

One year later, an optimized protocol was reported.[378] Specifically, EG solution of PVP and Na_3RhCl_6 were slowly and concurrently introduced into an EG solution preheated to 140 °C. Rhodium multipods consisted of arms with a mean length of 11 nm were obtained. Given the characteristic plasmonic resonance peak of Rh nanostructures close to the visible region, the authors monitored the shape evolution using UV−vis spectroscopy. A peak around 380 nm, which could be ascribed to 19 nm tripods of Rh, developed after 90 min of heating, but gradually diminished in intensity thereafter. The authors attributed this change to oxidative etching, which could be mitigated through the introduction of Ar. Compared to the previous version of polyol synthesis, the replacement of $RhCl_3$ by Na_3RhCl_6 allowed a better control over the reduction kinetics, benefiting the formation of nanostructures more uniform in size. Alternatively,[379] if additional substances such as NaI and Na_2Asc were concurrently introduced into the growth solution, dramatic changes in morphology from tripods to wavy NWs was observed. The time-lapse study based on TEM imaging suggested that the wavy RhNWs emerged through a mechanism similar to that of the wavy PtNWs, in which the oriented attachment of intermediate nanocrystals played a critical role in shape evolution.

In another study,[380] the polyol synthesis was exploited to synthesize Rh tetrapods. Briefly, $Rh(acac)_3$ was dissolved in a mixture of 1,2-hexadecanediol and ODA at 90 °C, and the solution was then gradually heated to 130 °C under Ar protection. The reaction was allowed to proceed for 14 h at this temperature, and the solid products were collected through the addition of a methanol/toluene mixture. As confirmed by HRTEM imaging, each of the four arms was grown along its own ⟨111⟩ direction with a length in the range of 15−20 nm. In addition to tetrapods, the authors also noticed that their four tips could serve as the nucleation sites for further growth of NRs. In this case, the growth solution was the same as that for the preparation of tetrapods expect that Rh tetrapods were introduced as the seeds. Afterward, the branched nanostructures could serve as the seeds for the growth of tetrahedra on the very end of each rod, through which the new products could once more act as seeds for the growth of a total of 16 branches in a similar fashion. Given the vulnerability of both corner and edge to atom deposition, these highly branched structures are believed to offer unparalleled catalytic activity toward organic reactions.[380]

Alternatively, Rh 1D nanostructures can be obtained using hydrothermal or solvothermal methods. In one of the studies,[381] the morphology of the final products was adjusted through the choice of inorganic additives. In a typical experiment, aqueous solution containing $RhCl_3$, PVP, sodium halide, and sodium lauryl sulfate was mixed well before transferring into an autoclave. The mixture was then heated at 220 °C for up to 24 h. The presence of NaF and NaI led to the production of dendrites and networks made of NWs, respectively, whereas the participation of NaBr promoted the formation of nanostructures with a cubic shape. With the assistance of TEM images collected at different stages of a synthesis, the authors proposed that the dendrites were formed as an ensemble of tiny nanocrystals whose population in the reaction solution dropped over time. Regarding the network of NWs, HRTEM characterization confirmed that the resultant NW had a diameter of about 5 nm, and was mainly enclosed by {111} facets. The formation of NWs was believed to be through oriented attachment. In this method, many poorly defined shapes emerged in the absence of halides, whereas the solution devoid of sodium lauryl sulfate gave no solid products after heating. As such, it was proposed that the combination of sodium lauryl sulfate with Rh(III) helped transform the ions into unknown species that could be reduced under the given conditions. Afterward, the fate of the emerged intermediates

DOI: 10.1021/acs.chemrev.8b00745
Chem. Rev. XXXX, XXX, XXX−XXX

with regard to enlargement in size or attachment with adjacent counterparts was governed by the halide.

In a most recent study,[375] cyclic penta-twinned Rh nanodendrites were produced through a solvothermal synthesis. In a typical protocol, a mixture of $RhCl_3$, PVP, and *n*-octylamine was sealed in an autoclave before heating at 200 °C for 6 h. The solid products contained nanodendrites comprised of NRs featuring a mean diameter of 4.3 ± 0.6 nm and variable lengths (Figure 24C). Their *fcc* structure was confirmed by XRD pattern. Considering the enhanced (220) peak, the growth direction should be along ⟨110⟩, in agreement with the HRTEM data. In addition, the time-lapse TEM analysis suggested that Rh icosahedra emerged at the early stage of the synthesis, which was favored by thermodynamics. To minimize the high surface energy of the twin structure, atom deposition preferred to occur at the edges, followed by growth along the ⟨110⟩ direction to generate the branched nanostructures. Another critical parameter was the choice of $RhCl_3$ as the metal precursor, whose replacement with either $Rh(acac)_3$ or $Rh(OAC)_3$ failed to replicate the synthesis. In addition, the authors claimed that PVP, whose role is yet to be identified, seemed to serve as a stabilizer under this condition since the only consequence of its absence was the aggregation to a certain extent. To justify the effect exerted by alkylamine, a variety of analogous differ in length was introduced instead of *n*-octylamine. A library of structures, including free-standing or aggregates of NRs and triangular nanoplates, were obtained. The results can be explained by the difference in repulsion between alkylamine chains, which eventually affected its packing on Rh nanostructures.

5.3.4. Lead (Pb). Lead-based nanostructures have tremendous potential as an electrode material for batteries, as well as for the fabrication of optical filters.[138] In general, the progress in method development for such a heavy metal is not on par with the growing interest in exploring their intriguing properties. There are only a few reports on the wet-chemical synthesis of PbNWs.[138,382] One report involved thermal decomposition of $Pb(OAc)_2$ in the presence of PVP with EG under N_2.[138] Monocrystalline PbNWs grew along the ⟨110⟩ axis with a diameter of approximately 35 nm and lengths up to 250 μm (Figure 24D). The SAED pattern recorded from an individual NW exhibited a 6-fold symmetry along the ⟨111⟩ axis. Another SAED pattern showed diffraction spots from (1/3){422}, which is forbidden for *fcc* nanostructures. It was proposed the appearance of such forbidden spots was a consequence diffraction from a thin nanostructure that was enclosed by flat top and bottom faces.

A subsequent mechanistic study concluded that PbNWs were formed as a result of Ostwald ripening.[382] Specifically, Pb atoms originating from the thermal decomposition of metal precursor were able to nucleate and grow into structures with dimensions ranging from 5 to 10 nm to several micrometers. The reactive corners of the larger crystals could then serve as nucleation sites for the growth of PbNWs through the consumption of smaller nanoparticles, which may be in the molten state due to the low melting point of lead. Attraction of small molten droplets to these corners could lead to formation of liquid droplets, from which a PbNW could crystallize and grow. Such a growth mechanism is commonly referred to as solution−liquid−solid (SLS) process, which was originally proposed to explain the growth of semiconductor NWs from metallic liquid droplets.[383] The yield of PbNWs was optimized by varying two parameters: the amount of PVP and reaction temperature.[382] When the ratio of PVP to $Pb(OAc)_2$ was set to 3.5, PbNWs could be obtained with a purity approaching 100%. When the ratio was other than 3.5, the main products were switched to belt- or plate-like Pb nanostructures. A reaction temperature greater than 190 °C was essential to thermally decompose the metal precursor. Otherwise, no nanostructures could be found in the final product.

Lead NWs can also be prepared using a galvanic replacement process involving the use of Zn foil as a reducing agent and $Pb(OAc)_2$ as a metal precursor.[384] The as-synthesized PbNWs had a single-crystal structure, together with a mean diameter of 80 nm and lengths up to hundreds of micrometers. The PbNWs were initially covered by a thin layer of ZnO that could be removed by simply etching with dilute HCl. HRTEM results revealed that the PbNWs grew along the ⟨100⟩ axis.

6. BIMETALLIC AND TRIMETALLIC SYSTEMS

The use of more than one metal greatly increases the diversity and scope of 1D nanostructure configurations.[385] In addition to the increasing the functional diversity of nanostructures from simply combining two or more metals, the spatial distributions of the elements also play a significant role in tuning the properties of the final products. Figure 25 shows an illustration of the possible mixing configurations for bimetallic 1D nanostructures. Generally speaking, the structure can be alloyed or spatially segmented. A large number of bimetallic and trimetallic systems have been reported, and the synthesis of these nanostructures usually follows several typical strategies. Depending on the metals involved and the experimental conditions, different patterns of mixing can be

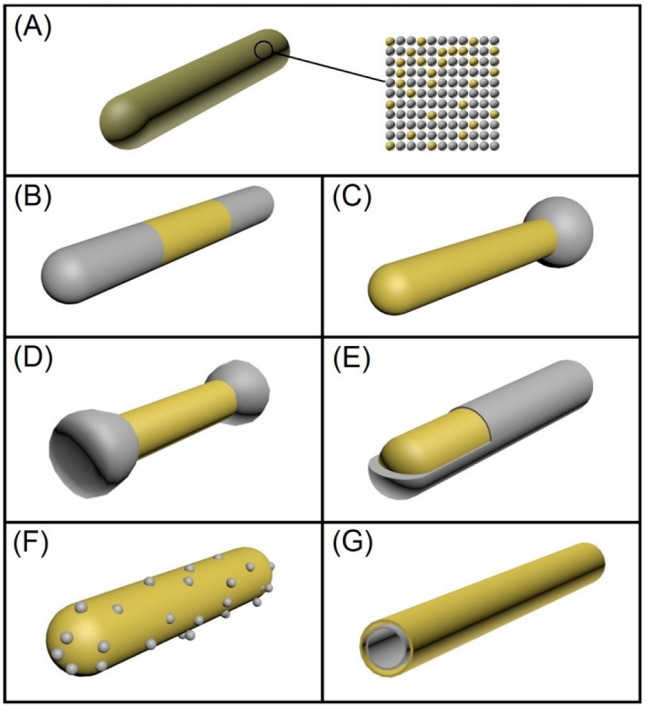

Figure 25. Schematic illustrations of different types of 1D bimetallic nanostructures: (A) alloyed, (B) segmented, (C) tadpole-like, (D) dumbbell-like, (E) core−shell, (F) core−satellite, and (G) multi-walled nanotube.

DOI: 10.1021/acs.chemrev.8b00745
Chem. Rev. XXXX, XXX, XXX−XXX

obtained, along with different properties that affect their suitability for applications.

6.1. Alloys

Alloys are mixtures of metals randomly mixed at the atomic level. The formation of an A−B alloy depends on a number of parameters, including the relative strength of the A−A, A−B, and B−B bonds; the relative atomic size; and the charge transfer between different types of atoms. When formed as nanostructures, the surface free energies of different types of facets for each individual metal can also play an important role. For a good reference on this subject, please refer to a review article published in 2008.[386] Here, we focus on the preparation methods, including coreduction and galvanic replacement.

6.1.1. Coreduction. Coreduction is a simple and straightforward method for the synthesis of alloyed nanostructures. This method involves the simultaneous reduction of different metal precursors in a reaction solution. The order of reduction is determined by the reduction potentials of the metal ions. For metal ions with a similar reduction potential, they can be reduced at roughly the same rate to generate alloys with elemental compositions largely determined by the ratio of the different metal precursors. In one example, the coreduction method was applied to generate alloyed Ag−Pd NWs.[387] The final products were made of a bimetallic alloy with multiple monocrystalline domains. In a typical synthesis, an EG solution containing PVP was heated at 170 °C for 1 h. $Pd(NO_3)_2$ and $AgNO_3$ were codissolved in water at room temperature, and this mixture of precursors was injected into the EG solution, followed by heating at 170 °C for 1 h. This one-pot synthesis generates worm-like NW with an average diameter of 5−8 nm and a length up to 200 nm. The same morphology was also applied to Pt−Ag.[57] The formation of such wavy nanostructures was proposed to follow an attachment mechanism, in which primary nanoparticles assembled into worm-like NWs. According to an MD simulation for Pt−Ag alloyed NW, Ag atoms can readily diffuse at 200 °C, while Pt atoms cannot. This result suggests that the diffusion of Ag atoms played an important role in reconstruction upon particle−particle collision.

The requirement for a similar reduction potential means that coreduction method can only be applied to a limited combination of metal ions. One way around this problem involves the introduction of nonmetal seeds (i.e., templates) to reduce the nucleation energy, followed by the dissolution of the templates at the end of the synthesis. In one example, a hard template made of ZnO NRs was used for the synthesis of Pt−Pd−Ag trimetallic nanotubes.[388] This method involves two main steps: (i) synthesis of an array of ZnO NRs on a Si wafer and (ii) immersion of the arrayed ZnO NRs in a solution containing a mixture of K_2PtCl_4, K_2PdCl_4, and $AgNO_3$, along with Na_3CA. The reaction mixture was heated at 90 °C for 1 h in a conventional drying oven. During this process, the metal precursors were reduced on the surface of the ZnO NRs while the ZnO NRs were dissolved due to the acidic environment, leaving behind Pt−Pd−Ag alloyed nanotubes as the final product. The ZnO NRs not only served as sacrificial templates to direct the formation of nanotubes but also facilitated heterogeneous nucleation by greatly decreasing the energy barrier to precursor reduction.

Another approach to mitigating the effect of the difference in reduction potential between metal ions is to vary the coordination ligand. As is mentioned in section 3.4.2, the strongly binding ligand can make a metal ion more difficult to reduce. Taking Ag as an example, Table 2 shows the changes in reduction potential when Ag(I) ions are coordinated with different ligands.[389] The reduction potential can be readily tuned by coordinating Ag(I) with different ligands. In addition, the reduction rate is also sensitive to the strength of the reducing agent, the pH of the solution, as well as the chemical properties of the solvent.[390−393] All these strategies can be used to expand the scope of alloyed nanostructures synthesized using a coreduction method.

Table 2. Reduction Potentials of Ag(I) Ions As in Different Complexes

redox system	E_0 (V)
$Ag^+ + e^- \rightarrow Ag^0$	+0.80
$[Ag(NH_3)_2]^+ + e^- \rightarrow Ag^0 + 2NH_3$	+0.38
$[Ag(SO_3)_2]^{3-} + e^- \rightarrow Ag^0 + 2SO_3^{2-}$	+0.29
$[Ag(S_2O_3)_2]^{3-} + e^- \rightarrow Ag^0 + 2S_2O_3^{2-}$	+0.01
$[AgI_4]^{3-} + e^- \rightarrow Ag^0 + 4I^-$	−0.09
$[Ag(CN)_3]^{2-} + e^- \rightarrow Ag^0 + 3CN^-$	−0.51

Unlike monometallic systems, it is more difficult to define the role of the capping agent for alloyed nanostructures. The apparent facet-selective stabilization from a capping agent is dependent on the metal. For example, PVP can cap the {100} facets on Ag nanostructures, but caps the {111} facets for Au.[112] However, it is still possible for certain molecules to act as a capping agent for alloyed nanostructures. A typical example is the synthesis of Cu−Pt NRs.[394] The synthesis involved mixing $Pt(acac)_2$, $Cu(acac)_2$, 1,2-hexadecanediol, OA, and OLA in 1-octadecene. The reaction mixture was then bubbled with Ar prior to heating to 120 °C for 20 min, and then to 225 °C at a rate of 20 °C/min. The reaction was allowed to proceed for 30 min before being terminated and cooled down to room temperature. During the whole process, the reaction solution was protected with Ar. Increasing the ratio of OLA to OA increased the AR of the NRs. The change in AR suggests that OLA stabilized certain facets on the Cu−Pt alloyed NRs. Although a detailed mechanism remains to be elucidated, this work suggests that one can apply capping agents to synthesize alloyed nanostructures with well-defined shapes and facets.

Mixtures of metals can also form ordered intermetallic compounds instead of random alloys. Such intermetallic compounds can exhibit enhanced catalytic properties.[395] A good example can be found in the case of Pt−Pb intermetallic NRs.[396] In a typical synthesis, $Pt(acac)_2$ and $Pb(acac)_2$ were added into a mixture containing 1-adamantanecarboxylic acid (ACA), hexadecanethiol (HDT), and HDA heated at 180 °C under argon atmosphere. When the temperature was stabilized, a *tert*-butylamine borane complex (TBAB) was injected and the mixture was kept at 180 °C for another 30 min. The authors proposed that the Pt−Pb NRs grew along the ⟨001⟩ direction because of the larger coordination number available for atoms binding to a crystal growing in this direction relative other low index directions. However, it is not clear whether the role of facet-dependent differences in coordination number is more important that the role of capping agents in this synthesis.

6.1.2. Galvanic Replacement. As briefly mentioned in section 3.4.4, galvanic replacement represents another simple route to the synthesis of a wide range of bimetallic and

DOI: 10.1021/acs.chemrev.8b00745
Chem. Rev. XXXX, XXX, XXX−XXX

trimetallic alloyed nanostructures. The general process involves the electrons from the oxidation of one metal reducing ions of a more noble metal.[150] This process is driven by the difference in reduction potential between the two metals. The higher the reduction potential difference is, the easier it is for the galvanic replacement reaction to occur. This method is especially well-suited for the synthesis of hollow nanostructures due to the destructive nature of a replacement process. Nanostructures made of Ag are often used as the sacrificial template due to its low reduction potential and the well-established synthetic chemistry.[397,398] An early study reported that single-walled and multiple-walled Ag−Au alloy nanotubes with a pentagonal cross section could be synthesized using galvanic replacement.[154] For the synthesis of single-walled nanotubes, AgNWs were diluted with deionized water and refluxed for 15 min. Then, aqueous $HAuCl_4$ solution was added dropwise into the reaction mixture and refluxing continued for 10 min. For double-walled nanotubes, the as-formed nanotube was coated with a layer of Ag (with the use of $AgNO_3$ as a precursor and H_2Asc as a reducing agent), followed by another round of galvanic replacement. In the same report, the authors found that by switching the precursor from $HAuCl_4$ to $Pd(NO_3)_2$, Pd−Ag alloyed nanotubes were also synthesized.[154] Figure 26

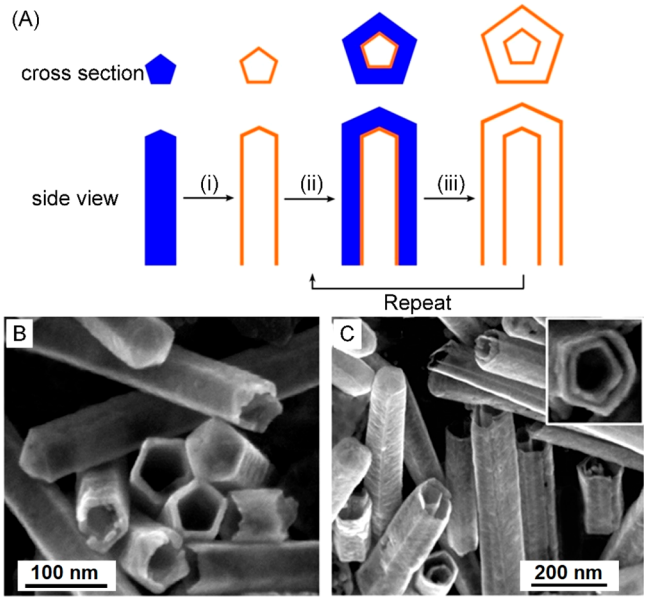

Figure 26. (A) Schematic illustration showing how to generate multiple-walled nanotubes: (i and iii) template-engaged galvanic replacement and (ii) electroless planting of Ag. (B, C) SEM images of (B) single-walled and (C) double-walled Au−Ag alloy nanotubes, respectively. Reprinted with permission from ref 154. Copyright 2004 Wiley-VCH.

shows a schematic illustration for the process to generate multiple-walled NWs, along with SEM images for single and double-walled Au−Ag nanotubes. As can be seen from Figure 26C, different layers of the nanotubes could be clearly resolved under electron microscopy. This simple and robust synthesis could be readily extended to various kinds of metals to obtain alloyed nanotubes with different compositions.

As illustrated above, the composition of the product derived from galvanic replacement could be tailored by varying the reaction condition. This protocol could also be readily extended to trimetallic systems for the fabrication of various unique nanostructures. Taking advantages of the effect from ligand stabilization mentioned discussed in section 6.1.1, by tailoring reaction parameters, even a stable metal like Au could function as a sacrificial template for galvanic replacement. It was reported that Pt−Au−Ag trimetallic hollow NRs could be synthesized through galvanic replacement between Au@Ag core−sheath NRs and $PtCl_4^{2-}$.[399] In a typical protocol, AuNRs were coated with a thin shell of Ag to create Au@Ag NRs, which were then reacted with K_2PtCl_4 at 60 °C in the presence of CTAB for 6 h. EDS mapping confirmed that the hollow NRs consisted of a homogeneous alloy of Au, Ag, and Pt. Interestingly, the AuNRs with the Ag shell could not be etched by K_2PtCl_4 to create hollow nanostructures. The authors proposed that charge transfer from the Au core to the Ag shell promoted the oxidation of the Au by Pt(II).[400]

In summary, the two main strategies for the syntheses of 1D alloy nanostructures are coreduction and galvanic replacement. In general, coreduction generates solid NRs and NWs while galvanic replacement favors the formation of hollow nanostructures such as nanotubes. The parameter most critical to the generation of alloys is the difference in reduction potential among different metals. The reduction potential can be readily tuned by varying the ligand binding to the metal ions, the concentration of metal ions in the solution, the pH, and the solvent.

6.2. Segmented Structures

It is more challenging to synthesize segmented nanostructures when compared with either single-metal or alloyed nanostructures. The final morphology is highly susceptible to the facets exposed on the seeds, reaction conditions, and the presence of a surfactant or capping agent in the solution. These factors would influence the nucleation and diffusion processes involved in the formation of heterostructures. This is especially important for 1D nanostructures as they are highly anisotropic, with different types of facets exposed on the side surface and two ends. Generally, heterostructures can be divided into two subgroups: segmented and core−sheath. In this section, we focus on the synthesis of segmented structures. Core−sheath structures will be discussed in the next section. The segmented nanostructures can be synthesized using two different methods: coreduction and seed-meditated growth.

6.2.1. Coreduction. Similar to the case of alloyed nanostructures, coreduction is also widely used for the synthesis of segmented nanostructures. As discussed in section 6.1, for a reaction solution containing multiple precursors to different metals, the one with the highest reduction potential will be reduced first, followed by the heterogeneous nucleation and growth of other metals on the as-formed seeds.

In the presence of a suitable surfactant, Au−Ag heterostructured NRs were synthesized using a one-pot polyol reduction.[76] In a typical synthesis, poly(diallyldimethylammonium) chloride (PDDA), $HAuCl_4$, and $AgNO_3$ were dissolved in EG. The mixture was then stirred vigorously to convert $AgNO_3$ into AgCl. The as-prepared mixture was heated at 200 °C for 60 h. In this synthesis, Au(III) was readily reduced due to the higher reduction potential of $AuCl_4^-$. At the same time, Ag(I) was released from AgCl at a comparatively low rate even at the elevated temperature.[401] The low concentration of free Ag(I) in the solution led to a slow rate for the generation of Ag atoms. poly(diallyldimethylammonium) chloride also played a crucial role in this synthesis, probably as a stabilizer and a surfactant.

DOI: 10.1021/acs.chemrev.8b00745
Chem. Rev. XXXX, XXX, XXX−XXX

By tuning the concentration of PDDA in the reaction solution, the AR of the NRs could be readily manipulated. It was observed that increasing the concentration of PDDA led to greater ARs. However, when the concentration of PDDA went above 40 mM, both the quality and uniformity of the ARs decreased.

6.2.2. Seed-Meditated Growth. Although coreduction is straightforward for the formation of segmented nanostructures, it is hard to control both the morphology and uniformity of the final products. Therefore, seed-meditated growth has been extensively explored as an alternative approach. This method involves the formation of seeds made of one metal, followed by the deposition of another metal onto the surface.

In seed-meditated growth, it is usually desirable to prevent homogeneous nucleation in the solution. To eliminate self-nucleation, the concentration of the reduced atoms must be below the minimum level for homogeneous nucleation. A typical example can be found in the synthesis of Ag−Au−Ag segmented NRs,[77] with Ag segments attached to both ends of a AuNR. In a typical synthesis, a mixture of penta-twinned AuNRs and benzyldimethylhexadecylammonium chloride (BDAC) was heated to 60 °C. Then, $AgNO_3$ and H_2Asc were added continuously using separate syringe pumps while keeping the reaction temperature fixed. The final products were uniform in length even at ARs above 100. Figure 27

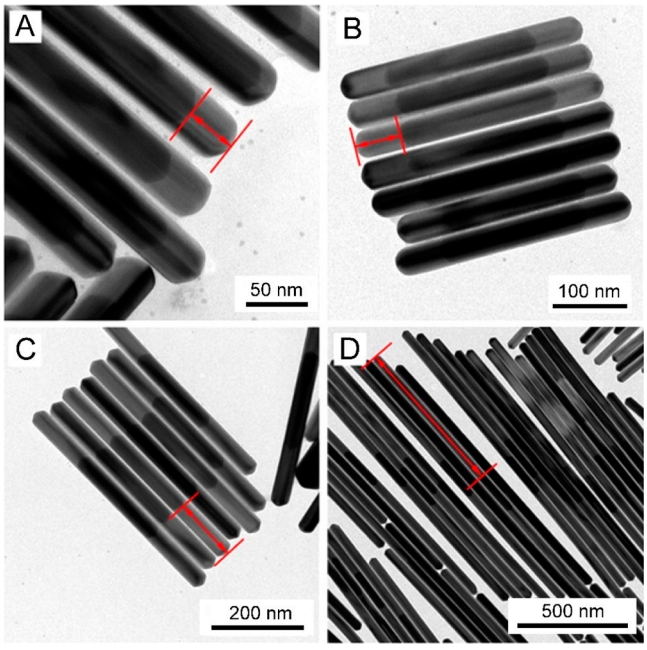

Figure 27. TEM images of segmented Ag−Au−Ag NRs with Ag segments of different lengths at the tips. The Ag segments were (A) 33 ± 6, (B) 61 ± 9, (C) 130 ± 20, and (D) 660 ± 90 nm, respectively, in length. Reprinted with permission from ref 77. Copyright 2015 American Chemical Society.

shows TEM images of the multisegmented NRs, which shows essentially no change in thickness along the axial direction. Several factors contribute to the successful synthesis of this 1D segmented nanostructure: (i) the presence of a capping agent toward the side {100} facets on each AuNR, allowing Ag atoms to be deposited only on the ends (compared with pure CTAB, the combination of CTAB and BDAC was better at preventing lateral growth of AuNRs); (ii) the low injection rate of the Ag(I) precursor into the reaction solution, leading a low concentration of precursor in the reaction mixture to promote heterogeneous atomic addition onto both ends of the NR; and (iii) the slightly acidic environment and elevated temperature that both favor the slow reduction of Ag(I).[402] By controlling the ratio of the reducing agent H_2Asc and metal precursor Ag(I), another group reported obtaining arrowhead-like end-caps on the AuNRs.[403]

In the above examples, the Au seeds were already in the morphology of rod. One or more capping agents were applied block atomic addition to the side surfaces of AuNRs, and thus promote axial deposition of Ag. In other examples, the seeds could be in an arbitrary shape and only serve as nucleation sites, and it is the capping agent for the second metal that promotes the formation of an anisotropic structure. Notable examples include Au−Ag NRs,[76] Pt−Ag NWs,[250] and Pd−Cu NRs.[113] Taking Pd−Cu bimetallic NRs as an example,[113] it was reported that penta-twinned CuNRs could be grown in the presence of Pd decahedral seeds, Cl^-, and HDA. To obtain the NRs, Pd decahedral seeds were first synthesized using a polyol method based on DEG. A solution containing $CuCl_2$, HDA, and glucose was prepared by magnetically stirring the mixture overnight. Pd decahedral seeds were added to this mixture and it was purged with Ar to reduce the oxygen content. Finally, the vial containing the mixture was placed in an oil bath held at 110 °C for 3 h to obtain the NRs. The success of this synthesis depends on two critical factors: the presence of Pd decahedral seeds and the addition of HDA as a capping agent toward Cu{100} facets. The Pd seeds not only offered nucleation sites for the deposition of Cu atoms, but also helped control the length of the NRs by altering the ratio between Cu(II) precursor and Pd seeds. As shown in Figure 28, A and B, due to the large lattice mismatch between Cu and Pd (7.1%), the Cu only grew from one side of the decahedral seeds.

Palladium can also be grown from both sides of a Au decahedral seed to create Pd−Au−Pd NRs. The preparation of segmented Pd−Au−Pd NRs started with mixing Au decahedral seeds, H_2PdCl_4, CTAB, and KI in an aqueous solution. The mixture was heated at 90 °C for 30 min and then cooled down to about 30 °C. The ratio of KI to CTAB was important for heterogeneous growth of NRs. Since I^- has a stronger binding to the Au surface, a high ratio of KI/CTAB resulted in more homogeneous nucleation and no deposition of Pd on the Au seeds. When no KI was added, only Au@Pd nanoparticles formed. A moderate amount of KI facilitated the formation of PdNRs on the Au decahedral seed. It was proposed that I^- preferentially bonded to the Pd(100) surfaces on the sides of the NR, facilitating anisotropic growth. Figure 28, C and D, shows TEM images of Pd−Au−Pd segmented NRs, in which the Au seed was positioned at the midpoint of each rod. The fact that Pd grows from both sides of the Au seed versus just one side for growth of Cu from Pd seeds may be due to both a difference in reduction kinetics and the smaller lattice mismatch between Au and Pd relative to Cu and Pd.[78]

To summarize, the exact configuration of 1D segmented nanostructures is highly dependent on the reaction conditions, including temperature, pH, the capping agent, as well as the intrinsic material properties of the metals such as lattice mismatch. The successful syntheses of symmetry-reduced 1D segmented nanostructures containing two or more metals was mainly determined by two factors: (i) the existence of a twin plane that promotes the atomic deposition in an anisotropic way[404,405] and (ii) the presence of a proper capping agent or

DOI: 10.1021/acs.chemrev.8b00745
Chem. Rev. XXXX, XXX, XXX−XXX

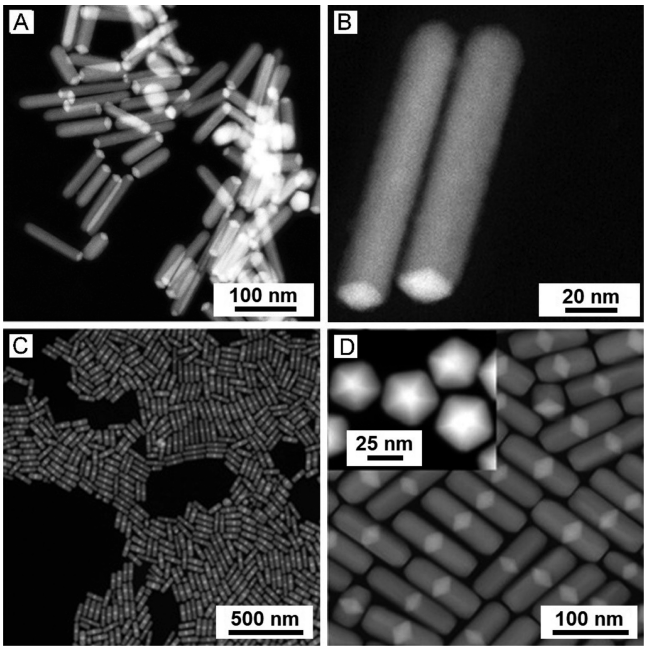

Figure 28. Two different types of segmented NRs, with (A, B) a Pd decahedral seed located at one of two tips of each CuNR and (C, D) a Au decahedral seed located at the midpoint of each PdNR. (A, B) Reprinted with permission from ref 113. Copyright 2016 Wiley-VCH. (C, D) Reprinted with permission from ref 78. Copyright 2016 ACS publications, respectively.

surfactant to passivate certain facets. It is generally believed that the presence of twin planes is a crucial factor for generating anisotropic structures. The twin plane could either come from the seeds with a twin structure, like decahedral or bipyramid seeds,[406,407] or generated during the reaction due to large lattice mismatch between the two metals.[111] So far, the side surface of most of the reported 1D metal nanostructures is covered by {100} facets, which are comparatively higher in surface energy than {111} facets. As a result, their formation requires the assistance of a capping agent to stabilize the {100} facets.

6.3. Core–Sheath and Core–Satellite Structures

A core–sheath nanostructure consists of an inner core coated with a sheath made of another metal. The introduction of core–sheath structures can bring up several advantages, including enhancement in catalytic performance due to electronic coupling or strain effects; improvement in chemical and thermal stability; tuning of optical properties; augmentation of magnetic anisotropy; and serving as an intermediate for the formation of other types of structures (e.g., cages and frames).[385] Thanks to the efforts made in the past two decades, a variety of synthetic methods have been developed for generating core–sheath structures, including coreduction, seed-mediated growth, electrochemical deposition, and chemical vapor deposition, among others. In the following discussion, we focus on the wet-chemistry approaches.[385,408]

Typically, the conformal deposition of another metal can lead to the formation of core–sheath nanostructures with a shape or morphology similar to that of the core that serves as a physical template for the coating process.[37] By tuning the amount of metal precursor added, one should be able to precisely control the shell thickness if the deposition follows a layered growth mode. To date, core–sheath 1D nanostructures have been reported for a number of systems, with notable examples including NRs and NWs, as well as other types of structures with more exotic morphologies.

6.3.1. Coreduction Method. By taking advantage of the difference in reduction potential between metal precursors, core–sheath 1D nanostructures can be produced in one pot through coreduction. In general, such a one-pot synthesis can be considered to occur in two sequential steps: (i) formation of the core for the metal with the higher reduction potential and (ii) epitaxial growth of the second metal with the lower reduction potential as the sheath. The one-pot method is not only simple and time-saving but also makes it easier to scale-up to larger production volume. However, it might be difficult to precisely control and reproduce the shape of the nanostructures due to the difficulty in manipulating the nucleation process and the reduction kinetics of different metal precursors. Several reports have demonstrated the successful synthesis of various 1D metal nanostructures using a one-pot, coreduction method.[409,410] For example, Au@Pd core–sheath nanostructures with a thorn-like shape have been synthesized through the coreduction of Au(III) and Pd(II) precursors, and the nanothorns exhibited remarkably enhanced electrocatalytic activity and durability for the ORR in alkaline media.[409] In a typical protocol, $HAuCl_4$ and $PdCl_2$ were reduced at 20 °C by H_2Asc in an aqueous solution containing poly(allylamine hydrochloride) (PAH) and EG to produce thorn-like structures with diameters of 30–50 nm and lengths of 100–400 nm. Since $AuCl_4^-$ has a higher standard reduction potential than $PdCl_4^{2-}$, the Au core was generated before the Pd sheath. Considering the Pd sheath had a porous structure, the formation of Au@Pd nanothorns most likely took place through the deposition of Pd nanoparticles. It was presumed that PAH and EG acted as both stabilizing agents that prevented the particles from aggregation and shape-directing agents that lead to the formation of a thorn-like morphology.

6.3.2. Seed-Mediated Growth. Seed-mediated growth is the most commonly used approach for the synthesis of core–sheath nanostructures, in which preformed nanostructures act as heterogeneous nucleation sites for the deposition of atoms from another metal.[98,411,412] Repeating this process sequentially can result in the generation of multilayered core–sheath nanostructures. Typically, the introduction of single-crystal seeds often lead to the formation of single-crystal nanostructures, while multiply twinned seeds will result in the generation of nanostructures with a similar twin structure.[37] In addition to seeds made of 1D nanostructures, preformed 0D nanostructures, such as cubes and spheres, can also serve as seeds for the formation of 1D nanostructures. For example, single-crystal Au nanospheres can seed the growth of Pd nanobars by reducing H_2PdCl_4 with H_2Asc in the presence of CTAB.[413]

As discussed in section 3.3.1, the ratio between the deposition rate ($V_{deposition}$) and surface diffusion rate ($V_{diffusion}$) ultimately determines which pathway a growing nanostructure will follow.[116] When $V_{deposition} > V_{diffusion}$, the deposited atoms tend to "hit and stick" to the site of deposition, facilitating the site-selective, kinetically controlled overgrowth. If $V_{deposition} < V_{diffusion}$, the atoms hit and then diffuse across the surface of a seed, resulting in a conformal growth mode favored by thermodynamics. To achieve a conformal sheath, one can either decrease $V_{deposition}$ by slowing down the reduction rate or injection rate of the metal precursor, or increase $V_{diffusion}$ by elevating the reaction temperature. For example, Ag@Au core–sheath NWs with a conformal Au sheath could be

DOI: 10.1021/acs.chemrev.8b00745
Chem. Rev. XXXX, XXX, XXX–XXX

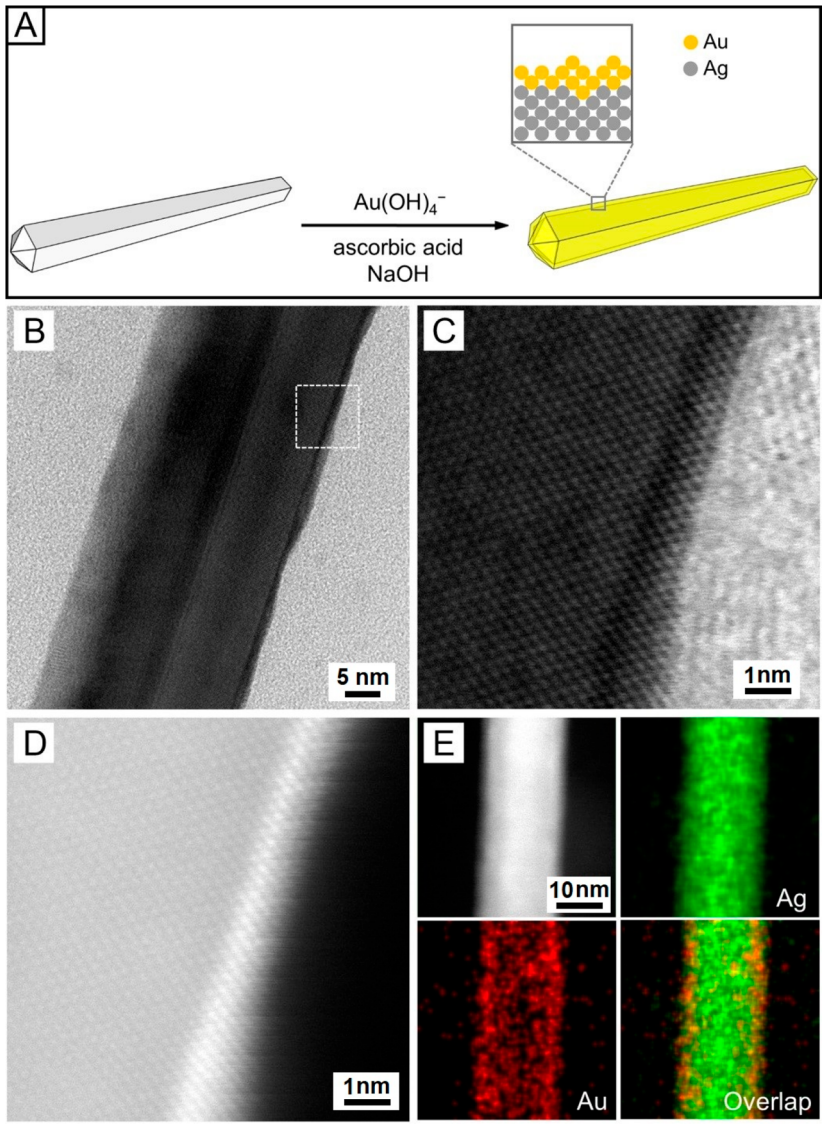

Figure 29. (A) Schematic illustration showing the conformal coating of AgNW with a Au sheath. (B) TEM, (C) HRTEM, and (D) HAADF-STEM images of a Ag@Au NW taken from the region marked by a box in (B). (E) EDS mapping of Ag and Au in a Ag@Au NW. Reprinted with permission from ref 414. Copyright 2017 The Royal Society of Chemistry.

generated at an elevated reaction temperature of 60 °C and a slow injection rate for the Au(III) precursor as both conditions enabled sufficient time for diffusion of the Au atoms after their deposition to cover the entire surface of the AgNWs.[414] When the synthesis was conducted at room temperature, NWs with a rough surface were obtained, presumably due to inadequate surface diffusion.

By repeating the deposition process sequentially, multilayered core−sheath structures can be generated. For example, Au@Pd@Cu core−sheath NRs with two shells comprised of different metals were generated through a stepwise growth mode.[415] In a typical protocol, Au@Pd NRs were first produced by depositing a Pd sheath on AuNRs, followed by the deposition of a Cu sheath onto the Pd surface. Switching from sequential reduction to coreduction lead to the formation of an alloyed sheath instead of a multilayered sheath. For example, Pt@PtPb core−sheath NWs were produced by sequential introduction of $Pt(acac)_2$ and $Pb(acac)_2$.[416] In the initial step of the reaction, PtNWs were formed. The remaining Pt(II) and newly introduced Pb(II) precursors were then reduced to Pt and Pb atoms for codeposition onto the PtNWs, generating a PtPb alloy sheath. Another interesting example is the formation of Pd@PtNi core−sheath NWs.[417] In a typical synthesis, PtNi alloy NWs were generated by reducing $Pt(acac)_2$ and $Ni(acac)_2$ in the presence of CTAC, glucose, and OLA. When $Pd(acac)_2$ was added dropwise into the above mixture, alloy NWs were transformed into core−sheath structures. The initially formed PtNi NWs served as templates for the subsequent deposition of a thick sheath of Pd. However, because of the diffusion of Pt and Ni atoms to the surface, Pd was gradually concentrated at the center of a NW to become the new core, whose surface was covered by a PtNi alloy sheath. It is not clear why the Pd sheath became a core in this case.

In addition to the core−sheath nanostructures with monometallic core or sheath, a more complex structure with both core and sheath as alloys has also been reported. For example, FePtM@FePt (M = Pd, Au) core−sheath NWs have been prepared using a seed-mediated growth method.[88] Through controlled decomposition of $Fe(CO)_5$ and reduction

DOI: 10.1021/acs.chemrev.8b00745
Chem. Rev. XXXX, XXX, XXX−XXX

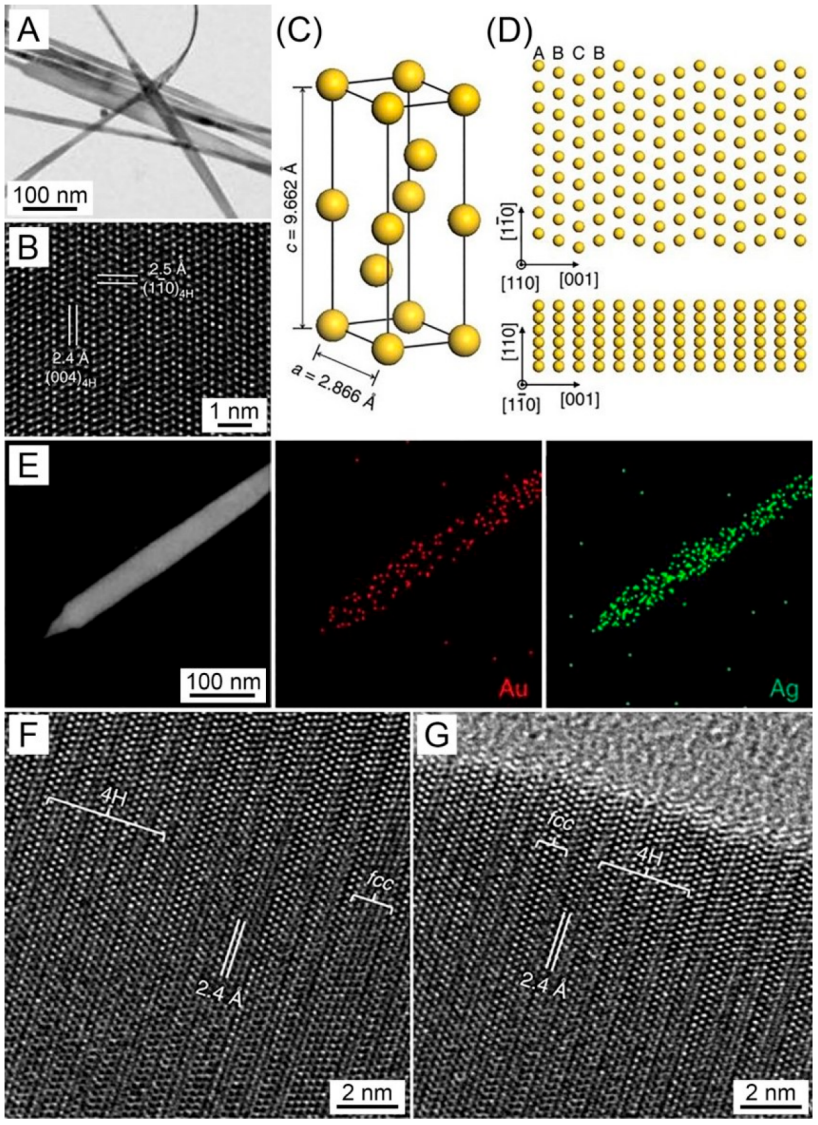

Figure 30. (A) TEM image of 4H Au nanoribbons. (B) HRTEM image taken from the center of a Au nanoribbon. (C) Schematic illustration of a unit cell of 4H Au. (D) Atomic models showing the top view (top) and side view (bottom) of a typical 4H Au nanoribbon. (E) HAADF-STEM image and the corresponding EDS mapping of a Au@Ag nanoribbon. (F, G) HRTEM images of a Au@Ag nanoribbon taken from (F) the center and (G) the edge, respectively. Reprinted with permission from ref 427. Copyright 2015 Nature Publishing Group.

of $Pt(acac)_2$ in the presence of 2.5 nm thick FePtM NWs as seeds, FePt sheath with a thickness of 0.3−1.3 nm was deposited around the FePtM core. The as-prepared alloy NWs exhibited enhanced activity and stability toward ORR when compared with a commercial Pt/C catalyst, and the synthetic concept was proposed to be extendible to other multimetallic core−sheath NWs.

6.3.3. Deposition without Involving Galvanic Replacement. As discussed in section 3.4.3, when the ions of one metal with a higher reduction potential are added to a solution containing a reduced metal with a lower reduction potential, the metal with the lower reduction potential will be oxidized and replaced by atoms of the metal with a higher reduction potential through galvanic replacement. In this case, voids can be generated, and a hollow, alloy structure can be obtained. To avoid the removal of the core due to galvanic replacement, several methods can be applied, such as adding a reducing agent to serve as an alternative source of electrons, modifying the reduction potential of the metal ions, and the use of protective layers.[89] For example, Ag@Au core−sheath NWs could be obtained via the reduction of $HAuCl_4$ by H_2Asc and the deposition of generated Au atoms onto preformed AgNWs (Figure 29).[414] Because of the higher reduction potential of Au^{3+}/Au compared to Ag^+/Ag (1.52 and 0.80 V versus SHE for Au^{3+}/Au and Ag^+/Ag pairs, respectively), galvanic replacement can be favored, making it challenging to generate a core−sheath structure with a Ag core. To prevent galvanic replacement, an alkaline solution (pH ≈ 11.0) containing H_2Asc was used to enable electrons from H_2Asc oxidation to replace those from Ag oxidation. In addition, the Cl^- in $AuCl_4^-$ can be replaced by OH^- to form $Au(OH)_4^-$, thereby decreasing the reduction potential of Au(III). By both enhancing the reducing ability of H_2Asc and decreasing the reduction potential of the Au(III) precursor in an alkaline condition, the galvanic replacement was effectively suppressed and Ag@Au core−sheath NWs were obtained. The protection from the Au sheath greatly improved the stability of AgNWs against oxidative etching.

DOI: 10.1021/acs.chemrev.8b00745
Chem. Rev. XXXX, XXX, XXX−XXX

In another example on the synthesis of Cu@Au core−sheath NWs, trioctylphosphine (TOP) was used as a strong binding ligand to prevent galvanic replacement.[90] According to the hard and soft acids and bases (HSAB) theory, Au(III) ion is a soft Lewis acid, therefore, the introduction of a soft Lewis base such as phosphine would strongly bind to the Au(III) ion and lead to a decrease in the reduction potential. When Au(III) precursor was added in the presence of TOP, the reduction rate of Au(III) was suppressed, and a core−sheath structure was generated. When OLA was used instead of TOP, OLA was a hard Lewis base and could not bind strongly to Au(III). In this case, galvanic replacement dominated the reaction and pores and voids could be observed in the final products. Alternatively, some remaining Tris(trimethylsily)silane that was used to reduce Cu(II) to form NWs in the first stage of the synthesis may have also reduced Au(III) in the second stage. A control reaction in which the NWs are washed before the introduction of Au(III) may clarify what serves as the reduction agent for Au(III) in this reaction.

6.3.4. Galvanic Replacement. Although galvanic replacement should be avoided when one tries to deposit a metal with a higher reduction potential onto another one with a lower potential, in some cases, it can be used to completely remove the initially deposited metal and generate core−sheath nanostructures with the desired sheath composition. For example, Pd@Pt NWs were prepared through the UPD of Cu on PdNWs, followed by the conversion of Cu to Pt via galvanic replacement.[418] When immersing the Cu-deposited PdNWs into a solution containing K_2PtCl_4 and H_2SO_4, the Cu sheath was replaced by Pt because of the large difference in standard reduction potentials (0.34 and 1.19 V versus SHE for Cu^{2+}/Cu and Pt^{2+}/Pt pairs, respectively) and the presence of H_2SO_4, which further facilitated the removal of Cu. A similar approach was also extended to the synthesis of Au@Pd and Au@Pt NRs by using Au@Ag NRs as templates.[419]

Hollow structures, such as yolk−shell or multiwalled 1D nanostructures, have also been created by using galvanic replacement to generate the voids. As an example, rod-shaped Au nanorattles have been synthesized through the replacement reaction between Au(III) and Ag.[420] In a typical protocol, AuNRs were first coated with a thin layer of Ag via the reduction of $AgNO_3$ with H_2Asc, followed by the galvanic replacement between the Ag sheath and an aqueous $HAuCl_4$ solution. The final product consisted of a thin Au sheath surrounding the inner AuNRs with voids between them. The advantages of NRs (e.g., low plasmon resonance frequency, large polarizability, small damping) combined with the high surface area of hollow structures make the yolk−shell Au@Au NRs a promising candidate for optical sensing.

6.3.5. Core−Sheath Nanostructures with Novel Crystal Structures. Epitaxial growth can also be used to generate metal nanostructures with novel crystal structures.[72,421−423] When the metals in the core and shell have similar radii and a small lattice mismatch, it is possible for the metal in the sheath to follow the atomic packing of the underlying core metal during epitaxial deposition.[424−426] In this case, a metallic sheath with a novel crystal structure can be obtained. As an example, 4H hexagonal structured Au nanoribbons, with a characteristic stacking sequence of "ABCB" along their close-packed direction, were successfully used as substrates for the epitaxial growth of other noble metals with a 4H structure (Figure 30).[427] When Ag was deposited onto the Au nanoribbons by reducing $AgNO_3$ with OLA, a 4H-structured Ag sheath mixed with an *fcc* phase was obtained, indicating the 4H phase of Ag was stabilized through the epitaxial growth process. Similarly, polytypic 4H Pd and Pt were also obtained via epitaxial growth on Au nanoribbons by reducing H_2PdCl_4 and H_2PtCl_6 with $NaBH_4$ in the absence of OLA.[427,428] This approach offers a new route to non-*fcc* structured noble-metal nanostructures that may exhibit enhanced activities for catalysis.

Novel crystal structures can also be obtained without templates.[429] It was reported that Ag with a 4H crystal structure was formed at the tips of anisotropic or highly branched nanostructures, such as rod−needle and plate−belt heterostructures,[430] rice-shaped,[431] and flower-like structures.[432] According to simulations, the 4H phase has a lower surface energy then *fcc* but a higher internal energy.[433] This may explain why the 4H phase would be favored at tips with a higher ratio of surface atoms. In addition, manipulation of size and reaction kinetics can also lead to the formation of nanoparticles with novel crystal structures.[433,434]

6.3.6. Core−Satellite Structures. Core−satellite structures, including dendrites and multipods can be considered as derivatives of 1D nanostructures. A dendritic nanostructure consists of a core surrounded by several self-repeated shells of branches or arms, whereas multipods consist of a core surrounded by a limited number of branches.[435] These types of nanostructures may be excellent catalysts due to their high surface areas and possible coverage of high-index facets. However, the synthesis of highly branched structures can be challenging because the anisotropic structure is not favored surface energy considerations and requires growth under kinetic control. At a low deposition rate, a nanostructure may undergo a relaxation process in which atoms can migrate on the surface to minimize the total surface energy, and accordingly, a polyhedral nanocrystal covered by low-index facets will be preferred. When the deposition rate higher than the diffusion rate, anisotropic overgrowth can occur with high-energy facets growing more quickly than low-energy facets.

In most cases, bimetallic nanodendrites or multipods are synthesized through seed-mediated growth. The formation of core−satellite nanostructures relies on the precise control of reduction kinetics, together with the selection of an appropriate capping or stabilizing agent and seeds with a suitable structure. For example, in the synthesis of Au@Pt dendritic nanostructures, CTAB was believed to play an important role in directing the shape evolution.[436] After mixing Au seeds with CTAB, the molecular chains of CTAB would be adsorbed on the surface of Au seeds due to the interaction of Au and Br^- ions in the CTAB molecules. The existence of CTAB around the Au surface could serve as a capping agent and direct the growth of the branched Pt arms, leading to the formation of Au@Pt dendritic nanostructures.

In addition to the heterogeneous growth, a new mechanism based on homogeneous nucleation and particle attachment has been proposed for the generation of Pd@Pt nanodendrites.[123,437] In a typical protocol, K_2PtCl_4 was reduced by H_2Asc in the presence of truncated Pd octahedra that served as seeds. The resultant Pd@Pt bimetallic nanodendrites exhibited open 3D morphology, with Pt branches distributed over the entire surface of the Pd seed. It was believed that both homogeneous and heterogeneous nucleation of Pt occurred at the early stages of the reaction and the growth proceeded via oriented attachment. The fast reduction of Pt(II) precursor by H_2Asc and limited nucleation sites provided by Pd seeds led to

DOI: 10.1021/acs.chemrev.8b00745
Chem. Rev. XXXX, XXX, XXX−XXX

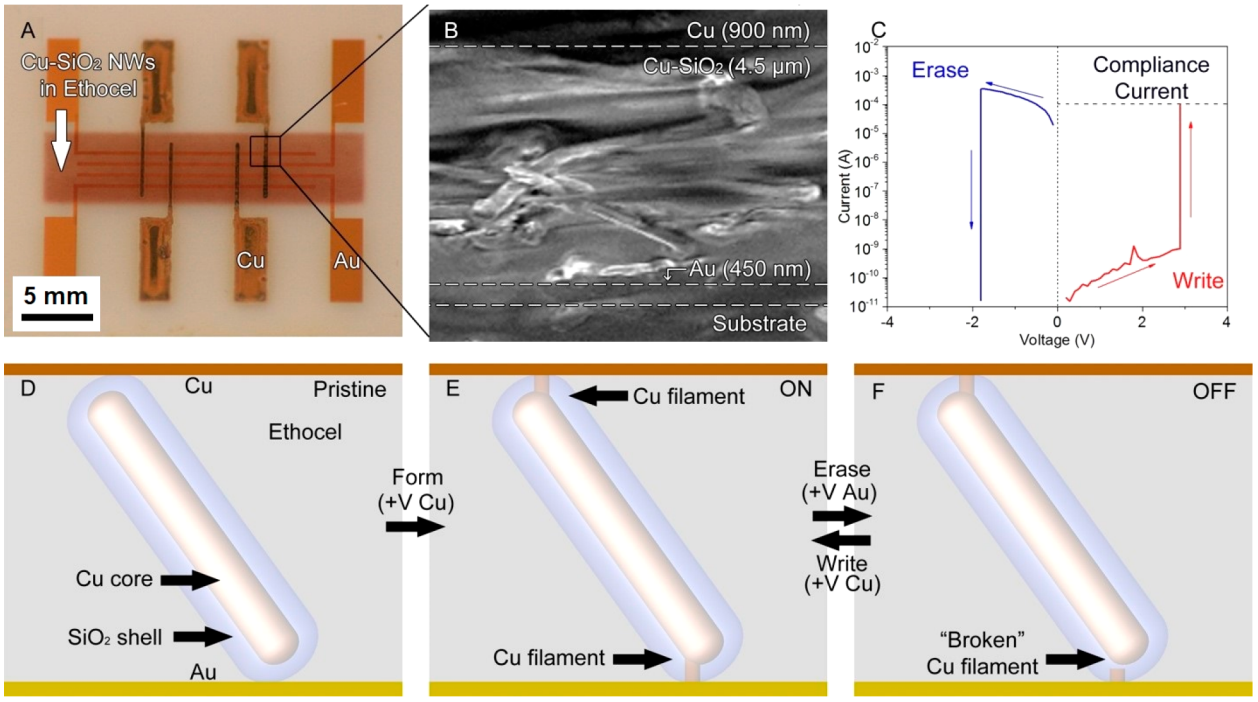

Figure 31. Memristors fabricated from heterostructured NWs. (A) Top-view photograph of fully printed memristors. (B) SEM image of a cross-section of the polymer/NW composite film. (C) Current and voltage in the memristor during erasing and writing. (D) Schematic of the device illustrating the operating mechanism of the memristor. (E) Application of a positive bias to the Cu top contact induces the growth of Cu filaments into the SiO_2 shell, resulting in the ON state. (F) The memristor can be erased by applying a reverse bias to dissolve the filament and achieve the OFF state. Reprinted with permission from ref 442. Copyright 2017 Springer Nature.

the self-nucleation of Pt atoms and the formation of small Pt particles. Because of the ineffective stabilization by PVP, the small particles with a high chemical potential tended to attach to the seeds, and thus grew into dendritic structures. It is worth pointing out that the truncated octahedral shape of the Pd seeds played a pivotal role in achieving an open, dendritic nanostructure by providing multiple nucleation sites for Pt. In this case, attachment would be initiated at the Pt particles that are spatially separated from each other on the Pd seed, and the branches could grow without significant overlap and fusion between them.

7. HETEROSTRUCTURED SYSTEMS

So far, we have discussed the colloidal synthesis of monometallic 1D nanostructures, as well as bimetallic and trimetallic systems with alloyed or spatially segmented compositions. As the number of metals in the system is increased, the variations in structure and properties are also greatly expanded. However, many metal nanostructures are susceptible to oxidation by O_2 from the air and to etching/dissolution by a strong acid.[438] In addition, the electronic structures and thus the related properties/applications of metal nanostructures are limited when compared with those made of semiconductors.[439] To address these issues, metals have also been integrated with other materials for the fabrication of heterostructured systems with enhanced and/or expanded properties.

7.1. Metal–Dielectric

By coating the entire surface of a 1D metal nanostructure with a dielectric material, one can form a protective layer to prevent the metal from oxidation or corrosion; generate an insulating layer to confine electrical conduction; enhance the mechanical strength; and manipulate the plasmonic or other optical properties. In an early demonstration,[440] a simple sol–gel process was employed to coat the surface of AgNWs with amorphous SiO_2, generating Ag@SiO_2 core–sheath NWs. This method involved the hydrolysis of tetraethoxysilane (TEOS) in a mixture of 2-propanol and water in the presence of ammonia as a catalyst to accelerate the hydrolysis reaction, followed by condensation of the SiO_2 sol particles onto the AgNWs. The surface of the AgNWs was originally covered by PVP, a capping agent and colloidal stabilizer commonly used in the polyol synthesis of metal nanostructures. The PVP on the surface was crucial to the formation of a smooth SiO_2 coating. Under the reaction conditions used, the PVP on the surface could function as a silane coupling agent, assisting the formation of SiO_2 sheath.[441] The thickness of the SiO_2 sheath could be readily controlled in the range of 2–100 nm by varying the deposition time from 5–45 min. If the sample was left in the reaction solution for a prolonged period of time, the AgNW in the core would be partially or completely dissolved due to oxidative etching enabled by ammonia and O_2. Upon dissolution of AgNW in the core, the core–sheath nanostructure evolved into a SiO_2 nanotube with porous walls.

The simple sol–gel coating process has been successfully applied to a large number of 1D metal nanostructures with diverse elemental compositions, surface properties, and morphologies. Notable examples include PVP-stabilized AgNWs,[440] and CTAB-stabilized AuNRs.[442,443] However, it should be pointed out that the success of SiO_2 coating critically depends on the surface properties of the nanostructures. For example, unlike the case of AgNWs whose surface was covered by PVP, the sol–gel coating process usually requires the introduction of a silane coupling agent or a polymer coating when applied to CTAB-stabilized AuNRs. In one demon-

DOI: 10.1021/acs.chemrev.8b00745
Chem. Rev. XXXX, XXX, XXX–XXX

stration, the layer-by-layer (LBL) technique was combined with the hydrolysis of TEOS in a mixture of 2-propanol and water to successfully coat the surface of CTAB-stabilized AuNRs with SiO_2.[442] In a typical process, an aqueous suspension of the AuNRs was added dropwise into an aqueous solution of poly(styrenesulfonate) (PSS, a negatively charged polymer) under vigorous stirring. This process was then repeated with a positively charged electrolyte and then PVP to serve as the promoter of SiO_2 coating. These two layers of polyelectrolytes apparently displaced CTAB and allowed for PVP coating, which in turn facilitated the deposition of a uniform SiO_2 shell on the surface of each AuNR with precise control over the thickness.

The dielectric coating could serve as a protective layer to increase the stability and mechanical strength of 1D metal nanostructures. For the Ag@SiO_2 core−sheath NWs prepared using the sol−gel method, they could withstand a pressure of 15 GPa without visible fractures during a bending experiment.[444] This value was almost doubled when benchmarked against the pristine AgNWs without SiO_2 coating. The SiO_2 sheath on AuNRs could serve as an electrically insulating layer in the fabrication of organic photovoltaic (OPV) devices.[442] CuNWs coated with SiO_2 shells could serve as memristive switches (see Figure 31) in a printed, nonvolatile memory that exhibited on−off ratios of 10^6, switching speeds as low as 50 ns, operating voltages as low as 2 V, no degradation over 10^4 switching cycles, and a data retention time of 10 years.[445] These performance characteristics are similar to or better than commercial flash memory devices.

7.2. Metal−Semiconductor

By depositing a semiconductor sheath on the surface of 1D metal nanostructures, one can generate a protective layer to prevent the metal from corrosion or oxidation and create a heterojunction at the interface to enhance the charge-transfer process and prevent electron−hole recombination.[446−448] As a result, the semiconductor coating is expected to improve the stability and durability of the metal nanostructures, while enhancing its properties and applications. For example, semiconductor nanostructures have been actively explored for the detection of volatile organic compounds.[449,450] However, most semiconductors have weak interactions with the visible light because of their small optical cross sections. By introducing a metal−semiconductor interface, the sensitivity, selectivity, and operation conditions of the sensors could all be greatly improved.[451]

A recent study demonstrated the fabrication of Ag−ZnO heterostructured NWs under laser treatment.[70] In a typical process (Figure 32A and B), the as-synthesized AgNWs were deposited on a clean glass or Si substrate and dried under ambient conditions by removing the polyol through evaporation. The surface of the AgNW was then seeded with ZnO quantum dots. Laser-induced hydrothermal growth was applied to obtain a dense array of ZnO NRs on the surface of the AgNW. Figure 32C shows a typical SEM image of the Ag−ZnO heterostructured NWs, indicating high selectivity toward the surface of AgNW because the laser beam heated a small area on the AgNW.

The exposed metal surface in the heterostructures similar to the one shown in Figure 32 may still suffer from corrosion and dissolution when brought into contact with a harsh environment,[452,453] whereas a core−sheath structure could prevent such degradation. Thanks to the efforts from many research

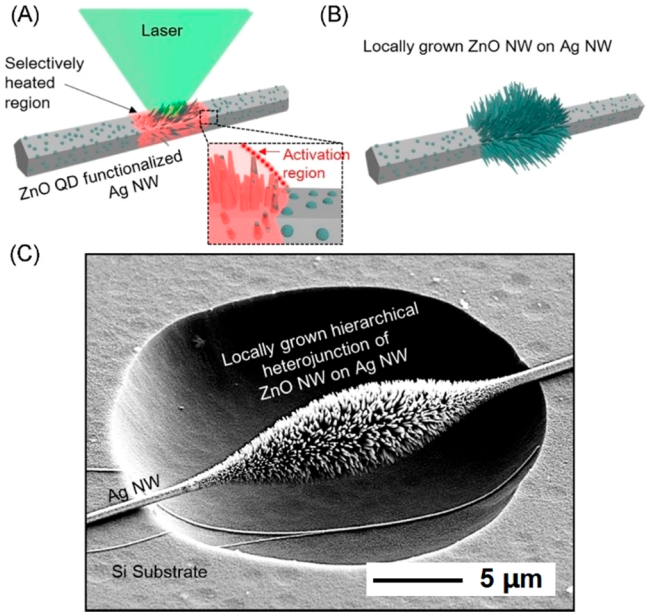

Figure 32. (A) Schematic showing the fabrication of Ag−ZnO heterostructured NWs under laser irradiation. (B) Illustration of the resultant hierarchical structure comprised of ZnNW branches on a AgNW backbone. (C) SEM image of the hierarchical structure suspended on an etched Si substrate. Reprinted with permission from ref 70. Copyright 2017 American Chemical Society.

groups, various kinds of core−sheath nanostructures have been successfully synthesized, including Au@Cu_2O NRs,[454] Ag@TiO_2 NWs,[455,456] and Pt@SnO_2 NRs,[457] among others. For the Au@Cu_2O NRs, they were synthesized using a protocol that involved mixing $CuCl_2$, SDS, AuNRs, NaOH in water. $NH_2OH{\cdot}HCl$ was added, and the mixture was allowed to react for 2 h under magnetic stirring to obtain a uniform, conformal coating of Cu_2O on the surface of each AuNR. These core−sheath NRs were later explored by other research groups for CO gas sensing.[454] It was found that the Au core could trap the mobile electrons for a longer period of time because of the large difference in band structure between the metal and the semiconductor at their interface. The electronic sensitization provided by the Au core resulted in greatly enhanced detection sensitivity toward various gases.

Researchers have taken full advantage of the metal core to enhance the capabilities of a variety of semiconductors toward photocatalysis and related applications. Except for the unique interaction between the metal and semiconductor at their interface, the semiconductor sheath in a core−sheath structure could also protect the metal core from the harsh environment, increasing its durability and lifespan. A typical example can be found in Ag@TiO_2 NRs,[458] where the TiO_2 coating can serve as a multifunctional layer that greatly enhances the physiochemical properties of the AgNRs as a SERS substrate. In one report, AgNRs were prepared by oblique angle deposition, followed by atomic layer deposition (ALD) of TiO_2 on the surface of each NR. The wall thickness could be readily tuned by changing the cycles of ALD. It was found that when the coating thickness was about 2 nm, the Ag core could be insulated from the air without showing any decrease in SERS sensitivity. More significantly, the TiO_2 layer also introduced self-cleaning capability that could increase the lifespan of the AgNRs.

DOI: 10.1021/acs.chemrev.8b00745
Chem. Rev. XXXX, XXX, XXX−XXX

7.3. Other Materials

7.3.1. Metal−Graphene. Both graphene and reduced graphene oxide (RGO) are also interesting for integration with 1D metal nanostructures. Graphene is known to have high conductivity, making it attractive for the fabrication of transparent electrodes. Perfect graphene is impermeable to gas molecules, and can therefore serve as a passivation layer for metal NRs and NWs to increase their chemical and mechanical stability. As reported in a number of studies, graphene was able to reduce the oxidation of metals, such as CuNi and Ag.[459,460] However, these hybrid structures are typically fabricated by coating graphene on a thin film of NWs in instead of forming a uniform, conformal coating on individual NWs.

Reduced graphene oxide has been applied to hyperthermia therapy because it can convert UV to NIR light to heat through radiative decay.[461] In one report, RGO was successfully coated as a thin layer about 2.5 nm thick on the surface of AuNRs.[462] The protocol involved the synthesis of AuNRs and GO separately, followed by mixing and incubation for 1 h. The sample was then washed and redispersed in DI water. Finally, the product was transferred into a solution containing ammonium hydroxide (pH 10−11), followed by fast injection of hydrazine as a reducing agent to obtain RGO on the surface. The mixture was stirred at 95 °C for 1 h, cooled, washed, and redispersed in water. The key to the success of this coating process is the attractive force between positively charged AuNR and negatively charged GO in the solution. For CTAB-capped AuNRs, there is no need to do any pretreatment before coating. When switching to Au nanoparticles prepared using the citrate method, the Au nanoparticles had to go through a pretreatment with cysteamine to make the surface positively charged.

7.3.2. Metal−Polymer. In addition to inorganic materials, organic polymers are also of great interest for the fabrication of heterostructured NRs and NWs. It is widely known that some of the polymers can be directly applied as capping agents or colloidal stabilizers during syntheses to regulate the morphology, stabilize the surface, and increase the colloidal stability of the final products. A typical example is PVP, which is used in the colloidal synthesis of most metal nanostructures.[112] However, polymers can also be added after the synthesis to tailor the surface properties of the 1D metal nanostructures.

Different methods have been reported for coating the surface of 1D metal nanostructures with a polymer. A good example involves the coating of AuNRs with a polyelectrolyte.[463] In this method, AuNRs were synthesized using seed-mediated growth in the presence of CTAB. After removal of the excess surfactant on the surface, the AuNRs were dispersed in a microcentrifuge tube. Stock solutions containing PSS or poly(diallyldimethylammonium chloride) (PDACMAC, positively charged) were then injected into the centrifuge tube. After incubation for 30 min, the excess polymers were removed through centrifugation and the solid product was redistributed in aqueous NaCl. This process could be repeated several times to obtain the desired thickness for the polyelectrolyte coating. This LBL strategy allows for the presentation of either cationic or anionic polyelectrolyte on the surface of AuNRs for their immobilization on either positively or negatively charged substrates.

In another demonstration,[464] AgNWs were soldered together using a mixture of poly(3,4-ethylenedioxythiophene) (PEDOT) and PSS for the fabrication of flexible touch panels. The first step involved the synthesis of AgNWs, which were subsequently dispersed in isopropyl alcohol (IPA). Then a solution containing AgNWs and IPA was deposited on a glass substrate or polymer substrate through pipetting and coating by a Mayer rod. After the evaporation of IPA, the mixture of PEDOT and PSS solution was deposited onto the same substrate using the same method. The resistance of the film could be adjusted by changing the thickness of AgNW through repetition of the coating. In this case, nanosoldering of AgNWs at room temperature could be obtained.

8. APPLICATIONS

8.1. Plasmonics

8.1.1. Localized Surface Plasmon Resonance. *8.1.1.1. Theory.* Surface plasmon resonance (SPR) refers to the collective oscillation of conduction electrons at a metal surface in the presence of an electromagnetic wave. When the conduction electrons (or so-called free electrons) in a metal feel the electric field of an electromagnetic wave, they will be displaced from the positively charged nuclei, creating a polarization that will drive the electrons back to their original positions. If the frequency of the incident wave matches the natural frequency at which the electrons seek to return to their original positions, resonance will occur, leading to strong coupling of the energy from the incident electromagnetic wave to the SPR mode. An SPR wave can propagate over several microns on a metal surface, but when it is confined to a nanoparticle, it becomes an LSPR mode. The optical extinction of a metal nanoparticle made of Ag or Au is characterized by a Gaussian-like peak, with the maximum corresponding to the frequency at which resonance occurs. The LSPR peak position is affected by the composition, size, and shape of the nanoparticle, as well as the dielectric constant of the surrounding medium. While spherical particles below 50 nm in diameter only show one resonance frequency, 1D nanostructures can have at least two LSPR peaks, corresponding to the transverse and longitudinal modes,[465−467] and they can be leveraged as substrates for surface-enhanced infrared absorption and also as nanoantenna.[406]

Gustav Mie was the first to solve Maxwell's equations for the optical extinction, scattering, and absorption cross sections of a spherical particle whose diameter is considerably smaller than the wavelengths of visible light.[28,468] The extinction (σ_{ext}) and scattering (σ_{sca}) cross sections can be expressed as[29]

$$\sigma_{ext} = \frac{18\pi\varepsilon_m^{3/2}V}{\lambda}\frac{\varepsilon_2(\lambda)}{[\varepsilon_1(\lambda) + 2\varepsilon_m]^2 + \varepsilon_2(\lambda)^2} \quad (3)$$

$$\sigma_{sca} = \frac{32\pi^4\varepsilon_m^2V^2}{\lambda^4}\frac{(\varepsilon_1 - \varepsilon_m)^2 + (\varepsilon_2)^2}{(\varepsilon_1 + 2\varepsilon_m)^2 + (\varepsilon_2)^2} \quad (4)$$

where ε_m is the dielectric constant of the surrounding medium, V is the volume of the particle, λ is the wavelength, and ε_1 and ε_2 are the real and imaginary parts of the dielectric function of the metal particle. The absorption cross section (σ_{abs}) can be obtained from $\sigma_{abs} = \sigma_{ext} - \sigma_{sca}$. Mie theory indicates that the extinction cross section is determined by both the dielectric function and size of the particle, as well as the dielectric constant of the surrounding medium (ε_m). In addition, Mie theory suggests that resonance takes place when $\varepsilon_1 = -2\varepsilon_m$, and the wavelength at the maximum extinction (λ_{max}) can be expressed as[28]

DOI: 10.1021/acs.chemrev.8b00745
Chem. Rev. XXXX, XXX, XXX−XXX

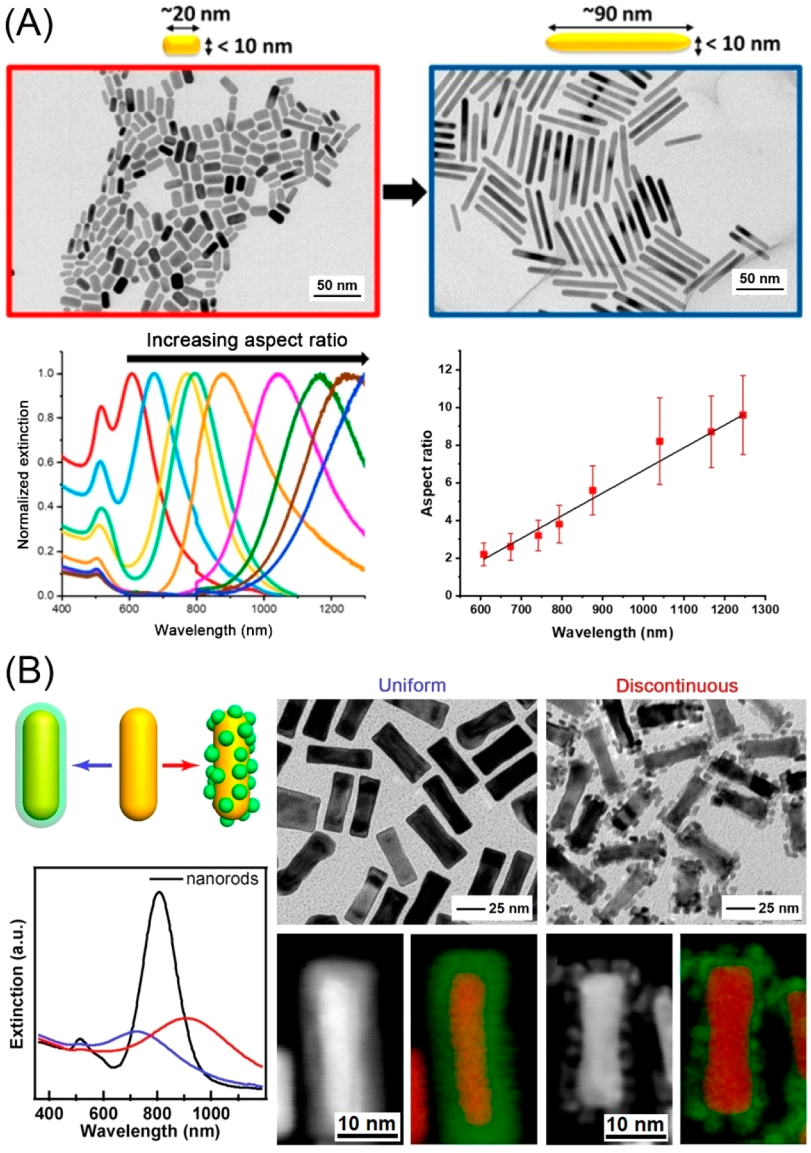

Figure 33. (A) TEM images and UV−vis spectra of the AuNRs with ARs between 2 and 11, and a plot of the longitudinal peak position as a function of AR. (B) The formation of a uniform Pd shell causes the LSPR peak of AuNRs to blue-shift, while a discontinuous coating of Pd particles causes the peak to red-shift. (A) Reprinted with permission from ref 26. Copyright 2018 American Chemical Society. (B) Reprinted with permission from ref 490. Copyright 2012 American Chemical Society.

$$\lambda_{max} = \lambda_p \sqrt{2n_m{}^2 + 1} \tag{5}$$

where λ_p is the plasma frequency of bulk metal and n_m is the real refractive index (RI) of the surrounding medium. This simple equation shows how an LSPR resonance peak can be shifted with changes in the RI of the medium.

Richard Gans further extended the capability of Mie theory to describe the LSPR modes of a spheroidal particle.[469] Because of the anisotropic shape of a spheroidal particle, there are two LSPR modes, corresponding to the transverse and longitudinal directions. The scattering cross section of a 1D nanostructure can be described by the following equations:[28]

$$\sigma_{sca} = \frac{2\pi}{3\lambda}\varepsilon_m{}^{3/2}V\sum_j \frac{(1/P_j{}^2)\varepsilon_2}{\{\varepsilon_1 + [(1-P_j)/P_j]\varepsilon_m\}^2 + \varepsilon_2{}^2} \tag{6}$$

$$P_z = \frac{1-e^2}{e^2}\left[\frac{1}{2e}\ln\left(\frac{1+e}{1-e}\right) - 1\right] \tag{7}$$

$$P_x = P_y = \frac{1-P_z}{2} \tag{8}$$

$$e = \left(1 - \frac{1}{\alpha^2}\right)^{0.5} \tag{9}$$

P_j is the depolarization factor for the three axes. P_x and P_y are the depolarization factors for the transverse axes, and P_z is the depolarization factor for the longitudinal axis. α corresponds to the AR of the 1D nanostructure. Plotting σ_{sca} versus α reveals that the longitudinal LSPR peak red shifts with increasing AR.[28]

Numerical methods are required to calculate the extinction spectra of anisotropic particles with different shapes, such as disks, rings, rods, and wires. The most commonly used

DOI: 10.1021/acs.chemrev.8b00745
Chem. Rev. XXXX, XXX, XXX−XXX

methods include discrete dipole approximation (DDA), finite difference time domain (FDTD), and the finite element method (FEM).[470] In DDA, the nanoparticle is represented as a cubic array of polarizable elements, with the polarizability of each element determined by the dielectric function of the material for the particle.[471−473] The extinction spectrum of the particle is a function of the interaction of these dipoles with the incident electric field, as well as the other dipoles in the array. This method has been used to predict the LSPR spectra for spheres, cubes, tetrahedra, octahedra, core−shell particles, triangular plates, disks, rings, and many other shapes.[473] The FDTD method solves Maxwell's equations for two grids, one for the electric and the other for the magnetic field, that is shifted by half grid points relative to one another. This method has been used to predict, for example, how the spectrum of a single nanocube changes as it approaches a glass surface.[474] The FEM method does not require the use of a discrete grid but instead can use elements that best fit the geometry of the problem. This method is best suited for modeling large domains that contain small details, such as sharp points.

8.1.1.2. Tuning the LSPR of 1D Metal Nanostructures. Most efforts to control the LSPR of 1D metal nanostructures have focused on control of AR, particularly, for AuNRs.[134,214,265,286,303,475−477] The focus on AuNRs is likely because Au does not readily oxidize so its spectra will be stable over time under ambient conditions. In addition, the seed-mediated growth approach allows for excellent control over AR.

Figure 33A shows examples of AuNRs with ARs ranging from 2 to 11.[26] The mini AuNRs with a diameter below 10 nm were synthesized via a seed-mediated growth method. The Au seed particles were, in turn, prepared from a solution containing CTAB, $HAuCl_4$, and $NaBH_4$, which was identical to the standard AuNR synthesis. To reduce the diameter of the final AuNRs, HCl was added into the growth solution to reduce the solution pH, and a relatively large volume of the seed suspension was used. As a result, the mean diameter of the AuNRs was decreased to below 10 nm, while the standard AuNR synthesis typically resulted in the formation of AuNRs with a mean diameter between 10−20 nm. In this new protocol, the AR could be tuned from 2.2 to 10.8 by varying the amount of Ag(I) ions and/or the volume of the seed suspension. The red shift of the longitudinal peak was linearly dependent on the AR of the AuNRs, as shown by the plot in Figure 33A. The peak position of the longitudinal peak was shifted from 607 nm (at an AR of 2.2) to over 1300 nm (at 10.8) whereas the transverse peak remained at a wavelength in the range of 504−523 nm.[27]

Silver is another popular material for studying LSPR because the spectra of AgNRs are narrower and more intense than those of AuNRs.[28] This is because the energy required for interband transition in Au is close to the energy of light at the resonance frequency, leading to greater absorption and band broadening in Au relative to Ag.[478] There are reports on the successful control of AgNR's AR, and the LSPR was found to be linearly dependent on the AR according to both experiments and DDA simulations.[28] For example, the longitudinal LSPR peak of AgNRs was shifted from 545 to 900 nm by changing the AR from 2 to 4.6. At the same AR, the LSPR peak of AgNR occurs at a shorter (by ∼100 nm) wavelength relative to that of AuNR.

There are a number of reports on the synthesis of CuNRs.[111,113,235,479] In one study, Pd decahedral particles were used as the seed for the growth of penta-twinned CuNRs.[113] The growth of CuNRs occurred in the presence of HDA, the same organic capping agent used for CuNW synthesis. The diameter of the CuNRs was around 21 nm, which was largely determined by the size of the Pd seeds. By varying the amount of Pd decahedral seeds while keeping the amount of the Cu(II) precursor fixed, the length of CuNRs could be tuned from 50 to 170 nm, corresponding to ARs of 2.6 and 7.9, respectively. The corresponding longitudinal peak was shifted from 630 to 1100 nm, which was again linearly dependent on the AR. The transverse LSPR peak remained at 560 nm regardless of the AR.

Controlling the exact shape of 1D metal nanostructures can also be used to control the LSPR spectrum.[39,296,480−482] For example, the longitudinal LSPR peak of AgNRs with a square cross section was red-shifted by 50−70 nm relative to that of Ag nanorice with truncated corners.[245] Discrete dipole approximation calculation results for the NRs with ideally sharp edges were also more red-shifted than the synthesized particles, which are typically truncated at edges. These results indicate that sharper edges caused the longitudinal LSPR peak to red-shift for nanostructures with the same AR. The effect of shape was also investigated by selectively etching a Au−Ag core−shell NR into nanorice or a dumbbell-shaped structure.[483] It was found that Cu(II) ions etched Ag from the tips of a core−shell NR in the presence of CTAC, generating a rice-shaped nanoparticle. In comparison, a combination of Fe(III) ions with CTAB led to selective etching of Ag from the middle of the core−shell NR for the formation of a dumbbell-shaped nanoparticle. The selective etching at the tips initially caused a blue-shift for the longitudinal LSPR peak because of the decrease in AR and the truncation of edges, but a red-shift occurred after Au was exposed at the tips. A similar red-shift was observed upon etching the sides of the NRs to create the protuberant corners of the dumbbell-shaped structure.

The formation of shells on AuNRs has also been used to tune their optical properties.[483−493] For example, it was observed that a shell of Pd nanoparticles could cause the LSPR peak of a AuNR to red-shift, while a continuous thin shell of Pd causes the LSPR peak of a AuNR to blue-shift (Figure 33B).[490] These changes were ascribed to a percolation transition for the shell as it changes from a dielectric to a metallic medium. The transition causes the real part of the dielectric function of the shell to shift from a positive to a negative value, which changes the direction of the LSPR peak shift accordingly.

8.1.1.3. Chemical and Biological Sensing. Changes in the dielectric constant of the medium surrounding a 1D Au or Ag nanostructure can be detected by observing a shift in the longitudinal LSPR peak. The shift in LSPR peak position can be described by[494]

$$\lambda^2 = {\lambda_p}^2\left(\varepsilon^0 + \varepsilon_m\left(\frac{1}{P} - 1\right)\right) \tag{10}$$

where λ is the peak position, λ_p is the plasma wavelength, ε^0 and ε_m are the dielectric constants of vacuum and the surrounding medium, and P is the depolarization factor. This equation indicates that the longitudinal LSPR peak is more sensitive to changes in ε_m compared to the transverse LSPR peak because $P_z < P_x = P_y$ for AR > 1. In addition, it can be expected that NRs with larger ARs are more sensitive because P_z decreases with AR. It was also experimentally confirmed that

DOI: 10.1021/acs.chemrev.8b00745
Chem. Rev. XXXX, XXX, XXX−XXX

the RI sensitivity of a AuNR was higher than that of a Au nanosphere.[495] This phenomenon makes the longitudinal LSPR peak of Au or Ag NRs particularly sensitive toward the local environment.

To make 1D metal nanostructures into sensors, it is often necessary to modify their surfaces after the synthesis. For the case of AuNRs, the removal of CTAB is particularly important because CTAB is a toxic surfactant for cells while bare AuNRs have negligible toxicity.[496−498] Since the adsorption of CTAB via the amine is weaker than the ligand bearing a thiol group, various thiolate molecules have been used to replace CTAB, and thereby modify the functionality of AuNRs.[499−504] For example, replacement of CTAB with lipids having a thiol headgroup enabled the label-free detection of a lipophilic drug in water, and a lipopeptide in serum.[503] In addition, the deposition of Ag on Au nanostructures was found to be effective for the removal of CTAC from Au nanostructures.[505] The subsequent selective etching of the deposited Ag layer enabled citrate ions to adsorb onto the Au nanostructures. Alternatively, the positively charged CTAB layer can be overcoated with an anionic surfactant.[463] LBL coating, that is, alternative coatings of anionic and cationic polymers, have also been used to obtain a multilayer of polyelectrolytes.[463,501−508] Such surface functionalization methods play an important role in modifying the properties of AuNRs for use in optical sensing, imaging, photothermal therapy, and drug/gene delivery.

Surface modification is also used to enable specific binding of an analyte of interest while minimizing nonspecific binding. By measuring the shift in the longitudinal LSPR peak as a function of analyte concentration and binding time, the amount of analyte in the solution can be quantified.[509−512] For example, biotin-modified AuNRs immobilized on a glass substrate could detect as little as 94 pM and 19 nM of streptavidin in phosphate-buffered saline and serum solutions, respectively.[510] For multiplexed detection, three AuNRs with different ARs (and thus different LSPR peak positions), functionalized with three different recognition agents, could simultaneously detect three different targets in the same solution.[511]

The ability of a nanostructure to measure the binding of an analyte can be benchmarked with the shift in the LSPR peak per refractive index unit (RIU). The RI sensitivity can be obtained by measuring the peak shift by dispersing the nanostructures in liquids having different refractive indices. For Au nanostructures, the RI sensitivity of different morphologies was found to decrease in the following order: nanoplate ≈ NR > concave nanocube > nanocube.[513] This order can be attributed to the fact that the RI sensitivity increased linearly with the LSPR peak position. This result indicates that the longitudinal LSPR peak of NRs is particularly well-suited for RI sensing as they are red-shifted from the peaks of many nanostructures. In addition, immobilization of the nanostructures reduced the RI sensitivity by up to 36%, and the removal of CTAB increased the RI sensitivity by up to 40%.

Because of their small size and RI sensitivity, the shift in the plasmon resonance of AuNRs can detect the binding/detachment events of single molecules.[514,515] In one example, AuNRs with tips functionalized with thiolated biotin were used for tracking the binding and detachment of proteins with molecular weights as small as 53 kDa in real time without any need for a protein label.[514] Rather than measuring the plasmon shift caused by the binding event directly, the researchers heated the NR with a beam at 785 nm and detected the change in the temperature of the NR upon a shift in the LSPR resonance with a detection beam at 693 nm. Every 1 nm shift in the plasmon peak induced a 4% change in the photothermal signal. Since the detection relies on the absorption of light (which scales with particle volume) rather than scattering of light (which scales with the square of particle volume), the sensitivity of this approach is ca. 700 times greater than methods that rely on spectral measurements with dark-field scattering.

Aggregation of nanoparticles can be used as a sensitive, but qualitative, method for the detection of chemicals. The LSPR alters when nanocrystals aggregate because the electric fields from each nanoparticle couple with one another.[516−518] End-to-end coupling of AuNRs causes the longitudinal LSPR peak to red-shift, whereas a side-by-side binding causes a blue shift.[519−523] For example, the addition of cysteine or glutathione (a tripeptide which contains cysteine) could be specifically detected among other peptides upon introduction into a mixture of AuNRs.[524] Addition of cysteine caused the NRs to assemble end to end, leading to plasmonic coupling between the NRs and a red-shift in their longitudinal peak. Other amino acids did not cause such end-to-end assembly, presumably because they lacked the thiol functional group necessary to displace CTAB from the surface of the NRs. Another example used AuNRs sequentially coated with PSS and goat anti-h-IgG to detect h-IgG.[525] The addition of h-IgG to PSS-coated AuNRs/goat anti-h-IgG conjugates caused side-to-side assembly due to antibody−antigen binding, resulting in a red-shift for the longitudinal peak. The detection limit of the functionalized AuNRs for h-IgG was 60 ng/mL, suggesting that AuNRs functionalized with appropriate antibodies can be used as sensitive sensors for detecting antigens of interest.

Another analytical technique in which anisotropic metal nanostructures have played a role is SERS.[526−532] Although it cannot be used to quantify the amount of an analyte, the SERS spectrum can serve as a fingerprint for identifying the adsorbed analyte, and tracking changes in surface chemistry. The LSPR-enhanced electromagnetic field around a metal nanoparticle increases the SERS signal of adsorbed molecules because the intensity of SERS is proportional to the forth power of the electric field.[526] SERS can also be enhanced through the interaction of the molecules with the metal surface, that is, a chemical enhancement effect, but the contribution of this effect to the signal is small relative to the contribution from the electric field.[526] The enhancement of SERS from different particles can be compared through the enhancement factor:

$$\text{enhancement factor} = \frac{\text{SERS intensity/no. of molecules}}{\text{Raman intensity/no. of molecules}} \tag{11}$$

The enhancement factor for Ag and Au NRs is above 10^7, depending on the AR and the analytes.[527,529,530,532] The SERS signal is most significant at the ends of the NRs due to a lightning rod effect from the high curvature at the ends of NRs. Early work reported that the optimum ARs of Ag and Au NRs for SERS were 10 and 1.7, respectively, because the longitudinal peaks of these NRs were closest to the wavelength of the excitation laser (633 nm).[527] At the optimum AR, the SERS enhancement was 10−100 times greater compared to the NRs with other ARs. The shape of the anisotropic nanostructures can also affect the SERS signal. Experiments comparing the SERS signals from different shapes showed that

DOI: 10.1021/acs.chemrev.8b00745
Chem. Rev. XXXX, XXX, XXX−XXX

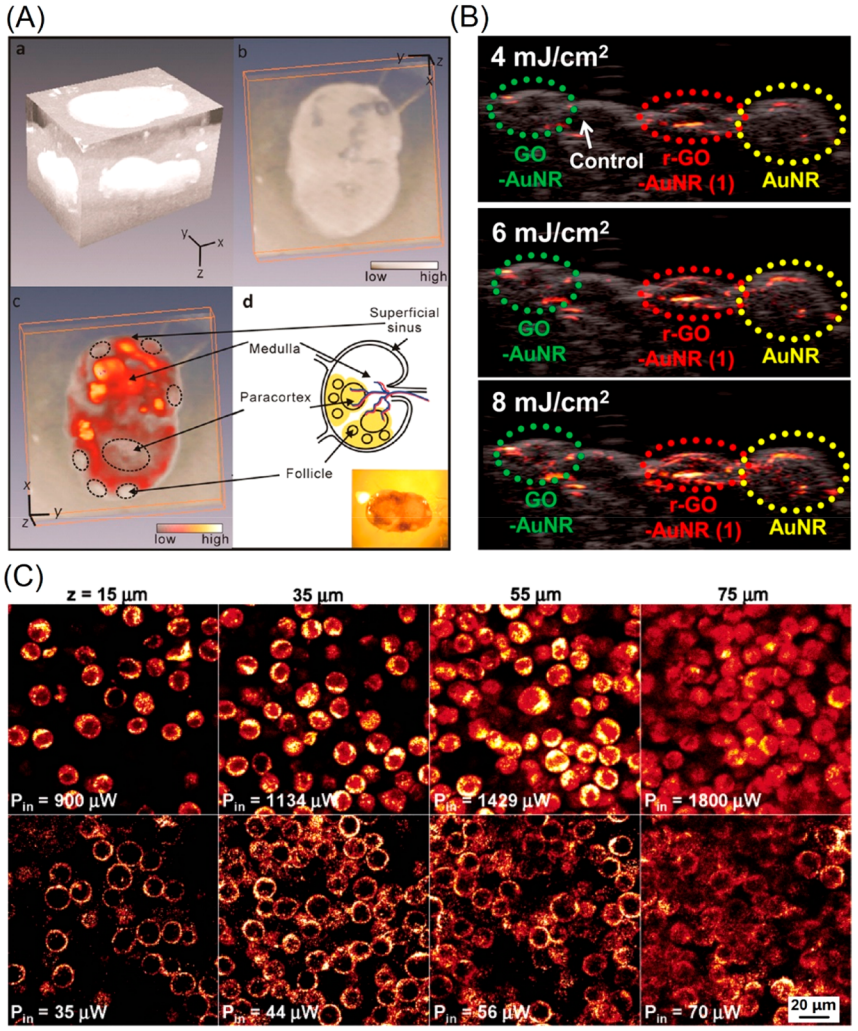

Figure 34. Representative images of tissues or cells obtained using (A) OCT or PT-OCT, (B) PAT, and (C) TPAF or TPL. (A) Reprinted with permission from ref 553. Copyright 2011 American Chemical Society. (B) Reprinted with permission from ref 462. Copyright 2015 American Chemical Society. (C) Reprinted with permission from ref 562. Copyright 2007 American Chemical Society.

the enhancement factor decreased in the order of dogbone > tetrapod > NR.[532] The enhancement from the dogbone was 15 times greater than the NR, suggesting that the sharpened edges could contribute to enhancement. Assembly of NRs into 3D supercrystals was able to further enhance the Raman signal by creating an array of hotspots between the NRs.[293,533−538] Another example of SERS enhancement was the use of aligned AgNWs prepared using the Langmuir−Blodgett technique.[539] The assembled monolayer of AgNWs exhibited an enhancement factor of 2×10^5 for thiol and 2,4-dinitrotoluene, as well as 2×10^9 for Rhodamine 6G.

8.1.1.4. Optical Imaging. The ability to tune the longitudinal LSPR peak of AuNRs to the near-infrared window (650−1350 nm) where light penetrates soft tissues most deeply makes them useful for optical imaging. One approach is to simply detect the light scattered from the NRs with DFOM.[540−547] Although dark-field imaging generally has more signal from the background than fluorescence imaging, the light scattered from AuNRs is much brighter than a fluorescent dye and does not photobleach.[548] In one study, AuNRs conjugated with the antiepidermal growth factor receptor (anti-EGFR) were used to distinguish between a malignant and nonmalignant epithelial cell line using DFOM in vitro.[542] Subsequent work showed that while tumor-targeting peptides enhanced the attachment of AuNRs to cells in vitro, this did not always translate into improved tumor uptake in mouse models due to preferential uptake of such particles by the liver and spleen.[547] The accumulation of Au in organs and tumors was also quantified using elemental analysis, while the intratumoral distribution of AuNRs was analyzed with TEM, demonstrating the suitability of AuNRs for several complementary analytical methods.

Optical coherence tomography (OCT) uses interferometry to detect the depth from which light backscatters from a tissue sample to create an image with micrometer resolution down to a depth of several millimeters.[549−552] This imaging modality has enabled advances in clinical diagnosis, particularly in ophthalmology, but the need for optical coherence limits the contrast agents that can be used with OCT to those that can modulate the optical scattering and absorption.[550] For this reason, AuNRs whose scattering peak can be tuned to the wavelength of the commonly used laser (780−900 nm) are promising contrast agents for OCT imaging.[550] Work to date has demonstrated OCT imaging of the distribution of AuNRs in human breast carcinoma tissue,[550] visualization of tumor blood vessels at depths that would otherwise make the vessels

DOI: 10.1021/acs.chemrev.8b00745
Chem. Rev. XXXX, XXX, XXX−XXX

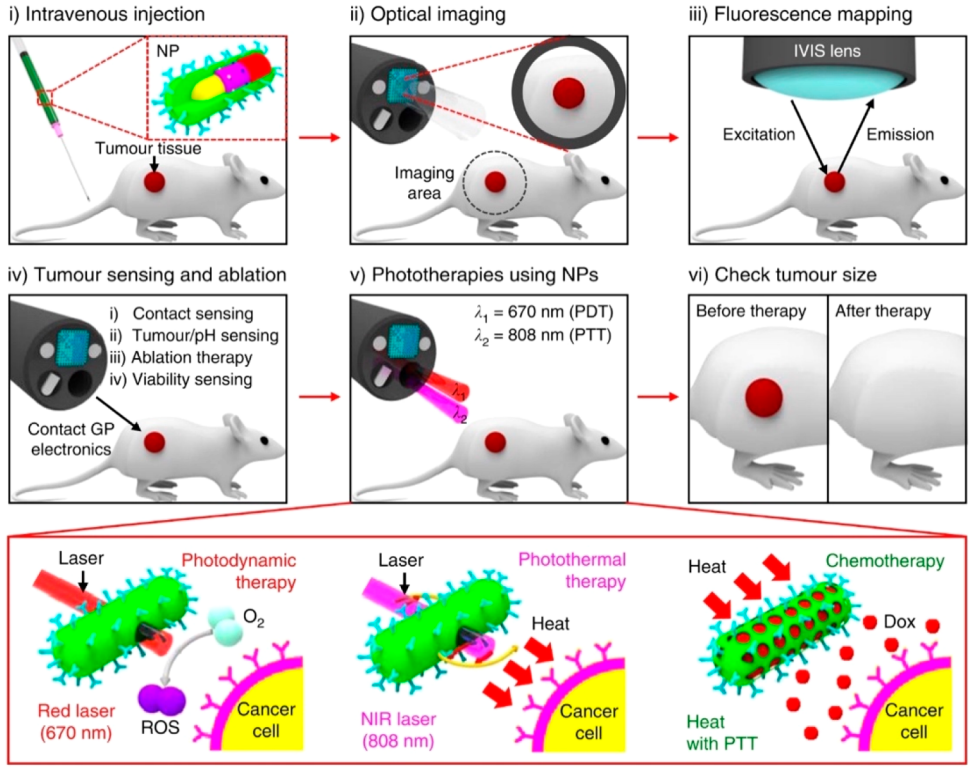

Figure 35. Schematic of the procedures of tumor diagnosis and treatment based on optical imaging with photothermal, photodynamic, and chemotherapy with multifunctional AuNRs and an endoscope. Reprinted with permission from ref 583. Copyright 2015 Nature Publishing Group.

undetectable,[552] as well as mapping of the internal structure of biological materials.[551] Photothermal OCT (PT-OCT) was also developed to take better advantage of the ability of AuNRs to strongly absorb light, and thereby modify the phase of the light scattered back to the detector.[553] As shown in Figure 34A, the contrast of AuNR-infused tissue is enhanced to a much greater extent in PT-OCT relative to OCT.[553]

Besides changing the phase of light, the strong absorption of light and subsequent heating by AuNRs can be used to generate an acoustic wave for photoacoustic tomography (PAT).[554−560] By relying on an acoustic instead of an optical response, PAT can probe greater depths than optical methods, such as OCT.[559] In one example, AuNRs were coated with a SERS reporter molecule to enable simultaneous SERS and PAT of ovarian cancer tumors in vivo.[555] SERS imaging was also used to allow for high-sensitivity detection of tumor margins during image-guided resection, while PAT enable greater depth penetration. Figure 34B presents one example of photoacoustic imaging. Although the AuNRs without any surface coating can be used for PAT, it was found that the coating of AuNRs with RGO further enhanced the photoacoustic amplitude.[462] At the same laser power of 6 mJ/cm^2, the intensity of photoacoustic signals from AuNRs coated with RGO was 1.5 times stronger than those from bare or GO-coated AuNRs.

Optical imaging based on two-photon luminescence (TPL) is another example of how AuNRs can be used to enhance the optical imaging of cancer cells.[561−567] In TPL with AuNRs, the first infrared photon excites one electron in the *sp*-conduction band to an energy level above the Fermi energy, creating a hole into which the second photon subsequently excites an electron from the *d* band.[568,569] Visible light is emitted as electrons in the *sp*-conduction band recombine with holes in the *d* band. The intensity of TPL is 58 times that of two-photon fluorescence (TPF),[561] enabling the imaging of individual AuNRs in vivo. The TPL signal is also 3 orders of magnitude greater than two-photon autofluorescence (TPAF) from unlabeled cancer cells.[562] Figure 34C shows the examples of TPAF (top) and TPL (bottom) images of cancer cells.[562] TPL imaging was also used to monitor how the surface modification of AuNRs affected their circulation and clearance from the blood vessels of mice.[565]

8.1.1.5. Photothermal Therapy. The enhanced permeation and retention (EPR) effect, as well as surface modifications with tumor-targeting ligands, can enable the accumulation of AuNRs in the targeted tissues such as cancerous tumors.[548,570−572] The accumulated AuNRs can then be used for drug delivery or photothermal therapy. As a review article covered this topic in 2015,[2] here, we briefly introduce the basics of this therapy and some recent research results.

The vast majority of the energy from light that is converted into the LSPR in a AuNR is eventually released as heat. As hyperthermia has long been used in conjunction with chemotherapy to treat cancer, it was envisioned that the heat generated from AuNRs could more effectively direct heat to tumors, while minimizing the damage to healthy tissues. For example, a solution containing 28 nm × 8 nm AuNRs at a concentration of ca. 10 nM could be heated to 65 °C with a continuous wave laser (5 W cm^{-2}) at 808 nm in 30 s.[573] Such heating was more than sufficient to kill cancer cells.[573] However, this power is much higher than the maximal permissible exposure (MPE) of skin (0.33 W cm^{-2}),[574] and the intensity of light at this wavelength will rapidly decay over a few hundred micrometers in soft tissues. Thus, researchers have sought to combine the photothermal effect with other treatment modalities to improve its efficacy and applicability.

DOI: 10.1021/acs.chemrev.8b00745
Chem. Rev. XXXX, XXX, XXX−XXX

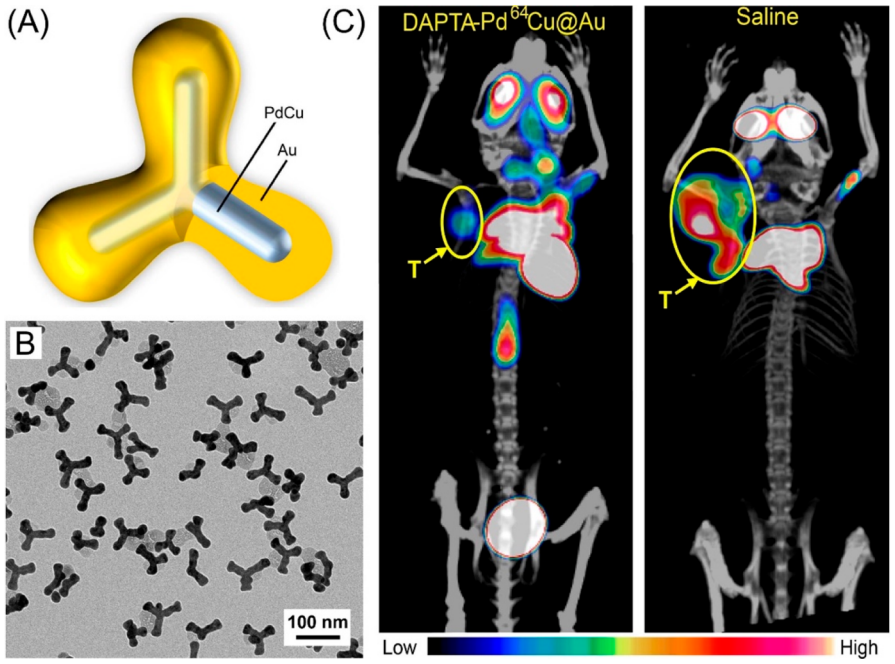

Figure 36. (A) Schematic illustration of the PdCu@Au tripod. (B) TEM image of the trimetallic tripods. (C) ^{18}F-FDG PET/CT fused images of a mouse after receiving photothermal treatment as mediated by the tripods. For comparison, the mouse treated with saline was also tested. Reprinted with permission from ref 584. Copyright 2016 American Chemical Society.

An alternative light-based therapy to photothermal therapy is photodynamic therapy (PDT), which involves the generation of singlet oxygen with light to kill cells. Molecular photosensitizers are hydrophobic, making it difficult to use them in the body. However, it was recently demonstrated that AuNRs alone could generate singlet oxygen upon irradiation by light at a wavelength of 915 nm.[574] This effect was used to kill cells and arrest tumor growth at illumination intensities of 0.13 W cm^{-2}, below the skin tolerance threshold. By changing the laser wavelength between 780 nm for photothermal therapy and 915 nm for PDT, the authors found the latter method to be much more effective in inducing cancer cell death both in vitro and in vivo. Photodynamic therapy was even more effective than treatment with an anticancer drug such as doxorubicin.

Gold NRs can also act as a carrier for drug and gene delivery. The various ways to attach such molecules to the surface of a AuNR include the use of a thiolate bond, the grafting of drugs to the capping agent adsorbed on the Au surface, as well as electrostatic, hydrogen bonding, and van der Waals interactions.[2,10,572,575−582] Subsequent release of the compounds can be initiated by light and/or light-induced heating. One benefit of the use of AuNRs for this application is the potential ability to selectively release compounds in different areas by using NRs featuring resonances at different wavelengths. In one example, two different AuNRs were synthesized with resonance wavelengths at 800 (short NR) and 1110 nm (long NR).[575] Two different oligonucleotides (FAM-DNA and TMR-DNA) were then loaded onto the short and long NRs, respectively. These oligonucleotides could be selectively released with an efficiency of 50−80% by irradiating the NRs with laser light at their respective resonance wavelengths.

Combing multiple therapeutic modalities can potentially provide the best outcome for cancer treatment. In one example, AuNRs were loaded with a PDT dye, a fluorescent marker, and doxorubicin, encapsulated with poly(*N*-isopropylacrylamide), and conjugated with a tumor-targeting antibody (Figure 35).[583] The AuNRs were first injected into a mouse model, and the fluorescent marker was used to confirm the uptake of AuNRs into the tumor. The tumor tissue was removed with forceps, and the tumor site was further treated with RF ablation. The remaining cancer cells were treated by photothermal therapy, PDT, and chemotherapy. The combination of these therapies proved to be most effective at killing cancer cells in vitro, as well as in a mouse model. This study also used a multifunctional endoscope with a AgNW-based transparent electrode for monitoring temperature, contact, and cell/tissue viability during RF ablation in real time.[583]

Other platform nanomaterials other than AuNRs have also been used for the ablation of tumor tissue through imaging-guided photothermal therapy. In one study,[584] the authors synthesized PdCu@Au core−shell tripods by conformally coating the surface of PdCu tripods with Au in an aqueous system (Figure 36, A and B). When a portion of the Cu atoms were replaced with radioactive ^{64}Cu, the resultant trimetallic nanostructures emitted positrons that could be detected using positron emission tomography (PET, Figure 36C) in addition to its intrinsic adsorption of near-infrared light. Once functionalized with a peptide to target the receptor overexpressed on triple negative breast cancer cells, a considerable portion of the injected tripods were able to accumulate inside tumor tissue. Upon laser irradiation, the lesion as depicted by the PET imaging could be destroyed while sparing the normal, surrounding tissues.

8.1.1.6. Plasmonic Photocatalysis. Surface plasmons excited by light can decay into energetic "hot" electrons and holes.[585−587] These charge carriers can then go on to do chemistry on the surface of the metallic nanoparticle. The ability of the SPR of NRs to be tuned across the visible and infrared regions can potentially enable the broadband harvesting of sunlight for plasmon-mediated photocatalysis. The plasmonically active NRs can be combined with catalytic

DOI: 10.1021/acs.chemrev.8b00745
Chem. Rev. XXXX, XXX, XXX−XXX

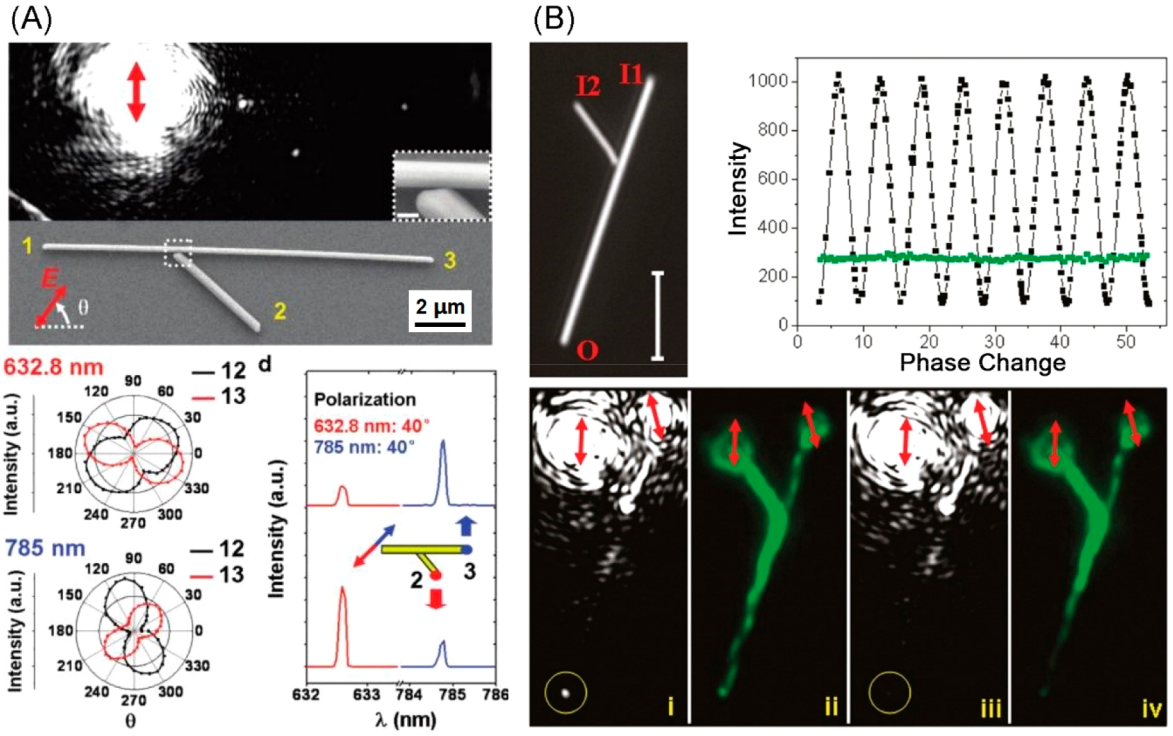

Figure 37. Examples of nanophotonic devices enabled by AgNWs, including (A) a router and wavelength splitter and (B) an OR logic gate. (A) Reprinted with permission from ref 591. Copyright 2010 American Chemical Society. (B) Reprinted with permission from ref 595. Copyright 2011 American Chemical Society.

metals to further enhance the rate and efficiency of photon-to-chemical conversion. To this end, Pd or Pt-tipped AuNRs have been used as photocatalysts for Suzuki coupling,[588] methanol oxidation,[81] and formic acid dehydrogenation.[82,83] For Suzuki coupling with Pd-tipped AuNRs, the yield for the reaction increased from 55% to 95.8% upon laser irradiation at 809 nm, which corresponded to the resonance peak of the nanostructures.[588] Up to 15-fold enhancement in the H_2 generation rate was observed for Pd-tipped AuNRs with visible light relative to the case without light.[82] However, the degree of enhancement depends on a multitude of factors, including the reaction temperature, the illumination wavelengths, the light intensity, the type of reaction, and the type of nanostructure, making it difficult to make comparisons between different efforts.

Comparisons based on the internal quantum efficiency, the ratio of collected electrons (i.e., the amount of chemical product) to absorbed photons can help deconvolute the effects of nanoscale structures on the absorption of light and subsequent photocatalysis. For example, in a study of the plasmon-enhanced H_2 generation by Pt-modified AuNRs, the authors compared the quantum efficiency of Pt-tipped and Pt-covered AuNRs and found the Pt-tipped NRs had an internal quantum efficiency twice that of the Pt-covered AuNRs.[81] They attributed this result to the improvement in charge separation for the Pt-tipped NRs. However, even the internal quantum efficiency of the Pt-tipped NRs was less than 1%, suggesting that much work remains to be done in order to understand and improve the efficiency of 1D metal nanostructures for plasmon-enhanced catalysis.

8.1.2. Waveguiding. Miniaturization of photonic devices with dielectric waveguides is fundamentally limited by the wavelength of visible light. Confinement of light to plasmons at a metal-dielectric interface can enable the localization of light to dimensions about 10 times smaller than those achieved with dielectric waveguides, facilitating the miniaturization of on-chip optical components and their integration with silicon-based electronic devices. A detailed review of plasmonic waveguiding was published in 2018.[589] Here, we briefly introduce a few examples of NW-based waveguides.

The atomically smooth surfaces provided by most synthesized 1D nanostructures can serve to minimize losses of light due to surface scattering relative to rough polycrystalline structures.[589] This lower loss enables atomically smooth, synthesized nanostructures to support the propagation of surface plasmons over longer distances. Plasmons can be coupled into synthesized NWs by focusing light on one end of the NW using a microscope objective, a tapered optical fiber, or a dielectric waveguide. Early work demonstrated that light could propagate along the NW and exit at the opposite end with little loss due to scattering, even when bent with a curvature as small as 4 μm in radius.[590] Light leaked out of sharp kinks in NWs, which could be used to estimate the plasmon propagation distance. Light was also observed to couple from one NW to adjacent NWs in this work.

Later work demonstrated that the extent of inter-NW coupling could be controlled using the polarization of incident light.[591] As shown in Figure 37A, the excitation source was focused onto one end of a backbone AgNW (marked with "1" in Figure 37A), and the light was emitted from the ends of a branch and the backbone AgNW (marked with "2" and "3", respectively).[591] This result illustrates that a surface plasmon can propagate along one NW while also coupling to and emitting from an adjacent NW. The emission of light at positions 2 and 3 was modulated by the polarization and the wavelength of the incident light. At an incident light wavelength of 633 nm, the maximum intensities of the light

DOI: 10.1021/acs.chemrev.8b00745
Chem. Rev. XXXX, XXX, XXX−XXX

at 2 and 3 were observed at polarization angles of 30° and 160°, respectively. Generally, the maximum coupling efficiency occurs when the polarization is parallel to the NW to be coupled with. When two lasers with wavelengths of 633 and 785 nm were simultaneously focused on position 1 at a polarization angle of 40°, the 633 nm light primarily emitted from the NW branch while the 785 nm light mainly emitted from the backbone. These results suggest the use of branched NWs for use as a router and wavelength splitter.[591]

Excitation via a microscope objective is impractical for device operation. Subsequent work demonstrated the excitation of propagating plasmons in AgNWs through a dielectric waveguide. Although this method allowed coupling to many NWs simultaneously, and to a degree that could be tuned with the polarization of light, one drawback of this approach is that the coupling efficiency to any individual NWs was only about 1%. An efficiency of 82% could be achieved by coupling light into a AgNW via a ZnO NW in a butt-coupling scheme.[592] Hybrid nanophotonic polarization splitters, Mach–Zehnder interferometers, and cavities were all fabricated from the Ag and ZnO NWs.

Another exciting application of NW-based plasmonics is their use for the fabrication of logic gates.[593−596] Instead of shining light on one end of a backbone AgNW and using polarization to route it to two different NW branches, the light can be aimed at the ends of the two branches (marked with "I1" and "I2" in Figure 37B) and combined constructively or destructively on the NW backbone. By changing the relative phases of incident light at the inputs of the two branches, the intensity of light at the output (marked with "O" in Figure 37B) can be modulated between an ON and OFF state. This phenomenon can be used as an OR gate, which can be combined with a NOT gate to create a NOR gate in a four-terminal plasmonic device. These logic gates demonstrate the potential to create plasmonic circuits using synthesized metal NWs.

8.2. Interconnected Networks of Metal Nanowires

The anisotropic morphology of NWs allows them to form interconnected networks at very low volume fractions. These networks can be used to transmit electricity or thermal energy through materials. While 2D networks of NWs have large void spaces that can enable the transmission of 99% of visible light, 3D networks of NWs with a porosity of 90% fracture when stretched to a strain of ca. 2%. However, they can be stretched to strains of 300% when the void spaces are filled with an elastomer. In this section, we discuss the AR-dependent properties of NW networks in the context of transparent conductors as well as electrically and thermally conductive composites.

8.2.1. Percolation Threshold. As conductive particles are added into a nonconducting film or composite, there will be a minimum concentration above which a conductive path forms, resulting in a sharp increase in the conductivity of the material. This minimum concentration is referred to as the percolation threshold. For a 2D system, the concentration necessary for percolation can be described in terms of a critical area $A_c = N_c a$, where N_c is the number density of the objects, and a is the area of the individual object. For a system of interpretable objects, the critical area fraction ϕ_c^{AF} is given by[30]

$$\phi_c^{AF} = 1 - e^{-A_c} \quad (12)$$

For a circle, $A_c = 1.13$ and $\phi_c^{AF} = 0.68$. For a widthless stick with a length of L and area L^2, $A_c = N_c L^2 = 5.64$, and $\phi_c^{AF} = 1$. To determine the effect of AR on the percolation threshold, one can compare the critical circle diameter $D_c = 1.2N_c^{-0.5}$ with the critical stick length $L_c = 2.37N_c^{-0.5}$ necessary for percolation.[597] Such a comparison suggests that AR has little effect on the percolation threshold in 2D, because increasing the AR by going from a circle of diameter D to a stick of length L can at most decrease the number of objects necessary for percolation by a factor of 2.[598]

In contrast to the 2D case, AR has a huge impact on the percolation threshold for a 3D system. For example, the critical volume fraction ϕ_c^{VF} for spheres is 0.29, but for a spherocylinder (a cylinder with hemispherical end-caps) with an AR of 100, the ϕ_c^{VF} is only 0.007.[599] This difference indicates that the ϕ_c^{VF} depends strongly on the ratio between the volume V and the excluded volume V_{ex} of an object. The excluded volume is the volume around an object in which the center of an identical object cannot be present if interpenetration of the two objects is to be avoided. The dependence of the percolation on excluded volume was first found in 1984 by comparing the scaling of N_c with radius r for soft-core (interpenetrating) spherocylinders in Monte Carlo simulations.[600] For the simulations, the length L of the cylinder was 0.15. Figure 38 shows that at large r (small AR), $1/N_c$ scales with r^3, consistent with previous results for spheres that showed $N_c \propto V$. At $l/r \geq 5$, however, the dependence of $1/N_c$ becomes linear. This result suggested a dependence of the percolation threshold on the total excluded volume, which, for the case of $L/r \gg 1$, is $4L^2rN_c$.

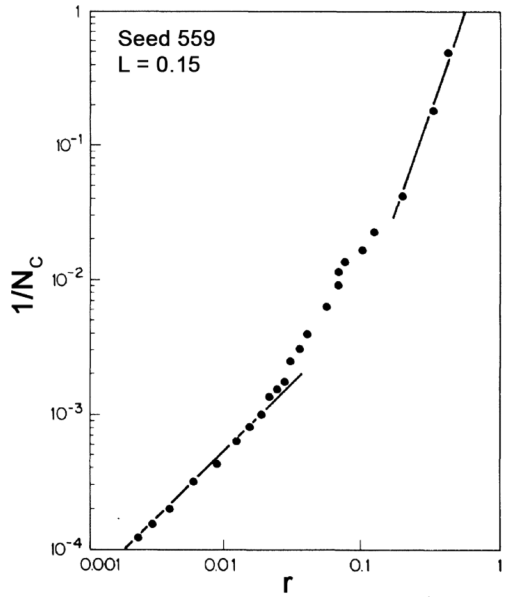

Figure 38. Dependence of the critical concentration of spherocylinders (N_c) necessary for percolation as a function of their radius r for length $L = 0.15$. Reprinted with permission from ref 600. Copyright 1984 American Physical Society.

The following equation for ϕ_c^{VF} was subsequently proposed:[601]

$$\phi_c^{VF} = 1 - e^{-(cV/V_{ex})} \quad (13)$$

DOI: 10.1021/acs.chemrev.8b00745
Chem. Rev. XXXX, XXX, XXX−XXX

Here, $c = N_c V_{ex}$, and it is approximately a constant of the order 1, so a large V_{ex}/V ratio will result in a small ϕ_c^{VF}. For spheres, $V_{ex}/V = 8$, but for spherocylinders

$$\frac{V_{ex}}{V} = 2 + \frac{6(1+\alpha)(1+0.5\alpha)}{1+1.5\alpha} \quad (14)$$

The AR $\alpha = L/D$, where L is the height of the cylindrical part of the spherocylinders and D is their diameter. From this equation, one can see $V_{ex}/V = 8$ at $\alpha = 0$, and $V_{ex}/V = L/r$ at $\alpha = \infty$. Thus, large ARs will result in a large V_{ex}/V and a small ϕ_c^{VF}.

It was also found that the values of c are 2.8 for spheres and 1.4 for spherocylinders with $L/D \gg 1$. With the benefit of improved algorithms and computational power, it was shown in 2016 that c is clearly a function of AR (α) and, from fits to numerical results, this function had the following approximate form:[599]

$$c(\alpha) = 1 + (0.136\alpha + 0.166)^{-0.3235} \quad (15)$$

This equation indicates that the lower bound is $c = 1$ for infinitely long cylinders, and the upper bound is $c = 2.79$ for spheres. Using this equation, the authors demonstrated excellent fits to experimental results for AgNW−polystyrene composites (Figure 39).[31,32,599]

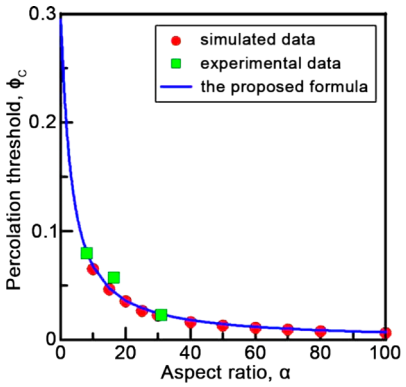

Figure 39. Experimental and simulated percolation thresholds for spherocylinders as a function of their AR (α). Reprinted with permission from ref 599. Copyright 2016 American Physical Society.

8.2.2. Transparent Conductors. Materials that are transparent and conductive are essential components for photovoltaics, OLEDs, smart windows, displays, transparent heaters, and transparent antennas.[602−612] Indium tin oxide, an *n*-type semiconductor with a band gap of 4 eV, is the most widely used transparent conductor due to its high transmittance at low sheet resistances (>90% at 10 Ω sq^{-1}). Indium tin oxide films are usually produced with a sputtering process, in which high energy Argon ions bombard and vaporize an ITO target.[4] The sputtering process requires a vacuum, the film coating rates are relatively low (~1 cm s^{-1}), and most of the vapor is deposited on the walls of the chambers instead of on the film. There has also been concern over the cost and availability of indium since it has a similar crustal abundance as Ag, but for a 100 nm-thick ITO film, indium accounts for only 2% of the film cost.[4] This means most of the cost of ITO film is due to the slow and inefficient sputtering process. The cost of ITO is a significant problem for the development of low-cost, solution-processable OLEDs and OPVs, for which the ITO film can represent a majority of the overall materials cost.[613] The brittleness of ITO also means it cannot be used in applications that require flexibility or stretching capability.

Many new transparent, conducting materials have been developed to address these issues with ITO, including conducting polymers,[614−616] CNT films,[608,617,618] graphene,[619−622] and metal NWs.[229,623,624] Among these materials, metal NW is the only material that can both exceed the performance of ITO and be coated from solution at rates >100 times faster than ITO sputtering, thereby eliminating the need for the costly sputtering process. Figure 40A and B show a picture and an SEM image of transparent conductors made of Cu and Ag NWs, respectively.[216,625] The optoelectronic properties of the various transparent conductors in Figure 40C illustrates that the properties of AgNW networks are comparable to ITO.[626] The cost comparison shown in Figure 40D highlights that the processing cost is significantly lower for NWs than for ITO.[626] Their potential to be more cost-effective than ITO while showing comparable performance has motivated research into how to replace ITO with 2D networks of metal NWs in numerous applications. Researchers have also demonstrated that NW networks can be much more flexible and stretchable than ITO, enabling the development of flexible and stretchable electronics. The following sections discuss the optical, electronic, and mechanical properties of metal NW networks, the methods for fabricating transparent conductors using metal NWs, and applications of the networks.

8.2.3. Optical Properties of the Networks. Generally, researchers would like to create a NW network that is as transparent as possible. The transmittance, $\%T$, of a NW network can be described using

$$\%T = e^{-\phi^{AF} Q_{ext}} \quad (16)$$

where ϕ^{AF} is the area of the film covered by the NWs and Q_{ext} is the extinction efficiency of the NWs. The area fraction ϕ^{AF} can be approximated as $\phi^{AF} = \text{NLD}$, where N is the number density of the NWs, with L being their length and D being their diameter. Q_{ext} can be determined from Mie theory or with the FDTD method.[627] Figure 41 shows the extinction efficiency decreases with diameter, so researchers have sought to improve the optical properties of NW films by synthesizing thinner NWs.[628] However, as the diameter is decreased, the NWs will become more fragile and potentially break during processing. For example, NW breakup during rapid stirring becomes noticeable with diameters of about 20 nm or less, but to date, the breakup of NWs during processing has not been thoroughly studied. In addition, the transmittance of a film increases with a decreasing area fraction of NWs, so it is desirable to maximize the conductivity of NW network for a given area fraction of NWs.

Haze is another optical property that can affect how well suited a NW network is for a given application.[629−631] Haze is the light that is scattered from the NWs between 2.5° and 90° relative to the incident beam. For a display, ideally, haze should be below 1%, whereas for an OPV haze is desirable as it increases the amount of light that is scattered into the absorber layer. Haze increases exponentially with increasing NW diameter, indicating different NW diameters may be appropriate for touch screens versus solar cells.

8.2.4. Electrical Properties of the Networks. To understand how the electrical conductivity of a random NW network changes with the dimensions or number of NWs, it is instructive to start with the simpler case of a square grid of wires with diameter D and length (or periodicity) L. According

DOI: 10.1021/acs.chemrev.8b00745
Chem. Rev. XXXX, XXX, XXX−XXX

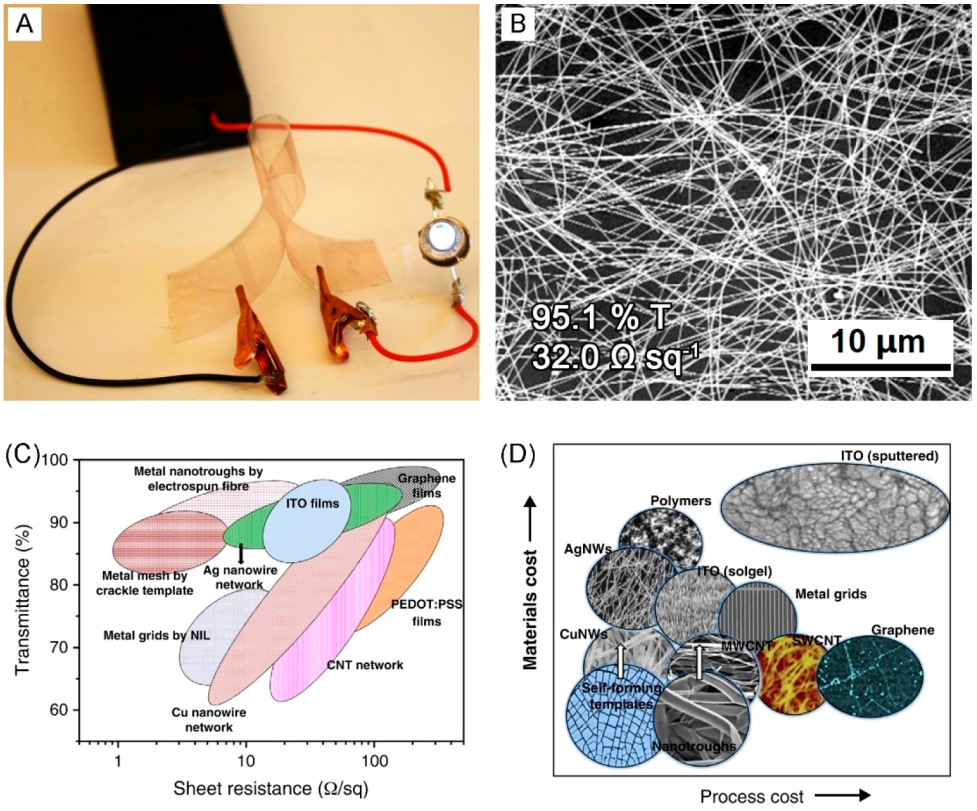

Figure 40. (A) Photograph and (B) SEM image of transparent conductors fabricated from Cu and Ag NWs, respectively. (C) Optoelectronic properties and (D) material versus process cost of various transparent conductors. (A) Reprinted with permission from ref 625. Copyright 2011 Wiley-VCH. (B) Reprinted with permission from ref 216. Copyright 2015 American Chemical Society. (C, D) Reprinted with permission from ref 526. Copyright 2015 Elsevier.

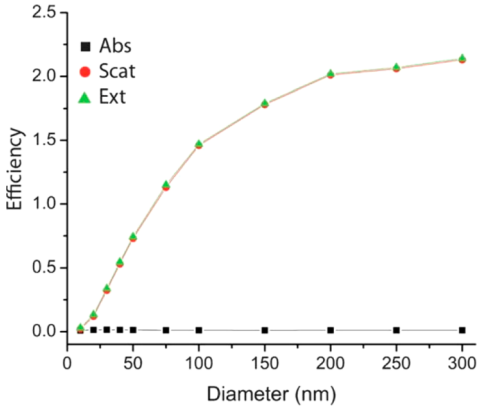

Figure 41. Efficiency of absorption, scattering, and extinction of AgNWs as a function of their diameters. Reprinted with permission from ref 628. Copyright 2012 Royal Society of Chemistry.

to Kirchoff's laws, the sheet resistance R_s for a square network with $N \times N$ wires is[527,632]

$$R_s = \frac{N}{N+1} R_{wire} \tag{17}$$

For the case of cylindrical wires, $R_{wire} = 4\rho L/\pi D^2$, where ρ is the resistivity of the wire. If the measurement of R_s is made over a distance much larger than L, then

$$R_s = \frac{4\rho L}{\pi D^2} \tag{18}$$

Thus, the sheet resistance of a large square network of wires is just equal to the resistance of an individual wire. This equation can be rewritten in terms of the area fraction of the wires with $\phi^{AF} = \left(1 - \frac{D}{L}\right)^2 \approx \frac{2D}{L}$ for a square grid of wires with $L \gg D$

$$R_s = \frac{8\rho}{\pi D \phi^{AF}} \tag{19}$$

This equation indicates that R_s will increase linearly with D and ϕ^{AF}.

Percolation theory indicates that the relationship between the area fraction of NWs and the sheet resistance should likely have the following form:[633]

$$R_s = M'(\phi^{AF} - \phi_c^{AF})^{-t} \tag{20}$$

Here, M' is a scaling constant, and t is the conductivity exponent. The value of t is usually taken to be 1.3, but Monte Carlo simulations have shown its value can range from 1.2−1.4 as the ratio of the inter-NW junction resistance to NW resistance increases from 0.01 to 100 at relatively low NW densities with $\left(\frac{\phi^{AF} - \phi_c^{AF}}{\phi_c^{AF}}\right) < 1$.[634] As the NW density increases, the potential range of values of t widens to be between 1−1.8 for junction-to-NW resistance ratios of 0.01−100.[635] This theoretical work suggests that the value of the conductivity exponent can be used as a qualitative measure of the junction-to-NW resistance ratio for a given NW density. Reported values for t range from 1.23−1.75 for AgNWs,[29,627,628,636,637]

DOI: 10.1021/acs.chemrev.8b00745
Chem. Rev. XXXX, XXX, XXX−XXX

with high values of t generally corresponding to networks with high junction resistances. Values of t for CNTs (1.46−1.65) are usually higher than those for AgNWs, which is expected from their higher junction resistance.[638−640]

A comparison of eqs 19 and 20 suggests that $M' \approx \frac{C8\rho}{\pi D}$ when $\phi^{AF} \gg \phi_c^{AF}$.[627] Here, C is a constant that takes into account the fact that the random NW network will have a higher resistivity than a metal grid because of the contract resistance between the wires. Fitting this equation to experimental data gave a value of $C = 2.4$.[627]

A very useful analytical expression for the sheet resistance of a NW network was derived by treating the network as an array of resistors (see Figure 42).[641] If the length (W_e) of the electrodes equals the distance (W_s) between them, the sheet resistance between the electrodes in Figure 42 can be expressed as

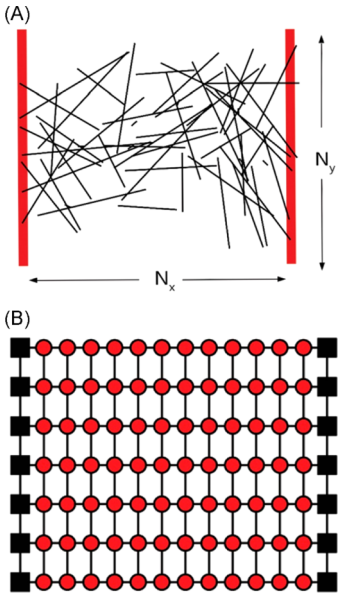

Figure 42. Drawing of (A) a NW network between two electrodes and (B) the equivalent square lattice of resistors. Reprinted with permission from ref 641. Copyright 2016 Royal Society of Chemistry.

$$R_s = \frac{R(n_w)N_x}{N_y} \tag{21}$$

Here, N_x and N_y is the number of resistors connected in series and parallel. The values of N_x and N_y can be derived from

$$N_y = \frac{LW_e n_w}{\pi} \tag{22}$$

$$N_x = \frac{W_s C}{\langle L\rangle P_i}\log(6\alpha {n_w}^2 \langle L\rangle^2 P_i) \tag{23}$$

where the probability P_i of forming an intrawire conductor is given by

$$P_i = \frac{2\alpha {n_w}^2 - n_w}{3\alpha {n_w}^2 + n_w} \tag{24}$$

and the average wire segment length $\langle L\rangle$ is given by

$$\langle L\rangle = \frac{L}{P\pi L^2 n_w + 1} \tag{25}$$

Here, C is a constant (∼1), $\alpha = 0.5P\pi L^2$, and the contact probability (P) is approximately 0.18. $R(n_w)$, the effective resistance of the NW network, maps the resistance of an ordered lattice normalized to the resistance of a NW network with the following expression:

$$\frac{1}{R(n_w)} = \{[g_i\alpha n_w - 3g_i - g_j - g_i\alpha n_w]/[2(3\alpha n_w + 1)]\} + \{[(12g_ig_j(\alpha n_w - 1)(3\alpha n_w + 1) + (g_i(\alpha n_w - 3) - g_j(\alpha n_w + 1))^2)^{0.5}] /[2(3\alpha n_w + 1)]\} \tag{26}$$

Here g_j is the average conductance of a NW junction, and g_i, the average conductance of a NW, is obtained as

$$g_i = \frac{\pi D^2}{4L\rho} \tag{27}$$

Note that we have modified the original equation for N_x by replacing L with $\langle L\rangle$ so that the value of N_x (the number of nodes in the x-direction) increases with increasing L, and the effect of L on R_s becomes small at high n_w and small g_j. This analytical model produced predictions for R_s that were identical to those obtained by much more complicated numerical simulations that involve solving Kirchhoff's circuit equations. The model also enabled good fits to experimental data and showed that the experimental values of R_s were about 10 times higher than is theoretically possible if the junction resistance was zero.

We have used this analytical model to plot the effects of changing L, D, and g_j (the junction resistance) on the sheet resistance of a NW network as a function of area fraction (note $n_w = \phi^{AF}/DL$). Figure 43A shows how, at a junction resistance of 1 kΩ, increasing length while keeping the diameter constant (i.e., increasing the AR) lowers the sheet resistance at a given area fraction. This is because increasing length decreases the probability of having a "dead-end" NW segment, which lowers the network resistance $R(n_w)$ at low area fractions but has less effect at high area fractions. At a junction resistance of 10 Ω, Figure 43B shows that the reduction in sheet resistance gained by increasing NW length is diminished, primarily because the contribution of dead-end resistors to $R(n_w)$ is less significant at low junction resistances.

One can also increase AR by decreasing NW diameter, but Figure 43C shows that doing so will actually increase the network resistance at a given area fraction. This is simple to understand because decreasing the diameter will decrease the volume of metal in the NW network at a given area fraction. This effect might be surprising given that decreasing NW diameter increases the transmittance of a NW network at a given sheet resistance. The optoelectronic performance of the film increases with decreasing diameter because the reduction in the extinction efficiency gained by reducing the diameter more than compensates for the decrease in the sheet resistance at a given area fraction. For example, the Q_{ext} for a AgNW decreases more than 10× when decreasing D from 100 to 12.5 nm, whereas the R_s increases roughly 3.4× when decreasing D from 100 to 12.5 nm at $\phi^{AF} = 0.1$. Thus, increasing AR by decreasing diameter can increase performance, but it does so by decreasing extinction efficiency more than it increases sheet resistance.

DOI: 10.1021/acs.chemrev.8b00745
Chem. Rev. XXXX, XXX, XXX−XXX

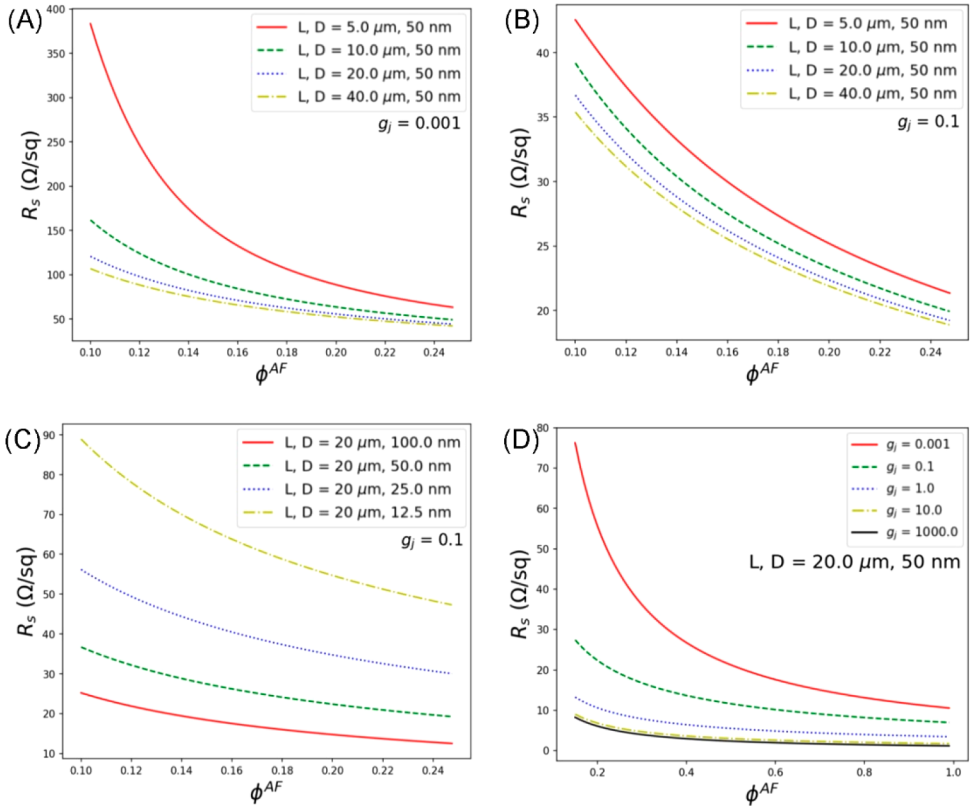

Figure 43. Plots of sheet resistance versus area fraction obtained from an analytical model. The effect of increasing NW length with a NW junction conductance of (A) 1 mS and (B) 0.1 S, respectively. (C) The effect of increasing NW diameter on sheet resistance with a junction conductance of 0.1 S. (D) The effect of junction conductance on the sheet resistance with the length L = 20 μm and diameter D = 50 nm.

Figure 43D shows the effect of junction conductance on the sheet resistance of a NW network at fixed dimensions for the metal NWs. Obviously decreasing junction resistance will improve performance, but the effect becomes negligible above a junction resistance of 1 Ω because the network resistance is limited by the resistance of the NWs and the intrinsic resistivity of the metal. Values of the junction (or contact) resistance between NWs reported in the literature vary widely. For a thermally annealed AgNW network, a value between 1−40 Ω in a computer simulation seemed to provide the best fit to the data, but there is no information about how the simulation and fit were performed.[623] The junction resistance of plasmonically welded AgNWs obtained with a four-point probe measurement was ∼8 kΩ.[642] The junction resistance of Au-coated AgNWs obtained with a 2-point probe measurement was 0.5 kΩ.[643] The junction resistance, obtained with a 2-point probe measurement, of a mat of AgNWs welding with Joule heating was 185 Ω. Silver NWs that were not thermally annealed were fit with a model that assumed the junction resistance was much larger than the resistance of individual NWs, and an effective junction resistance of 2 kΩ was obtained. Another study measured the resistance of 32 junctions with the 4-point probe method and obtained a median junction resistance of 11 Ω, with several outlier junctions exhibiting a resistance >100 Ω.[644] The value of 11 Ω is comparable to the resistance of a NW segment within a network, and did not vary much with the type of annealing method (e.g., furnace, hot plate, or electrical).[644]

8.2.5. Fabrication Methods for Transparent Conductors. Transparent conducting films can be made from metal NWs using a number of different coating methods, including dip coating,[645] drop casting,[646] spin coating,[647−649] spray coating,[650,651] filtration,[652−655] and coating with a Meyer rod.[4,643] Dip coating involves simply dipping a substrate into a suspension of the NWs.[645] The viscosity of the suspension, the concentration of NWs, and the withdrawal velocity can all be used to control the thickness of the NW film. Drop casting involves dropping a suspension of the NWs on a substrate, and the NWs can form a 2D network after the solvent has evaporated.[646] However, it is difficult to obtain uniform films with this method because the NWs will likely move due to evaporative flows, resulting in a coffee-ring pattern. Spin coating involves dropping the NW suspension at the center of a substrate and spinning the substrate to obtain a uniform coating.[647−649] Spray coating involves spraying a NW suspension with an air gun or electrostatic spray.[650,651] The amount of NWs in the coating can be adjusted by the number of spray passes and the concentration of the feed solution. Spray coating can be difficult to control and is fairly low throughput relative to spin coating but can be used to apply NWs to surfaces or substrates for which spin coating is not well-suited (i.e., surfaces that are not flat). Nanowire films can also be formed through vacuum filtration followed by transfer of the NWs from the filter to various substrates.[652−655] The filtration method can easily pattern the NWs by filtering the solution with a patterned mask,[653] and the amount of NWs in the film can be known and precisely controlled by changing the concentration of NWs in the feed solution. Meyer rod coating involves spreading a NW suspension across a surface with a wire-wound metering rod (known as a Meyer rod).[4,643] The thickness of the wet film and, thus, the thickness of the NW film can be adjusted by using rods wrapped with wires of

DOI: 10.1021/acs.chemrev.8b00745
Chem. Rev. XXXX, XXX, XXX−XXX

different sizes. This and similar methods such as doctor blade and slot die coating are compatible with large-scale, roll-to-roll coating processes.[656−662]

Methods to align AgNWs during coating have also been developed in an attempt to improve the optoelectronic properties of the film.[663] Instead of using a Meyer rod, a polydimethylsiloxane (PDMS) stamp with 400 nm-wide channels was dragged across a NW solution, resulting in their alignment. The alignment was presumably due to the confinement of the NWs by the long channel, and trapping them in the aligned state by removing the liquid, but the authors proposed capillary forces also played a role. The alignment was also improved by applying a surface coating such as poly-L-lysine that promoted adhesion of the NWs to the substrate. The aligned NWs were about 4% more transparent than random NW networks at a sheet resistance of 20 Ω/sq and, surprisingly, did not exhibit an anisotropic conductivity.[663]

Nanowire films are usually further processed after coating to improve the conductivity of the films. Thermal annealing is the method most commonly used for improving conductivity. Temperatures between 80−180 °C are sufficient to fuse AgNWs together, and the annealing can be performed in air because of the chemical stability of Ag.[216,623] Copper NWs must be annealed in a reducing atmosphere, such as H_2, to remove the surface oxide.[165,625] Annealing cannot be used with plastic substrates that deform at the annealing temperature, and thin NWs are easily melted and fragmented into particles during thermal annealing.[623] Therefore, the appropriate annealing conditions should be carefully determined to minimize thermal damage to the NWs and the substrate.

Another method to make contacts between NWs is mechanical pressing.[664−666] In one example, the mechanical pressing of AgNW films reduced the sheet resistance from 10^4 to 10 Ω sq^{-1} when the pressing pressure was 25 MPa.[664] This reduction in resistance was similar to what was obtained when annealing the NW film at 200 °C. Another study showed that while annealing at 165 °C resulted in a conductivity of 370 Ω sq^{-1}, this could be reduced to 36 Ω sq^{-1} by applying pressure from a roller at 0.344 MPa.[665] In the case of CuNWs, the surface oxide must still be removed prior to mechanical pressing, which can be accomplished by washing the CuNWs with aqueous H_2Asc.[666] Pressing after this chemical treatment reduced the sheet resistance from 89 to 61 Ω sq^{-1}, but also decreased the transmittance from 93% to 91% because of flattening of the NWs, which increased their optical cross section. Although pressing, in this case, resulted in no change to the optoelectronic performance, it reduced the surface roughness of the films from 78 to 37 nm. This reduction in surface roughness was critical to the prevention of shorts during the use of the NW film as the transparent electrode in an organic solar cell.[666]

Silver NW films can also be annealed by exciting a plasmon at the NW junctions with a tungsten halogen lamp at a power density of 30 W/cm^2. The intense electric field at the junctions results in localized heating and annealing of the NW junctions without damaging the NWs or the substrate.[642,667−670] At the initial stage of this plasmonic welding process, the heat generation was concentrated at the gaps between the NWs that formed due to the presence of adsorbed capping agents. After the closure of the gap due to localized heating, the rate of heat generation decreased dramatically, such that the process was self-limiting.[642] The plasmonic welding can be completed in 1 min, and is compatible with roll-to-roll fabrication.[659] This localized heating effect was also used to reduce $AgNO_3$ with Na_3CA specifically at the NW junctions at a power density that was 1000 times lower (30 mW/cm^2) than plasmonic welding.[671]

Another way to join NWs is to use capillary forces in a process referred to as cold-welding.[464,672] It is thought that a liquid bridge forms at the NW junctions, resulting in very strong capillary forces that drive the NWs together during drying.[672] Capillary forces were also used to selectively coat the junction of NWs with PEDOT:PSS and improve the adhesion of the NWs to the substrate.[464]

The sheet resistance of a AgNW network could also be reduced from 81.5 to 35 Ω sq^{-1} by simply dipping it in a solution of $NaBH_4$.[673] It was proposed that PVP on the surface of the AgNWs was displaced by a hydride ion. The welding of AgNWs at room temperature without heat and light was also achieved via simply cleaning the surface of AgNWs.[673] The NWs were subsequently functionalized with dodecanethiol to provide better resistance to degradation in the presence of a trace amount of H_2S.

8.2.6. Improvement of the Optoelectronic Performance and Stability. As explained in the previous sections, the length and diameter of NWs have an impact on the optoelectronic performance of the NW film. Longer NWs can reduce the threshold for percolation and increase network conductivity by reducing the number of "dead-ends", that is, parts of NWs that do not contribute to the overall network resistance. Decreasing NW diameter decreases the extinction coefficient of the NWs in the film, thereby improving its transmittance. Therefore, researchers have developed new synthetic methods to increase the AR of metal NWs so as to improve their performance in transparent conducting films.

Addition of bromide to the polyol synthesis of AgNWs is an effective way to reduce the diameter of the resultant NWs.[216] In the absence of bromide, the average diameter of AgNWs was approximately 72 nm. The addition of bromide into the same synthesis resulted in a decrease of the diameter to 20 nm. Experimental results suggested that the reduction in diameter was primarily caused by an increase in the number of nucleation events upon addition of NaBr to the reaction solution. Addition of NaBr increased the number of NWs produced in the reaction by a factor of 13, indicating there were more nuclei formed in the early stages of the reaction. Addition of NaBr also increased the number of AgBr nanoparticles formed in solution by a factor of 12. The AgBr nanoparticles can act as seeds for the growth of AgNWs.[674,675] Thus, the 13-fold increase in the number of NWs (which resulted in a 13- and 3.6-fold decrease in the average NW volume and diameter, respectively) could be attributed to the 12-fold increase in the number of AgBr nanoparticles that formed in the presence of NaBr. The reduction in NW diameter allowed the NW film to achieve a transmittance of 99.1% at a sheet resistance of 130 Ω/sq.[216]

The addition of benzoin to a polyol synthesis of AgNWs with bromide could further reduce their diameter even to 13 nm.[217] Benzoin-derived radicals acted as a reducing agent at a lower temperature than EG. This lower temperature was hypothesized to reduce the lateral growth of NWs by increasing the adsorption of bromide ions onto the sides of the NWs. The transparent conductor made from these NWs had a transmittance of about 95% at a sheet resistance of 28 Ω

DOI: 10.1021/acs.chemrev.8b00745
Chem. Rev. XXXX, XXX, XXX−XXX

sq^{-1}.[217] The haze of the NW films was also reduced by about 3× by reducing the diameter of the AgNWs from 40 to 13 nm.

Efforts have also been made to reduce the diameter of CuNWs to improve the optoelectronic performance of transparent conducting films. Copper NWs synthesized with alkylamines can have a diameter between 24 and 60 nm. In comparison, a combination of tris(trimethylsilyl)silane and OLA yielded CuNWs with a diameter of 17.5 nm.[223] The use of dual capping agents, such as a combination of HDA and ODA, has also been reported to decrease the diameter of CuNWs to 13.5 nm.[676] The use benzoin-derived radicals as a reducing agent with OLA as a capping agent resulted in the formation of CuNWs with a diameter of 18.5 nm.[230] Apparently, the effect of temperature on the diameter of CuNWs synthesized with benzoin-derived radicals is the opposite of the case for AgNWs. The diameter of AgNWs decreased with decreasing reaction temperature whereas the diameter of CuNWs increased with decreasing reaction temperature.[217,230] This may be due to lower temperatures resulting in less lateral growth in the former case but fewer nuclei in the latter case.

Maximizing the length of Cu and Ag NWs and, thereby, improving the optoelectronic properties of NW films has also been the topic of several synthetic studies.[677−681] In one example, a hydrothermal synthesis using an aqueous solution with glucose as a reducing agent and PVP as a capping agent led to the formation of AgNWs with lengths of 200−500 μm and diameters of 45−60 nm.[678] In comparison, a typical polyol synthesis produces AgNWs with average lengths up to 25 μm.[628] Subsequently, multistep growth has been used to increase the average length of AgNWs from 50 to 120 μm.[679] In this method, short AgNWs acted as the seeds for further longitudinal growth. For the case of CuNWs, a combination of HDA and CTAB as dual capping agents was reported to produce NWs with lengths of hundreds of micrometers.[681] A combination of OLA and OA in water and glycerol resulted in CuNWs with an average length of 250 μm and a diameter of 50 nm.[677]

Purification of the NW product can also improve the performance of NW-based transparent conductors.[216,682−684] Nanoparticles are often produced along with NWs in the alkylamine-mediated synthesis of Cu and PVP/EG-mediated synthesis of Ag NWs. It is undesirable to have these nanoparticles in the NW film because they will block light without lowering the sheet resistance of the film. Therefore, it is desirable to remove these nanoparticles from the NW product to prevent their incorporation into the film. One simple, scalable way to separate nanoparticles from NWs is based on selective precipitation. For the case of AgNWs, this process involves the addition of acetone into a mixture of the EG-based reaction solution and water.[216] Since PVP is not soluble in acetone, the addition of acetone will cause the NWs to precipitate out from the suspension. This occurs at a lower concentration of acetone for NWs than for nanoparticles, presumably because collisions between NWs are much more likely than between nanoparticles or between a nanoparticle and a NW. After removing the supernatant, the precipitated AgNWs can be collected and redispersed in water or an ink for coating. This purification step resulted in an increase in the transmittance of the NW film up to 4%, and enabled the production of films with a transmittance over 99%.[216] The difference in the dispersion capability between NWs and nanoparticles was also used to purify CuNWs.[683] In this case, $CHCl_3$ was added into an aqueous suspension containing CuNWs and nanoparticles synthesized with HDA. The NWs were transferred to the $CHCl_3$ phase while the nanoparticles remained in the water phase. Cross-flow filtration has also been used for removing nanoparticles from the product solution.[682] This process involves pumping a solution containing both nanoparticles and NWs into a hollow cross-filter with a pore diameter of 0.5 μm. The nanoparticles diffused out through the pores but the NWs did not, enabling the production of a purified NW product.[682]

Nanowire-based transparent electrodes must also be chemically stable if they are to be used in electronic devices. The surface of Ag is gradually converted to silver sulfide in the air due to reactions with ambient hydrogen sulfide and carbonyl sulfide.[460,647,655,658,685−687] Metallic Cu also corrodes in air through reactions with oxygen and sulfides.[87,89,651,666,688−691] Both Ag and Cu NWs must, therefore, be protected against such corrosion if they are to be used for transparent conducting films. Methods to improve the stability of Ag and Cu NWs include coating with graphene,[460,647,658,687,691] coating with shells of corrosion resistant metals or transparent metal oxides,[89,90,655,666,688,689] and coating with poly(methyl methacrylate)[690] or dodecanethiol.[673]

8.2.6.1. Flexibility and Stretching Capability. One clear advantage of a metal NW-based transparent conductor compared to ITO is its mechanical flexibility and stretchability. Several research groups have demonstrated that metal NW films can retain their conductivity after hundreds of bending cycles, whereas ITO is not conductive after a few cycles of bending.[5,624,625,692,693] Subsequent work suggested that curved CuNWs could retain their conductivity under bending to an even greater extent than linear CuNWs.[694] In terms of stretchability, films made of metal NWs can retain their conductivity up to strains of ∼50%,[653,695−697] and this can be increased to several hundred percents if the films start in a prestrained, buckled state[653] and consist of NWs hundreds of micrometers in length. In comparison, individual NWs fracture at strains <5%.[698] It is thought that the stretchability of a NW network is accommodated by a mixture of network deformation and sliding.[696,699] Reversible sliding was observed at low NW densities for a CuNW-based dielectric elastomer actuator that achieved area strains of 200%. Higher NW densities led to NW entanglement and fracture.[699] Prestraining the substrate before stretching leads to out of plane bending of the NWs, allowing them to accommodate greater strains before fracture.[653,695,696]

One can also create wavy NWs by bending them in-plane. One way to accomplish this is by compressing a NW film in a Langmuir−Blodgett trough, followed by transfer of the film to a stretchable substrate.[654] The resulting wavy NW networks exhibited much less fracture and greatly reduced resistance during stretching. A more practical approach to improved stretchability is to use spray coating to form rings of AgNWs on the substrate.[700] The AgNWs were apparently bent into ring structures inside the micrometer-sized liquid droplets rather than by the coffee ring effect during drying. The AgNW rings exhibited a stable electrical resistance during 5000 cycles of mechanical stretching/releasing with 30% strain, whereas the randomly distributed AgNWs showed a dramatic increase in the electrical resistance with cycling.

8.2.6.2. Applications of NW-Based Transparent Conductors. Transparent conductors made of Ag and CuNWs can now match the optoelectronic properties of ITO. The

DOI: 10.1021/acs.chemrev.8b00745
Chem. Rev. XXXX, XXX, XXX−XXX

fabrication of a NW-based transparent conductor can be more cost-effective because they can be deposited from a suspension at high coating rates relative to the vapor-phase sputtering process for ITO. Furthermore, metal NW-based transparent conductors are flexible and stretchable, whereas ITO is brittle. These advantages are motivating the study of metal NW-based transparent conductors in a wide range of applications, including touch screens,[653,662,667,668,678,701,702] solar cells,[623,629,646,648,650,663,666,671,703−711] OLEDs,[712−716] supercapacitors,[655,717,718] transparent memory,[670] air filters,[719] transparent radio frequency antennas,[654] electromagnetic interference (EMI) shielding,[720,721] and skin-attachable speakers and microphones.[722] Here, we only highlight example applications of metal NW-based transparent conductors in touch screens, solar cells, OLEDs, and supercapacitors.

Touch screen panels consisting of two parallel metal NW-based transparent conductors have been reported by several groups.[653,662,667] The two transparent conductors were separated by a spacer or optically clear adhesive, while the driving and sensing lines were fabricated by metal evaporation or screen printing. In addition to touch screens that can detect the location of touch, a force-sensitive touch screen was recently reported.[702] A mechanochromic spiropyran−PDMS composite film was added to a touch screen made of AgNWs. A touching force between 5 and 25 N was measured by analyzing the color change with a spectroradiometer. This enabled the touch screen to measure the distribution of writing forces used to draw a single letter, potentially enabling screens that can verify the authenticity of personal signatures using such force distributions.

Many articles have explored the replacement of ITO in solar cells with NW-based transparent conductors because of their potential to lower the cost and enable the fabrication of more flexible, durable solar cells.[623,629,646,648,650,663,666,671,703−711] Transparent metal NW networks, however, have some disadvantages relative to ITO. One disadvantage is that, unlike ITO, the NW film is not continuous. The transparency of NW films comes from the fact that only a few percents of the surface is covered by metal, leaving behind micrometer-sized open areas in which charge carriers cannot be effectively collected. A second disadvantage is that the halide ions in perovskite solar cells can react with metal NWs to form metal halides, leading to the degradation in the electrical conductivity of the metal NW network. A third disadvantage is the relatively large surface roughness of metal NW networks (on the order of two NW diameters) relative to ITO (<3 nm) can result in the formation of electrical shorts in relatively thin organic solar cells.[646] Finally, the poor adhesion of NWs to most substrates can lead to their removal from the substrate during solution processing steps.

One approach to addressing some of these disadvantages is the deposition of an additional transparent conductive material on top of the NW-based conductor. Metal oxide,[616,629,648,705,706] graphene or GO,[707] ITO nanoparticles, and PEDOT:PSS films[623,646,650,663,666,671,703,709−711] have all been applied to NW-based transparent conductors to improve their performance in solar cells. The deposition of conductive films fills the vacant area between NWs and increases the probability of charge collection. The role of NWs in such composite films is to act as a highly conductive backbone in the low-conductivity film that improves transport of charge carriers to busbars. Such layers can improve the adhesion of metal NWs to the substrate and prevent reactions between metal NWs and halide ions.[648,723−725] The issue of surface roughness could also be solved by embedding metal NWs in a conductive polymer layer.[646,726] These solutions enabled the construction of more cost-effective, stable, and flexible solar cells with metal NW-based transparent electrodes.

The modulation of haze is another approach to improving the performance of a solar cell.[629,707−709] A transparent conductor with a higher haze factor can increase the light path length in the active material, leading to an increase in light absorption. Since the haze factor increases with decreasing transmittance, this trade-off must be optimized to maximize the performance of a solar cell. Simulation results indicated that thicker NWs have a higher haze factor, but lower transmittance. In one example, the optical haze factor of ITO film was below 1% at the wavelength of 550 nm, whereas a AgNW film with a transmittance of 65% exhibited a haze factor of 59%.[708] Simulation results indicated that the higher haze provided by AgNW films could improve the light absorption by 25% for silicon thin films, and 45% for GaAs thin films.[708] In another example, a composite film of AgNWs and fluorine-doped ZnO exhibited a transmittance of 84%, a sheet resistance of 17 Ω/sq, and a haze of 37%.[629] Although perovskite solar cells fabricated with this composite electrode had a slightly higher efficiency that those fabricated with fluorine-doped tin oxide (FTO), they still exhibited a power conversion efficiency of only 3.3%. Adding AgNWs to the top contact of PEDOT:PSS on a silicon solar cell resulted in lower electrical resistance, increased haze, and a power conversion efficiency of 10.1%.[709]

The ability to coat NWs from liquids can enable the deposition of transparent electrodes in unconventional geometries. In one example, a double-twisted fibrous perovskite solar cell was fabricated on a CNT fiber with a AgNW transparent electrode.[727] The CNT fiber was first coated with TiO_2, followed by $CH_3NH_3PbI_xCl_{3-x}$, and then a P3HT/SWNT hole transport layer. Then, AgNWs were coated on the outer surface of the composite fiber. Finally, a second CNT fiber was twisted with the composite fiber to create an electrical contact with the AgNW layer. The double-twist fibrous solar cell exhibited a power conversion efficiency of 3% and was stable under mechanical bending over 1000 cycles. Such fibrous solar cells may someday be employed to power wearable electronics.

Another promising application of the transparent conductors based upon metal NWs is for OLEDs.[722−726] Replacing ITO with a metal NW-based transparent conductor enables the fabrication of an OLED that is flexible and stretchable, and can be potentially manufactured with roll-to-roll fabrication.[722−726] The primary technical hurdle for using metal NWs as the transparent electrode in an OLED is the higher surface roughness of a metal NW-based transparent conductor than ITO, which can lead to the formation of electrical shorts and a decrease in the efficiency of the OLED.[712,713,715] Weak adhesion between metal NWs and the substrate can also reduce the mechanical stability of the devices.[713,715] Similar solutions to those discussed for solar cells were employed to address these problems, including embedding metal NWs in a conductive polymer and coating of an additional buffer layer.[712−716] In one example, AgNWs were coated on a glass substrate, followed by overcoating and polymerization of a vinyl monomer.[712] The composite electrode could then be peeled off from the substrate to reveal the NWs embedded in a smooth polymer surface.[712] The NW composite electrodes

DOI: 10.1021/acs.chemrev.8b00745
Chem. Rev. XXXX, XXX, XXX−XXX

exhibited moderate improvements in their maximum current efficiency and a 20−50% higher luminance relative to OLEDs fabricated using ITO. OLEDs produced with the composite AgNW electrode largely retained their performance after 100 bending cycles.

Another way to fill the vacant area in a NW electrode is to use a mixture of long, thick NWs that act as highly conductive backbones, and short, thin NWs that act as branches.[715] Such a dual-scale electrode was fabricated from AgNWs and embedded in a flexible substrate for use as the transparent electrode for an OLED. The current and power efficiency improved by 40% and 70%, respectively, for devices made with the dual-scale electrode compared to previous work that used AgNWs with a smaller range of dimensions.

Metal NW-based transparent conductors also enabled the fabrication of a flexible/transparent supercapacitor.[655,717,718] However, bare Cu and Ag NWs are not stable because they are easily oxidized electrochemically at the voltages commonly used for a supercapacitor. In one example, AgNWs were protected with a Au sheath with a thickness between 3−5 nm.[655] The Au sheath prevented the oxidation of AgNWs during 500 cycles of charging/discharging. Subsequent work reported that a coating of polypyrrole on the Ag@Au core−sheath NW electrode improved the specific capacitance and created a transparent/bendable/stretchable pseudocapacitor.[718] WO_3 particles were also combined with a AgNW transparent conductor to create a photoresponsive electrochromic supercapacitor.[717] In this case, AgNWs were deposited on cellulose nanofibers, followed by coating with RGO and WO_3. The performance of the electrochromic supercapacitor only dropped by 12.6% after 20 000 cycles and could retain its performance after bending. Such an electrochromic supercapacitor could power changes in coloration in mobile and wearable applications.

8.2.7. Bulk Composites Based on the Networks. *8.2.7.1. Fabrication of Composites from Metal NWs.* As discussed above, NWs with large ARs can form electrically conductive networks at very low volume fractions. This allows the voids between the metal NWs to be filled with various materials to produce multifunctional composites. For example, an individual NW can be stretched by only a few percent before fracture,[698,728−731] and NW networks are mechanically weak, so a 3D network of metal NWs cannot be used directly for flexible/stretchable electronics. For the case of a thermally annealed Cu@Ag core−sheath NW felt, the material exhibited a yield strength of 0.1 MPa at a strain of only 1.5%, and a strain at failure of 4%.[732] However, this porous NW felt could be infiltrated with PDMS elastomer to improve the strength by >10 times, and increase the strain at failure to over 300%. Interestingly, the elastic modulus of the NW-PDMS composite was up to 13 times greater than the elastomer alone, even though the NWs comprised only 10% of the composite. Such a large increase can be attributed to the fact that the elastic modulus of CuNWs has been calculated to be 145 GPa, which is more than 10^6 times greater than the elastic modulus of PDMS. In addition, increasing the elastic modulus of the PDMS matrix from 0.07 to 0.59 MPa at 100% strain resulted in a greater increase in the electrical resistance at 150% strain by a factor of 5. The increase in resistance was attributed to an increase in the delamination of the PDMS from the surface of the NWs for PDMS with the higher elastic modulus. This example illustrates how the properties of a NW composite can change depending on the matrix material.[732]

A variety of methods are available for the fabrication of metal NW composites. Perhaps the simplest one involves drop casting NWs into a patterned mask[733] or filtration of NWs on membrane filters, followed by transfer of NWs to a polymer substrate and overcoating with additional polymer.[16,695,734] This method is suitable for the creation of thin composite films, such as those used for stretchable electrodes. Alternatively, metal NWs can be combined with RGO and filtered from a suspension to create conductive composite films.[735,736] Such a film can be peeled off a membrane to make it free-standing, or the NWs can be filtered onto cloth to create a flexible, conductive electrode on clothing. The RGO improves the mechanical properties of the NW network and prevents the oxidation of CuNWs. Alternatively, NWs can simply be dispersed in PDMS, and molded into a desired shape.[15] This required replacing the hydrophilic PVP surface ligand with a hydrophobic hexylamine ligand. Dip coating is another option to fabricate a NW-based, stretchable conductor with 3D polymeric substrates or even with tissue paper.[737] In one example, a cellulose paper consisting of microcellulose fibers was dipped into a NW solution to coat the surface of the cellulose fibers with NWs.[738] Infiltration of polymers into a 3D NW network prepared via vacuum filtration has also been used for producing a flexible and stretchable composite.[732] In another example, polymer infiltration was used to produce a 3D monolithic composite consisting of graphene-coated AgNWs and PDMS.[739] This was prepared by dipping polyurethane foam into a suspension of GO-coated metal NWs, followed by pyrolysis to remove the polyurethane, and infiltration with PDMS. Fibrous stretchable conductors can be obtained via brush coating metal NWs on the fibrous polymer,[740] or wet spinning metal NW-polymer composite.[741,742] Freeze-drying is another method that can be used to prepare an elastic NW-PDMS composite.[743] A highly porous CuNW−PVA aerogel was prepared by freeze-drying and then filled with PDMS, and the final CuNW−PVA−PDMS rubber could be cut into a variety of shapes. Various printing methods, including screen printing and direct writing of NW inks with needles, have also been exploited to fabricate flexible/stretchable metal NW-polymer composites.[744−749]

Further improvement of the flexibility and stretching capability of a NW-polymer composite can be achieved via prestrain[16,695,740,750] and patterning.[15,732,751] The prestrain strategy involves the transfer or the coating of NWs onto a prestrained (i.e., stretched) substrate.[696,740] Upon relaxation of the strain, the NW film can buckle out of the stretching plane, creating wrinkles that can enable the film to accommodate greater strains before fracture than would otherwise be possible. Prestraining can be combined with spray coating of NWs on a sawtooth-shaped PDMS substrate to achieve retention of conductivity to strains over 700%.[750] Patterning NW−polymer composites into serpentine patterns or a 3D helix structure has been used to greatly improve the stretchability of NW−polymer composites.[15,695,732,751]

8.2.7.2. Applications of Metal NW-Based Bulk Composites. Metal NW-based composites have been utilized to fabricate flexible and stretchable strain and touch sensors,[16,733,735,737,741,747,751−753] biomedical devices,[15] and EMI shielding.[754−756] In addition, metal NW−thermoplastic composites were adopted as conductive filaments for 3D printing,[757] and 3D networks of metal NWs were used as the current collector for Li-ion battery.[758−762]

DOI: 10.1021/acs.chemrev.8b00745
Chem. Rev. XXXX, XXX, XXX−XXX

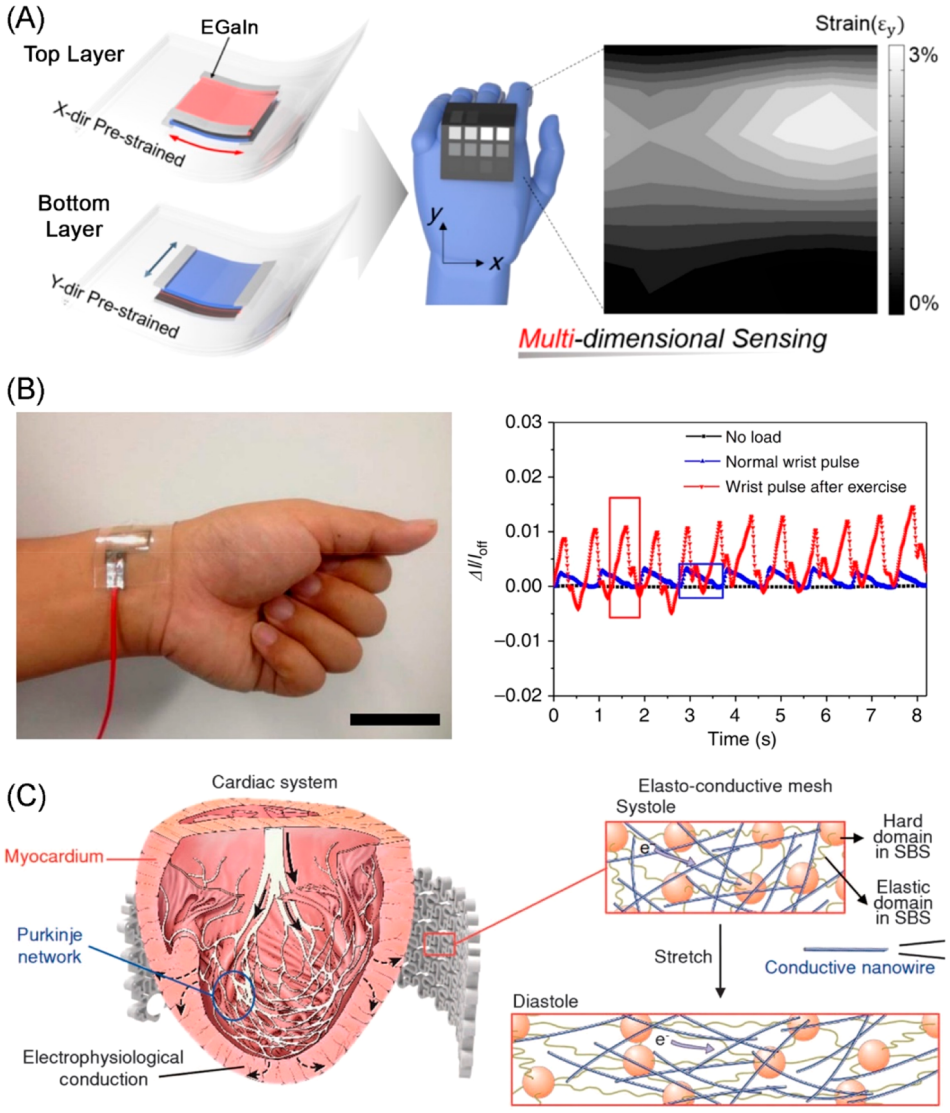

Figure 44. (A) Multidimensional strain sensor array for monitoring hand motion, (B) AuNW-based pressure sensor for monitoring heartbeat, and (C) a serpentine patterned AgNW-based epicardial mesh. (A) Reprinted with permission from ref 15. Copyright 2015 American Chemical Society. (B) Reprinted with permission from ref 737. Copyright 2014 Nature Publishing Group. (C) Reprinted with permission from ref 14. Copyright 2016 AAAS.

Strain and touch sensors that are enabled through the use of highly conductive, stretchable NW composites are particularly exciting as they enable new applications in wearable electronics, as well as for monitoring the motion of body parts, organs, and muscles. Accurate monitoring of motion can facilitate the development of human/robot interfaces, as well as disease diagnosis. Most strain and touch sensors rely on changes in the resistance or capacitance for detection. For strain sensing, research has focused on improving the stretching capability, stability, and sensitivity of the strain sensor while under linear strain.[733,735] As explained above, the prestraining strategy is one of the most popular methods to fabricate a strain sensor since a high stretching capability can be achieved using this approach. For wearable applications, however, it is likely that a strain of 50−100% will be sufficient. By stacking two perpendicular, prestrained AgNW networks, a multidimensional strain sensor was developed, which could monitor strain patterns across a surface (Figure 44A).[16] Multiple stacks of perpendicular, prestrained NW networks were combined into an array of strain sensors that was then used to map the strain distribution across the back of a hand during a gripping motion.

Pressure sensors can be designed based on changes in either resistance or capacitance. In one simple example, researchers used a piece of tissue paper coated with ultrathin AuNWs as a pressure sensitive contact between interdigitated electrodes in a planar film.[737] The magnitude of pressure increase correlated to the decrease in electrical resistance of the AuNW-coated tissue paper between the interdigitated electrodes. This device could also differentiate among pressing, bending, and torsion-based on the differences in the time-dependent current profiles, and was sensitive enough to monitor the acoustic vibrations from a heartbeat on a human wrist (Figure 44B).[737] A capacitive-based pressure sensor was constructed by separating two orthogonal arrays of lines made of AgNWs with PDMS.[752] The researchers used this device to demonstrate the monitoring of strains during thumb movement, walking, running and jumping, as well as mapping of pressure.

DOI: 10.1021/acs.chemrev.8b00745
Chem. Rev. XXXX, XXX, XXX−XXX

Metal NW−polymer composites also have the potential to monitor motion in vivo. In one example, researchers developed an epicardial mesh made from a AgNW−styrene−butadiene−styrene (SBS) composite that could be wrapped around the heart. A serpentine pattern was used to match the elasticity of the composite to that of the myocardium. This stretchable, conductive mesh was used not only to record the intracardiac electrogram of a beating heart but also to apply electrical signals to the heart, acting as a pacemaker or defibrillator (Figure 44C).[15] Subsequent research improved the biocompatibility of the implantable bioelectronics by coating AgNWs with Au.[763]

8.3. Thermal Management

8.3.1. Heat Dissipation of the Bulk Composites. Heat management of electronic devices is essential for preventing their failure. A heat sink with a large surface area and high thermal conductivity is typically placed in contact with an electronic heat source, such as a central processing unit (CPU), to facilitate heat dissipation.[764] Air can be trapped between the rough surfaces of a heat source and heat sink, thereby reducing heat transfer, so a thermal interface material (TIM) is usually applied to improve the thermal conductivity of this interface.[765] Common TIMs include thermal grease, solder, and particle-laden adhesive tapes.[766] Metal NW-elastomer composites have also been evaluated for use as TIMs.[765,767−770] The ability of metal NWs to form percolating networks at low volume fractions means they can be added into an elastomer at volume fractions less than 2% and achieve the desired level of thermal conductivity. In contrast, spherical particles must be used at a volume fraction between 10−50%. Such a high loading causes the elastomer composite to become brittle and crack under pressure rather than conform to the interface between the heat sink and source.

A variety of effective medium models have been developed to account for the effect of a filler's AR, orientation, and Kapitza resistance (interfacial thermal resistance) on the thermal conductivity of composites.[765,771−775] Similar to the case of electrical conductivity, the thermal conductivity of a NW composite is predicted to increase with the AR,[775−777] although the increase levels out at an AR of ca. 1000 for a volume fraction of 1.8%.[765] Experimental results qualitatively confirmed these predictions. In one comparison, a dimethicone composite containing 10 vol % of CuNWs with an AR of ∼22 exhibited a thermal conductivity 1.6 times greater than that of a composite containing Cu nanoparticles at the same volume fraction.[775] Another study compared the thermal conductivity of composites containing short (<20 μm in length) and long (few tens to hundreds of micrometers) CuNWs with a diameter of ca. 80 nm.[777] The short NWs were produced by sonicating the long NWs. The addition of short NWs into polyacrylate increased the thermal conductivity by 350% at a volume fraction of 1.5%, whereas the long NWs increased the thermal conductivity by 1350% at a volume fraction of 0.9%.[777]

Further improvement of the thermal conductivity was achieved by coating metal NWs with thin sheaths of SiO_2 or TiO_2 (see section 7.1).[778−780] These thin shells were observed to improve the dispersion of NWs within a polymer matrix, as well as increase interfacial adhesion as determined by the elimination of air gaps at the NW−matrix interface. The thin sheaths of SiO_2 or TiO_2 also decreased the electrical conductivity of the composites relative to composites made from plain NWs. If the thickness of the SiO_2 sheath increased beyond a certain point, the thermal conductivity of the composite decreased because of the lower thermal conductivity of SiO_2 relative to the metal.[780] Thus, the improved thermal conductivity was attributed to improved bonding between the oxide-coated NWs and the matrix.

8.3.2. Fabrication of Transparent, Flexible, and Stretchable Heaters. Metal NW networks can also be used to generate heat through the passage of electrical current, that is, Joule heating.[17,781−791] A transparent heater fabricated with metal NWs can be used for defogging windows[792] or for a thermochromic display.[783,791] Since a metal NW-based composite can also be flexible and stretchable, it can be used for the fabrication of wearable heaters for personal thermal management or thermal therapy.

Residential heating consumes 42% of global energy, much of which is wasted to maintain the temperature of empty space. An alternative approach would be to create a wearable thermal management device that could maintain the comfort level of building occupants at lower indoor temperatures. It was demonstrated that cloth impregnated with AgNWs could be used for personal thermal management by passively blocking IR radiation from the body, as well by actively heating the body through Joule heating.[17] Carbon nanotubes could be used for active heating but not IR reflection because of their low thermal emissivity.[17] Figure 45A shows IR images of gloves made of CNT-cloth and AgNW-cloth, respectively. The AgNW-based glove appears to be several degrees colder in the image because of its low emissivity. The addition of AgNWs to the cloth improved its thermal insulation by 21% due to the reduction of radiative loss. A 1 in. × 1 in. sample of AgNW-based cloth could also be heated from room temperature to 55 °C by applying only 1.2 V, whereas a CNT-based cloth required a bias of 12 V to reach the same temperature. Thus, the higher conductivity of AgNWs could enable them to be used as more efficient heaters that use smaller, low-voltage batteries. Wearable devices made of NWs are permeable to air and moisture, ensuring they are as comfortable as normal cloth.[17,788]

Thermal therapy is another potential application for stretchable, conductive NW composites.[763,786] Thermal therapy is often prescribed to alleviate the symptoms of painful or swollen joints, but current heat wraps are heavy, bulky, inconvenient, and do not maintain a desired temperature set point. Electrically programmable heaters on polyimide substrates cannot conform to the human body. To address this problem, researchers suspended AgNWs in an SBS elastomer, and molded the elastomer to create a stretchable, conductive serpentine mesh. This heater was connected to a battery and microcontroller to serve as a programmable heater for the wrist (Figure 45B).[786] An alternative approach to the construction of a stretchable heater is to start by creating stretchable, conductive yarn with CuNWs.[788] A helical yarn composed of polyester microfibers was coated with CuNWs and then silicone by dip coating. A wearable heater was created by weaving the conductive threads through the fabric, and its temperature could be controlled with a phone via Bluetooth. The fabrics created using this conductive yarn were washable, breathable, and highly deformable.

8.4. Electrocatalysis

Electrochemistry plays a pivotal role in energy conversion, enabling a number of sustainable processes for future technologies.[793] As an important component of most electro-

DOI: 10.1021/acs.chemrev.8b00745
Chem. Rev. XXXX, XXX, XXX−XXX

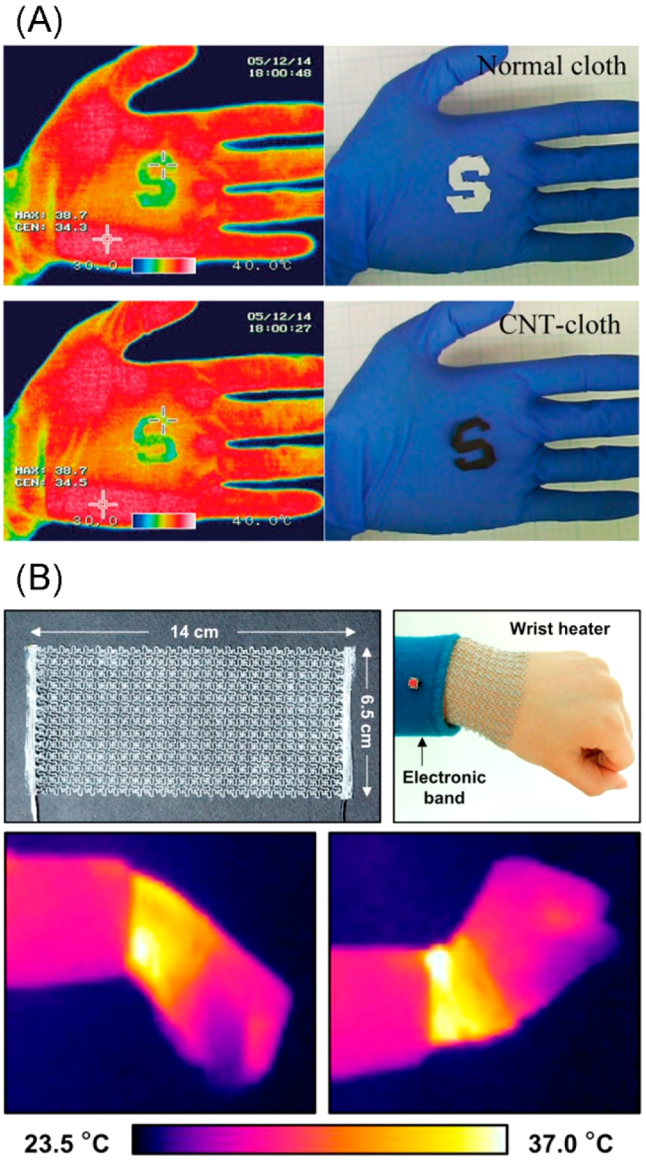

Figure 45. (A) Thermal images (left) and photographs (right) of gloves fabricated using CNT-based cloth (top) and AgNW-based cloth (bottom), respectively. (B) Photographs of AgNW-based wrist heaters (top) and thermal images during heating (bottom). (A) Reprinted with permission from ref 16. Copyright 2015 American Chemical Society. (B) Reprinted with permission from ref 786. Copyright 2015 American Chemical Society.

chemical processes, electrocatalysts reduce energy barriers and increase reaction rates. Generally speaking, two strategies can be used to improve the activity of an electrocatalyst: (i) increasing the number of active sites per unit mass, as exemplified by reducing the size of catalytic particles to expose more active sites on the surface, and (ii) increasing the intrinsic activity of surface atoms, as illustrated by maneuvering the shape (and thus surface structure) or elemental composition.[794]

Metal nanostructures have been explored for a variety of electrocatalytic applications, with notable examples including Pt for ORR,[795,796] Pd for formic acid oxidation reaction (FOR),[387,797] Ir for oxygen evolution reaction (OER),[798,799] and Cu for CO_2 reduction,[800] among others. When reducing the size of metal nanostructures to the nanoscale, they may exhibit improved activities because of the corresponding increase in the surface-to-volume ratio. Additionally, surface strains on nanostructures can affect their catalytic performance. For example, it was demonstrated that icosahedral Pt_3Ni nanocrystals exhibited an area-specific activity 1.5 times greater than its octahedral counterpart toward ORR, and this enhancement could be mainly attributed to the tensile field induced by the twin boundaries.[801] The tensile strain shifted *d*-band center up, resulting in an increase in the adsorption strength for reactants and intermediates and thus enhancing the ORR activity.

In this section, we focus on the use of 1D metal nanostructures in various electrochemical processes, including ORR, methanol oxidation reaction (MOR), FOR, and CO_2 reduction. In addition, 1D nanostructures have also been used as transparent electrocatalysts for the fabrication of photoelectrochemical cells (PECs).

8.4.1. Oxygen Reduction Reaction. Though small in size and diverse in shape and morphology, nanoparticles (i.e., 0D nanostructures) traditionally used as catalysts are not ideal for long-term operation because of two possible deactivation mechanisms: Ostwald ripening and particle coalescence.[802] Ostwald ripening involves interparticle transport of mobile species, with larger particles growing at the expense of smaller ones because of their difference in potential energy. Coalescence occurs when particles get close enough to each other as a result of migration. A notable example is the poor durability of the commercial Pt/C catalyst, in which irregularly shaped Pt nanoparticles of 3−5 nm in size are dispersed on carbon powders. During accelerated durability tests (ADTs), which involved 5000 cycles of potential cycling in the range of 0.6−1.1 V in O_2-saturated 0.1 M $HClO_4$, the electrochemically active surface area (ECSA) and mass activity of Pt/C catalyst decreased by around 54% and 44%, respectively.[803] It was demonstrated that the size of Pt particles increased to 10−20 nm after 5000 cycles of potential cycling. The gradual loss of ECSA will inevitably lead to efficiency loss for the fuel cell and can eventually reach an unacceptable level, compromising the lifetime of a fuel cell. Such a decrease in the ECSA of a catalyst during ADT testing was also observed for many other types of 0D nanostructures.[437] Additionally, the corrosion of carbon can lead to the detachment of catalytic particles, contributing to a further decrease in catalytic activity.[437]

The loss in ECSA as induced by the Ostwald ripening or coalescence of nanoparticles can be mitigated by switching to 1D nanostructures. Compared with nanoparticles, 1D nanostructures often exhibit higher stability because of a larger contact area with the support.[804,805] For example, when similar thermal annealing process was applied, ultrafine Pt nanoparticles underwent severe aggregation (with a size increase from ∼7 nm to 10−30 nm), which could be partially attributed to the migration and fusion of the nanoparticles.[806] In contrast, PtNWs supported on carbon black had multiple anchoring points and their mobility was much lower than that of nanoparticles, leading to a limited increase in size. In addition to their greater stability, 1D nanostructures can also have high specific surface areas because of the nanometer-sized thickness. When the diameter of a NW is decreased, one will achieve both higher specific surface areas and surface-to-volume ratios. For example, the ECSA of PtNWs with a diameter of ∼1.8 nm reached 110 m^2/g_{Pt} in a N_2-saturated 0.1 M $HClO_4$ solution, which was 1.5 times greater than that of the commercial Pt/C catalyst.[806] Additionally, the anisotropic morphology of 1D

DOI: 10.1021/acs.chemrev.8b00745
Chem. Rev. XXXX, XXX, XXX−XXX

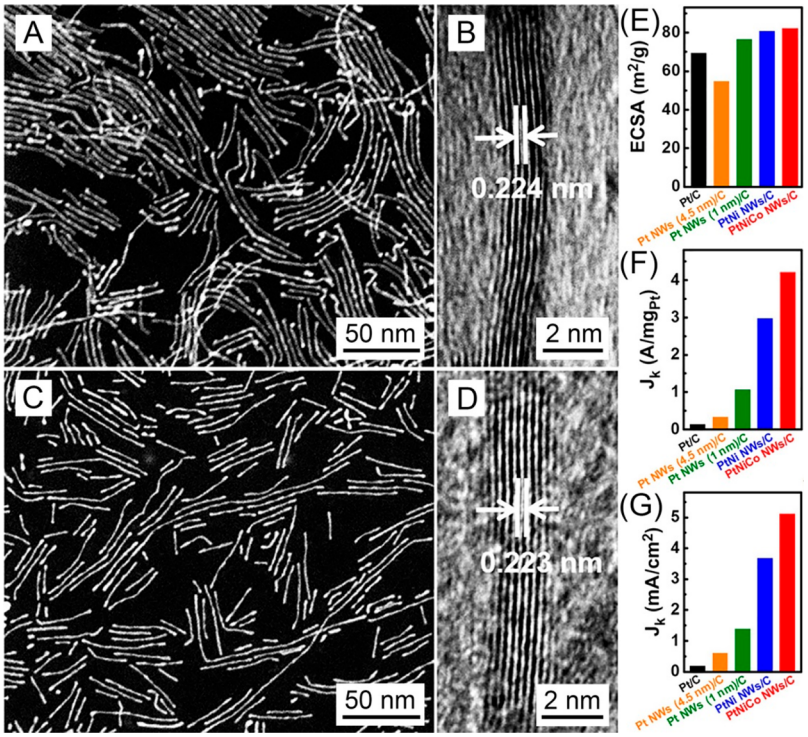

Figure 46. (A) STEM and (B) HRTEM images of subnanometer PtCo NWs. (C) STEM and (D) HRTEM images of subnanometer PtNiCo NWs. (E) ECSAs, (F) mass activities, and (G) specific activities of PtNiCoNW/C, PtNiNW/C, PtNWs (1 nm)/C, PtNWs (4.5 nm)/C, and commercial Pt/C. Reprinted with permission from ref 796. Copyright 2017 AAAS.

nanostructures can help improve mass transport and catalyst utilization. In the conventional formulation of catalyst ink, Nafion has to be added for proton transport, but it tends to isolate catalytic particles from the carbon support, leading to poor electron transport. The use of 1D nanostructures can ensure the formation of a conductive path, helping eliminate the problems caused by Nafion and thereby improve the utilization rate of catalysts.[11,807]

8.4.1.1. Core–Sheath Structures. Although monometallic nanostructures usually exhibit superb performance as electrocatalysts, their activity and cost-effectiveness can be improved through the introduction of another metal. The addition of a second metal can result in three effects: (i) an ensemble effect, in which multiple metals create multiple reaction sites and provide more opportunities to form appropriate binding configurations with the reactants or intermediates; (ii) a ligand effect, in which charge transfer between two dissimilar surface atoms alters their electronic structure and activity; and (iii) a geometric effect, in which the spatial arrangement of surface atoms are affected by strain, geometric shape, and size.[808] To this end, bi-, tri-, or multimetallic 1D nanostructures have been designed to improve catalytic performance (Section 6).

Multimetallic nanostructures can be categorized into two major groups: core–sheath and alloy structures. The core–sheath structure has stimulated the development of a number of electrocatalysts. It is generally accepted that the compressive strain in the sheath can dramatically influence the binding strength of adsorbates and thereby their chemical reactivity.[809] For example, it has been reported that Pd@Pt core–sheath NWs exhibited a mass activity 10 times greater than that of a commercial Pt/C catalyst toward ORR.[13] The excellent activity of the Pd@Pt NWs could be mainly attributed to the strain effect caused by their core–sheath structure. In addition, the strong coupling between the metal atoms in the core and sheath also helped enhance the stability of the sheath by positively shifting the oxidation potential. In another study, it was demonstrated that Pd@Pt core–shell NWs supported on carbon black maintained 63% of their initial ECSA after 30 000 cycles of potential cycling, while the commercial Pt/C was only able to maintain slightly over 50% of the initial ECSA.[418] The core–sheath structures can also be used to tune the composition of the catalysts. Although noble metals exhibit excellent performance in various catalytic reactions, their high costs greatly limit their application. Through the use of core–sheath structures and the introduction of nonprecious metals, one can effectively reduce the loading amount of noble metals while enhancing the catalytic activity. To this end, FePtCu@Pt and PtNi@Pt NWs with cores partially made of nonprecious metals have been synthesized, which not only showed higher activity than commercial Pt/C but also helped reduce the loading of Pt.[806,810]

8.4.1.2. Alloy Structures. In addition to core–sheath structures with spatially separated compositions, alloy nanostructures where different metals are mixed together are also widely used as catalysts for electrochemical reactions. Similar to core–sheath structures, the incorporation of other metals not only reduces the overall cost of the catalyst by reducing the amount of noble metal utilized but also enhances the catalytic performance through a favorable synergistic electronic interaction between the different metals.[811−814] For example, PtNi alloy nanoparticles demonstrated a higher activity than pure Pt nanoparticles because the introduction of Ni lowered the *d*-band center and thus accelerated desorption of O and OH species, leading to an increase in the kinetics for ORR.[815] It was reported that PtNi NWs supported on carbon showed a

DOI: 10.1021/acs.chemrev.8b00745
Chem. Rev. XXXX, XXX, XXX−XXX

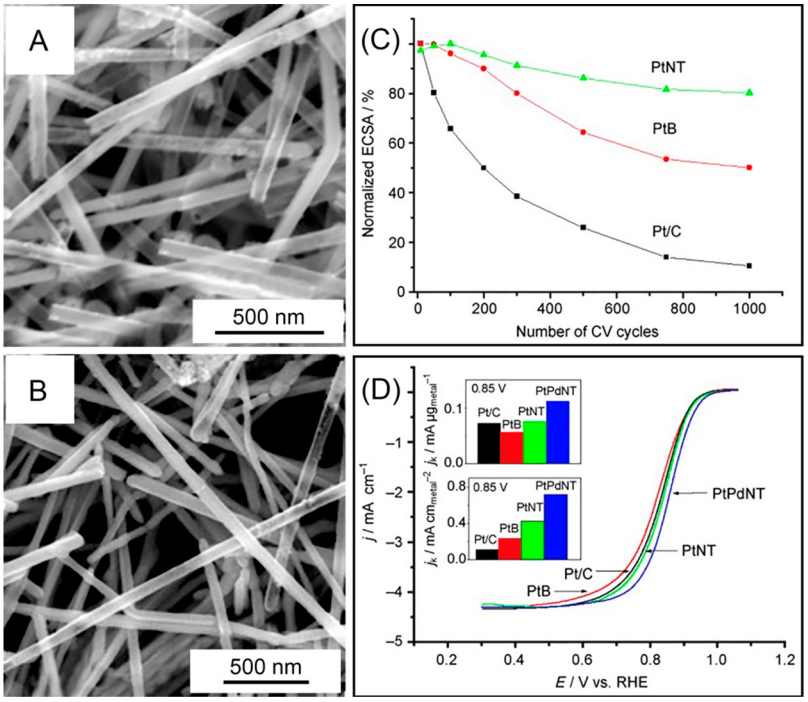

Figure 47. SEM images of (A) Pt and (B) PdPt nanotubes, respectively. (C) Loss of ECSA for Pt/C, Pt black, and Pt nanotubes as a function of the number of CV cycles. (D) ORR curves of Pt/C, Pt black, Pt nanotubes, and PdPt nanotubes in O_2-saturated 0.5 M H_2SO_4 solution at room temperature. Inset: Mass activity (top) and specific activity (bottom) for the four catalysts at 0.85 V. Reprinted with permission from ref 11. Copyright 2007 Wiley-VCH.

mass activity 3- and 23-fold higher than that of PtNWs/C and commercial Pt/C catalyst, respectively (Figure 46).[796] The authors showed the presence of Ni could reduce the bond strength between oxygen atoms and the surface of the NWs, and proposed this could enhance the ORR activity. Because of their low reduction potentials, nonprecious metals can also be removed after several potential cycles, resulting in a rough, Pt-enriched sheath with improved performance. Using FePtCu NRs as an example, the ternary alloy structures could be successfully converted into FePtCu@Pt core−sheath structures via selective dissolution of Fe and Cu from the surface after treatment with acetic acid and electrochemical etching in 0.1 M $HClO_4$. The core−sheath NRs with a Pt-enriched sheath exhibited mass and specific activities 6.3 and 4.4 times higher, respectively, than those of a commercial Pt/C catalyst. Furthermore, the durability test with the core−sheath NRs showed no degradation after 5000 cycles, with only a slight decrease in the Fe and Cu contents (1−2 atomic%).[810]

8.4.1.3. Hollow and Porous Structures. Increasing the surface area of 1D nanostructures provides another effective approach to further enhancing their catalytic performance. To this end, porous and hollow structures, such as nanotubes, generated from etching or galvanic replacement are promising materials.[816] It has been demonstrated that etching is initiated by oxidizing the metal atoms in the outermost layer of the sheath to generate vacancies, followed by diffusion of metal atoms from underlying layers to enlarge the vacancies. The hollow structure generated by etching not only provides a larger reactive surface area but also allows for efficient mass transport of both the products and reactants in and out of the catalytic system. In addition to etching, hollow structures can be produced through galvanic replacement that takes advantage of the difference in standard reduction potentials between two metals. The alloy structures and tunable compositions, which can be controlled by varying the number of metal ions introduced, allow for the optimization of catalytic activity for specific reactions. As an example, through galvanic replacement, porous Pt dendritic tubes were produced using Ag dendrites as a template. The hollow Pt dendrites showed a specific activity 4.4 times greater than that of a commercial Pt/C catalyst, which can be attributed to their large surface area and improved mass transport and gas diffusion.[817]

8.4.1.4. Support-Free Electrocatalysts. As briefly discussed at the beginning of this section, the corrosion of the carbon support is one of the major causes of the decrease in the catalyst activity, as it accelerates the detachment of catalytic particles from the carbon surface. It has also been explained in section 8.2 that a network of metal NWs is electrically conductive enough to be directly used as an electrocatalyst, making the carbon support unnecessary.

Support-free electrocatalysts were first developed with Pt- and Pt-based nanotubes.[11] In a typical protocol, AgNWs synthesized via the polyol method were used as a sacrificial template for the galvanic replacement with Pt(II) or Pt(II) and Pd(II) precursors to generate Pt or PtPd nanotubes (Figure 47). The diameter and the length of the nanotubes were 50 nm and 5−20 μm, respectively, and the shell thickness was controlled in the range of 4−7 nm. The ADT test revealed an enhanced stability for the nanotubes without carbon support when benchmarked Pt black and Pt/C. There was no remarkable change to the morphology of the Pt nanotubes after the ADT test, and the minor dissolution of Pt during the test led to a slight decrease in ECSA. Although the mass activity of Pt nanotubes was already higher than those of Pt/C and Pt black, PtPd nanotubes showed even greater mass and specific activities, which were 1.4× and 5.8× those of commercial Pt/C. The support-free Pt-based electrocatalysts have been further optimized to improve their stability and

DOI: 10.1021/acs.chemrev.8b00745
Chem. Rev. XXXX, XXX, XXX−XXX

activity, including the development of porous Pt nanotubes, PtPd alloyed nanotubes, and Cu@Pt core−sheath NWs.[94,818,819]

8.4.1.5. Summary. The high specific surface area, large contact area with the support, as well as the anisotropic morphology and the corresponding improvement in mass transport, all make 1D nanostructures attractive electrocatalysts toward ORR. At the current stage of development, their performance is still plagued by a number of shortcomings. For example, it is hard to precisely control the type of facet on 1D metal nanostructures, in particular, for those derived from attachment growth or galvanic replacement. In addition, the stability of 1D metal nanostructures is also a potential concern. As discussed in section 3, 1D metal nanostructures are highly vulnerable to oxidative etching, and they may break into short segments when exposed to a corrosive environment containing a strong acid and/or an oxidant.[97] Once broken, the segments tend to fuse together to generate relatively large particles through Ostwald ripening, leading to a sharp decrease in ECSA and thus electrocatalytic activity. Coating with carbon or with polymers may help improve the stability of electrocatalysts based on 1D metal nanostructures.[820−822]

8.4.2. Methanol Oxidation and Formic Acid Oxidation. The electrochemical oxidation of methanol is a two-step reaction that consists of fast oxidation of methanol to CO and the subsequent oxidation of CO to CO_2. To achieve superior catalytic activity, a higher conversion rate of methanol and better CO tolerance are both of great importance. Since catalysts based on pure Pt have weak tolerance against CO poisoning, many studies have been conducted to develop binary or ternary 1D nanostructures to provide a better catalytic activity and CO tolerance. In addition, to avoid problems such as carbon corrosion and particle detachment, support-free electrocatalysts based on NWs or nanotubes have also been applied to the MOR.

A good example of 1D alloy electrocatalysts for MOR is based on PtAgNWs.[823] In a standard protocol, PtAg NWs (6−20% of Ag atomic concentration) were synthesized via particle attachment in an aqueous solution. The as-prepared alloy NWs had a diameter of 6 nm and length of 2−3 μm. Although the ECSA of the PtAg NWs was smaller than that of the Pt/C catalyst, the mass activities were 3.8 and 3.6 times higher at 6 and 20 atomic% of Ag when compared with a Pt/C catalyst. Furthermore, the ratio of forward to backward current obtained from cyclic voltammetry showed that the PtAg NWs had a better CO tolerance than a Pt/C catalyst. The forward current is from the oxidation of methanol, and the backward current is from the oxidation of remaining CO on the surface of the catalyst. Therefore, the higher ratio of forward to backward current implies a superior tolerance to CO poisoning. The ratio for PtAg NWs was over 1.5, whereas that for Pt/C catalyst was around 1.1, demonstrating better CO tolerance of PtAg NWs than Pt/C. It was proposed that the codeposited Ag might decrease the Pt−CO bond strength by modifying the Pt 4*f* energy and assisted the formation of Pt active sites, leading to better CO tolerance and higher catalytic activity. A similar alloying effect which improved catalytic activity toward MOR and CO tolerance was also reported for other 1D nanostructures, including those based on PtRu,[824] PtNi,[825] PtCu,[784,826] PtCo,[827] PtFePd,[828] and PtRuCu.[824]

Among different types of 1D-structured catalysts, PtRu nanotubes and Cu@PtRu core−sheath NWs were explored as support-free electrocatalysts without using any carbon support for MOR.[783] In a typical protocol, CuNWs were first synthesized through the reduction of $Cu(NO_3)_2$ by hydrazine and EDA in a basic aqueous solution. The PtRu nanotubes and Cu@PtRu core−sheath NWs were then produced through complete and partial galvanic replacement with the as-prepared CuNWs. It was demonstrated that Cu@PtRu core−sheath NWs showed the highest specific activity, which was 3.2 and 5.5 times higher than those of the PtRu nanotubes and PtRu/C catalyst, respectively. Less current decay was also observed for the Cu@PtRu core−sheath NWs, revealing the higher stability of Cu@PtRu core−sheath NWs relative to PtRu nanotubes and PtRu/C.

For FOR, Pd and Pd-based nanostructures are most widely used as electrocatalysts.[829] Compared with 0D nanostructures, the higher stability and presence of more active facets for NWs and NRs lead to a major improvement in catalytic activity. For example, penta-twinned PdNWs supported on carbon showed a specific activity 5 times higher than that of commercial Pd/C.[96] The increase in surface strain caused by twin boundaries, together with the presence of {100} side faces, greatly improved the catalytic performance of PdNWs. In addition to pure Pd catalysts, PdAg NWs exhibited greatly enhanced electrocatalytic activity toward FOR with a larger oxidation current density, higher tolerance to CO poisoning, and more negative onset potential in comparison with a Pd/C catalyst.[387] When maintained at the same potential, the as-synthesized PdAg NWs also exhibited higher stability than commercial Pd/C in the chronoamperometric analyses. It is thought that oxygen-containing species adsorbed on the Ag sites can enhance the oxidation of formic acid adsorbed on nearby Pd sites. The synergistic effect between Pd and Ag greatly contributed to the enhanced catalytic performance, leading to an electronic structure and thus reactivity different from those of Pd nanostructures.[830,831]

8.4.3. CO_2 Reduction. Electrochemical reduction of CO_2 has received a lot of attention in recent years because of its potential to convert CO_2 into valuable chemical products. Metal electrocatalysts with various compositions, shapes, and structures have been applied to the electrochemical reduction of CO_2.[832] Although there are only a small number of reports on the application of 1D catalysts toward CO_2 reduction and the investigation of reaction mechanisms, 1D nanostructures can improve the electrocatalytic performance in a way similar to the cases of ORR and MOR.

Gold is one of the noble metals that are widely used as electrocatalysts for CO_2 reduction. Ultrathin AuNWs with a diameter of 2 nm and different lengths (15, 100, and 500 nm) were used to investigate the effect of the edge-to-corner ratio of NWs in CO_2 reduction.[833] Theoretical calculations indicated that the edge between two side faces of NWs was more active than the corner sites at the ends of the NWs. Therefore, when the total number of surface Au atoms was fixed, 1D NWs were more active than nanoparticles because of the existence of more edge sites and fewer corner sites. Further investigation revealed that both CO and COOH, an intermediate, preferentially bound to the edge sites on AuNWs. Compared to other Au nanostructures such as Au_{13} clusters and Au(211) surface, the adsorption of CO on the edge sites of a NW was weaker than on the corner sites of Au_{13}, while the adsorption of COOH on the edge sites of a NW was marginally stronger than that on the Au(211) surface. This result suggests that COOH could be activated on the edge sites of AuNWs, and the produced CO could be easily released from

DOI: 10.1021/acs.chemrev.8b00745
Chem. Rev. XXXX, XXX, XXX−XXX

the surface of NWs. As a result, a higher activity was observed with the ultrathin AuNWs compared to polycrystalline Au nanoparticles, and the longer NWs were more active than the shorter ones. Furthermore, the onset potential of CO_2 reduction for the NWs with a length of 500 nm was more positive than those for the shorter ones, and the faradaic efficiency for CO production also increased with the length of the AuNWs. These observations supported the hypothesis that the edge sites on NWs were more active than the corner sites.

In addition to Au, Cu-based catalysts have been extensively explored for CO_2 reduction.[800,834,835] Several products, including CO, methane, and ethylene, can be produced when Cu nanostructures are used as catalysts and the improvement in selectivity toward a specific product is one of the major efforts for this research. Penta-twinned CuNWs with a diameter of 20 nm have been investigated for the electrochemical reduction of CO_2.[834] It was observed that the difference between Cu foil and CuNWs were largely negligible at a relatively low overpotential. However, when the voltage was decreased to −1.25 V (versus RHE, reversible hydrogen electrode), the partial current for methane production significantly increased only with CuNWs. When the passed charge was below 1 C, methane was selectively produced with negligible formation of CO and ethylene. However, when the passed charge for CO_2 reduction was over 2 C, the main product was changed and a significant amount of ethylene was produced. This change in selectivity could be attributed to the morphological change to the CuNWs. Specifically, wire bundling, disintegration, and fracturing were all observed under TEM. It was further confirmed that the selectivity toward methane could be preserved by coating the CuNWs with RGO because of the suppression of morphology changes to the CuNWs.

8.4.4. Photoelectrochemical Cells. Metal NWs and their derivatives can also be used to fabricate transparent electrocatalysts because of their electrical conductivity, mechanical flexibility, and optical transparency. It was reported that CuNW networks could serve as transparent, flexible electrocatalysts for applications in PECs (Figure 48A and B).[836] Currently, most designs of PECs rely on the use of ITO coating as a transparent electrode onto which an active layer of catalyst is coated. However, in addition to the scarcity of indium, ITO is brittle and expensive, and it is not catalytically active toward most reactions such as water oxidation. As an attractive alternative to ITO, CuNWs can be directly deposited from solution at rates several orders of magnitude faster than gas-phase ITO sputtering, and their networks offer nearly the same level of optoelectric performance. Additionally, Cu is 425 times more abundant and 100 times cheaper than indium, making CuNWs more competitive and promising catalysts for PECs.

As shown in Figure 48C, while repeated catalytic waves for water oxidation could be observed with $E_{p,o}$ = 1.02 V versus normal hydrogen electrode (NHE) when a CuNW film was used as a catalyst, only a small oxygen evolution wave was obtained on an ITO electrode under identical conditions. Figure 48D shows the electrolysis process at a stable current density of 0.6 mA cm^{-2} at 1.2 V. After 2.5 h, about 13.2 μmol of O_2 was generated with a columbic efficiency as high as 94%. The CuNWs were intact after sustained water oxidation with only a slight increase in surface roughness, and the CuNW film maintained excellent optical (77%) and electrical (48 Ω sq^{-1}) properties. Higher current densities can be achieved with thicker layers of NWs at the expense of transmittance (Figure 48E). Once optimized in terms of the balance between transmittance and catalytic performance, films fabricated from metal NWs are generally much more flexible than that of ITO (Figure 48F). It was demonstrated that the sheet resistance of a film based on a CuNW network on polyethylene terephthalate (PETP) increased by only 4 times after 1000 bends. In comparison, for the ITO film on PET, the sheet resistance increased 400 times after just 250 bends. In addition to CuNWs, other mono- or multimetallic NWs have also been reported as potential transparent electrocatalysts, including PtCu alloy NWs and Ni-coated CuNWs.[837,838]

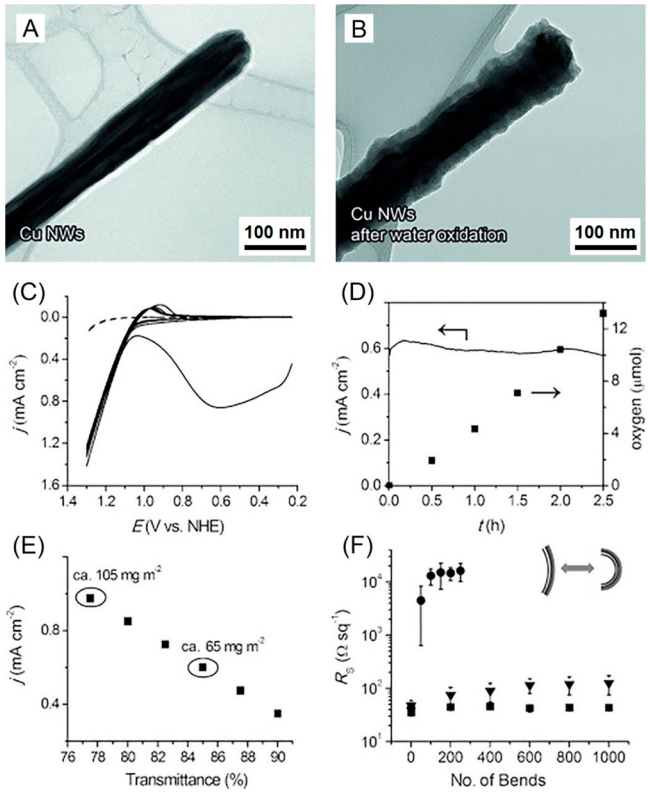

Figure 48. (A, B) TEM images of CuNWs (A) before and (B) after sustained water oxidation. (C) CVs (10 scan cycles) of a CuNW network on glass in 1 M Na_2CO_3. For comparison, a CV of an ITO electrode is shown as a dashed line. (D) Constant potential electrolysis with a CuNW network at 1.20 V vs NHE with 0.8 mM $CuSO_4$ added into the solution. (E) A plot of the transmittance of CuNW networks vs catalytic current density of water oxidation. (F) Plots of sheet resistance vs number of bends for ITO film (●), Cu NW film (■), and CuNW film after water oxidation (▼) on PET. Reprinted with permission from ref 836. Copyright 2007 Wiley-VCH.

9. CONCLUDING REMARKS

Over the last two decades, we have witnessed a staggering amount of progress in the synthesis, mechanistic understanding, processing, and application of 1D metal nanostructures, such that it is difficult to adequately summarize the field in a review article even as long as this one. Syntheses of 1D metal nanostructures have been reported for 23 different metals since the turn of the century; many of which have been refined or modified in hundreds of subsequent studies to improve control over the dimensions of the nanostructures, ensure reproducibility, as well as lower the cost[839] and environmental impact.[840−843] In many cases, the reason why

DOI: 10.1021/acs.chemrev.8b00745
Chem. Rev. XXXX, XXX, XXX−XXX

nanostructures made of metals with a cubic crystal lattice grow anisotropically remains poorly understood, but the advent of new analytical tools and methods is beginning to shed light on this mystery. In situ TEM, in particular, is offering new insights into how NRs or NWs can be assembled from isotropic nanoparticles, while in situ DFOM can be used to differentiate between growth pathways limited by mass- and charge-transfer, respectively. Single-crystal electrochemistry and computational simulations are providing unexpected surprises as to the explicit roles played by capping agents and halides in driving the anisotropic growth. We expect that additional studies with these and other analytical methods will continue to shed light on the facet-selective surface chemistry and reduction kinetics responsible for the anisotropic growth.

Improving the mechanistic understanding of nanostructure growth has the potential to make the development of new synthetic protocols much more efficient. For a given synthesis, one can change a myriad of variables, including (i) reaction temperature, (ii) concentration of the precursor to the metal, (iii) concentration of the reducing agent (or a precursor to the reducing agent), (iv) concentrations of capping agents/stabilizers, and (v) concentrations of halides and other types of additives. On top of these five variables, there are also many different types of capping agents, reducing agents, and precursors that one can choose for a synthesis, resulting in a variable space with a dimensionality in the hundreds. Having a better understanding of the factors that promote the anisotropic growth or affect the rate-limiting step can help reduce the variable space and/or enable more intelligent search algorithms, and thus accelerate the pace with which one can identify the optimal reaction conditions.

New applications, such as the use of AuNRs in imaging and medicine, and the use of Ag and Cu NWs for transparent electrodes and stretchable electronics, have motivated efforts for improved control over the length and diameter of these nanostructures, as well as the development of methods for scale-up syntheses. Applications in electrocatalysis have motivated the development of core−sheath and alloyed 1D nanostructures that improve the intrinsic activity of the nanostructures, as well as hollow and/or porous nanostructures that increase the specific surface area. Even with the most recent progress, there is still much room for improvement in control over the nanostructure's dimensions, composition, and uniformity. For example, whereas the length and diameter of AuNRs can be relatively uniform, those of Cu and Ag NRs or NWs still vary over a very broad range. Studies of the effect of the dimensions of Cu and Ag NWs might benefit from the development of a seed-mediated synthesis that could narrow the variations. The issue of structural control is, even more, pressing for studying the electrocatalytic properties of 1D metal nanostructures, in which the variation in either composition or shell thickness between particles makes it very challenging to develop definitive structure−property relationships. In this case, the development of methods for measuring the electrocatalytic properties of individual, well-characterized nanostructures may bring immediate advantages.[844]

The development of additional commercial applications for the 1D metal nanostructures is often limited by their high costs with respect to more mature materials, in addition to the small scales they are commonly produced. Figure 49A illustrates the progression for scaling up the production of Cu-based NWs from milligram to gram scale, enabling their use in the

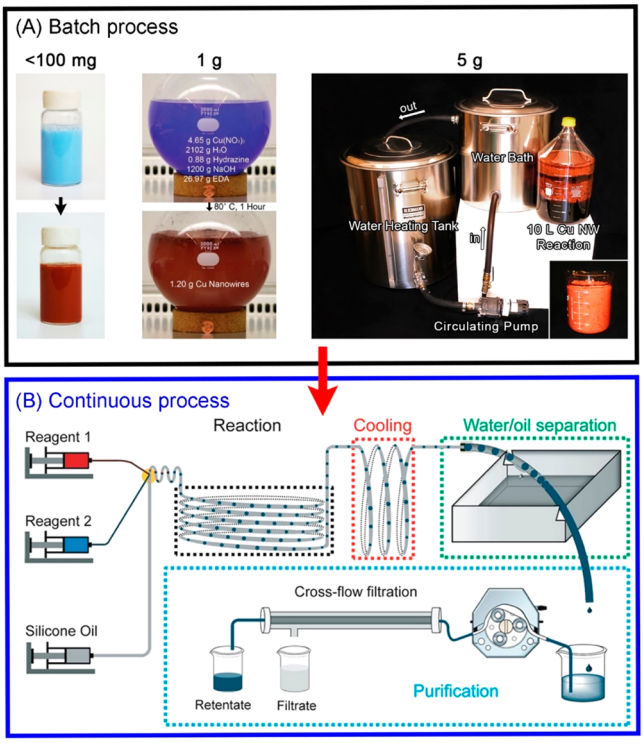

Figure 49. (A) Scale-up of CuNW synthesis from milligram to gram per batch. (B) Continuous flow reactor for scalable production of nanostructures. (A) Reprinted with permission from refs 168, 229, and 757 Copyright 2018 American Chemical Society, 2010 Wiley-VCH, and 2018 Wiley-VCH, respectively. (B) Reprinted with permission from ref 845. Copyright 2018 American Chemical Society.

fabrication and testing of conductive composites.[732,757] This approach simply involved the use of larger reaction vessels with moderate changes to the experimental conditions.[229,300,757] This approach to scale-up, however, can lead to greater heterogeneity for the products because it does not allow for the same degree of control over temperature as in a small-scale synthesis. An alternative approach to scale-up involve the use of continuous flow reactors.[845] Further integration of such a system with purification and recycling capabilities is expected to pave the way for the production of metal nanostructures at scales relevant to industrial applications. As demonstrated in a recent study, the droplet-reactor system shown in Figure 49B can be applied to the continuous and scalable production of Pd nanostructures. Aqueous droplets containing the reaction constituents were generated by flowing an aqueous phase containing the reactants and a carrier phase based on silicone oil (or air) in a polytetrafluoroethylene (PTFE) tube. The droplets passed through a mixing zone, followed by a heating zone to induce the nucleation and growth of nanostructures. After it passed through a cooling zone, the silicone oil selectively flowed through holes in the PTFE tube, achieving the separation of the carrier fluid for recycling. The solid products were then separated from the solvent through cross-flow filtration.

As most colloidal syntheses only produce about 1 g of nanostructures for every liter of reaction solution, they have a waste to product ratio of about 1000. This large volume of waste, and the need to use a new solvent for each synthesis, is the largest contributor to the high cost of nanostructures even made of earth-abundant metals. In addition, it makes the

DOI: 10.1021/acs.chemrev.8b00745
Chem. Rev. XXXX, XXX, XXX−XXX

production of 1D metal nanostructures a potential environmental hazard if this issue is not addressed at large scales. This problem could potentially be addressed through either process intensification, in which the same amount of product is produced in a much smaller reaction volume, or through integrated purification and recycling of the reaction solvent to reduce the volume of the waste stream. Currently, neither of these avenues are very active areas of research, but this is expected to change as more applications pull 1D metal nanostructures into the market at larger volumes.

Similarly, although the assessment of potential environmental impacts of nanomaterials has progressed dramatically over the past decade,[846−848] the possible adverse impacts of 1D metal nanostructures have received relatively little attention.[849] This makes sense given that most 1D nanostructures are yet to be used to any appreciable extent in commercial applications. To this end, AgNWs are perhaps the only 1D metal nanostructures currently used in consumer products, and as such AgNWs have received the most scrutiny.[849] Fortunately, work to date indicates that AgNWs are less toxic than Ag nanoparticles[850] or Ag ions,[851] suggesting that the relatively larger dimension of 1D nanostructures relative to nanoparticles or metal ions may serve to mitigate their environmental impact.[852] As other types of 1D nanostructures begin to enter commercial products, similar studies will be required to assess their potential ecological damage and determine their fate in the environment.

AUTHOR INFORMATION

Corresponding Authors

*E-mail: benjamin.wiley@duke.edu.
*E-mail: younan.xia@bme.gatech.edu.

ORCID

Zhiheng Lyu: 0000-0002-1343-4057
Younan Xia: 0000-0003-2431-7048

Author Contributions

#D.H., M.J.K., Z.L., and Y.S. contributed equally to the preparation of this Review.

Notes

The authors declare no competing financial interest.

Biographies

Da Huo received his B.S. in 2010 and Ph.D. in 2015 with Prof. Yong Hu, both in Materials Science and Engineering, from Nanjing University, China. Since 2015, he has been working as a postdoctoral fellow in the Xia group at the Georgia Institute of Technology. His research interests include the development of gold-based nanomedicines and understanding of their interactions with cells and their behaviors upon entering cells.

Myung Jun Kim received his B.S. from Seoul National University in 2007. He obtained his Ph.D. in Chemical and Biological Engineering from the same university in 2013 after studying electrochemical deposition of metals and alloys under Prof. Jae Jeong Kim. He continued this research as a postdoctoral researcher in the same university at the Research Center for Energy Conversion and Storage (RCECS) and the Institute of Chemical Process (ICP) from 2013−2015. Since 2016, he has been exploring the growth mechanism of anisotropic metal nanostructures and the applications of metal nanowires to electrosynthesis as a postdoctoral fellow in the Wiley group at Duke University.

Zhiheng Lyu received her B.S. from the University of Science and Technology of China in 2016, where she worked on noble-metal nanocrystals for photocatalysis. She is pursuing her Ph.D. in Chemistry and Biochemistry at the Georgia Institute of Technology under the supervision of Prof. Xia. Her research interest includes shape-controlled synthesis of metal nanocrystals and their utilization for energy-related applications.

Yifeng Shi received her B.S. in 2017 from Sichuan University, China. She is pursuing her Ph.D. in Chemical and Biomolecular Engineering at the Georgia Institute of Technology under the supervision of Prof. Xia. Her research interest includes shape-controlled synthesis of metal nanocrystals for heterogeneous catalysis and related applications.

Benjamin J. Wiley is an Associate Professor in the Department of Chemistry at Duke University. He received his B.S. from the University of Minnesota in 2003, and his Ph.D. in Chemical Engineering from the University of Washington, Seattle, in 2007 (with Xia). From 2007−2009, he was a postdoctoral fellow at Harvard University (with Whitesides). His current research focuses on sustainable, economical synthesis of nanostructures, understanding the processes that drive anisotropic growth of nanostructures, and elucidating the structure−property relationship of nanostructures and nanostructured composites for applications in electronics, medicine, and electrochemistry.

Younan Xia received his B.S. from the University of Science and Technology of China in 1987, and his Ph.D. in Physical Chemistry from Harvard University in 1996 (with Whitesides). He started as an Assistant Professor of Chemistry at the University of Washington, Seattle, in 1997 and then joined the Department of Biomedical Engineering at Washington University in St. Louis in 2007 as the James M. McKelvey Professor. Since 2012, he has held the position of Brock Family Chair and GRA Eminent Scholar in Nanomedicine at the Georgia Institute of Technology. He has served as an Associate Editor of Nano Letters since 2012.

ACKNOWLEDGMENTS

The work from the Xia group was supported in part by the NSF (DMR-0804088, DMR-1215034, DMR-1505400, and CHE-1505441) and startup funds from the Georgia Institute of Technology and Washington University in St. Louis. The work from the Wiley group was supported in part by the NSF (DMR-1253534 and CHE-1808108).

ABBREVIATIONS

0D	zero-dimensional
1D	one-dimensional
2D	two-dimensional
AAO	anodic aluminum oxide
ACA	1-adamantanecarboxylic acid
acac	acetylacetonate
ADT	accelerated durability test
AFM	atomic force microscopy
ALD	atomic layer deposition
anti-EGFR	anti-epidermal growth factor receptor
AR	aspect ratio
BDAC	benzyldimethylhexadecylammonium chloride
BET measurements	Brunauer−Emmet−Teller measurements
CMC	critical micelle concentration
CNT	carbon nanotube
CPC	cetylpyridinium chloride
CPU	central processing unit

DOI: 10.1021/acs.chemrev.8b00745
Chem. Rev. XXXX, XXX, XXX−XXX

CTA^+	cetyltrimethylammonium ion
CTAB	cetyltrimethylammonium bromide
CTAC	cetyltrimethylammonium chloride
DDA	discrete dipole approximation
DEG	diethylene glycol
DFOM	dark-field optical microscopy
DFT	density functional theory
DLVO theory	Derjaguin, Landau, Verwey, and Overbeek theory
DMAB	dimethylamine borane
DMF	dimethylformamide
DODAC	dioctadecyldimethylammonium chloride
DTAB	dodecyltrimethylammonium bromide
ECSA	electrochemically active surface area
EDA	ethylenediamine
EG	ethylene glycol
EMI	electromagnetic interference
EPR	enhanced permeation and retention
EQCM	electrochemical quartz crystal microbalance
fcc	face-centered cubic
FDTD	finite difference time domain
FEM	finite element method
FOR	formic acid oxidation reaction
FT-IR	Fourier-transform infrared spectroscopy
FTO	fluorine-doped tin oxide
GO	graphene oxide
H_2Asc	ascorbic acid
hcp	hexagonal close-packed
HDA	hexadecylamine
HDT	hexadecanethiol
HRTEM	high-resolution transmission electron microscopy
HSAB theory	hard and soft acids and bases theory
ICP-MS	inductively coupled plasma mass spectrometry
IPA	isopropyl alcohol
ITO	indium tin oxide
LBL	layer-by-layer
LSPR	localized surface plasmon resonance
MD	molecular dynamics
MOF	metal-organic framework
MOR	methanol oxidation reaction
MPE	maximal permissible exposure
Na_3CA	trisodium citrate
NHE	normal hydrogen electrode
NR	nanorod
NW	nanowire
OA	oleic acid
OAc	acetate
OCT	optical coherence tomography
ODA	octadecylamine
OER	oxygen evolution reaction
OLA	oleylamine
OLED	organic light-emitting diode
OPV	organic photovoltaic
ORR	oxygen reduction reaction
PAH	poly(allylamine hydrochloride)
PAT	photoacoustic tomography
PDDA	poly(diallyldimethylammonium) chloride
PDMS	polydimethylsiloxane
PDT	photodynamic therapy
PEC	photoelectrochemical cell
PEDOT	poly(3,4-ethylenedioxythiophene)
PEO	poly(ethylene oxide)
PET	positron emission tomography
PETP	polyethylene terephthalate
PMB-Cl	poly(methacryloyloxyethyl dimethylbenzylammonium chloride)
PSS	poly(styrenesulfonate)
PTFE	polytetrafluoroethylene
PT-OCT	photothermal optical coherence tomography
PVP	poly(vinylpyrrolidone)
RGO	reduced graphene oxide
RHE	reversible hydrogen electrode
RI	refractive index
RIU	refractive index unit
SAED	selected area electron diffraction
SAM	self-assembled monolayer
SAXS	small-angle X-ray scattering
SBS	styrene−butadiene−styrene
SDBS	sodium dodecyl benzenesulfonate
SDS	sodium dodecyl sulfate
SEM	scanning electron microscopy
SERS	surface-enhanced Raman scattering
SHE	standard hydrogen electrode
SLS	solution−liquid−solid
SPR	surface plasmon resonance
TBAB	*tert*-butylamine borane
TDA	tetradecylamine
TEG	tri(ethylene glycol)
TTEG	tetra(ethylene glycol)
TEM	transmission electron microscopy
TEOS	tetraethoxysilane
TIM	thermal interface material
TMEDA	tetramethylenediamine
TMV	tobacco mosaic virus
TPAF	two-photon autofluorescence
TPF	two-photon fluorescence
TPL	two-photon luminescence
TXM	transmission X-ray microscopy
UPD	underpotential deposition
XANES	X-ray absorption near-edge structure
XRD	X-ray diffraction

REFERENCES

(1) Xia, Y.; Yang, P.; Sun, Y.; Wu, Y.; Mayers, B.; Gates, B.; Yin, Y.; Kim, F.; Yan, H. One-Dimensional Nanostructures: Synthesis, Characterization, and Applications. *Adv. Mater.* **2003**, *15*, 353−389.

(2) Alkilany, A. M.; Lohse, S. E.; Murphy, C. J. The Gold Standard: Gold Nanoparticle Libraries to Understand the Nano−Bio Interface. *Acc. Chem. Res.* **2013**, *46*, 650−661.

(3) Yang, X.; Yang, M.; Pang, B.; Vara, M.; Xia, Y. Gold Nanomaterials at Work in Biomedicine. *Chem. Rev.* **2015**, *115*, 10410−10488.

(4) Ye, S.; Rathmell, A. R.; Chen, Z.; Stewart, I. E.; Wiley, B. J. Metal Nanowire Networks: The Next Generation of Transparent Conductors. *Adv. Mater.* **2014**, *26*, 6670−6687.

(5) Guo, C. F.; Ren, Z. Flexible Transparent Conductors Based on Metal Nanowire Networks. *Mater. Today* **2015**, *18*, 143−154.

(6) Lu, A.; Salabas, E. L.; Schüth, F. Magnetic Nanoparticles: Synthesis, Protection, Functionalization, and Application. *Angew. Chem., Int. Ed.* **2007**, *46*, 1222−1244.

(7) Jeong, U.; Teng, X.; Wang, Y.; Yang, H.; Xia, Y. Superparamagnetic Colloids: Controlled Synthesis and Niche Applications. *Adv. Mater.* **2007**, *19*, 33−60.

DOI: 10.1021/acs.chemrev.8b00745
Chem. Rev. XXXX, XXX, XXX−XXX

(8) Jana, N. R.; Gearheart, L.; Murphy, C. J. Seed-Mediated Growth Approach for Shape-Controlled Synthesis of Spheroidal and Rod-like Gold Nanoparticles Using a Surfactant Template. *Adv. Mater.* **2001**, *13*, 1389−1393.
(9) Sun, Y.; Gates, B.; Mayers, B.; Xia, Y. Crystalline Silver Nanowires by Soft Solution Processing. *Nano Lett.* **2002**, *2*, 165−168.
(10) Huang, X.; Neretina, S.; El-Sayed, M. A. Gold Nanorods: From Synthesis and Properties to Biological and Biomedical Applications. *Adv. Mater.* **2009**, *21*, 4880−4910.
(11) Chen, Z.; Waje, M.; Li, W.; Yan, Y. Supportless Pt and PtPd Nanotubes as Electrocatalysts for Oxygen-Reduction Reactions. *Angew. Chem., Int. Ed.* **2007**, *46*, 4060−4063.
(12) Lu, Y.; Du, S.; Steinberger-Wilckens, R. One-Dimensional Nanostructured Electrocatalysts for Polymer Electrolyte Membrane Fuel Cells—A Review. *Appl. Catal., B* **2016**, *199*, 292−314.
(13) Li, H.; Ma, S.; Fu, Q.; Liu, X.; Wu, L.; Yu, S. Scalable Bromide-Triggered Synthesis of Pd@Pt Core-Shell Ultrathin Nanowires with Enhanced Electrocatalytic Performance toward Oxygen Reduction Reaction. *J. Am. Chem. Soc.* **2015**, *137*, 7862−7868.
(14) Park, J.; Choi, S.; Janardhan, A. H.; Lee, S.-Y.; Raut, S.; Soares, J.; Shin, K.; Yang, S.; Lee, C.; Kang, K.-W.; et al. Electromechanical Cardioplasty Using a Wrapped Elasto-Conductive Epicardial Mesh. *Sci. Transl. Med.* **2016**, *8*, 344ra86.
(15) Kim, K. K.; Hong, S.; Cho, H. M.; Lee, J.; Suh, Y. D.; Ham, J.; Ko, S. H. Highly Sensitive and Stretchable Multidimensional Strain Sensor with Prestrained Anisotropic Metal Nanowire Percolation Networks. *Nano Lett.* **2015**, *15*, 5240−5247.
(16) Hsu, P.-C.; Liu, X.; Liu, C.; Xie, X.; Lee, H. R.; Welch, A. J.; Zhao, T.; Cui, Y. Personal Thermal Management by Metallic Nanowire-Coated Textile. *Nano Lett.* **2015**, *15*, 365−371.
(17) Cambrios Film Solutions. https://www.cambrios.com/.
(18) Liao, H.-G.; Cui, L.; Whitelam, S.; Zheng, H. Real-Time Imaging of Pt_3Fe Nanorod Growth in Solution. *Science* **2012**, *336*, 1011−1014.
(19) Ye, S.; Chen, Z.; Ha, Y.-C.; Wiley, B. J. Real-Time Visualization of Diffusion-Controlled Nanowire Growth in Solution. *Nano Lett.* **2014**, *14*, 4671−4676.
(20) Kim, M. J.; Alvarez, S.; Chen, Z.; Fichthorn, K. A.; Wiley, B. J. Single-Crystal Electrochemistry Reveals Why Metal Nanowires Grow. *J. Am. Chem. Soc.* **2018**, *140*, 14740−14746.
(21) Almora-Barrios, N.; Novell-Leruth, G.; Whiting, P.; Liz-Marzán, L. M.; López, N. Theoretical Description of the Role of Halides, Silver, and Surfactants on the Structure of Gold Nanorods. *Nano Lett.* **2014**, *14*, 871−875.
(22) Meena, S. K.; Sulpizi, M. Understanding the Microscopic Origin of Gold Nanoparticle Anisotropic Growth from Molecular Dynamics Simulations. *Langmuir* **2013**, *29*, 14954−14961.
(23) Meena, S. K.; Celiksoy, S.; Schäfer, P.; Henkel, A.; Sönnichsen, C.; Sulpizi, M. The Role of Halide Ions in the Anisotropic Growth of Gold Nanoparticles: A Microscopic, Atomistic Perspective. *Phys. Chem. Chem. Phys.* **2016**, *18*, 13246−13254.
(24) Ni, W.; Kou, X.; Yang, Z.; Wang, J. Tailoring Longitudinal Surface Plasmon Wavelengths, Scattering and Absorption Cross Sections of Gold Nanorods. *ACS Nano* **2008**, *2*, 677−686.
(25) Burgin, J.; Florea, I.; Majimel, J.; Dobri, A.; Ersen, O.; Tréguer-Delapierre, M. 3D Morphology of Au and Au@Ag Nanobipyramids. *Nanoscale* **2012**, *4*, 1299−1303.
(26) Chang, H.-H.; Murphy, C. J. Mini Gold Nanorods with Tunable Plasmonic Peaks beyond 1000 nm. *Chem. Mater.* **2018**, *30*, 1427−1435.
(27) Mahmoud, M. A.; El-Sayed, M. A. Different Plasmon Sensing Behavior of Silver and Gold Nanorods. *J. Phys. Chem. Lett.* **2013**, *4*, 1541−1545.
(28) Mayer, K. M.; Hafner, J. H. Localized Surface Plasmon Resonance Sensors. *Chem. Rev.* **2011**, *111*, 3828−3857.
(29) Mutiso, R. M.; Sherrott, M. C.; Rathmell, A. R.; Wiley, B. J.; Winey, K. I. Integrating Simulations and Experiments to Predict Sheet Resistance and Optical Transmittance in Nanowire Films for Transparent Conductors. *ACS Nano* **2013**, *7*, 7654−7663.
(30) Mertens, S.; Moore, C. Continuum Percolation Thresholds in Two Dimensions. *Phys. Rev. E* **2012**, *86*, 61109.
(31) Mutiso, R. M.; Sherrott, M. C.; Li, J.; Winey, K. I. Simulations and Generalized Model of the Effect of Filler Size Dispersity on Electrical Percolation in Rod Networks. *Phys. Rev. B: Condens. Matter Mater. Phys.* **2012**, *86*, 214306.
(32) White, S. I.; Mutiso, R. M.; Vora, P. M.; Jahnke, D.; Hsu, S.; Kikkawa, J. M.; Li, J.; Fischer, J. E.; Winey, K. I. Electrical Percolation Behavior in Silver Nanowire-Polystyrene Composites: Simulation and Experiment. *Adv. Funct. Mater.* **2010**, *20*, 2709−2716.
(33) Zheng, Y.; Tao, J.; Liu, H.; Zeng, J.; Yu, T.; Ma, Y.; et al. Facile Synthesis of Gold Nanorice Enclosed by High-Index Facets and Its Application for CO Oxidation. *Small* **2011**, *7*, 2307−2312.
(34) Ruditskiy, A.; Vara, M.; Huang, H.; Xia, Y. Oxidative Etching of Pd Decahedral Nanocrystals with a Penta-Twinned Structure and Its Impact on Their Growth Behavior. *Chem. Mater.* **2017**, *29*, 5394−5400.
(35) Wiley, B.; Herricks, T.; Sun, Y.; Xia, Y. Polyol Synthesis of Silver Nanoparticles: Use of Chloride and Oxygen to Promote the Formation of Single-Crystal, Truncated Cubes and Tetrahedrons. *Nano Lett.* **2004**, *4*, 1733−1739.
(36) Yang, T.-H.; Gilroy, K. D.; Xia, Y. Reduction Rate as a Quantitative Knob for Achieving Deterministic Synthesis of Colloidal Metal Nanocrystals. *Chem. Sci.* **2017**, *8*, 6730−6749.
(37) Xia, Y.; Xiong, Y.; Lim, B.; Skrabalak, S. E. Shape-Controlled Synthesis of Metal Nanocrystals: Simple Chemistry Meets Complex Physics? *Angew. Chem., Int. Ed.* **2009**, *48*, 60−103.
(38) Xiong, Y.; Cai, H.; Wiley, B. J.; Wang, J.; Kim, M. J.; Xia, Y. Synthesis and Mechanistic Study of Palladium Nanobars and Nanorods. *J. Am. Chem. Soc.* **2007**, *129*, 3665−3675.
(39) Wiley, B. J.; Chen, Y.; McLellan, J. M.; Xiong, Y.; Li, Z.-Y.; Ginger, D.; Xia, Y. Synthesis and Optical Properties of Silver Nanobars and Nanorice. *Nano Lett.* **2007**, *7*, 1032−1036.
(40) Zhang, Q.; Moran, C. H.; Xia, X.; Rycenga, M.; Li, N.; Xia, Y. Synthesis of Ag Nanobars in the Presence of Single-Crystal Seeds and a Bromide Compound, and Their Surface-Enhanced Raman Scattering (SERS) Properties. *Langmuir* **2012**, *28*, 9047−9054.
(41) Wang, Z. L.; Mohamed, M. B.; Link, S.; El-Sayed, M. A. Crystallographic Facets and Shapes of Gold Nanorods of Different Aspect Ratios. *Surf. Sci.* **1999**, *440*, L809−L814.
(42) Wang, Z. L.; Gao, R. P.; Nikoobakht, B.; El-Sayed, M. A. Surface Reconstruction of the Unstable {110} Surface in Gold Nanorods. *J. Phys. Chem. B* **2000**, *104*, 5417−5420.
(43) Carbó-Argibay, E.; Rodríguez-González, B.; Gómez-Graña, S.; Guerrero-Martínez, A.; Pastoriza-Santos, I.; Pérez-Juste, J.; Liz-Marzán, L. M. The Crystalline Structure of Gold Nanorods Revisited: Evidence for Higher-Index Lateral Facets. *Angew. Chem., Int. Ed.* **2010**, *49*, 9397−9400.
(44) Goris, B.; Bals, S.; Van Den Broek, W.; Carbó-Argibay, E.; Gómez-Graña, S.; Liz-Marzán, L. M.; Van Tendeloo, G. Atomic-Scale Determination of Surface Facets in Gold Nanorods. *Nat. Mater.* **2012**, *11*, 930−935.
(45) Pan, Z. W.; Dai, Z. R.; Wang, Z. L. Nanobelts of Semiconducting Oxides. *Science* **2001**, *291*, 1947−1949.
(46) Wiley, B. J.; Wang, Z.; Wei, J.; Yin, Y.; Cobden, D. H.; Xia, Y. Synthesis and Electrical Characterization of Silver Nanobeams. *Nano Lett.* **2006**, *6*, 2273−2278.
(47) Sun, Y.; Mayers, B.; Herricks, T.; Xia, Y. Polyol Synthesis of Uniform Silver Nanowires: A Plausible Growth Mechanism and the Supporting Evidence. *Nano Lett.* **2003**, *3*, 955−960.
(48) Zhang, S.-H.; Jiang, Z.-Y.; Xie, Z.-X.; Xu, X.; Huang, R.-B.; Zheng, L.-S. Growth of Silver Nanowires from Solutions: A Cyclic Penta-Twinned-Crystal Growth Mechanism. *J. Phys. Chem. B* **2005**, *109*, 9416−9421.
(49) Da Silva, R. R.; Yang, M.; Choi, S. Il; Chi, M.; Luo, M.; Zhang, C.; Li, Z.-Y.; Camargo, P. H. C.; Ribeiro, S. J. L.; Xia, Y. Facile Synthesis of Sub-20 nm Silver Nanowires through a Bromide-Mediated Polyol Method. *ACS Nano* **2016**, *10*, 7892−7900.

DOI: 10.1021/acs.chemrev.8b00745
Chem. Rev. XXXX, XXX, XXX−XXX

(50) Carbó-Argibay, E.; Rodríguez-González, B.; Pastoriza-Santos, I.; Pérez-Juste, J.; Liz-Marzán, L. M. Growth of Pentatwinned Gold Nanorods into Truncated Decahedra. *Nanoscale* **2010**, *2*, 2377−2383.
(51) Johnson, C. J.; Dujardin, E.; Davis, S. A.; Murphy, C. J.; Mann, S. Growth and Form of Gold Nanorods Prepared by Seed-Mediated, Surfactant-Directed Synthesis. *J. Mater. Chem.* **2002**, *12*, 1765−1770.
(52) Seo, D.; Park, J. H.; Jung, J.; Park, S. M.; Ryu, S.; Kwak, J.; Song, H. One-Dimensional Gold Nanostructures through Directed Anisotropic Overgrowth from Gold Decahedrons. *J. Phys. Chem. C* **2009**, *113*, 3449−3454.
(53) Jin, M.; He, G.; Zhang, H.; Zeng, J.; Xie, Z.; Xia, Y. Shape-Controlled Synthesis of Copper Nanocrystals in an Aqueous Solution with Glucose as a Reducing Agent and Hexadecylamine as a Capping Agent. *Angew. Chem., Int. Ed.* **2011**, *50*, 10560−10564.
(54) Luo, M.; Zhou, M.; Rosa da Silva, R.; Tao, J.; Figueroa-Cosme, L.; Gilroy, K. D.; Peng, H.-C.; He, Z.; Xia, Y. Pentatwinned Cu Nanowires with Ultrathin Diameters below 20 nm and Their Use as Templates for the Synthesis of Au-Based Nanotubes. *ChemNanoMat* **2017**, *3*, 190−195.
(55) Yang, H. J.; He, S. Y.; Tuan, H. Y. Self-Seeded Growth of Five-Fold Twinned Copper Nanowires: Mechanistic Study, Characterization, and SERS Applications. *Langmuir* **2014**, *30*, 602−610.
(56) Luo, M.; Huang, H.; Choi, S.; Zhang, C.; Rosa da Silva, R.; Peng, H.-C.; Li, Z.; Liu, J.; He, Z.; Xia, Y. Facile Synthesis of Ag Nanorods with No Plasmon Resonance Peak in the Visible Region by Using Pd Decahedra of 16 nm in Size as Seeds. *ACS Nano* **2015**, *9*, 10523−10532.
(57) Peng, Z.; You, H.; Yang, H. Composition-Dependent Formation of Platinum Silver Nanowires. *ACS Nano* **2010**, *4*, 1501−1510.
(58) Ma, Y.; Gao, W.; Shan, H.; Chen, W.; Shang, W.; Tao, P.; Song, C.; Addiego, C.; Deng, T.; Pan, X.; et al. Platinum-Based Nanowires as Active Catalysts toward Oxygen Reduction Reaction: In Situ Observation of Surface-Diffusion-Assisted, Solid-State Oriented Attachment. *Adv. Mater.* **2017**, *29*, 1703460.
(59) Liang, H.; Zhao, H.; Rossouw, D.; Wang, W.; Xu, H.; Botton, G. A.; Ma, D. Silver Nanorice Structures: Oriented Attachment-Dominated Growth, High Environmental Sensitivity, and Real-Space Visualization of Multipolar Resonances. *Chem. Mater.* **2012**, *24*, 2339−2346.
(60) Zhu, C.; Peng, H.-C.; Zeng, J.; Liu, J.; Gu, Z.; Xia, Y. Facile Synthesis of Gold Wavy Nanowires and Investigation of Their Growth Mechanism. *J. Am. Chem. Soc.* **2012**, *134*, 20234−20237.
(61) Yu, X.; Wang, D.; Peng, Q.; Li, Y. Pt-M (M = Cu, Co, Ni, Fe) Nanocrystals: From Small Nanoparticles to Wormlike Nanowires by Oriented Attachment. *Chem. - Eur. J.* **2013**, *19*, 233−239.
(62) Aabdin, Z.; Lu, J.; Zhu, X.; Anand, U.; Loh, N. D.; Su, H.; Mirsaidov, U. Bonding Pathways of Gold Nanocrystals in Solution. *Nano Lett.* **2014**, *14*, 6639−6643.
(63) Wang, Y.; Choi, S.-I.; Zhao, X.; Xie, S.; Peng, H.-C.; Chi, M.; Huang, C. Z.; Xia, Y. Polyol Synthesis of Ultrathin Pd Nanowires via Attachment-Based Growth and Their Enhanced Activity towards Formic Acid Oxidation. *Adv. Funct. Mater.* **2014**, *24*, 131−139.
(64) Welch, D. A.; Woehl, T. J.; Park, C.; Faller, R.; Evans, J. E.; Browning, N. D. Understanding the Role of Solvation Forces on the Preferential Attachment of Nanoparticles in Liquid. *ACS Nano* **2016**, *10*, 181−187.
(65) Yu, Y.; Cui, F.; Sun, J.; Yang, P. Atomic Structure of Ultrathin Gold Nanowires. *Nano Lett.* **2016**, *16*, 3078−3084.
(66) Takahata, R.; Yamazoe, S.; Koyasu, K.; Tsukuda, T. Structural Model of Ultrathin Gold Nanorods Based on High-Resolution Transmission Electron Microscopy: Twinned 1D Oligomers of Cuboctahedrons. *J. Phys. Chem. C* **2017**, *121*, 10942−10947.
(67) Soumare, Y.; Piquemal, J.-Y.; Maurer, T.; Ott, F.; Chaboussant, G.; Falqui, A.; Viau, G. Oriented Magnetic Nanowires with High Coercivity. *J. Mater. Chem.* **2008**, *18*, 5696−5702.
(68) Desantis, C. J.; Skrabalak, S. E. Core Values: Elucidating the Role of Seed Structure in the Synthesis of Symmetrically Branched Nanocrystals. *J. Am. Chem. Soc.* **2013**, *135*, 10−13.
(69) Weiner, R. G.; Desantis, C. J.; Cardoso, M. B. T.; Skrabalak, S. E. Diffusion and Seed Shape: Intertwined Parameters in the Synthesis of Branched Metal Nanostructures. *ACS Nano* **2014**, *8*, 8625−8635.
(70) Lee, H.; Manorotkul, W.; Lee, J.; Kwon, J.; Suh, Y. D.; Paeng, D.; Grigoropoulos, C. P.; Han, S.; Hong, S.; Yeo, J.; et al. Nanowire-on-Nanowire: All-Nanowire Electronics by On-Demand Selective Integration of Hierarchical Heterogeneous Nanowires. *ACS Nano* **2017**, *11*, 12311−12317.
(71) Lee, H.; Yeo, J.; Lee, J.; Cho, H.; Kwon, J.; Han, S.; Kim, S.; Hong, S.; Ko, S. H. Selective Thermochemical Growth of Hierarchical ZnO Nanowire Branches on Silver Nanowire Backbone Percolation Network Heaters. *J. Phys. Chem. C* **2017**, *121*, 22542−22549.
(72) Lu, Q.; Wang, A.-L.; Gong, Y.; Hao, W.; Cheng, H.; Chen, J.; Li, B.; Yang, N.; Niu, W.; Wang, J.; et al. Crystal Phase-Based Epitaxial Growth of Hybrid Noble Metal Nanostructures on 4H/fcc Au Nanowires. *Nat. Chem.* **2018**, *10*, 456−461.
(73) Seo, D.; Yoo, C. I.; Jung, J.; Song, H. Ag-Au-Ag Heterometallic Nanorods Formed through Directed Anisotropic Growth. *J. Am. Chem. Soc.* **2008**, *130*, 2940−2941.
(74) Kim, S.; Kim, S. K.; Park, S. Bimetallic Gold-Silver Nanorods Produce Multiple Surface Plasmon Bands. *J. Am. Chem. Soc.* **2009**, *131*, 8380−8381.
(75) Yang, Y.; Wang, W.; Li, X.; Chen, W.; Fan, N.; Zou, C.; Chen, X.; Xu, X.; Zhang, L.; Huang, S. Controlled Growth of Ag/Au Bimetallic Nanorods through Kinetics Control. *Chem. Mater.* **2013**, *25*, 34−41.
(76) Li, C.; Sun, L.; Sun, Y.; Teranishi, T. One-Pot Controllable Synthesis of Au@Ag Heterogeneous Nanorods with Highly Tunable Plasmonic Absorption. *Chem. Mater.* **2013**, *25*, 2580−2590.
(77) Mayer, M.; Scarabelli, L.; March, K.; Altantzis, T.; Tebbe, M.; Kociak, M.; Bals, S.; Garciá De Abajo, F. J.; Fery, A.; Liz-Marzán, L. M. Controlled Living Nanowire Growth: Precise Control over the Morphology and Optical Properties of AgAuAg Bimetallic Nanowires. *Nano Lett.* **2015**, *15*, 5427−5437.
(78) Xu, L.; Wang, K.; Jiang, B.; Chen, W.; Liu, F.; Hao, H.; Zou, C.; Yang, Y.; Huang, S. Competitive Effect in the Growth of Pd-Au-Pd Segmental Nanorods. *Chem. Mater.* **2016**, *28*, 7394−7403.
(79) Camargo, P. H. C.; Xiong, Y.; Ji, L.; Zuo, J. M.; Xia, Y. Facile Synthesis of Tadpole-like Nanostructures Consisting of Au Heads and Pd Tails. *J. Am. Chem. Soc.* **2007**, *129*, 15452−15453.
(80) Huang, J.; Zhu, Y.; Lin, M.; Wang, Q.; Zhao, L.; Yang, Y.; Yao, K. X.; Han, Y. Site-Specific Growth of Au-Pd Alloy Horns on Au Nanorods: A Platform for Highly Sensitive Monitoring of Catalytic Reactions by Surface Enhancement Raman Spectroscopy. *J. Am. Chem. Soc.* **2013**, *135*, 8552−8561.
(81) Zheng, Z.; Tachikawa, T.; Majima, T. Single-Particle Study of Pt-Modified Au Nanorods for Plasmon-Enhanced Hydrogen Generation in Visible to Near-Infrared Region. *J. Am. Chem. Soc.* **2014**, *136*, 6870−6873.
(82) Zheng, Z.; Tachikawa, T.; Majima, T. Plasmon-Enhanced Formic Acid Dehydrogenation Using Anisotropic Pd-Au Nanorods Studied at the Single-Particle Level. *J. Am. Chem. Soc.* **2015**, *137*, 948−957.
(83) Yin, Y.; Yang, Y.; Zhang, L.; Li, Y.; Li, Z.; Lei, W.; Ma, Y.; Huang, Z. Facile Synthesis of Au/Pd Nano-Dogbones and Their Plasmon-Enhanced Visible-to-NIR Light Photocatalytic Performance. *RSC Adv.* **2017**, *7*, 36923−36928.
(84) Sun, Y.; Tao, Z.; Chen, J.; Herricks, T.; Xia, Y. Ag Nanowires Coated with Ag/Pd Alloy Sheaths and Their Use as Substrates for Reversible Absorption and Desorption of Hydrogen. *J. Am. Chem. Soc.* **2004**, *126*, 5940−5941.
(85) Zhang, S.; Zeng, H. C. Solution-Based Epitaxial Growth of Magnetically Responsive Cu@Ni Nanowires. *Chem. Mater.* **2010**, *22*, 1282−1284.
(86) Wang, A.; Peng, Q.; Li, Y. Rod-Shaped Au-Pd Core-Shell Nanostructures. *Chem. Mater.* **2011**, *23*, 3217−3222.
(87) Rathmell, A. R.; Nguyen, M.; Chi, M.; Wiley, B. J. Synthesis of Oxidation-Resistant Cupronickel Nanowires for Transparent Conducting Nanowire Networks. *Nano Lett.* **2012**, *12*, 3193−3199.

DOI: 10.1021/acs.chemrev.8b00745
Chem. Rev. XXXX, XXX, XXX−XXX

(88) Guo, S.; Zhang, S.; Su, D.; Sun, S. Seed-Mediated Synthesis of Core/Shell FePtM/FePt (M = Pd, Au) Nanowires and Their Electrocatalysis for Oxygen Reduction Reaction. *J. Am. Chem. Soc.* **2013**, *135*, 13879−13884.
(89) Stewart, I. E.; Ye, S.; Chen, Z.; Flowers, P. F.; Wiley, B. J. Synthesis of Cu-Ag, Cu-Au, and Cu-Pt Core-Shell Nanowires and Their Use in Transparent Conducting Films. *Chem. Mater.* **2015**, *27*, 7788−7794.
(90) Niu, Z.; Cui, F.; Yu, Y.; Becknell, N.; Sun, Y.; Khanarian, G.; Kim, D.; Dou, L.; Dehestani, A.; Schierle-Arndt, K.; et al. Ultrathin Epitaxial Cu@Au Core-Shell Nanowires for Stable Transparent Conductors. *J. Am. Chem. Soc.* **2017**, *139*, 7348−7354.
(91) Xiong, Y.; Mayers, B. T.; Xia, Y. Some Recent Developments in the Chemical Synthesis of Inorganic Nanotubes. *Chem. Commun.* **2005**, *40*, 5013−5022.
(92) Seo, D.; Song, H. Asymmetric Hollow Nanorod Formation through a Partial Galvanic Replacement Reaction. *J. Am. Chem. Soc.* **2009**, *131*, 18210−18211.
(93) Alia, S. M.; Jensen, K. O.; Pivovar, B. S.; Yan, Y. Platinum-Coated Palladium Nanotubes as Oxygen Reduction Reaction Electrocatalysts. *ACS Catal.* **2012**, *2*, 858−863.
(94) Gilroy, K. D.; Peng, H.; Yang, X.; Ruditskiy, A.; Xia, Y. Symmetry Breaking During Nanocrystal Growth. *Chem. Commun.* **2017**, *53*, 4530−4541.
(95) Peng, H.; Park, J.; Zhang, L.; Xia, Y. Toward a Quantitative Understanding of Symmetry Reduction Involved in the Seed-Mediated Growth of Pd Nanocrystals. *J. Am. Chem. Soc.* **2015**, *137*, 6643−6652.
(96) Huang, H.; Ruditskiy, A.; Choi, S. Il; Zhang, L.; Liu, J.; Ye, Z.; Xia, Y. One-Pot Synthesis of Penta-Twinned Palladium Nanowires and Their Enhanced Electrocatalytic Properties. *ACS Appl. Mater. Interfaces* **2017**, *9*, 31203−31212.
(97) Lamer, V. K.; Dinegar, R. H. Theory, Production and Mechanism of Formation of Monodispersed Hydrosols. *J. Am. Chem. Soc.* **1950**, *72*, 4847−4854.
(98) Xia, Y.; Gilroy, K. D.; Peng, H.; Xia, X. Seed-Mediated Growth of Colloidal Metal Nanocrystals. *Angew. Chem., Int. Ed.* **2017**, *56*, 60−95.
(99) Yang, T.; Peng, H.; Zhou, S.; Lee, C.; Bao, X.; Lee, Y.; Wu, J.; Xia, Y. Toward a Quantitative Understanding of the Reduction Pathways of a Salt Precursor in the Synthesis of Metal Nanocrystals. *Nano Lett.* **2017**, *17*, 334−340.
(100) Yang, T.; Zhou, S.; Gilroy, K. D.; Figueroa-Cosme, L.; Lee, Y.; Wu, J.; Xia, Y. Autocatalytic Surface Reduction and Its Role in Controlling Seed-Mediated Growth of Colloidal Metal Nanocrystals. *Proc. Natl. Acad. Sci. U. S. A.* **2017**, *114*, 13619−13624.
(101) Zhou, S.; Yang, T.; Zhao, M.; Xia, Y. Quantitative Analysis of the Reduction Kinetics of a Pt(II) Precursor in the Context of Pt Nanocrystal Synthesis. *Chin. J. Chem. Phys.* **2018**, *31*, 370.
(102) Xia, X.; Zeng, J.; Oetjen, K.; Li, Q.; Xia, Y. Quantitative Analysis of the Role Played by Poly(vinylpyrrolidone) in Seed-Mediated Growth of Ag Nanocrystals. *J. Am. Chem. Soc.* **2012**, *134*, 1793−1801.
(103) Sun, Y.; Xia, Y. Shape-Controlled Synthesis of Gold and Silver Nanoparticles. *Science* **2002**, *298*, 2176−2179.
(104) Zeng, J.; Zheng, Y.; Rycenga, M.; Tao, J.; Li, Z.; Zhang, Q.; Zhu, Y.; Xia, Y. Controlling the Shapes of Silver Nanocrystals with Different Capping Agents. *J. Am. Chem. Soc.* **2010**, *132*, 8552−8553.
(105) Cobley, C. M.; Rycenga, M.; Zhou, F.; Li, Z.; Xia, Y. Etching and Growth: An Intertwined Pathway to Silver Nanocrystals with Exotic Shapes. *Angew. Chem.* **2009**, *121*, 4918−4921.
(106) Zeng, J.; Zhu, C.; Tao, J.; Jin, M.; Zhang, H.; Li, Z.; Zhu, Y.; Xia, Y. Controlling the Nucleation and Growth of Silver on Palladium Nanocubes by Manipulating the Reaction Kinetics. *Angew. Chem., Int. Ed.* **2012**, *51*, 2354−2358.
(107) Zhu, C.; Zeng, J.; Tao, J.; Johnson, M. C.; Schmidt-krey, I.; Blubaugh, L.; Zhu, Y.; Gu, Z.; Xia, Y. Kinetically Controlled Overgrowth of Ag or Au on Pd Nanocrystal Seeds : From Hybrid Dimers to Nonconcentric and Concentric Bimetallic Nanocrystals. *J. Am. Chem. Soc.* **2012**, *134*, 15822−15831.
(108) Xia, X.; Xia, Y. Symmetry Breaking during Seeded Growth of Nanocrystals. *Nano Lett.* **2012**, *12*, 6038−6042.
(109) Zhou, S.; Zhao, M.; Yang, T. H.; Xia, Y. Decahedral Nanocrystals of Noble Metals: Synthesis, Characterization, and Applications. *Mater. Today* **2019**, *22*, 108.
(110) Sun, Y.; Ren, Y.; Liu, Y.; Wen, J.; Okasinski, J. S.; Miller, D. J. Ambient-Stable Tetragonal Phase in Silver Nanostructures. *Nat. Commun.* **2012**, *3*, 971.
(111) Wang, Z.; Chen, Z.; Zhang, H.; Zhang, Z.; Wu, H.; Jin, M.; Wu, C.; Yang, D.; Yin, Y. Lattice-Mismatch-Induced Twinning for Seeded Growth of Anisotropic Nanostructures. *ACS Nano* **2015**, *9*, 3307−3313.
(112) Koczkur, K. M.; Mourdikoudis, S.; Polavarapu, L.; Skrabalak, S. E. Polyvinylpyrrolidone (PVP) in Nanoparticle Synthesis. *Dalton Trans* **2015**, *44*, 17883−17905.
(113) Luo, M.; Ruditskiy, A.; Peng, H.-C.; Tao, J.; Figueroa-Cosme, L.; He, Z.; Xia, Y. Penta-Twinned Copper Nanorods: Facile Synthesis via Seed-Mediated Growth and Their Tunable Plasmonic Properties. *Adv. Funct. Mater.* **2016**, *26*, 1209−1216.
(114) Herrero, E.; Buller, L. J.; Abruña, H. D. Underpotential Deposition at Single Crystal Surfaces of Au, Pt, Ag and Other Materials. *Chem. Rev.* **2001**, *101*, 1897−1930.
(115) Lohse, S. E.; Burrows, N. D.; Scarabelli, L.; Liz-Marzán, L. M.; Murphy, C. J. Anisotropic Noble Metal Nanocrystal Growth: The Role of Halides. *Chem. Mater.* **2014**, *26*, 34−43.
(116) Xia, X.; Xie, S.; Liu, M.; Peng, H.-C.; Lu, N.; Wang, J.; Kim, M. J.; Xia, Y. On the Role of Surface Diffusion in Determining the Shape or Morphology of Noble-Metal Nanocrystals. *Proc. Natl. Acad. Sci. U. S. A.* **2013**, *110*, 6669−6673.
(117) Zhang, H.; De Yoreo, J. J.; Banfield, J. F. A Unified Description of Attachment-Based Crystal Growth. *ACS Nano* **2014**, *8*, 6526−6530.
(118) Zhang, Q.; Liu, S. J.; Yu, S. H. Recent Advances in Oriented Attachment Growth and Synthesis of Functional Materials: Concept, Evidence, Mechanism, and Future. *J. Mater. Chem.* **2009**, *19*, 191−207.
(119) Lv, W.; He, W.; Wang, X.; Niu, Y.; Cao, H.; Dickerson, J. H.; Wang, Z. Understanding the Oriented-Attachment Growth of Nanocrystals from an Energy Point of View: A Review. *Nanoscale* **2014**, *6*, 2531−2547.
(120) De Yoreo, J. J.; Gilbert, P. U. P. A.; Sommerdijk, N. A. J. M.; Penn, R. L.; Whitelam, S.; Joester, D.; Zhang, H.; Rimer, J. D.; Navrotsky, A.; Banfield, J. F.; et al. Crystallization by Particle Attachment in Synthetic, Biogenic, and Geologic Environments. *Science* **2015**, *349*, aaa6760.
(121) Penn, R. L. Imperfect Oriented Attachment: Dislocation Generation in Defect-Free Nanocrystals. *Science* **1998**, *281*, 969−971.
(122) Banfield, J. F.; Welch, S. A.; Zhang, H.; Ebert, T. T.; Penn, R. L. Aggregation-Based Crystal Growth and Microstructure Development in Natural Iron Oxyhydroxide Biomineralization Products. *Science* **2000**, *289*, 751−754.
(123) Halder, A.; Ravishankar, N. Ultrafine Single-Crystalline Gold Nanowire Arrays by Oriented Attachment. *Adv. Mater.* **2007**, *19*, 1854−1858.
(124) Lim, B.; Jiang, M.; Yu, T.; Camargo, P. H. C.; Xia, Y. Nucleation and Growth Mechanisms for Pd−Pt Bimetallic Nanodendrites and Their Electrocatalytic Properties. *Nano Res.* **2010**, *3*, 69−80.
(125) Lu, L.; Kobayashi, A.; Kikkawa, Y.; Tawa, K.; Ozaki, Y. Oriented Attachment-Based Assembly of Dendritic Silver Nanostructures at Room Temperature. *J. Phys. Chem. B* **2006**, *110*, 23234−23241.
(126) Walter, E. C.; Murray, B. J.; Favier, F.; Kaltenpoth, G.; Grunze, M.; Penner, R. M. Noble and Coinage Metal Nanowires by Electrochemical Step Edge Decoration. *J. Phys. Chem. B* **2002**, *106*, 11407−11411.

DOI: 10.1021/acs.chemrev.8b00745
Chem. Rev. XXXX, XXX, XXX−XXX

(127) Huang, M. H.; Choudrey, A.; Yang, P. Ag Nanowire Formation within Mesoporous Silica. *Chem. Commun.* **2000**, 1063−1064.
(128) Song, Y.; Garcia, R. M.; Dorin, R. M.; Wang, H.; Qiu, Y.; Coker, E. N.; Steen, W. A.; Miller, J. E.; Shelnutt, J. A. Synthesis of Platinum Nanowire Networks Using a Soft Template. *Nano Lett.* **2007**, *7*, 3650−3655.
(129) Monson, C. F.; Woolley, A. T. DNA-Templated Construction of Copper Nanowires. *Nano Lett.* **2003**, *3*, 359−363.
(130) Sun, Y.; Mayers, B. T.; Xia, Y. Template-Engaged Replacement Reaction : A One-Step Approach to the Large-Scale Synthesis of Metal Nanostructures with Hollow Interiors. *Nano Lett.* **2002**, *2*, 481−485.
(131) Hurst, S. J.; Payne, E. K.; Qin, L.; Mirkin, C. A. Multisegmented One-Dimensional Nanorods Prepared by Hard-Template Synthetic Methods. *Angew. Chem., Int. Ed.* **2006**, *45*, 2672−2692.
(132) Zhao, G. Y.; Xu, C. L.; Guo, D. J.; Li, H.; Li, H. L. Template Preparation of Pt Nanowire Array Electrode on Ti/Si Substrate for Methanol Electro-Oxidation. *Appl. Surf. Sci.* **2007**, *253*, 3242−3246.
(133) Sloan, J.; Hammer, J.; Zwiefka-Sibley, M.; Green, M. L. H.; Sloan, J. The Opening and Filling of Single Walled Carbon Nanotubes (SWTs). *Chem. Commun.* **1998**, *1*, 347−348.
(134) Murphy, C. J.; Jana, N. R. Controlling the Aspect Ratio of Inorganic Nanorods and Nanowires. *Adv. Mater.* **2002**, *14*, 80−82.
(135) Zhang, D.; Qi, L.; Ma, J.; Cheng, H. Formation of Silver Nanowires in Aqueous Solutions of a Double-Hydrophilic Block Copolymer. *Chem. Mater.* **2001**, *13*, 2753−2755.
(136) Cornelissen, J. J. L. M.; Van Heerbeek, R.; Kamer, P. C. J.; Reek, J. N. H.; Sommerdijk, N. A. J. M.; Nolte, R. J. M. Silver Nanoarrays Templated by Block Copolymers of Carbosilane Dendrimers and Polyisocyanopeptides. *Adv. Mater.* **2002**, *14*, 489−492.
(137) Kim, J. U.; Cha, S. H.; Shin, K.; Jho, J. Y.; Lee, J. C. Preparation of Gold Nanowires and Nanosheets in Bulk Block Copolymer Phases Under Mild Conditions. *Adv. Mater.* **2004**, *16*, 459−464.
(138) Wang, Y.; Herricks, T.; Xia, Y. Single Crystalline Nanowires of Lead Can Be Synthesized through Thermal Decomposition of Lead Acetate in Ethylene Glycol. *Nano Lett.* **2003**, *3*, 1163−1166.
(139) Xia, Y.; Xia, X.; Peng, H. Shape-Controlled Synthesis of Colloidal Metal Nanocrystals : Thermodynamic versus Kinetic Products. *J. Am. Chem. Soc.* **2015**, *137*, 7947−7966.
(140) Wang, Y.; He, J.; Liu, C.; Chong, W. H.; Chen, H. Thermodynamics versus Kinetics in Nanosynthesis. *Angew. Chem., Int. Ed.* **2015**, *54*, 2022−2051.
(141) Jin, M.; Liu, H.; Zhang, H.; Xie, Z.; Liu, J.; Xia, Y. Synthesis of Pd Nanocrystals Enclosed by {100} Facets and with Sizes < 10 nm for Application in CO Oxidation. *Nano Res.* **2011**, *4*, 83−91.
(142) Ruditskiy, A.; Xia, Y. Toward the Synthesis of Sub-15 nm Ag Nanocubes with Sharp Corners and Edges: the Roles of Heterogeneous Nucleation and Surface Capping. *J. Am. Chem. Soc.* **2016**, *138*, 3161−3167.
(143) Wang, Y.; Peng, H. C.; Liu, J.; Huang, C. Z.; Xia, Y. Use of Reduction Rate as a Quantitative Knob for Controlling the Twin Structure and Shape of Palladium Nanocrystals. *Nano Lett.* **2015**, *15*, 1445−1450.
(144) Meng, M.; Fang, Z.; Zhang, C.; Su, H.; He, R.; Zhang, R.; Li, H.; Li, Z. Y.; Wu, X.; Ma, C.; et al. Integration of Kinetic Control and Lattice Mismatch to Synthesize Pd@AuCu Core-Shell Planar Tetrapods with Size-Dependent Optical Properties. *Nano Lett.* **2016**, *16*, 3036−3041.
(145) Xiong, Y.; Chen, J.; Wiley, B.; Xia, Y.; et al. Understanding the Role of Oxidative Etching in the Polyol Synthesis of Pd Nanoparticles with Uniform Shape and Size. *J. Am. Chem. Soc.* **2005**, *127*, 7332−7333.
(146) Zheng, Y.; Zeng, J.; Ruditskiy, A.; Liu, M.; Xia, Y. Oxidative Etching and Its Role in Manipulating the Nucleation and Growth of Noble-Metal Nanocrystals. *Chem. Mater.* **2014**, *26*, 22−33.
(147) Long, R.; Zhou, S.; Wiley, B. J.; Xiong, Y. Oxidative Etching for Controlled Synthesis of Metal Nanocrystals: Atomic Addition and Subtraction. *Chem. Soc. Rev.* **2014**, *43*, 6288−6310.
(148) Li, Z.; Tao, J.; Lu, X.; Zhu, Y.; Xia, Y. Facile Synthesis of Ultrathin Au Nanorods by Aging the AuCl(Oleylamine) Complex with Amorphous Fe Nanoparticles in Chloroform. *Nano Lett.* **2008**, *8*, 3052−3055.
(149) Kisner, A.; Heggen, M.; Fernández, E.; Lenk, S.; Mayer, D.; Simon, U.; Offenhäusser, A.; Mourzina, Y. The Role of Oxidative Etching in the Synthesis of Ultrathin Single-Crystalline Au Nanowires. *Chem. - Eur. J.* **2011**, *17*, 9503−9507.
(150) Xia, X.; Wang, Y.; Ruditskiy, A.; Xia, Y. 25th Anniversary Article : Galvanic Replacement : A Simple and Versatile Route to Hollow Nanostructures with Tunable and Well-Controlled Properties. *Adv. Mater.* **2013**, *25*, 6313−6333.
(151) Hong, X.; Wang, D.; Cai, S.; Rong, H.; Li, Y. Single-Crystalline Octahedral Au−Ag Nanoframes. *J. Am. Chem. Soc.* **2012**, *134*, 18165−18168.
(152) Au, L.; Lu, X.; Xia, Y. A Comparative Study of Galvanic Replacement Reactions Involving Ag Nanocubes and $AuCl_2^-$ or $AuCl_4^-$. *Adv. Mater.* **2008**, *20*, 2517−2522.
(153) Zhu, C.; Guo, S.; Dong, S. PdM (M = Pt, Au) Bimetallic Alloy Nanowires with Enhanced Electrocatalytic Activity for Electro-Oxidation of Small Molecules. *Adv. Mater.* **2012**, *24*, 2326−2331.
(154) Sun, Y.; Xia, Y. Multiple-Walled Nanotubes Made of Metals. *Adv. Mater.* **2004**, *16*, 264−268.
(155) Grzelczak, M.; Pérez-Juste, J.; Mulvaney, P.; Liz-Marzán, L. M. Shape Control in Gold Nanoparticle Synthesis. *Chem. Soc. Rev.* **2008**, *37*, 1783−1791.
(156) Lohse, S. E.; Murphy, C. J. The Quest for Shape Control: A History of Gold Nanorod Synthesis. *Chem. Mater.* **2013**, *25*, 1250−1261.
(157) Ye, S.; Stewart, I. E.; Chen, Z.; Li, B.; Rathmell, A. R.; Wiley, B. J. How Copper Nanowires Grow and How to Control Their Properties. *Acc. Chem. Res.* **2016**, *49*, 442−451.
(158) Smith, D. K.; Miller, N. R.; Korgel, B. A. Iodide in CTAB Prevents Gold Nanorod Formation. *Langmuir* **2009**, *25*, 9518−9524.
(159) Wiley, B.; Sun, Y.; Xia, Y. Synthesis of Silver Nanostructures with Controlled Shapes and Properties. *Acc. Chem. Res.* **2007**, *40*, 1067−1076.
(160) Lim, B. B.; Jiang, M.; Tao, J.; Camargo, P. H. C.; Zhu, Y.; Xia, Y. Shape-Controlled Synthesis of Pd Nanocrystals in Aqueous Solutions. *Adv. Funct. Mater.* **2009**, *19*, 189−200.
(161) Murphy, C. J.; Thompson, L. B.; Chernak, D. J.; Yang, J. A.; Sivapalan, S. T.; Boulos, S. P.; Huang, J.; Alkilany, A. M.; Sisco, P. N. Gold Nanorod Crystal Growth: From Seed-Mediated Synthesis to Nanoscale Sculpting. *Curr. Opin. Colloid Interface Sci.* **2011**, *16*, 128−134.
(162) Liao, H.-G.; Niu, K.; Zheng, H. Observation of Growth of Metal Nanoparticles. *Chem. Commun.* **2013**, *49*, 11720−11727.
(163) Gan, L.; Cui, C.; Heggen, M.; Dionigi, F.; Rudi, S.; Strasser, P. Element-Specific Anisotropic Growth of Shaped Platinum Alloy Nanocrystals. *Science* **2014**, *346*, 1502−1506.
(164) Alloyeau, D.; Dachraoui, W.; Javed, Y.; Belkahla, H.; Wang, G.; Lecoq, H.; Ammar, S.; Ersen, O.; Wisnet, A.; Gazeau, F.; et al. Unravelling Kinetic and Thermodynamic Effects on the Growth of Gold Nanoplates by Liquid Transmission Electron Microscopy. *Nano Lett.* **2015**, *15*, 2574−2581.
(165) Ye, X.; Jones, M. R.; Frechette, L. B.; Chen, Q.; Nguyen, S. C.; Adiga, V. P.; Zettl, A.; Rabani, E.; Geissler, P. L.; Alivisatos, A. P.; et al. Single-Particle Mapping of Nonequilibrium Nanocrystal Transformation. *Science* **2016**, *354*, 874−877.
(166) Herrmann, L. O.; Baumberg, J. J. Watching Single Nanoparticles Grow in Real Time through Supercontinuum Spectroscopy. *Small* **2013**, *9*, 3743−3747.
(167) Ye, S.; Rathmell, A. R.; Stewart, I. E.; Ha, Y.-C.; Wilson, A. R.; Chen, Z.; Wiley, B. J. A Rapid Synthesis of High Aspect Ratio Copper Nanowires for High-Performance Transparent Conducting Films. *Chem. Commun.* **2014**, *50*, 2562−2564.

DOI: 10.1021/acs.chemrev.8b00745
Chem. Rev. XXXX, XXX, XXX−XXX

(168) Kim, M. J.; Alvarez, S.; Yan, T.; Tadepalli, V.; Fichthorn, K. A.; Wiley, B. J. Modulating the Growth Rate, Aspect Ratio, and Yield of Copper Nanowires with Alkylamines. *Chem. Mater.* **2018**, *30*, 2809−2818.
(169) Sun, Y.; Wang, Y. Monitoring of Galvanic Replacement Reaction between Silver Nanowires and $HAuCl_4$ by in Situ Transmission X-Ray Microscopy. *Nano Lett.* **2011**, *11*, 4386−4392.
(170) Sun, Y. Watching Nanoparticle Kinetics in Liquid. *Mater. Today* **2012**, *15*, 140−147.
(171) Yu, L.; Yan, Z.; Cai, Z.; Zhang, D.; Han, P.; Cheng, X.; Sun, Y. Quantitatively in Situ Imaging Silver Nanowire Hollowing Kinetics. *Nano Lett.* **2016**, *16*, 6555−6559.
(172) Vivek, J. P.; Burgess, I. J. Adsorption of a Quaternary Ammonium Surfactant on Au(100). *J. Electroanal. Chem.* **2010**, *649*, 16−22.
(173) Vivek, J. P.; Burgess, I. J. Quaternary Ammonium Bromide Surfactant Adsorption on Low-Index Surfaces of Gold. 1. Au(111). *Langmuir* **2012**, *28*, 5031−5039.
(174) Vivek, J. P.; Burgess, I. J. Quaternary Ammonium Bromide Surfactant Adsorption on Low-Index Surfaces of Gold. 2. Au(100) and the Role of Crystallographic-Dependent Adsorption in the Formation of Anisotropic Nanoparticles. *Langmuir* **2012**, *28*, 5040−5047.
(175) Vivek, J. P.; Monsur, A.; Burgess, I. J. Differential Capacity and Chronocoulometry Studies of a Quaternary Ammonium Surfactant Adsorbed on Au(111). *Surf. Interface Anal.* **2013**, *45*, 1402−1409.
(176) Skołuda, P. The Influence of Surface Crystallography on the Interfacial Behaviour of Tetrabutylammonium Cations at Au(100) and Au(111) Electrodes. *J. Electroanal. Chem.* **2014**, *731*, 153−156.
(177) Kim, M. J.; Flowers, P. F.; Stewart, I. E.; Ye, S.; Baek, S.; Kim, J. J.; Wiley, B. J. Ethylenediamine Promotes Cu Nanowire Growth by Inhibiting Oxidation of Cu(111). *J. Am. Chem. Soc.* **2017**, *139*, 277−284.
(178) Fisher, E. A.; Leung, K. K.; Casanova-Moreno, J.; Masuda, T.; Young, J.; Bizzotto, D. Quantifying the Selective Modification of Au(111) Facets via Electrochemical and Electroless Treatments for Manipulating Gold Nanorod Surface Composition. *Langmuir* **2017**, *33*, 12887−12896.
(179) Danger, B. R.; Fan, D.; Vivek, J. P.; Burgess, I. J. Electrochemical Studies of Capping Agent Adsorption Provide Insight into the Formation of Anisotropic Gold Nanocrystals. *ACS Nano* **2012**, *6*, 11018−11026.
(180) Qi, X.; Balankura, T.; Zhou, Y.; Fichthorn, K. A. How Structure-Directing Agents Control Nanocrystal Shape: Polyvinylpyrrolidone-Mediated Growth of Ag Nanocubes. *Nano Lett.* **2015**, *15*, 7711−7717.
(181) Saidi, W. A.; Feng, H.; Fichthorn, K. A. Binding of Polyvinylpyrrolidone to Ag Surfaces: Insight into a Structure-Directing Agent from Dispersion-Corrected Density Functional Theory. *J. Phys. Chem. C* **2013**, *117*, 1163−1171.
(182) Sathiyanarayanan, R.; Alimohammadi, M.; Zhou, Y.; Fichthorn, K. A. Role of Solvent in the Shape-Controlled Synthesis of Anisotropic Colloidal Nanostructures. *J. Phys. Chem. C* **2011**, *115*, 18983−18990.
(183) Zhou, Y.; Saidi, W. A.; Fichthorn, K. A. Comparison of the Binding of Polyvinylpyrrolidone and Polyethylene Oxide to Ag Surfaces: Elements of a Successful Structure-Directing Agent. *J. Phys. Chem. C* **2013**, *117*, 11444−11448.
(184) Zhou, Y.; Saidi, W. A.; Fichthorn, K. A. A Force Field for Describing the Polyvinylpyrrolidone-Mediated Solution-Phase Synthesis of Shape-Selective Ag Nanoparticles. *J. Phys. Chem. C* **2014**, *118*, 3366−3374.
(185) Chiu, C.; Li, Y.; Ruan, L.; Ye, X.; Murray, C. B.; Huang, Y. Platinum Nanocrystals Selectively Shaped Using Facet-Specific Peptide Sequences. *Nat. Chem.* **2011**, *3*, 393−399.
(186) Chiu, C.; Ruan, L.; Huang, Y. Biomolecular Specificity Controlled Nanomaterial Synthesis. *Chem. Soc. Rev.* **2013**, *42*, 2512−2527.
(187) Heinz, H.; Farmer, B. L.; Pandey, R. B.; Slocik, J. M.; Patnaik, S. S.; Pachter, R.; Naik, R. R. Nature of Molecular Interactions of Peptides with Gold, Palladium, and Pd−Au Bimetal Surfaces in Aqueous Solution. *J. Am. Chem. Soc.* **2009**, *131*, 9704−9714.
(188) Al-Saidi, W. A.; Feng, H.; Fichthorn, K. A. Adsorption of Polyvinylpyrrolidone on Ag Surfaces: Insight into a Structure-Directing Agent. *Nano Lett.* **2012**, *12*, 997−1001.
(189) Balankura, T.; Qi, X.; Zhou, Y.; Fichthorn, K. A. Predicting Kinetic Nanocrystal Shapes through Multi-Scale Theory and Simulation: Polyvinylpyrrolidone-Mediated Growth of Ag Nanocrystals. *J. Chem. Phys.* **2016**, *145*, 144106.
(190) Qi, X.; Zhou, Y.; Fichthorn, K. A. Obtaining the Solid-Liquid Interfacial Free Energy via Multi-Scheme Thermodynamic Integration : Ag-Ethylene Glycol Interfaces. *J. Chem. Phys.* **2016**, *145*, 194108.
(191) Kim, B. H.; Yang, J.; Lee, D.; Choi, B. K.; Hyeon, T.; Park, J. Liquid-Phase Transmission Electron Microscopy for Studying Colloidal Inorganic Nanoparticles. *Adv. Mater.* **2018**, *30*, 1703316.
(192) Dukes, M. J.; Jacobs, B. W.; Morgan, D. G.; Hegde, H.; Kelly, D. F. Visualizing Nanoparticle Mobility in Liquid at Atomic Resolution. *Chem. Commun.* **2013**, *49*, 3007−3009.
(193) Williamson, M. J.; Tromp, R. M.; Vereecken, P. M.; Hull, R.; Ross, F. M. Dynamic Microscopy of Nanoscale Cluster Growth at the Solid-Liquid Interface. *Nat. Mater.* **2003**, *2*, 532−536.
(194) Xin, H. L.; Zheng, H. In Situ Observation of Oscillatory Growth of Bismuth Nanoparticles. *Nano Lett.* **2012**, *12*, 1470−1474.
(195) Nielsen, M. H.; Aloni, S.; De Yoreo, J. J. In Situ TEM Imaging of $CaCO_3$ Nucleation Reveals Coexistence of Direct and Indirect Pathways. *Science* **2014**, *345*, 1158−1162.
(196) Cho, H.; Jones, M. R.; Nguyen, S. C.; Hauwiller, M. R.; Zettl, A.; Alivisatos, A. P. The Use of Graphene and Its Derivatives for Liquid-Phase Transmission Electron Microscopy of Radiation-Sensitive Specimens. *Nano Lett.* **2017**, *17*, 414−420.
(197) Moser, T. H.; Mehta, H.; Park, C.; Kelly, R. T.; Shokuhfar, T.; Evans, J. E. The Role of Electron Irradiation History in Liquid Cell Transmission Electron Microscopy. *Sci. Adv.* **2018**, *4*, eaaq1202.
(198) Abellan, P.; Woehl, T. J.; Parent, L. R.; Browning, N. D.; Evans, J. E.; Arslan, I. Factors Influencing Quantitative Liquid (Scanning) Transmission Electron Microscopy. *Chem. Commun.* **2014**, *50*, 4873−4880.
(199) Sutter, E.; Jungjohann, K.; Bliznakov, S.; Courty, A.; Maisonhaute, E.; Tenney, S.; Sutter, P. In Situ Liquid-Cell Electron Microscopy of Silver-Palladium Galvanic Replacement Reactions on Silver Nanoparticles. *Nat. Commun.* **2014**, *5*, 4946.
(200) Wang, J. H.; Robinson, C. V.; Edelman, I. S. Self-Diffusion and Structure of Liquid Water. III. Measurement of the Self-Diffusion of Liquid Water with H^2, H^3 and O^{18} as Tracers. *J. Am. Chem. Soc.* **1953**, *75*, 466−470.
(201) Schouten, K. J. P.; Pérez Gallent, E.; Koper, M. T. M. Structure Sensitivity of the Electrochemical Reduction of Carbon Monoxide on Copper Single Crystals. *ACS Catal.* **2013**, *3*, 1292−1295.
(202) Schouten, K. J. P.; Qin, Z.; Pérez Gallent, E. P.; Koper, M. T. M. Two Pathways for the Formation of Ethylene in CO Reduction on Single-Crystal Copper Electrodes. *J. Am. Chem. Soc.* **2012**, *134*, 9864−9867.
(203) Hori, Y.; Takahashi, I.; Koga, O.; Hoshi, N. Selective Formation of C_2 Compounds from Electrochemical Reduction of CO_2 at a Series of Copper Single Crystal Electrodes. *J. Phys. Chem. B* **2002**, *106*, 15−17.
(204) Blizanac, B. B.; Ross, P. N.; Marković, N. M. Oxygen Reduction on Silver Low-Index Single-Crystal Surfaces in Alkaline Solution: Rotating Ring $Disk_{Ag(hkl)}$ Studies. *J. Phys. Chem. B* **2006**, *110*, 4735−4741.
(205) Polewska, W.; Behm, R. J.; Magnussen, O. M. In-Situ Video-STM Studies of Cu Electrodeposition on Cu(100) in HCl Solution. *Electrochim. Acta* **2003**, *48*, 2915−2921.

DOI: 10.1021/acs.chemrev.8b00745
Chem. Rev. XXXX, XXX, XXX−XXX

(206) Moffat, T. P. Electrochemical Production of Single-Crystal Cu-Ni Strained-Layer Superlattices on Cu(100). *J. Electrochem. Soc.* **1995**, *142*, 3767−3770.
(207) Moffat, T. P.; Ou Yang, L.-Y. Accelerator Surface Phase Associated with Superconformal Cu Electrodeposition. *J. Electrochem. Soc.* **2010**, *157*, D228−D241.
(208) Bae, S.-E.; Gewirth, A. A. In Situ EC-STM Studies of MPS, SPS, and Chloride on Cu(100): Structural Studies of Accelerators for Dual Damascene Electrodeposition. *Langmuir* **2006**, *22*, 10315−10321.
(209) Vogt, M. R.; Lachenwitzer, A.; Magnussen, O. M.; Behm, R. J. In-Situ STM Study of the Initial Stages of Corrosion of Cu(100) Electrodes in Sulfuric and Hydrochloric Acid Solution. *Surf. Sci.* **1998**, *399*, 49−69.
(210) Maurice, V.; Strehblow, H.-H.; Marcus, P. In Situ Scanning Tunneling Microscope Study of the Passivation of Cu(111). *J. Electrochem. Soc.* **1999**, *146*, 524−530.
(211) Vogt, M. R.; Nichols, R. J.; Magnussen, O. M.; Behm, R. J. Benzotriazole Adsorption and Inhibition of Cu(100) Corrosion in HCl: A Combined in Situ STM and in Situ FTIR Spectroscopy Study. *J. Phys. Chem. B* **1998**, *102*, 5859−5865.
(212) Scherer, J.; Vogt, M. R.; Magnussen, O. M.; Behm, R. J. Corrosion of Alkanethiol-Covered Cu(100) Surfaces in Hydrochloric Acid Solution Studied by in-Situ Scanning Tunneling Microscopy. *Langmuir* **1997**, *13*, 7045−7051.
(213) Kang, H.; Kim, B. G.; Na, H. B.; Hwang, S. Anti-Galvanic Reduction of Silver Ion on Gold and Its Role in Anisotropic Growth of Gold Nanomaterials. *J. Phys. Chem. C* **2015**, *119*, 25974−25982.
(214) Gao, J.; Bender, C. M.; Murphy, C. J. Dependence of the Gold Nanorod Aspect Ratio on the Nature of the Directing Surfactant in Aqueous Solution. *Langmuir* **2003**, *19*, 9065−9070.
(215) Sau, T. K.; Murphy, C. J. Role of Ions in the Colloidal Synthesis of Gold Nanowires. *Philos. Mag.* **2007**, *87*, 2143−2158.
(216) Li, B.; Ye, S.; Stewart, I. E.; Alvarez, S.; Wiley, B. J. Synthesis and Purification of Silver Nanowires to Make Conducting Films with a Transmittance of 99%. *Nano Lett.* **2015**, *15*, 6722−6726.
(217) Niu, Z.; Cui, F.; Kuttner, E.; Xie, C.; Chen, H.; Sun, Y.; Dehestani, A.; Schierle-Arndt, K.; Yang, P. Synthesis of Silver Nanowires with Reduced Diameters Using Benzoin-Derived Radicals to Make Transparent Conductors with High Transparency and Low Haze. *Nano Lett.* **2018**, *18*, 5329−5334.
(218) Wiley, B.; Sun, Y.; Xia, Y. Polyol Synthesis of Silver Nanostructures: Control of Product Morphology with Fe(II) or Fe(III) Species. *Langmuir* **2005**, *21*, 8077−8080.
(219) Sun, Y.; Xia, Y. Large-Scale Synthesis of Uniform Silver Nanowires through a Soft, Self-Seeding, Polyol Process. *Adv. Mater.* **2002**, *14*, 833−837.
(220) Gawande, M. B.; Goswami, A.; Felpin, F. X.; Asefa, T.; Huang, X.; Silva, R.; Zou, X.; Zboril, R.; Varma, R. S. Cu and Cu-Based Nanoparticles: Synthesis and Applications in Catalysis. *Chem. Rev.* **2016**, *116*, 3722−3811.
(221) Luo, W.; Nie, X.; Janik, M. J.; Asthagiri, A. Facet Dependence of CO_2 Reduction Paths on Cu Electrodes. *ACS Catal.* **2016**, *6*, 219−229.
(222) Loiudice, A.; Lobaccaro, P.; Kamali, E. A.; Thao, T.; Huang, B. H.; Ager, J. W.; Buonsanti, R. Tailoring Copper Nanocrystals Towards C_2 Products in Electrochemical CO_2 Reduction. *Angew. Chem., Int. Ed.* **2016**, *55*, 5789−5792.
(223) Cui, F.; Yu, Y.; Dou, L.; Sun, J.; Yang, Q.; Schildknecht, C.; Schierle-Arndt, K.; Yang, P. Synthesis of Ultrathin Copper Nanowires Using Tris(Trimethylsilyl)Silane for High-Performance and Low-Haze Transparent Conductors. *Nano Lett.* **2015**, *15*, 7610−7615.
(224) Zhang, P.; Sui, Y.; Wang, C.; Wang, Y.; Cui, G.; Wang, C.; Liu, B.; Zou, B. A One-Step Green Route to Synthesize Copper Nanocrystals and Their Applications in Catalysis and Surface Enhanced Raman Scattering. *Nanoscale* **2014**, *6*, 5343−5350.
(225) Ravi Kumar, D. V.; Kim, I.; Zhong, Z.; Kim, K.; Lee, D.; Moon, J. Cu(II)-Alkyl Amine Complex Mediated Hydrothermal Synthesis of Cu Nanowires: Exploring the Dual Role of Alkyl Amines. *Phys. Chem. Chem. Phys.* **2014**, *16*, 22107−22115.
(226) Guo, H.; Chen, Y.; Ping, H.; Jin, J.; Peng, D. L. Facile Synthesis of Cu and Cu@Cu-Ni Nanocubes and Nanowires in Hydrophobic Solution in the Presence of Nickel and Chloride Ions. *Nanoscale* **2013**, *5*, 2394−2402.
(227) Huang, X.; Chen, Y.; Chiu, C. Y.; Zhang, H.; Xu, Y.; Duan, X.; Huang, Y. A Versatile Strategy to the Selective Synthesis of Cu Nanocrystals and the in Situ Conversion to CuRu Nanotubes. *Nanoscale* **2013**, *5*, 6284−6290.
(228) Cui, F.; Dou, L.; Yang, Q.; Yu, Y.; Niu, Z.; Sun, Y.; Liu, H.; Dehestani, A.; Schierle-Arndt, K.; Yang, P. Benzoin Radicals as Reducing Agent for Synthesizing Ultrathin Copper Nanowires. *J. Am. Chem. Soc.* **2017**, *139*, 3027−3032.
(229) Rathmell, A. R.; Bergin, S. M.; Hua, Y. L.; Li, Z. Y.; Wiley, B. J. The Growth Mechanism of Copper Nanowires and Their Properties in Flexible, Transparent Conducting Films. *Adv. Mater.* **2010**, *22*, 3558−3563.
(230) Ye, S.; Rathmell, A. R.; Ha, Y. C.; Wilson, A. R.; Wiley, B. J. The Role of Cuprous Oxide Seeds in the One-Pot and Seeded Syntheses of Copper Nanowires. *Small* **2014**, *10*, 1771−1778.
(231) Cho, Y. S.; Huh, Y. D. Synthesis of Ultralong Copper Nanowires by Reduction of Copper-Amine Complexes. *Mater. Lett.* **2009**, *63*, 227−229.
(232) Wen, X.; Xie, Y.; Choi, C. L.; Wan, K. C.; Li, X. Y.; Yang, S. Copper-Based Nanowire Materials: Templated Syntheses, Characterizations, and Applications. *Langmuir* **2005**, *21*, 4729−4737.
(233) Balci, S.; Bittner, A. M.; Hahn, K.; Scheu, C.; Knez, M.; Kadri, A.; Wege, C.; Jeske, H.; Kern, K. Copper Nanowires within the Central Channel of Tobacco Mosaic Virus Particles. *Electrochim. Acta* **2006**, *51*, 6251−6257.
(234) Cha, S. I.; Mo, C. B.; Kim, K. T.; Jeong, Y. J.; Hong, S. H. Mechanism for Controlling the Shape of Cu Nanocrystals Prepared by the Polyol Process. *J. Mater. Res.* **2006**, *21*, 2371−2378.
(235) Mott, D.; Galkowski, J.; Wang, L.; Luo, J.; Zhong, C.-J. Synthesis of Size-Controlled and Shaped Copper Nanoparticles. *Langmuir* **2007**, *23*, 5740−5745.
(236) Panigrahi, S.; Kundu, S.; Ghosh, S. K.; Nath, S.; Praharaj, S.; Basu, S.; Pal, T. Selective One-Pot Synthesis of Copper Nanorods under Surfactantless Condition. *Polyhedron* **2006**, *25*, 1263−1269.
(237) Liu, C. M.; Guo, L.; Xu, H. B.; Wu, Z. Y.; Weber, J. Seed-Mediated Growth and Properties of Copper Nanoparticles, Nanoparticle 1D Arrays and Nanorods. *Microelectron. Eng.* **2003**, *66*, 107−114.
(238) Tanori, J.; Pileni, M. P. Control of the Shape of Copper Metallic Particles by Using a Colloidal System as Template. *Langmuir* **1997**, *13*, 639−646.
(239) Salzemann, C.; Lisiecki, I.; Urban, J.; Pileni, M. P. Anisotropic Copper Nanocrystals Synthesized in a Supersaturated Medium: Nanocrystal Growth. *Langmuir* **2004**, *20*, 11772−11777.
(240) Becerril, H. A.; Stoltenberg, R. M.; Monson, C. F.; Woolley, A. T. Ionic Surface Masking for Low Background in Single-and Double-Stranded DNA-Templated Silver and Copper Nanorods. *J. Mater. Chem.* **2004**, *14*, 611−616.
(241) Patra, A. K.; Dutta, A.; Bhaumik, A. Cu Nanorods and Nanospheres and Their Excellent Catalytic Activity in Chemoselective Reduction of Nitrobenzenes. *Catal. Commun.* **2010**, *11*, 651−655.
(242) Zhou, J. C.; Soto, C. M.; Chen, M. S.; Bruckman, M. A.; Moore, M. H.; Barry, E.; Ratna, B. R.; Pehrsson, P. E.; Spies, B. R.; Confer, T. S. Biotemplating Rod-like Viruses for the Synthesis of Copper Nanorods and Nanowires. *J. Nanobiotechnol.* **2012**, *10*, 18.
(243) Lyu, Z.; Xie, M.; Gilroy, K. D.; Hood, Z. D.; Zhao, M.; Zhou, S.; Liu, J.; Xia, Y. A Rationally Designed Route to the One-Pot Synthesis of Right Bipyramidal Nanocrystals of Copper. *Chem. Mater.* **2018**, *30*, 6469−6477.
(244) Li, N.; Yin, H.; Zhuo, X.; Yang, B.; Zhu, X.; Wang, J. Infrared-Responsive Colloidal Silver Nanorods for Surface-Enhanced Infrared Absorption. *Adv. Opt. Mater.* **2018**, *6*, 1800436.

DOI: 10.1021/acs.chemrev.8b00745
Chem. Rev. XXXX, XXX, XXX−XXX

(245) Zhou, S.; Mesina, D. S.; Organt, M. A.; Yang, T.; Yang, X.; Huo, D.; Zhao, M.; Xia, Y. Site-Selective Growth of Ag Nanocubes for Sharpening Their Corners and Edges, Followed by Elongation into Nanobars through Symmetry Reduction. *J. Mater. Chem. C* **2018**, *6*, 1384−1392.
(246) Zhou, S.; Li, J.; Gilroy, K. D.; Tao, J.; Zhu, C.; Yang, X.; Sun, X.; Xia, Y. Facile Synthesis of Silver Nanocubes with Sharp Corners and Edges in an Aqueous Solution. *ACS Nano* **2016**, *10*, 9861−9870.
(247) Sun, Y. Silver Nanowires-Unique Templates for Functional Nanostructures. *Nanoscale* **2010**, *2*, 1626−1642.
(248) Sun, Y.; Yin, Y.; Mayers, B. T.; Herricks, T.; Xia, Y. Uniform Silver Nanowires Synthesis by Reducing $AgNO_3$ with Ethylene Glycol in the Presence of Seeds and Poly(Vinyl Pyrrolidone). *Chem. Mater.* **2002**, *14*, 4736−4745.
(249) Korte, K. E.; Skrabalak, S. E.; Xia, Y. Rapid Synthesis of Silver Nanowires through a $CuCl^-$ or $CuCl_2^-$ Mediated Polyol Process. *J. Mater. Chem.* **2008**, *18*, 437−441.
(250) Cheng, T.; Zhang, Y. Z.; Lai, W. Y.; Chen, Y.; Zeng, W. J.; Huang, W. High-Performance Stretchable Transparent Electrodes Based on Silver Nanowires Synthesized via an Eco-Friendly Halogen-Free Method. *J. Mater. Chem. C* **2014**, *2*, 10369−10376.
(251) Tsuji, M.; Hashimoto, M.; Nishizawa, Y.; Kubokawa, M.; Tsuji, T. Microwave-Assisted Synthesis of Metallic Nanostructures in Solution. *Chem. - Eur. J.* **2005**, *11*, 440−452.
(252) Gou, L.; Chipara, M.; Zaleski, J. M. Convenient, Rapid Synthesis of Ag Nanowires. *Chem. Mater.* **2007**, *19*, 1755−1760.
(253) Tsuji, M.; Matsumoto, K.; Miyamae, N.; Tsuji, T.; Zhang, X. Rapid Preparation of Silver Nanorods and Nanowires by a Microwave-Polyol Method in the Presence of Pt Catalyst and Polyvinylpyrrolidone. *Cryst. Growth Des.* **2007**, *7*, 311−320.
(254) Jana, N. R.; Gearheart, L.; Murphy, C. J. Wet Chemical Synthesis of Silver Nanorods and Nanowires of Controllable Aspect Ratio. *Chem. Commun.* **2001**, 617−618.
(255) Sun, Y. Growth of Silver Nanowires on GaAs Wafers. *Nanoscale* **2011**, *3*, 2247−2255.
(256) Hu, J.; Chen, Q.; Xie, Z.; Han, G.; Wang, R.; Ren, B.; Zhang, Y.; Yang, Z.; Tian, Z. A Simple and Effective Route for the Synthesis of Crystalline Silver Nanorods and Nanowires. *Adv. Funct. Mater.* **2004**, *14*, 183−189.
(257) Jiu, J.; Sugahara, T.; Nogi, M.; Suganuma, K. Ag Nanowires: Large-Scale Synthesis via a Trace-Salt-Assisted Solvothermal Process and Application in Transparent Electrodes. *J. Nanopart. Res.* **2013**, *15*, 1588.
(258) Zhang, Y.; Guo, J.; Xu, D.; Sun, Y.; Yan, F. One-Pot Synthesis and Purification of Ultralong Silver Nanowires for Flexible Transparent Conductive Electrodes. *ACS Appl. Mater. Interfaces* **2017**, *9*, 25465−25473.
(259) Saha, K.; Agasti, S. S.; Kim, C.; Li, X.; Rotello, V. M. Gold Nanoparticles in Chemical and Biological Sensing. *Chem. Rev.* **2012**, *112*, 2739−2779.
(260) Doering, W. E.; Piotti, M. E.; Natan, M. J.; Freeman, R. G. SERS as a Foundation for Nanoscale, Optically Detected Biological Labels. *Adv. Mater.* **2007**, *19*, 3100−3108.
(261) Zhang, Q.; Zhou, Y.; Villarreal, E.; Lin, Y.; Zou, S.; Wang, H. Faceted Gold Nanorods: Nanocuboids, Convex Nanocuboids, and Concave Nanocuboids. *Nano Lett.* **2015**, *15*, 4161−4169.
(262) Rosi, N.; Mirkin, C. A. Nanostructures in Biodiagnostics. *Chem. Rev.* **2005**, *105*, 1547−1562.
(263) Jia, H.; Fang, H.; Zhu, X.; Ruan, Q.; Wang, Y. J.; Wang, J. Synthesis of Absorption-Dominant Small Gold Nanorods and Their Plasmonic Properties. *Langmuir* **2015**, *31*, 7418−7426.
(264) Boisselier, E.; Astruc, D. Gold Nanoparticles in Nanomedicine: Preparations, Imaging, Diagnostics, Therapies and Toxicity. *Chem. Soc. Rev.* **2009**, *38*, 1759−1782.
(265) Nikoobakht, B.; El-sayed, M. A. Preparation and Growth Mechanism of Gold Nanorods (NRs) Using Seed-Mediated Growth Method. *Chem. Mater.* **2003**, *15*, 1957−1962.
(266) Ye, X.; Zheng, C.; Chen, J.; Gao, Y.; Murray, C. B. Using Binary Surfactant Mixtures to Simultaneously Improve the Dimensional Tunability and Monodispersity in the Seeded Growth of Gold Nanorods. *Nano Lett.* **2013**, *13*, 765−771.
(267) Wu, H.; Chu, H.; Kuo, T.; Kuo, C.; Huang, M. Seed-Mediated Synthesis of High Aspect Ratio Gold Nanorods with Nitric Acid. *Chem. Mater.* **2005**, *17*, 6447−6451.
(268) Requejo, K. I.; Liopo, A. V.; Derry, P. J.; Zubarev, E. R. Accelerating Gold Nanorod Synthesis with Nanomolar Concentrations of Poly(Vinylpyrrolidone). *Langmuir* **2017**, *33*, 12681−12688.
(269) Pérez-Juste, J.; Liz-Marzán, L. M.; Carnie, S.; Chan, D. Y. C.; Mulvaney, P. Electric-Field-Directed Growth of Gold Nanorods in Aqueous Surfactant Solutions. *Adv. Funct. Mater.* **2004**, *14*, 571−579.
(270) Kou, X.; Zhang, S.; Tsung, C. K.; Yang, Z.; Yeung, M. H.; Stucky, G. D.; Sun, L.; Wang, J.; Yan, C. One-Step Synthesis of Large-Aspect-Ratio Single-Crystalline Gold Nanorods by Using CTPAB and CTBAB Surfactants. *Chem. - Eur. J.* **2007**, *13*, 2929−2936.
(271) Ye, X.; Gao, Y.; Chen, J.; Reifsnyder, D. C.; Zheng, C.; Murray, C. B. Seeded Growth of Monodisperse Gold Nanorods Using Bromide-Free Surfactant Mixtures. *Nano Lett.* **2013**, *13*, 2163−2171.
(272) González-Rubio, G.; Díaz-Núñez, P.; Rivera, A.; Prada, A.; Tardajos, G.; González-Izquierdo, J.; Bañares, L.; Llombart, P.; Macdowell, L. G.; Palafox, M. A.; et al. Femtosecond Laser Reshaping Yields Gold Nanorods with Ultranarrow Surface Plasmon Resonances. *Science* **2017**, *358*, 640−644.
(273) Grochola, G.; Snook, I. K.; Russo, S. P. Computational Modeling of Nanorod Growth. *J. Chem. Phys.* **2007**, *127*, 194707.
(274) Meena, S. K.; Sulpizi, M. From Gold Nanoseeds to Nanorods: The Microscopic Origin of the Anisotropic Growth. *Angew. Chem., Int. Ed.* **2016**, *55*, 11960−11964.
(275) Seyed-Razavi, A.; Snook, I. K.; Barnard, A. S. Surface Area Limited Model for Predicting Anisotropic Coarsening of Faceted Nanoparticles. *Cryst. Growth Des.* **2011**, *11*, 158−165.
(276) Carbó-Argibay, E.; Rodríguez-González, B.; Gómez-Graña, S.; Guerrero-Martínez, A.; Pastoriza-Santos, I.; Pérez-Juste, J.; Liz-Marzán, L. M. The Crystalline Structure of Gold Nanorods Revisited : Evidence for Higher-Index Lateral Facets. *Angew. Chem., Int. Ed.* **2010**, *49*, 9397−9400.
(277) Scarabelli, L.; Sánchez-Iglesias, A.; Pérez-Juste, J.; Liz-Marzán, L. M. A "Tips and Tricks" Practical Guide to the Synthesis of Gold Nanorods. *J. Phys. Chem. Lett.* **2015**, *6*, 4270−4279.
(278) Edgar, J. A.; Mcdonagh, A. M.; Cortie, M. B. Formation of Gold Nanorods by a Stochastic "Popcorn" Mechanism. *ACS Nano* **2012**, *6*, 1116−1125.
(279) Das, P.; Chini, T. K. Substrate Induced Symmetry Breaking in Penta-Twinned Gold Nanorod Probed by Free Electron Impact. *J. Phys. Chem. C* **2014**, *118*, 26284−26291.
(280) Huang, H.; Wang, Y.; Ruditskiy, A.; Peng, H.; Zhao, X.; Zhang, L.; Liu, J.; Ye, Z.; Xia, Y. Polyol Syntheses of Palladium Decahedra and Icosahedra as Pure Samples by Maneuvering the Reaction Kinetics with Additives. *ACS Nano* **2014**, *8*, 7041−7050.
(281) Wang, H.; Zhou, S.; Gilroy, K. D.; Cai, Z.; Xia, Y. Icosahedral Nanocrystals of Noble Metals : Synthesis and Applications. *Nano Today* **2017**, *15*, 121−144.
(282) Walsh, M. J.; Tong, W.; Katz-boon, H.; Mulvaney, P.; Etheridge, J.; Funston, A. M. A Mechanism for Symmetry Breaking and Shape Control in Single-Crystal Gold Nanorods. *Acc. Chem. Res.* **2017**, *50*, 2925−2935.
(283) Gole, A.; Murphy, C. J. Seed-Mediated Synthesis of Gold Nanorods: Role of the Size and Nature of the Seed. *Chem. Mater.* **2004**, *16*, 3633−3640.
(284) Jiang, X. C.; Pileni, M. P. Gold Nanorods: Influence of Various Parameters as Seeds, Solvent, Surfactant on Shape Control. *Colloids Surf., A* **2007**, *295*, 228−232.
(285) Voorhees, P. W. The Theory of Ostwald Ripening. *J. Stat. Phys.* **1985**, *38*, 231−252.
(286) Sau, T. K.; Murphy, C. J. Seeded High Yield Synthesis of Short Au Nanorods in Aqueous Solution. *Langmuir* **2004**, *20*, 6414−6420.

DOI: 10.1021/acs.chemrev.8b00745
Chem. Rev. XXXX, XXX, XXX−XXX

(287) Lin, Z.; Cai, J. J.; Scriven, L. E.; Davis, H. T. Spherical-to-Wormlike Micelle Transition in CTAB Solutions. *J. Phys. Chem.* **1994**, *98*, 5984−5993.
(288) Smith, D. K.; Korgel, B. A. The Importance of the CTAB Surfactant on the Colloidal Seed-Mediated Synthesis of Gold Nanorods. *Langmuir* **2008**, *24*, 644−649.
(289) Zhao, P.; Li, N.; Astruc, D. State of the Art in Gold Nanoparticle Synthesis. *Coord. Chem. Rev.* **2013**, *257*, 638−665.
(290) Nikoobakht, B.; El-Sayed, M. A. Evidence for Bilayer Assembly of Cationic Surfactants on the Surface of Gold Nanorods. *Langmuir* **2001**, *17*, 6368−6374.
(291) Murphy, C. J.; Thompson, L. B.; Alkilany, A. M.; Sisco, P. N.; Boulos, S. P.; Sivapalan, S. T.; Yang, J. A.; Chernak, D. J.; Huang, J. The Many Faces of Gold Nanorods. *J. Phys. Chem. Lett.* **2010**, *1*, 2867−2875.
(292) Meena, S. K.; Sulpizi, M. From Gold Nanoseeds to Nanorods: The Microscopic Origin of the Anisotropic Growth. *Angew. Chem.* **2016**, *128*, 12139−12143.
(293) Guerrero-Martínez, A.; Pérez-Juste, J.; Carbó-Argibay, E.; Tardajos, G.; Liz-Marzán, L. M. Gemini-Surfactant-Directed Self-Assembly of Monodisperse Gold Nanorods into Standing Superlattices. *Angew. Chem.* **2009**, *121*, 9648−9652.
(294) Rayavarapu, R. G.; Ungureanu, C.; Krystek, P.; Van Leeuwen, T. G.; Manohar, S. Iodide Impurities in Hexadecyltrimethylammonium Bromide (CTAB) Products: Lot-Lot Variations and Influence on Gold Nanorod Synthesis. *Langmuir* **2010**, *26*, 5050−5055.
(295) Millstone, J. E.; Wei, W.; Jones, M. R.; Yoo, H.; Mirkin, C. A. Iodide Ions Control Seed-Mediated Growth of Anisotropic Gold Nanoparticles. *Nano Lett.* **2008**, *8*, 2526−2529.
(296) Grzelczak, M.; Sánchez-Iglesias, A.; Rodríguez-González, B.; Alvarez-Puebla, R.; Pérez-Juste, J.; Liz-Marzán, L. M. Influence of Iodide Ions on the Growth of Gold Nanorods: Tuning Tip Curvature and Surface Plasmon Resonance. *Adv. Funct. Mater.* **2008**, *18*, 3780−3786.
(297) Jackson, S. R.; McBride, J. R.; Rosenthal, S. J.; Wright, D. W. Where's the Silver? Imaging Trace Silver Coverage on the Surface of Gold Nanorods. *J. Am. Chem. Soc.* **2014**, *136*, 5261−5263.
(298) Hubert, F.; Testard, F.; Spalla, O. Cetyltrimethylammonium Bromide Silver Bromide Complex as the Capping Agent of Gold Nanorods. *Langmuir* **2008**, *24*, 9219−9222.
(299) Soh, J. H.; Lin, Y.; Thomas, M. R.; Todorova, N.; Kallepitis, C.; Yarovsky, I.; Ying, J. Y.; Stevens, M. M. Distinct Bimodal Roles of Aromatic Molecules in Controlling Gold Nanorod Growth for Biosensing. *Adv. Funct. Mater.* **2017**, *27*, 1700523.
(300) Ye, X.; Jin, L.; Caglayan, H.; Chen, J.; Xing, G.; Zheng, C.; Doan-Nguyen, V.; Kang, Y.; Engheta, N.; Kagan, C. R.; et al. Improved Size-Tunable Synthesis of Monodisperse Gold Nanorods through the Use of Aromatic Additives. *ACS Nano* **2012**, *6*, 2804−2817.
(301) Busbee, B. D.; Obare, S. O.; Murphy, C. J. An Improved Synthesis of High-Aspect-Ratio Gold Nanorods. *Adv. Mater.* **2003**, *15*, 414−416.
(302) Liu, X.; Yao, J.; Luo, J.; Duan, X.; Yao, Y.; Liu, T. Effect of Growth Temperature on Tailoring the Size and Aspect Ratio of Gold Nanorods. *Langmuir* **2017**, *33*, 7479−7485.
(303) Scarabelli, L.; Grzelczak, M.; Liz-Marzán, L. M. Tuning Gold Nanorod Synthesis through Prereduction with Salicylic Acid. *Chem. Mater.* **2013**, *25*, 4232−4238.
(304) Kozek, K. A.; Kozek, K. M.; Wu, W. C.; Mishra, S. R.; Tracy, J. B. Large-Scale Synthesis of Gold Nanorods through Continuous Secondary Growth. *Chem. Mater.* **2013**, *25*, 4537−4544.
(305) Rodríguez-Fernández, J.; Pérez-Juste, J.; Mulvaney, P.; Liz-Marzán, L. M. Spatially-Directed Oxidation of Gold Nanoparticles by Au(III)-CTAB Complexes. *J. Phys. Chem. B* **2005**, *109*, 14257−14261.
(306) Jana, N. R. Gram-Scale Synthesis of Soluble, Near-Monodisperse Gold Nanorods and Other Anisotropic Nanoparticles. *Small* **2005**, *1*, 875−882.
(307) Wu, B.; Heidelberg, A.; Boland, J. J. Mechanical Properties of Ultrahigh-Strength Gold Nanowires. *Nat. Mater.* **2005**, *4*, 525−529.
(308) Forrer, P.; Schlottig, F.; Siegenthaler, H.; Textor, M. Electrochemical Preparation and Surface Properties of Gold Nanowire Arrays Formed by the Template Technique. *J. Appl. Electrochem.* **2000**, *30*, 533−541.
(309) Lu, X.; Yavuz, M. S.; Tuan, H.; Korgel, B. A.; Xia, Y. Ultrathin Gold Nanowires Can Be Obtained by Reducing Polymeric Strands of Oleylamine-AuCl Complexes Formed via Aurophilic Interaction. *J. Am. Chem. Soc.* **2008**, *130*, 8900−8901.
(310) Huo, Z.; Tsung, C.; Huang, W.; Zhang, X.; Yang, P. Sub-Two Nanometer Single Crystal Au Nanowires. *Nano Lett.* **2008**, *8*, 2041−2044.
(311) Wang, C.; Hu, Y.; Lieber, C. M.; Sun, S. Ultrathin Au Nanowires and Their Transport Properties. *J. Am. Chem. Soc.* **2008**, *130*, 8902−8903.
(312) Wang, C.; Wei, Y.; Jiang, H.; Sun, S. Bending Nanowire Growth in Solution by Mechanical Disturbance. *Nano Lett.* **2010**, *10*, 2121−2125.
(313) Hong, X.; Wang, D.; Li, Y. Kinked Gold Nanowires and Their SPR/SERS Properties. *Chem. Commun.* **2011**, *47*, 9909−9911.
(314) Huang, X.; Li, S.; Wu, S.; Huang, Y.; Boey, F.; Gan, C. L.; Zhang, H. Graphene Oxide-Templated Synthesis of Ultrathin or Tadpole-Shaped Au Nanowires with Alternating *hcp* and *fcc* Domains. *Adv. Mater.* **2012**, *24*, 979−983.
(315) Zhang, H.; Jin, M.; Xiong, Y.; Lim, B.; Xia, Y. Shape-Controlled Synthesis of Pd Nanocrystals and Their Catalytic Applications. *Acc. Chem. Res.* **2013**, *46*, 1783−1794.
(316) Baldi, A.; Narayan, T. C.; Koh, A. L.; Dionne, J. A. In Situ Detection of Hydrogen-Induced Phase Transitions in Individual Palladium Nanocrystals. *Nat. Mater.* **2014**, *13*, 1143−1148.
(317) Chen, A.; Ostrom, C. Palladium-Based Nanomaterials: Synthesis and Electrochemical Applications. *Chem. Rev.* **2015**, *115*, 11999−12044.
(318) Delin, A.; Tosatti, E.; Weht, R. Magnetism in Atomic-Size Palladium Contacts and Nanowires. *Phys. Rev. Lett.* **2004**, *92*, 057201.
(319) Xiong, Y.; Cai, H.; Yin, Y.; Xia, Y. Synthesis and Characterization of Fivefold Twinned Nanorods and Right Bipyramids of Palladium. *Chem. Phys. Lett.* **2007**, *440*, 273−278.
(320) Huang, H.; Zhang, L.; Lv, T.; Ruditskiy, A.; Liu, J.; Ye, Z.; Xia, Y. Five-Fold Twinned Pd Nanorods and Their Use as Templates for the Synthesis of Bimetallic or Hollow Nanostructures. *ChemNanoMat* **2015**, *1*, 246−252.
(321) Bisson, L.; Boissiere, C.; Nicole, L.; Grosso, D.; Jolivet, J. P.; Thomazeau, C.; Uzio, D.; Berhault, G.; Sanchez, C. Formation of Palladium Nanostructures in a Seed-Mediated Synthesis through an Oriented-Attachment-Directed Aggregation. *Chem. Mater.* **2009**, *21*, 2668−2678.
(322) Chen, Y. H.; Hung, H. H.; Huang, M. H. Seed-Mediated Synthesis of Palladium Nanorods and Branched Nanocrystals and Their Use as Recyclable Suzuki Coupling Reaction Catalysts. *J. Am. Chem. Soc.* **2009**, *131*, 9114−9121.
(323) Xiao, C.; Ding, H.; Shen, C.; Yang, T.; Hui, C.; Gao, H. Shape-Controlled Synthesis of Palladium Nanorods and Their Magnetic Properties. *J. Phys. Chem. C* **2009**, *113*, 13466−13469.
(324) Yu, Y.; Zhao, Y.; Huang, T.; Liu, H. Microwave-Assisted Synthesis of Palladium Nanocubes and Nanobars. *Mater. Res. Bull.* **2010**, *45*, 159−164.
(325) Shao, Z.; Zhu, W.; Wang, H.; Yang, Q.; Yang, S.; Liu, X.; Wang, G. Controllable Synthesis of Concave Nanocubes, Right Bipyramids, and 5-Fold Twinned Nanorods of Palladium and Their Enhanced Electrocatalytic Performance. *J. Phys. Chem. C* **2013**, *117*, 14289−14294.
(326) Tang, Y.; Edelmann, R. E.; Zou, S. Length Tunable Penta-Twinned Palladium Nanorods: Seedless Synthesis and Electrooxidation of Formic Acid. *Nanoscale* **2014**, *6*, 5630−5633.
(327) Huang, X.; Zheng, N. One-Pot, High-Yield Synthesis of 5-Fold Twinned Pd Nanowires and Nanorods. *J. Am. Chem. Soc.* **2009**, *131*, 4602−4603.

DOI: 10.1021/acs.chemrev.8b00745
Chem. Rev. XXXX, XXX, XXX−XXX

(328) Zhang, Z.-C.; Zhang, X.; Yu, Q.-Y.; Liu, Z.-C.; Xu, C.-M.; Gao, J.-S.; Zhuang, J.; Wang, X. Pd Cluster Nanowires as Highly Efficient Catalysts for Selective Hydrogenation Reactions. *Chem. - Eur. J.* **2012**, *18*, 2639−2645.
(329) Kiriy, A.; Minko, S.; Gorodyska, G.; Stamm, M.; Jaeger, W. Palladium Wire-Shaped Nanoparticles from Single Synthetic Polycation Molecules. *Nano Lett.* **2002**, *2*, 881−885.
(330) Al-Hinai, M. N.; Hassanien, R.; Wright, N. G.; Horsfall, A. B.; Houlton, A.; Horrocks, B. R. Networks of DNA-Templated Palladium Nanowires: Structural and Electrical Characterisation and Their Use as Hydrogen Gas Sensors. *Faraday Discuss.* **2013**, *164*, 71−91.
(331) Siril, P. F.; Lehoux, A.; Ramos, L.; Beaunier, P.; Remita, H. Facile Synthesis of Palladium Nanowires by a Soft Templating Method. *New J. Chem.* **2012**, *36*, 2135−2139.
(332) Xu, D.; Liu, X.; Han, M.; Bao, J. Facile Synthesis of Ultrathin Single-Crystalline Palladium Nanowires with Enhanced Electrocatalytic Activities. *Chem. Commun.* **2016**, *52*, 12996−12999.
(333) Teng, X.; Han, W. Q.; Ku, W.; Hücker, M. Synthesis of Ultrathin Palladium and Platinum Nanowires and a Study of Their Magnetic Properties. *Angew. Chem.* **2008**, *120*, 2085−2088.
(334) Liang, B. H.; Liu, S.; Gong, J.; Wang, S.; Wang, L.; Yu, S. Ultrathin Te Nanowires : An Excellent Platform for Controlled Synthesis of Ultrathin Platinum and Palladium Nanowires/Nanotubes with Very High Aspect Ratio. *Adv. Mater.* **2009**, *21*, 1850−1854.
(335) Gao, S.; Zhang, H.; Wang, X.; Mai, W.; Peng, C.; Ge, L. Palladium Nanowires Stabilized by Thiol-Functionalized Ionic Liquid: Seed-Mediated Synthesis and Heterogeneous Catalyst for Sonogashira Coupling Reaction. *Nanotechnology* **2005**, *16*, 1234−1237.
(336) Chen, J.; Lim, B.; Lee, E. P.; Xia, Y. Shape-Controlled Synthesis of Platinum Nanocrystals for Catalytic and Electrocatalytic Applications. *Nano Today* **2009**, *4*, 81−95.
(337) Chen, A.; Holt-hindle, P. Platinum-Based Nanostructured Materials: Synthesis, Properties, and Applications. *Chem. Rev.* **2010**, *110*, 3767−3804.
(338) Peng, Z.; Yang, H. Designer Platinum Nanoparticles: Control of Shape, Composition in Alloy, Nanostructure and Electrocatalytic Property. *Nano Today* **2009**, *4*, 143−164.
(339) Li, C.; Tan, H.; Lin, J.; Luo, X.; Wang, S.; You, J.; Kang, Y. M.; Bando, Y.; Yamauchi, Y.; Kim, J. Emerging Pt-Based Electrocatalysts with Highly Open Nanoarchitectures for Boosting Oxygen Reduction Reaction. *Nano Today* **2018**, *21*, 91−105.
(340) Lee, E. P.; Peng, Z.; Cate, D. M.; Yang, H.; Campbell, C. T.; Xia, Y. Growing Pt Nanowires as a Densely Packed Array on Metal Gauze. *J. Am. Chem. Soc.* **2007**, *129*, 10634−10635.
(341) Lee, E. P.; Peng, Z.; Chen, W.; Chen, S.; Yang, H.; Xia, Y. Electrocatalytic Properties of Pt Nanowires Supported on Pt and W Gauzes. *ACS Nano* **2008**, *2*, 2167−2173.
(342) Lee, E. P.; Xia, Y. Growth and Patterning of Pt Nanowires on Silicon Substrates. *Nano Res.* **2008**, *1*, 129−137.
(343) Chen, J.; Herricks, T.; Geissler, M.; Xia, Y. Single-Crystal Nanowires of Platinum Can. Be Synthesized by Controlling the Reaction Rate of a Polyol Process. *J. Am. Chem. Soc.* **2004**, *126*, 10854−10855.
(344) Chen, J.; Xiong, Y.; Yin, Y.; Xia, Y. Pt Nanoparticles Surfactant-Directed Assembled into Colloidal Spheres and Used as Substrates in Forming Pt Nanorods and Nanowires. *Small* **2006**, *2*, 1340−1343.
(345) Yin, H.; Zhao, S.; Zhao, K.; Muqsit, A.; Tang, H.; Chang, L.; Zhao, H.; Gao, Y.; Tang, Z. Ultrathin Platinum Nanowires Grown on Single-Layered Nickel Hydroxide with High Hydrogen Evolution Activity. *Nat. Commun.* **2015**, *6*, 6430.
(346) Hoque, M. A.; Hassan, F. M.; Higgins, D.; Choi, J. Y.; Pritzker, M.; Knights, S.; Ye, S.; Chen, Z. Multigrain Platinum Nanowires Consisting of Oriented Nanoparticles Anchored on Sulfur-Doped Graphene as a Highly Active and Durable Oxygen Reduction Electrocatalyst. *Adv. Mater.* **2015**, *27*, 1229−1234.
(347) Volosskiy, B.; Niwa, K.; Chen, Y.; Zhao, Z.; Weiss, N. O.; Zhong, X.; Ding, M.; Lee, C.; Huang, Y.; Duan, X. Metal-Organic Framework Templated Synthesis of Ultrathin, Well-Aligned Metallic Nanowires. *ACS Nano* **2015**, *9*, 3044−3049.
(348) Koenigsmann, C.; Zhou, W. P.; Adzic, R. R.; Sutter, E.; Wong, S. S. Size-Dependent Enhancement of Electrocatalytic Performance in Relatively Defect-Free, Processed Ultrathin Platinum Nanowires. *Nano Lett.* **2010**, *10*, 2806−2811.
(349) Ruan, L.; Zhu, E.; Chen, Y.; Lin, Z.; Huang, X.; Duan, X.; Huang, Y. Biomimetic Synthesis of an Ultrathin Platinum Nanowire Network with a High Twin Density for Enhanced Electrocatalytic Activity and Durability. *Angew. Chem., Int. Ed.* **2013**, *52*, 12577−12581.
(350) Chen, G.; Xu, C.; Huang, X.; Ye, J.; Gu, L.; Li, G.; Tang, Z.; Wu, B.; Yang, H.; Zhao, Z.; et al. Interfacial Electronic Effects Control the Reaction Selectivity of Platinum Catalysts. *Nat. Mater.* **2016**, *15*, 564−569.
(351) Xia, B. Y.; Wu, H. B.; Yan, Y.; Lou, X. W.; Wang, X. Ultrathin and Ultralong Single-Crystal Platinum Nanowire Assemblies with Highly Stable Electrocatalytic Activity. *J. Am. Chem. Soc.* **2013**, *135*, 9480−9485.
(352) Sun, S.; Murray, C. B.; Weller, D.; Folks, L.; Moser, A. Monodisperse FePt Nanoparticles and Ferromagnetic FePt Nanocrystal Superlattices. *Science* **2000**, *287*, 1989−1992.
(353) Zhu, Y.; Stubbs, L. P.; Ho, F.; Liu, R.; Ship, C. P.; Maguire, J. A.; Hosmane, N. S. Magnetic Nanocomposites: A New Perspective in Catalysis. *ChemCatChem* **2010**, *2*, 365−374.
(354) Nadagouda, M. N.; Varma, R. S. Microwave-Assisted Shape-Controlled Bulk Synthesis of Ag and Fe Nanorods in Poly(ethylene glycol) Solutions. *Cryst. Growth Des.* **2008**, *8*, 291−295.
(355) Ji, G.; Gong, Z.; Liu, Y.; Chang, X.; Du, Y.; Qamar, M. Fabrication and Magnetic Properties of Cobalt Nanorod Arrays Containing a Number of Ultrafine Nanowires Electrodeposited within an AAO/SBA-15 Template. *Solid State Commun.* **2011**, *151*, 1151−1155.
(356) Liu, Q.; Guo, X.; Chen, J.; Li, J.; Song, W.; Shen, W. Cobalt Nanowires Prepared by Heterogeneous Nucleation in Propanediol and Their Catalytic Properties. *Nanotechnology* **2008**, *19*, 365608.
(357) Soumare, Y.; Garcia, C.; Maurer, T.; Chaboussant, G.; Ott, F.; Fiévet, F.; Piquemal, J. Y.; Viau, G. Kinetically Controlled Synthesis of Hexagonally Close-Packed Cobalt Nanorods with High Magnetic Coercivity. *Adv. Funct. Mater.* **2009**, *19*, 1971−1977.
(358) Nethravathi, C.; Rajamathi, C. R.; Singh, S.; Rajamathi, M.; Felser, C. High Coercivity Stellated Cobalt Metal Multipods through Solvothermal Reduction of Cobalt Hydroxide Nanosheets. *RSC Adv.* **2017**, *7*, 1413−1417.
(359) Xie, B. Q.; Qian, Y.; Zhang, S.; Fu, S.; Yu, W. A Hydrothermal Reduction Route to Single-Crystalline Hexagonal Cobalt Nanowires. *Eur. J. Inorg. Chem.* **2006**, *2006*, 2454−2459.
(360) Zhu, L. P.; Xiao, H. M.; Zhang, W. D.; Yang, Y.; Fu, S. Y. Synthesis and Characterization of Novel Three-Dimensional Metallic Co Dendritic Superstructures by a Simple Hydrothermal Reduction Route. *Cryst. Growth Des.* **2008**, *8*, 1113−1118.
(361) Meziane, L.; Salzemann, C.; Aubert, C.; Gérard, H.; Petit, C.; Petit, M. Hcp Cobalt Nanocrystals with High Magnetic Anisotropy Prepared by Easy One-Pot Synthesis. *Nanoscale* **2016**, *8*, 18640−18645.
(362) Wang, Z. K.; Kuok, M. H.; Ng, S. C.; Lockwood, D. J.; Cottam, M. G.; Nielsch, K.; Wehrspohn, R. B.; Gösele, U. Spin-Wave Quantization in Ferromagnetic Nickel Nanowires. *Phys. Rev. Lett.* **2002**, *89*, 027201.
(363) Liu, Z.; Li, S.; Yang, Y.; Peng, S.; Hu, Z.; Qian, Y. Complex-Surfactant-Assisted Hydrothermal Route to Ferromagnetic Nickel Nanobelts. *Adv. Mater.* **2003**, *15*, 1946−1948.
(364) Knez, M.; Bittner, A. M.; Boes, F.; Wege, C.; Jeske, H.; Maiß, E.; Kern, K. Biotemplate Synthesis of 3-nm Nickel and Cobalt Nanowires. *Nano Lett.* **2003**, *3*, 1079−1082.
(365) DeSantis, C. J.; McClain, M. J.; Halas, N. J. *ACS Nano* **2016**, *10*, 9772−9775.

DOI: 10.1021/acs.chemrev.8b00745
Chem. Rev. XXXX, XXX, XXX−XXX

(366) Clark, B. D.; Jacobson, C. R.; Lou, M.; Yang, J.; Zhou, L.; Gottheim, S.; DeSantis, C. J.; Nordlander, P.; Halas, N. J. Aluminum Nanorods. *Nano Lett.* **2018**, *18*, 1234−1240.
(367) Lin, W.; Christensen, P. A.; Hamnett, A.; Zei, M. S.; Ertl, G. The Electro-Oxidation of CO at the Ru(0001) Single-Crystal Electrode Surface. *J. Phys. Chem. B* **2000**, *104*, 6642−6652.
(368) Su, F.; Lv, L.; Lee, F. Y.; Liu, T.; Cooper, A. I.; Zhao, X. S. Thermally Reduced Ruthenium Nanoparticles as a Highly Active Heterogeneous Catalyst for Hydrogenation of Monoaromatics. *J. Am. Chem. Soc.* **2007**, *129*, 14213−14223.
(369) Chen, G.; Zhang, J.; Gupta, A.; Rosei, F.; Ma, D. Shape-Controlled Synthesis of Ruthenium Nanocrystals and Their Catalytic Applications. *New J. Chem.* **2014**, *38*, 1827−1833.
(370) Ghosh, S.; Ghosh, M.; Rao, C. N. R. Nanocrystals, Nanorods and Other Nanostructures of Nickel, Ruthenium, Rhodium and Iridium Prepared by a Simple Solvothermal Procedure. *J. Cluster Sci.* **2007**, *18*, 97−111.
(371) Vanden Brink, M.; Peck, M. A.; More, K. L.; Hoefelmeyer, J. D. Alkylamine Stabilized Ruthenium Nanocrystals: Faceting and Branching. *J. Phys. Chem. C* **2008**, *112*, 12122−12126.
(372) Lignier, P.; Bellabarba, R.; Tooze, R. P.; Su, Z.; Landon, P.; Ménard, H.; Zhou, W. Facile Synthesis of Branched Ruthenium Nanocrystals and Their Use in Catalysis. *Cryst. Growth Des.* **2012**, *12*, 939−942.
(373) Watt, J.; Yu, C.; Chang, S. L. Y.; Cheong, S.; Tilley, R. D. Shape Control from Thermodynamic Growth Conditions: The Case of hcp Ruthenium Hourglass Nanocrystals. *J. Am. Chem. Soc.* **2013**, *135*, 606−609.
(374) Xie, S.; Liu, X.; Xia, Y. Shape-Controlled Syntheses of Rhodium Nanocrystals for the Enhancement of Their Catalytic properties. *Nano Res.* **2015**, *8*, 82−96.
(375) Zhang, J.; Ye, J.; Fan, Q.; Jiang, Y.; Zhu, Y.; Li, H.; Cao, Z.; Kuang, Q.; Cheng, J.; Zheng, J.; Xie, Z. Cyclic Penta-Twinned Rhodium Nanobranches as Superior Catalysts for Ethanol Electro-oxidation. *J. Am. Chem. Soc.* **2018**, *140*, 11232−11240.
(376) Hoefelmeyer, J. D.; Niesz, K.; Somorjai, G. A.; Tilley, T. D. Radial Anisotropic Growth of Rhodium Nanoparticles. *Nano Lett.* **2005**, *5*, 435−438.
(377) Biacchi, A. J.; Schaak, R. E. The Solvent Matters: Kinetic versus Thermodynamic Shape Control in the Polyol Synthesis of Rhodium Nanoparticles. *ACS Nano* **2011**, *5*, 8089−8099.
(378) Zettsu, N.; McLellan, J. M.; Wiley, B.; Yin, Y.; Li, Z.; Xia, Y. Synthesis, Stability, and Surface Plasmonic Properties of Rhodium Multipods, and Their Use as Substrates for Surface-Enhanced Raman Scattering. *Angew. Chem.* **2006**, *118*, 1310−1314.
(379) Huang, X.; Zhao, Z.; Chen, Y.; Chiu, C.-Y.; Ruan, L.; Liu, Y.; Li, M.; Duan, X.; Huang, Y. High Density Catalytic Hot Spots in Ultrafine Wavy Nanowires. *Nano Lett.* **2014**, *14*, 3887−3894.
(380) Kim, H.; Khi, N. T.; Yoon, J.; Yang, H.; Chae, Y.; Baik, H.; Lee, H.; Sohn, J.-H.; Lee, K. Fabrication of Hierarchical Rh Nanostructures by Understanding the Growth Kinetics of Facet-Controlled Rh Nanocrystals. *Chem. Commun.* **2013**, *49*, 2225−2227.
(381) Yuan, Q.; Zhou, Z.; Zhuang, J.; Wang, X. Tunable Aqueous Phase Synthesis and Shape-Dependent Electrochemical Properties of Rhodium Nanostructures. *Inorg. Chem.* **2010**, *49*, 5515−5521.
(382) Wang, Y.; Jiang, X.; Herricks, T.; Xia, Y. Single Crystalline Nanowires of Lead: Large-Scale Synthesis, Mechanistic Studies, and Transport Measurements. *J. Phys. Chem. B* **2004**, *108*, 8631−8640.
(383) Wang, F.; Dong, A.; Sun, J.; Tang, R.; Yu, H.; Buhro, W. E. Solution-Liquid-Solid Growth of Semiconductor Nanowires. *Inorg. Chem.* **2006**, *45*, 7511−7521.
(384) Wang, C. Y.; Lu, M. Y.; Chen, H. C.; Chen, L. J. Single-Crystalline Pb Nanowires Grown by Galvanic Displacement Reactions of Pb Ions on Zinc Foils and Their Superconducting Properties. *J. Phys. Chem. C* **2007**, *111*, 6215−6219.
(385) Gilroy, K. D.; Ruditskiy, A.; Peng, H. C.; Qin, D.; Xia, Y. Bimetallic Nanocrystals: Syntheses, Properties, and Applications. *Chem. Rev.* **2016**, *116*, 10414−10472.
(386) Ferrando, R.; Jellinek, J.; Johnston, R. L. Nanoalloys: From Theory to Applications of Alloy Clusters and Nanoparticles. *Chem. Rev.* **2008**, *108*, 845−910.
(387) Lu, Y.; Chen, W. PdAg Alloy Nanowires: Facile One-Step Synthesis and High Electrocatalytic Activity for Formic Acid Oxidation. *ACS Catal.* **2012**, *2*, 84−90.
(388) Choi, B. S.; Lee, Y. W.; Kang, S. W.; Hong, J. W.; Kim, J.; Park, I.; Han, S. W. Multimetallic Alloy Nanotubes with Nanoporous Framework. *ACS Nano* **2012**, *6*, 5659−5667.
(389) Goia, D. V.; Matijevic, E. Preparation of Monodispersed Metal Particles. *New J. Chem.* **1998**, *22*, 1203−1215.
(390) Dursun, A.; Pugh, D. V.; Corcoran, S. G. Dealloying of Ag-Au Alloys in Halide-Containing Electrolytes Affect on Critical Potential and Pore Size. *J. Electrochem. Soc.* **2003**, *150*, B355−B360.
(391) Jiang, X.; Zeng, Q.; Yu, A. A Self-Seeding Coreduction Method for Shape Control of Silver Nanoplates. *Nanotechnology* **2006**, *17*, 4929−4935.
(392) Xu, J. B.; Zhao, T. S.; Liang, Z. X. Synthesis of Active Platinum-Silver Alloy Electrocatalyst toward the Formic Acid Oxidation Reaction. *J. Phys. Chem. C* **2008**, *112*, 17362−17367.
(393) Bower, M. M.; Desantis, C. J.; Skrabalak, S. E. A Quantitative Analysis of Anions and pH on the Growth of Bimetallic Nanostructures. *J. Phys. Chem. C* **2014**, *118*, 18762−18770.
(394) Liu, Q.; Yan, Z.; Henderson, N. L.; Bauer, J. C.; Goodman, D. W.; Batteas, J. D.; Schaak, R. E. Synthesis of CuPt Nanorod Catalysts with Tunable Lengths. *J. Am. Chem. Soc.* **2009**, *131*, 5720−5721.
(395) Schwank, J. Bimetallic Catalysts: Discoveries, Concepts, and Applications. By John H. Sinfelt, John Wiley & Sons, 1983. XI + 164 pp. *AIChE J.* **1985**, *31*, 1405.
(396) Maksimuk, S.; Yang, S.; Peng, Z.; Yang, H. Synthesis and Characterization of Ordered Intermetallic PtPb Nanorods. *J. Am. Chem. Soc.* **2007**, *129*, 8684−8685.
(397) Gilroy, K. D.; Farzinpour, P.; Sundar, A.; Hughes, R. A.; Neretina, S. Sacrificial Templates for Galvanic Replacement Reactions: Design Criteria for the Synthesis of Pure Pt Nanoshells with a Smooth Surface Morphology. *Chem. Mater.* **2014**, *26*, 3340−3347.
(398) Cobley, C. M.; Xia, Y. Engineering the Properties of Metal Nanostructures via Galvanic Replacement Reactions. *Mater. Sci. Eng., R* **2010**, *70*, 44−62.
(399) Sun, H.; Guo, X.; Ye, W.; Kou, S.; Yang, J. Charge Transfer Accelerates Galvanic Replacement for PtAgAu Nanotubes with Enhanced Catalytic Activity. *Nano Res.* **2016**, *9*, 1173−1181.
(400) Nishimura, S.; Dao, A. T. N.; Mott, D.; Ebitani, K.; Maenosono, S. X-Ray Absorption near-Edge Structure and X-Ray Photoelectron Spectroscopy Studies of Interfacial Charge Transfer in Gold-Silver-Gold Double-Shell Nanoparticles. *J. Phys. Chem. C* **2012**, *116*, 4511−4516.
(401) Wang, Z.; Liu, J.; Chen, X.; Wan, J.; Qian, Y. A Simple Hydrothermal Route to Large-Scale Synthesis of Uniform Silver Nanowires. *Chem. - Eur. J.* **2005**, *11*, 160−163.
(402) Gómez-Graña, S.; Goris, B.; Altantzis, T.; Fernández-López, C.; Carbó-Argibay, E.; Guerrero-Martínez, A.; Almora-Barrios, N.; López, N.; Pastoriza-Santos, I.; Pérez-Juste, J.; Bals, S.; Van Tendeloo, G.; Liz-Marzán, L. M. Au@Ag Nanoparticles: Halides Stabilize {100} Facets. *J. Phys. Chem. Lett.* **2013**, *4*, 2209−2216.
(403) Park, K.; Vaia, R. A. Synthesis of Complex Au/Ag Nanorods by Controlled Overgrowth. *Adv. Mater.* **2008**, *20*, 3882−3886.
(404) Elechiguerra, J. L.; Reyes-Gasga, J.; Yacaman, M. J. The Role of Twinning in Shape Evolution of Anisotropic Noble Metal Nanostructures. *J. Mater. Chem.* **2006**, *16*, 3906−3919.
(405) Bögels, G.; Meekes, H.; Bennema, P.; Bollen, D. Growth Mechanism of Vapor-Grown Silver Crystals : Relation between Twin Formation and Morphology. *J. Phys. Chem. B* **1999**, *103*, 7577−7583.
(406) Zhuo, X.; Zhu, X.; Li, Q.; Yang, Z.; Wang, J. Gold Nanobipyramid-Directed Growth of Length-Variable Silver Nanorods with Multipolar Plasmon Resonances. *ACS Nano* **2015**, *9*, 7523−7535.

DOI: 10.1021/acs.chemrev.8b00745
Chem. Rev. XXXX, XXX, XXX−XXX

(407) Liu, S.; Niu, W.; Firdoz, S.; Zhang, W. Iodide-Switched Deposition for the Synthesis of Segmented Pd-Au-Pd Nanorods: Crystal Facet Matters. *Langmuir* **2017**, *33*, 12254−12259.
(408) Zhang, H.; Jin, M.; Xia, Y. Enhancing the Catalytic and Electrocatalytic Properties of Pt-Based Catalysts by Forming Bimetallic Nanocrystals with Pd. *Chem. Soc. Rev.* **2012**, *41*, 8035−8049.
(409) Fu, G.; Liu, Z.; Chen, Y.; Lin, J.; Tang, Y.; Lu, T. Synthesis and Electrocatalytic Activity of Au@Pd Core-Shell Nanothorns for the Oxygen Reduction Reaction. *Nano Res.* **2014**, *7*, 1205−1214.
(410) Chen, J.; Chen, J.; Li, Y.; Zhou, W.; Feng, X.; Huang, Q.; Zheng, J. G.; Liu, R.; Ma, Y.; Huang, W. Enhanced Oxidation-Resistant Cu-Ni Core-Shell Nanowires: Controllable One-Pot Synthesis and Solution Processing to Transparent Flexible Heaters. *Nanoscale* **2015**, *7*, 16874−16879.
(411) Zhang, K.; Xiang, Y.; Wu, X.; Feng, L.; He, W.; Liu, J.; Zhou, W.; Xie, S. Enhanced Optical Responses of Au@Pd Core/Shell Nanobars. *Langmuir* **2009**, *25*, 1162−1168.
(412) Guo, S.; Dong, S.; Wang, E. Ultralong Pt-on-Pd Bimetallic Nanowires with Nanoporous Surface: Nanodendritic Structure for Enhanced Electrocatalytic Activity. *Chem. Commun.* **2010**, *46*, 1869−1871.
(413) Li, J.; Zheng, Y.; Zeng, J.; Xia, Y. Controlling the Size and Morphology of Au@Pd Core−Shell Nanocrystals by Manipulating the Kinetics of Seeded Growth. *Chem. - Eur. J.* **2012**, *18*, 8150−8156.
(414) Yang, M.; Hood, Z. D.; Yang, X.; Chi, M.; Xia, Y. Facile Synthesis of Ag@Au Core-Sheath Nanowires with Greatly Improved Stability against Oxidation. *Chem. Commun.* **2017**, *53*, 1965−1968.
(415) Tsuji, M.; Ikedo, K.; Uto, K.; Matsunaga, M.; Yoshida, Y.; Takemura, K.; Niidome, Y. Formation of Au@Pd@Cu Core-Shell Nanorods from Au@Pd Nanorods through a New Stepwise Growth Mode. *CrystEngComm* **2013**, *15*, 6553−6563.
(416) Zhang, N.; Guo, S.; Zhu, X.; Guo, J.; Huang, X. Hierarchical Pt/Pt_xPb Core/Shell Nanowires as Efficient Catalysts for Electro-oxidation of Liquid Fuels. *Chem. Mater.* **2016**, *28*, 4447−4452.
(417) Zhang, N.; Feng, Y.; Zhu, X.; Guo, S.; Guo, J.; Huang, X. Superior Bifunctional Liquid Fuel Oxidation and Oxygen Reduction Electrocatalysis Enabled by PtNiPd Core−Shell Nanowires. *Adv. Mater.* **2017**, *29*, 1603774.
(418) Koenigsmann, C.; Santulli, A. C.; Gong, K.; Vukmirovic, M. B.; Zhou, W. P.; Sutter, E.; Wong, S. S.; Adzic, R. R. Enhanced Electrocatalytic Performance of Processed, Ultrathin, Supported Pd-Pt Core-Shell Nanowire Catalysts for the Oxygen Reduction Reaction. *J. Am. Chem. Soc.* **2011**, *133*, 9783−9795.
(419) Sławiński, G. W.; Zamborini, F. P. Synthesis and Alignment of Silver Nanorods and Nanowires and the Formation of Pt, Pd, and Core/Shell Structures by Galvanic Exchange Directly on Surfaces. *Langmuir* **2007**, *23*, 10357−10365.
(420) Khalavka, Y.; Becker, J.; Sönnichsen, C. Synthesis of Rod-Shaped Gold Nanorattles with Improved Plasmon Sensitivity and Catalytic Activity. *J. Am. Chem. Soc.* **2009**, *131*, 1871−1875.
(421) Fan, Z.; Zhang, H. Template Synthesis of Noble Metal Nanocrystals with Unusual Crystal Structures and Their Catalytic Applications. *Acc. Chem. Res.* **2016**, *49*, 2841−2850.
(422) Chen, Y.; Fan, Z.; Zhang, Z.; Niu, W.; Li, C.; Yang, N.; Chen, B.; Zhang, H. Two-Dimensional Metal Nanomaterials: Synthesis, Properties, and Applications. *Chem. Rev.* **2018**, *118*, 6409−6455.
(423) Fan, Z.; Huang, X.; Chen, Y.; Huang, W.; Zhang, H. Facile Synthesis of Gold Nanomaterials with Unusual Crystal Structures. *Nat. Protoc.* **2017**, *12*, 2367−2378.
(424) Zhao, M.; Figueroa-cosme, L.; Elnabawy, A. O.; Vara, M.; Yang, X.; Roling, L. T.; Chi, M.; Mavrikakis, M.; Xia, Y. Synthesis and Characterization of Ru Cubic Nanocages with a Face- Centered Cubic Structure by Templating with Pd Nanocubes. *Nano Lett.* **2016**, *16*, 5310−5317.
(425) Chen, Y.; Fan, Z.; Luo, Z.; Liu, X.; Lai, Z.; Li, B.; Zong, Y.; Gu, L.; Zhang, H. High-Yield Synthesis of Crystal-Phase-Heterostructured 4H/fcc Au@Pd Core−Shell Nanorods for Electrocatalytic Ethanol Oxidation. *Adv. Mater.* **2017**, *29*, 1701331.
(426) Fan, Z.; Luo, Z.; Chen, Y.; Wang, J.; Li, B.; Zong, Y.; Zhang, H. Synthesis of 4H/*fcc*-Au@M (M = Ir, Os, IrOs) Core-Shell Nanoribbons For Electrocatalytic Oxygen Evolution Reaction. *Small* **2016**, *12*, 3908−3913.
(427) Fan, Z.; Bosman, M.; Huang, X.; Huang, D.; Yu, Y.; Ong, K. P.; Akimov, Y. A.; Wu, L.; Li, B.; Wu, J.; et al. Stabilization of 4H Hexagonal Phase in Gold Nanoribbons. *Nat. Commun.* **2015**, *6*, 7684.
(428) Fan, Z.; Luo, Z.; Huang, X.; Li, B.; Chen, Y.; Wang, J.; Hu, Y.; Zhang, H. Synthesis of 4H/*fcc* Noble Multimetallic Nanoribbons for Electrocatalytic Hydrogen Evolution Reaction. *J. Am. Chem. Soc.* **2016**, *138*, 1414−1419.
(429) Cheng, H.; Yang, N.; Lu, Q.; Zhang, Z.; Zhang, H. Syntheses and Properties of Metal Nanomaterials with Novel Crystal Phases. *Adv. Mater.* **2018**, *30*, 1707189.
(430) Shen, X. S.; Wang, G. Z.; Hong, X.; Xie, X.; Zhu, W.; Li, D. P. Anisotropic Growth of One-Dimensional Silver Rod-Needle and Plate-Belt Heteronanostructures Induced by Twins and hcp Phase. *J. Am. Chem. Soc.* **2009**, *131*, 10812−10813.
(431) Liang, H.; Yang, H.; Wang, W.; Li, J.; Xu, H. High-Yield Uniform Synthesis and Microstructure-Determination of Rice-Shaped Silver Nanocrystals. *J. Am. Chem. Soc.* **2009**, *131*, 6068−6069.
(432) Liu, T.; Li, D.; Yang, D.; Jiang, M. Fabrication of Flower-like Silver Structures through Anisotropic Growth. *Langmuir* **2011**, *27*, 6211−6217.
(433) Liu, X.; Luo, J.; Zhu, J. Size Effect on the Crystal Structure of Silver Nanowires. *Nano Lett.* **2006**, *6*, 408−412.
(434) Singh, A.; Ghosh, A. Stabilizing High-Energy Crystal Structure in Silver Nanowires with Underpotential Electrochemistry. *J. Phys. Chem. C* **2008**, *112*, 3460−3463.
(435) Lim, B.; Xia, Y. Metal Nanocrystals with Highly Branched Morphologies. *Angew. Chem., Int. Ed.* **2011**, *50*, 76−85.
(436) Wang, S.; Kristian, N.; Jiang, S.; Wang, X. Controlled Synthesis of Dendritic Au@Pt Core-Shell Nanomaterials for Use as an Effective Fuel Cell Electrocatalyst. *Nanotechnology* **2009**, *20*, 025605.
(437) Lim, B.; Jiang, M.; Camargo, P. H. C.; Cho, E. C.; Tao, J.; Lu, X.; Zhu, Y.; Xia, Y. Pd-Pt Bimetallic Nanodendrites with High Activity for Oxygen Reduction. *Science* **2009**, *324*, 1302−1305.
(438) Elechiguerra, J. L.; Larios-Lopez, L.; Liu, C.; Garcia-Gutierrez, D.; Camacho-Bragado, A.; Yacaman, M. J. Corrosion at the Nanoscale: The Case of Silver Nanowires and Nanoparticles. *Chem. Mater.* **2005**, *17*, 6042−6052.
(439) Jiang, R.; Li, B.; Fang, C.; Wang, J. Metal/Semiconductor Hybrid Nanostructures for Plasmon-Enhanced Applications. *Adv. Mater.* **2014**, *26*, 5274−5309.
(440) Yin, Y.; Lu, Y.; Sun, Y.; Xia, Y. Silver Nanowires Can Be Directly Coated with Amorphous Silica To Generate Well-Controlled Coaxial Nanocables of Silver/Silica. *Nano Lett.* **2002**, *2*, 427−430.
(441) Liu, S.; Han, M. Y. Silica-Coated Metal Nanoparticles. *Chem. - Asian J.* **2009**, *5*, 36−45.
(442) Janković, V.; Yeng, Y.; You, J.; Dou, L.; Liu, Y.; Cheung, P.; Chang, J. P.; Yang, Y. Active Layer-Incorporated, Spectrally Tuned Au/SiO_2 Core/Shell Nanorod-Based Light Trapping for Organic Photovoltaics. *ACS Nano* **2013**, *7*, 3815−3822.
(443) Xu, B.; Ju, Y.; Cui, Y.; Song, G.; Iwase, Y.; Hosoi, A.; Morita, Y. TLyP-1−Conjugated Au-Nanorod@SiO_2 Core−Shell Nanoparticles for Tumor-Targeted Drug Delivery and Photothermal Therapy. *Langmuir* **2014**, *30*, 7789−7797.
(444) Vlassov, S.; Polyakov, B.; Dorogin, L. M.; Vahtrus, M.; Mets, M.; Antsov, M.; Saar, R.; Romanov, A. E.; Lõhmus, A.; Lõhmus, R. Shape Restoration Effect in Ag−SiO_2 Core−Shell Nanowires. *Nano Lett.* **2014**, *14*, 5201−5205.
(445) Catenacci, M. J.; Flowers, P. F.; Cao, C.; Andrews, J. B.; Franklin, A. D.; Wiley, B. J. Fully Printed Memristors from Cu−SiO_2 Core−Shell Nanowire Composites. *J. Electron. Mater.* **2017**, *46*, 4596−4603.
(446) Jakob, M.; Levanon, H.; Kamat, P. V. Charge Distribution between UV-Irradiated TiO_2 and Gold Nanoparticles: Determination of Shift in the Fermi Level. *Nano Lett.* **2003**, *3*, 353−358.

DOI: 10.1021/acs.chemrev.8b00745
Chem. Rev. XXXX, XXX, XXX−XXX

(447) Subramanian, V.; Wolf, E. E.; Kamat, P. V. Catalysis with TiO_2/Gold Nanocomposites. Effect of Metal Particle Size on the Fermi Level Equilibration. *J. Am. Chem. Soc.* **2004**, *126*, 4943−4950.
(448) Hirakawa, T.; Kamat, P. V. Photoinduced Electron Storage and Surface Plasmon Modulation in Ag@TiO_2 Clusters. *Langmuir* **2004**, *20*, 5645−5647.
(449) Franke, M. E.; Koplin, T. J.; Simon, U. Metal and Metal Oxide Nanoparticles in Chemiresistors: Does the Nanoscale Matter? *Small* **2006**, *2*, 36−50.
(450) Rai, P.; Kwak, W. K.; Yu, Y. T. Solvothermal Synthesis of ZnO Nanostructures and Their Morphology-Dependent Gas-Sensing Properties. *ACS Appl. Mater. Interfaces* **2013**, *5*, 3026−3032.
(451) Liu, R.; Sen, A. Controlled Synthesis of Heterogeneous Metal−Titania Nanostructures and Their Applications. *J. Am. Chem. Soc.* **2012**, *134*, 17505−17512.
(452) Elmalem, E.; Saunders, A. E.; Costi, R.; Salant, A.; Banin, U. Growth of Photocatalytic CdSe-Pt Nanorods and Nanonets. *Adv. Mater.* **2008**, *20*, 4312−4317.
(453) Mokari, T.; Sztrum, C. G.; Salant, A.; Rabani, E.; Banin, U. Formation of Asymmetric One-Sided Metal-Tipped Semiconductor Nanocrystal Dots and Rods. *Nat. Mater.* **2005**, *4*, 855−863.
(454) Majhi, S. M.; Rai, P.; Raj, S.; Chon, B.-S.; Park, K.-K.; Yu, Y.-T. Effect of Au Nanorods on Potential Barrier Modulation in Morphologically Controlled Au@Cu_2O Core−Shell Nanoreactors for Gas Sensor Applications. *ACS Appl. Mater. Interfaces* **2014**, *6*, 7491−7497.
(455) Manning, H. G.; Biswas, S.; Holmes, J. D.; Boland, J. J. Nonpolar Resistive Switching in Ag@TiO_2 Core−Shell Nanowires. *ACS Appl. Mater. Interfaces* **2017**, *9*, 38959−38966.
(456) Cheng, B.; Le, Y.; Yu, J. Preparation and Enhanced Photocatalytic Activity of Ag@TiO_2 Core-Shell Nanocomposite Nanowires. *J. Hazard. Mater.* **2010**, *177*, 971−977.
(457) Xue, X.; Chen, Z.; Ma, C.; Xing, L.; Chen, Y.; Wang, Y.; Wang, T. One-Step Synthesis and Gas-Sensing Characteristics of Uniformly Loaded Pt@SnO_2 Nanorods. *J. Phys. Chem. C* **2010**, *114*, 3968−3972.
(458) Ma, L.; Huang, Y.; Hou, M.; Xie, Z.; Zhang, Z. Ag Nanorods Coated with Ultrathin TiO_2 Shells as Stable and Recyclable SERS Substrates. *Sci. Rep.* **2015**, *5*, 15442.
(459) Chen, S.; Brown, L.; Levendorf, M.; Cai, W.; Ju, S. Y.; Edgeworth, J.; Li, X.; Magnuson, C. W.; Velamakanni, A.; Piner, R. D.; et al. Oxidation Resistance of Graphene-Coated Cu and Cu/Ni Alloy. *ACS Nano* **2011**, *5*, 1321−1327.
(460) Lee, D. D.-Y. Y.; Lee, H.; Ahn, Y.; Jeong, Y.; Lee, D. D.-Y. Y.; Lee, Y. Highly Stable and Flexible Silver Nanowire-Graphene Hybrid Transparent Conducting Electrodes for Emerging Optoelectronic Devices. *Nanoscale* **2013**, *5*, 7750−7755.
(461) Moon, H. K.; Lee, S. H.; Choi, H. C. In Vivo Near-Infrared Mediated Tumor Destruction by Photothermal Effect of Carbon Nanotubes. *ACS Nano* **2009**, *3*, 3707−3713.
(462) Moon, H.; Kumar, D.; Kim, H.; Sim, C.; Chang, J.-H.; Kim, J.-M.; Kim, H.; Lim, D.-K. Amplified Photoacoustic Performance and Enhanced Photothermal Stability of Reduced Graphene Oxide Coated Gold Nanorods for Sensitive Photoacoustic Imaging. *ACS Nano* **2015**, *9*, 2711−2719.
(463) Gole, A.; Murphy, C. J. Polyelectrolyte-Coated Gold Nanorods: Synthesis, Characterization and Immobilization. *Chem. Mater.* **2005**, *17*, 1325−1330.
(464) Lee, J.; Lee, P.; Lee, H. B.; Hong, S.; Lee, I.; Yeo, J.; Lee, S. S.; Kim, T.-S.; Lee, D.; Ko, S. H. Room-Temperature Nanosoldering of a Very Long Metal Nanowire Network by Conducting-Polymer-Assisted Joining for a Flexible Touch-Panel Application. *Adv. Funct. Mater.* **2013**, *23*, 4171−4176.
(465) Liz-Marzán, L. M. Tailoring Surface Plasmons through the Morphology and Assembly of Metal Nanoparticles. *Langmuir* **2006**, *22*, 32−41.
(466) Murphy, C. J.; Sau, T. K.; Gole, A.; Orendorff, C. J. Surfactant-Directed Synthesis and Optical Properties of One-Dimensional Plasmonic Metallic Nanostructures. *MRS Bull.* **2005**, *30*, 349−355.
(467) Cao, J.; Sun, T.; Grattan, K. T. V. Gold Nanorod-Based Localized Surface Plasmon Resonance Biosensors: A Review. *Sens. Actuators, B* **2014**, *195*, 332−351.
(468) Mie, G. Beiträge Zur Optik Trüber Medien, Speziell Kolloidaler Metallösungen. *Ann. Phys.* **1908**, *330*, 377−445.
(469) Gans, R. Über Die Form Ultramikroskopischer Silberteilchen. *Ann. Phys.* **1915**, *352*, 270−284.
(470) Zhao, J.; Pinchuk, A. O.; Mcmahon, J. M.; Li, S.; Ausman, L. K.; Atkinson, A. L.; Schatz, G. C. Methods for Describing the Electromagnetic Properties of Silver and Gold Nanoparticles. *Acc. Chem. Res.* **2008**, *41*, 1710−1720.
(471) Brioude, A.; Jiang, X. C.; Pileni, M. P. Optical Properties of Gold Nanorods: DDA Simulations Supported by Experiments. *J. Phys. Chem. B* **2005**, *109*, 13138−13142.
(472) Lee, K.-S.; El-Sayed, M. A. Gold and Silver Nanoparticles in Sensing and Imaging: Sensitivity of Plasmon Response to Size, Shape, and Metal Composition. *J. Phys. Chem. B* **2006**, *110*, 19220−19225.
(473) Wiley, B. J.; Im, S. H.; Li, Z.-Y.; McLellan, J.; Siekkinen, A.; Xia, Y. Maneuvering the Surface Plasmon Resonance of Silver Nanostructures through Shape-Controlled Synthesis. *J. Phys. Chem. B* **2006**, *110*, 15666−15675.
(474) Sherry, L. J.; Chang, S.-H.; Schatz, G. C.; Van Duyne, R. P.; Wiley, B. J.; Xia, Y. Localized Surface Plasmon Resonance Spectroscopy of Single Silver Nanocubes. *Nano Lett.* **2005**, *5*, 2034−2038.
(475) Mohamed, M. B.; Volkov, V.; Link, S.; El-Sayed, M. A. The "Lightning" Gold Nanorods: Fluorescence Enhancement of over a Million Compared to the Gold Metal. *Chem. Phys. Lett.* **2000**, *317*, 517−523.
(476) Orendorff, C. J.; Murphy, C. J. Quantitation of Metal Content in the Silver-Assisted Growth of Gold Nanorods. *J. Phys. Chem. B* **2006**, *110*, 3990−3994.
(477) Becker, J.; Trügler, A.; Jakab, A.; Hohenester, U.; Sönnichsen, C. The Optimal Aspect Ratio of Gold Nanorods for Plasmonic Bio-Sensing. *Plasmonics* **2010**, *5*, 161−167.
(478) Raether, H. *Surface Plasmons on Smooth and Rough Surfaces and on Gratings*; Springer-Verlag: Berlin, 1988; Vol. *111*.
(479) Liu, Z.; Bando, Y. A Novel Method for Preparing Copper Nanorods and Nanowires. *Adv. Mater.* **2003**, *15*, 303−305.
(480) Jana, N. R.; Gearheart, L.; Obare, S. O.; Murphy, C. J. Anisotropic Chemical Reactivity of Gold Spheroids and Nanorods. *Langmuir* **2002**, *18*, 922−927.
(481) Zhang, J.; Li, X.; Sun, X.; Li, Y. Surface Enhanced Raman Scattering Effects of Silver Colloids with Different Shapes. *J. Phys. Chem. B* **2005**, *109*, 12544−12548.
(482) Vigderman, L.; Zubarev, E. R. Starfruit-Shaped Gold Nanorods and Nanowires: Synthesis and SERS Characterization. *Langmuir* **2012**, *28*, 9034−9040.
(483) Jing, H.; Zhang, Q.; Large, N.; Yu, C.; Blom, D. A.; Nordlander, P.; Wang, H. Tunable Plasmonic Nanoparticles with Catalytically Active High-Index Facets. *Nano Lett.* **2014**, *14*, 3674−3682.
(484) Ah, C. S.; Hong, S. Do; Jang, D.-J. Preparation of $Au_{core}Ag_{shell}$ Nanorods and Characterization of Their Surface Plasmon Resonances. *J. Phys. Chem. B* **2001**, *105*, 7871−7873.
(485) Khlebtsov, B. N.; Liu, Z.; Ye, J.; Khlebtsov, N. G. Au@Ag Core/Shell Cuboids and Dumbbells: Optical Properties and SERS Response. *J. Quant. Spectrosc. Radiat. Transfer* **2015**, *167*, 64−75.
(486) Grzelczak, M.; Pérez-Juste, J.; García De Abajo, F. J.; Liz-Marzán, L. M. Optical Properties of Platinum-Coated Gold Nanorods. *J. Phys. Chem. C* **2007**, *111*, 6183−6188.
(487) Xiang, Y.; Wu, X.; Liu, D.; Li, Z.; Chu, W.; Feng, L.; Zhang, K.; Zhou, W.; Xie, S. Gold Nanorod-Seeded Growth of Silver Nanostructures: From Homogeneous Coating to Anisotropic Coating. *Langmuir* **2008**, *24*, 3465−3470.

DOI: 10.1021/acs.chemrev.8b00745
Chem. Rev. XXXX, XXX, XXX−XXX

(488) Feng, L.; Wu, X.; Ren, L.; Xiang, Y.; He, W.; Zhang, K.; Zhou, W.; Xie, S. Well-Controlled Synthesis of Au@Pt Nanostructures by Gold-Nanorod-Seeded Growth. *Chem. - Eur. J.* **2008**, *14*, 9764−9771.
(489) Okuno, Y.; Nishioka, K.; Kiya, A.; Nakashima, N.; Ishibashi, A.; Niidome, Y. Uniform and Controllable Preparation of Au-Ag Core-Shell Nanorods Using Anisotropic Silver Shell Formation on Gold Nanorods. *Nanoscale* **2010**, *2*, 1489−1493.
(490) Chen, H.; Wang, F.; Li, K.; Woo, K. C.; Wang, J.; Li, Q.; Sun, L.-D.; Zhang, X.; Lin, H.-Q.; Yan, C.-H. Plasmonic Percolation: Plasmon-Manifested Dielectric-to-Metal Transition. *ACS Nano* **2012**, *6*, 7162−7171.
(491) Li, Q.; Jiang, R.; Ming, T.; Fang, C.; Wang, J. Crystalline Structure-Dependent Growth of Bimetallic Nanostructures. *Nanoscale* **2012**, *4*, 7070−7077.
(492) Jiang, R.; Chen, H.; Shao, L.; Li, Q.; Wang, J. Unraveling the Evolution and Nature of the Plasmons in (Au Core)-(Ag Shell) Nanorods. *Adv. Mater.* **2012**, *24*, OP200−OP207.
(493) Jing, H.; Wang, H. Controlled Overgrowth of Pd on Au Nanorods. *CrystEngComm* **2014**, *16*, 9469−9477.
(494) Perez-Juste, J.; Pastoriza-Santos, I.; Liz-Marzán, L. M.; Mulvaney, P. Gold Nanorods: Synthesis, Characterization and Applications. *Coord. Chem. Rev.* **2005**, *249*, 1870−1901.
(495) Chen, H.; Kou, X.; Yang, Z.; Ni, W.; Wang, J. Shape- and Size-Dependent Refractive Index Sensitivity of Gold Nanoparticles. *Langmuir* **2008**, *24*, 5233−5237.
(496) Niidome, T.; Yamagata, M.; Okamoto, Y.; Akiyama, Y.; Takahashi, H.; Kawano, T.; Katayama, Y.; Niidome, Y. PEG-Modified Gold Nanorods with a Stealth Character for in Vivo Applications. *J. Controlled Release* **2006**, *114*, 343−347.
(497) Alkilany, A. M.; Nagaria, P. K.; Hexel, C. R.; Shaw, T. J.; Murphy, C. J.; Wyatt, M. D. Cellular Uptake and Cytotoxicity of Gold Nanorods: Molecular Origin of Cytotoxicity and Surface Effects. *Small* **2009**, *5*, 701−708.
(498) Qiu, Y.; Liu, Y.; Wang, L.; Xu, L.; Bai, R.; Ji, Y.; Wu, X.; Zhao, Y.; Li, Y.; Chen, C. Surface Chemistry and Aspect Ratio Mediated Cellular Uptake of Au Nanorods. *Biomaterials* **2010**, *31*, 7606−7619.
(499) Gole, A.; Murphy, C. J. Biotin-Streptavidin-Induced Aggregation of Gold Nanorods: Tuning Rod-Rod Orientation. *Langmuir* **2005**, *21*, 10756−10762.
(500) Khanal, B. P.; Zubarev, E. R. Rings of Nanorods. *Angew. Chem.* **2007**, *119*, 2245−2248.
(501) Thierry, B.; Ng, J.; Krieg, T.; Griesser, H. J. A Robust Procedure for the Functionalization of Gold Nanorods and Noble Metal Nanoparticles. *Chem. Commun.* **2009**, 1724−1726.
(502) Vigderman, L.; Manna, P.; Zubarev, E. R. Quantitative Replacement of Cetyl Trimethylammonium Bromide by Cationic Thiol Ligands on the Surface of Gold Nanorods and Their Extremely Large Uptake by Cancer Cells. *Angew. Chem., Int. Ed.* **2012**, *51*, 636−641.
(503) Castellana, E. T.; Gamez, R. C.; Russell, D. H. Label-Free Biosensing with Lipid-Functionalized Gold Nanorods. *J. Am. Chem. Soc.* **2011**, *133*, 4182−4185.
(504) Indrasekara, A. S. D. S.; Wadams, R. C.; Fabris, L. Ligand Exchange on Gold Nanorods: Going Back to the Future. *Part. Part. Syst. Charact.* **2014**, *31*, 819−838.
(505) Zhou, S.; Huo, D.; Goines, S.; Yang, T.-H.; Lyu, Z.; Zhao, M.; Gilroy, K. D.; Wu, Y.; Hood, Z. D.; Xie, M.; et al. Enabling Complete Ligand Exchange on the Surface of Gold Nanocrystals through the Deposition and Then Etching of Silver. *J. Am. Chem. Soc.* **2018**, *140*, 11898−11901.
(506) Huang, H.-C.; Barua, S.; Kay, D. B.; Rege, K. Simultaneous Enhancement of Photothermal Stability and Gene Delivery. *ACS Nano* **2009**, *3*, 2941−2952.
(507) Alkilany, A. M.; Thompson, L. B.; Murphy, C. J. Polyelectrolyte Coating Provides a Facile Route to Suspend Gold Nanorods in Polar Organic Solvents and Hydrophobic Polymers. *ACS Appl. Mater. Interfaces* **2010**, *2*, 3417−3421.
(508) Chen, S. H.; Ji, Y. X.; Lian, Q.; Wen, Y. L.; Shen, H. B.; Jia, N. Q. Gold Nanorods Coated with Multilayer Polyelectrolyte as Intracellular Delivery Vector of Antisense Oligonucleotides. *Nano Biomed. Eng.* **2010**, *2*, 15−23.
(509) Wang, C.; Ma, Z.; Wang, T.; Su, Z. Synthesis, Assembly, and Biofunctionalization of Silica-Coated Gold Nanorods for Colorimetric Biosensing. *Adv. Funct. Mater.* **2006**, *16*, 1673−1678.
(510) Marinakos, S. M.; Chen, S.; Chilkoti, A. Plasmonic Detection of a Model Analyte in Serum by a Gold Nanorod Sensor. *Anal. Chem.* **2007**, *79*, 5278−5283.
(511) Yu, C.; Irudayaraj, J. Multiplex Biosensor Using Gold Nanorods. *Anal. Chem.* **2007**, *79*, 572−579.
(512) Yu, C.; Varghese, L.; Irudayaraj, J. Surface Modification of Cetyltrimethylammonium Bromide-Capped Gold Nanorods to Make Molecular Probes. *Langmuir* **2007**, *23*, 9114−9119.
(513) Martinsson, E.; Shahjamali, M. M.; Large, N.; Zaraee, N.; Zhou, Y.; Schatz, G. C.; Mirkin, C. A.; Aili, D. Influence of Surfactant Bilayers on the Refractive Index Sensitivity and Catalytic Properties of Anisotropic Gold Nanoparticles. *Small* **2016**, *12*, 330−342.
(514) Zijlstra, P.; Paulo, P. M. R.; Orrit, M. Optical Detection of Single Non-Absorbing Molecules Using the Surface Plasmon of a Gold Nanorod. *Nat. Nanotechnol.* **2012**, *7*, 379−382.
(515) Ament, I.; Prasad, J.; Henkel, A.; Schmachtel, S.; Sönnichsen, C. Single Unlabeled Protein Detection on Individual Plasmonic Nanoparticles. *Nano Lett.* **2012**, *12*, 1092−1095.
(516) Willingham, B.; Brandl, D. W.; Nordlander, P. Plasmon Hybridization in Nanorod Dimers. *Appl. Phys. B: Lasers Opt.* **2008**, *93*, 209−216.
(517) Shao, L.; Woo, K. C.; Chen, H.; Jin, Z.; Wang, J.; Lin, H.-Q. Angle- and Energy-Resolved Plasmon Couplings in Gold Nanorod Dimers. *ACS Nano* **2010**, *4*, 3053−3062.
(518) Slaughter, L. S.; Wu, Y.; Willingham, B. A.; Nordlander, P.; Link, S. Effects of Symmetry Breaking and Conductive Contact on the Plasmon Coupling in Gold Nanorod Dimers. *ACS Nano* **2010**, *4*, 4657−4666.
(519) Sun, Z.; Ni, W.; Yang, Z.; Kou, X.; Li, L.; Wang, J. pH-Controlled Reversible Assembly and Disassembly of Gold Nanorods. *Small* **2008**, *4*, 1287−1292.
(520) Funston, A. M.; Novo, C.; Davis, T. J.; Mulvaney, P. Plasmon Coupling of Gold Nanorods at Short Distances and in Different Geometries. *Nano Lett.* **2009**, *9*, 1651−1658.
(521) Thomas, K. G.; Barazzouk, S.; Ipe, B. I.; Joseph, S. T. S.; Kamat, P. V. Uniaxial Plasmon Coupling through Longitudinal Self-Assembly of Gold Nanorods. *J. Phys. Chem. B* **2004**, *108*, 13066−13068.
(522) Nepal, D.; Park, K.; Vaia, R. A. High-Yield Assembly of Soluble and Stable Gold Nanorod Pairs for High-Temperature Plasmonics. *Small* **2012**, *8*, 1013−1020.
(523) Abtahi, S. M. H.; Burrows, N. D.; Idesis, F. A.; Murphy, C. J.; Saleh, N. B.; Vikesland, P. J. Sulfate-Mediated End-to-End Assembly of Gold Nanorods. *Langmuir* **2017**, *33*, 1486−1495.
(524) Sudeep, P. K.; Joseph, S. T. S.; Thomas, K. G. Selective Detection of Cysteine and Glutathione Using Gold Nanorods. *J. Am. Chem. Soc.* **2005**, *127*, 6516−6517.
(525) Wang, C.; Chen, Y.; Wang, T.; Ma, Z.; Su, Z. Biorecognition-Driven Self-Assembly of Gold Nanorods: A Rapid and Sensitive Approach toward Antibody Sensing. *Chem. Mater.* **2007**, *19*, 5809−5811.
(526) Murphy, C. J.; Gole, A. M.; Hunyadi, S. E.; Stone, J. W.; Sisco, P. N.; Alkilany, A.; Kinard, B. E.; Hankins, P. Chemical Sensing and Imaging with Metallic Nanorods. *Chem. Commun.* **2008**, 544−557.
(527) Orendorff, C. J.; Gearheart, L.; Jana, N. R.; Murphy, C. J. Aspect Ratio Dependence on Surface Enhanced Raman Scattering Using Silver and Gold Nanorod Substrates. *Phys. Chem. Chem. Phys.* **2006**, *8*, 165−170.
(528) Huang, X.; El-Sayed, I. H.; Qian, W.; El-Sayed, M. A. Cancer Cells Assemble and Align Gold Nanorods Conjugated to Antibodies to Produce Highly Enhanced, Sharp, and Polarized Surface Raman Spectra: A Potential Cancer Diagnostic Marker. *Nano Lett.* **2007**, *7*, 1591−1597.

DOI: 10.1021/acs.chemrev.8b00745
Chem. Rev. XXXX, XXX, XXX−XXX

(529) Smitha, S. L.; Gopchandran, K. G.; Ravindran, T. R.; Prasad, V. S. Gold Nanorods with Finely Tunable Longitudinal Surface Plasmon Resonance as SERS Substrates. *Nanotechnology* **2011**, *22*, 265705.
(530) Sivapalan, S. T.; Devetter, B. M.; Yang, T. K.; Van Dijk, T.; Schulmerich, M. V.; Carney, P. S.; Bhargava, R.; Murphy, C. J. Off-Resonance Surface-Enhanced Raman Spectroscopy from Gold Nanorod Suspensions as a Function of Aspect Ratio: Not What We Thought. *ACS Nano* **2013**, *7*, 2099−2105.
(531) Ali, M. R. K.; Wu, Y.; Han, T.; Zang, X.; Xiao, H.; Tang, Y.; Wu, R.; Fernández, F. M.; El-Sayed, M. A. Simultaneous Time-Dependent Surface-Enhanced Raman Spectroscopy, Metabolomics, and Proteomics Reveal Cancer Cell Death Mechanisms Associated with Gold Nanorod Photothermal Therapy. *J. Am. Chem. Soc.* **2016**, *138*, 15434−15442.
(532) Orendorff, C. J.; Gole, A.; Sau, T. K.; Murphy, C. J. Surface-Enhanced Raman Spectroscopy of Self-Assembled Monolayers: Sandwich Architecture and Nanoparticle Shape Dependence. *Anal. Chem.* **2005**, *77*, 3261−3266.
(533) Gómez-Graña, S.; Pérez-Juste, J.; Alvarez-Puebla, R. A.; Guerrero-Martínez, A.; Liz-Marzán, L. M. Self-Assembly of Au@Ag Nanorods Mediated by Gemini Surfactants for Highly Efficient SERS-Active Supercrystals. *Adv. Opt. Mater.* **2013**, *1*, 477−481.
(534) Sreeprasad, T. S.; Samal, A. K.; Pradeep, T. One-, Two-, and Three-Dimensional Superstructures of Gold Nanorods Induced by Dimercaptosuccinic Acid. *Langmuir* **2008**, *24*, 4589−4599.
(535) Alvarez-Puebla, R. A.; Agarwal, A.; Manna, P.; Khanal, B. P.; Aldeanueva-Potel, P.; Carbo-Argibay, E.; Pazos-Perez, N.; Vigderman, L.; Zubarev, E. R.; Kotov, N. A.; et al. Gold Nanorods 3D-Supercrystals as Surface Enhanced Raman Scattering Spectroscopy Substrates for the Rapid Detection of Scrambled Prions. *Proc. Natl. Acad. Sci. U. S. A.* **2011**, *108*, 8157−8161.
(536) Sreeprasad, T. S.; Pradeep, T. Reversible Assembly and Disassembly of Gold Nanorods Induced by EDTA and Its Application in SERS Tuning. *Langmuir* **2011**, *27*, 3381−3390.
(537) Xie, Y.; Guo, S.; Ji, Y.; Guo, C.; Liu, X.; Chen, Z.; Wu, X.; Liu, Q. Self-Assembly of Gold Nanorods into Symmetric Superlattices Directed by OH-Terminated Hexa(Ethylene Glycol) Alkanethiol. *Langmuir* **2011**, *27*, 11394−11400.
(538) Li, P.; Li, Y.; Zhou, Z.-K.; Tang, S.; Yu, X.-F.; Xiao, S.; Wu, Z.; Xiao, Q.; Zhao, Y.; Wang, H.; et al. Evaporative Self-Assembly of Gold Nanorods into Macroscopic 3D Plasmonic Superlattice Arrays. *Adv. Mater.* **2016**, *28*, 2511−2517.
(539) Tao, A.; Kim, F.; Hess, C.; Goldberger, J.; He, R.; Sun, Y.; Xia, Y.; Yang, P. Langmuir-Blodgett Silver Nanowire Monolayers for Molecular Sensing Using Surface-Enhanced Raman Spectroscopy. *Nano Lett.* **2003**, *3*, 1229−1233.
(540) Sönnichsen, C.; Alivisatos, A. P. Gold Nanorods as Novel Nonbleaching Plasmon-Based Orientation Sensors for Polarized Single-Particle Microscopy. *Nano Lett.* **2005**, *5*, 301−304.
(541) Orendorff, C. J.; Baxter, S. C.; Goldsmith, E. C.; Murphy, C. J. Light Scattering from Gold Nanorods: Tracking Material Deformation. *Nanotechnology* **2005**, *16*, 2601−2605.
(542) Huang, X.; El-sayed, I. H.; Qian, W.; El-sayed, M. A. Cancer Cell Imaging and Photothermal Therapy in the Near-Infrared Region by Using Gold Nanorods. *J. Am. Chem. Soc.* **2006**, *128*, 2115−2120.
(543) Ding, H.; Yong, K.-T.; Roy, I.; Pudavar, H. E.; Law, W. C.; Bergey, E. J.; Prasad, P. N. Gold Nanorods Coated with Multilayer Polyelectrolyte as Contrast Agents for Multimodal Imaging. *J. Phys. Chem. C* **2007**, *111*, 12552−12557.
(544) Stone, J. W.; Sisco, P. N.; Goldsmith, E. C.; Baxter, S. C.; Murphy, C. J. Using Gold Nanorods to Probe Cell-Induced Collagen Deformation. *Nano Lett.* **2007**, *7*, 116−119.
(545) Oyelere, A. K.; Chen, C. P.; Huang, X.; El-Sayed, I. H.; El-Sayed, M. A. Peptide-Conjugated Gold Nanorods for Nuclear Targeting. *Bioconjugate Chem.* **2007**, *18*, 1490−1497.
(546) Chanda, N.; Shukla, R.; Katti, K. V.; Kannan, R. Gastrin Releasing Protein Receptor−Specific Gold Nanorods: Breast and Prostate Tumor-Avid Nanovectors for Molecular Imaging. *Nano Lett.* **2009**, *9*, 1798−1805.
(547) Huang, X.; Peng, X.; Wang, Y.; Wang, Y.; Shin, D. M.; El-Sayed, M. a.; Nie, S. Reexamination of Active and Passive Tumor Targeting by Using Rod-Shaped Gold Nanocrystals and Covalently Conjugated Peptide Ligands. *ACS Nano* **2010**, *4*, 5887−5896.
(548) Dreaden, E. C.; Alkilany, A. M.; Huang, X.; Murphy, C. J.; El-Sayed, M. A. The Golden Age: Gold Nanoparticles for Biomedicine. *Chem. Soc. Rev.* **2012**, *41*, 2740−2779.
(549) Oldenburg, A. L.; Hansen, M. N.; Zweifel, D. A.; Wei, A.; Boppart, S. A. Plasmon-Resonant Gold Nanorods as Low Backscattering Albedo Contrast Agents for Optical Coherence Tomography. *Opt. Express* **2006**, *14*, 6724−6738.
(550) Oldenburg, A. L.; Hansen, M. N.; Ralston, T. S.; Wei, A.; Boppart, S. A. Imaging Gold Nanorods in Excised Human Breast Carcinoma by Spectroscopic Optical Coherence Tomography. *J. Mater. Chem.* **2009**, *19*, 6407−6411.
(551) Chhetri, R. K.; Blackmon, R. L.; Wu, W.-C.; Hill, D. B.; Button, B.; Casbas-Hernandez, P.; Troester, M. A.; Tracy, J. B.; Oldenburg, A. L. Probing Biological Nanotopology via Diffusion of Weakly Constrained Plasmonic Nanorods with Optical Coherence Tomography. *Proc. Natl. Acad. Sci. U. S. A.* **2014**, *111*, E4289−E4297.
(552) SoRelle, E. D.; Liba, O.; Hussain, Z.; Gambhir, M.; De La Zerda, A. Biofunctionalization of Large Gold Nanorods Realizes Ultrahigh-Sensitivity Optical Imaging Agents. *Langmuir* **2015**, *31*, 12339−12347.
(553) Jung, Y.; Reif, R.; Zeng, Y.; Wang, R. K. Three-Dimensional High-Resolution Imaging of Gold Nanorods Uptake in Sentinel Lymph Nodes. *Nano Lett.* **2011**, *11*, 2938−2943.
(554) Kim, K.; Huang, S.-W.; Ashkenazi, S.; O'Donnell, M.; Agarwal, A.; Kotov, N. A.; Denny, M. F.; Kaplan, M. J. Photoacoustic Imaging of Early Inflammatory Response Using Gold Nanorods. *Appl. Phys. Lett.* **2007**, *90*, 223901.
(555) Agarwal, A.; Huang, S. W.; O'Donnell, M.; Day, K. C.; Day, M.; Kotov, N.; Ashkenazi, S. Targeted Gold Nanorod Contrast Agent for Prostate Cancer Detection by Photoacoustic Imaging. *J. Appl. Phys.* **2007**, *102*, 064701.
(556) Li, P.-C.; Wang, C.-R. C.; Shieh, D.-B.; Wei, C.-W.; Liao, C.-K.; Poe, C.; Jhan, S.; Ding, A.-A.; Wu, Y.-N. In Vivo Photoacoustic Molecular Imaging with Simultaneous Multiple Selective Targeting Using Antibody-Conjugated Gold Nanorods. *Opt. Express* **2008**, *16*, 18605−18615.
(557) Galanzha, E. I.; Shashkov, E. V.; Spring, P. M.; Suen, J. Y.; Zharov, V. P. In Vivo, Noninvasive, Label-Free Detection and Eradication of Circulating Metastatic Melanoma Cells Using Two-Color Photoacoustic Flow Cytometry with a Diode Laser. *Cancer Res.* **2009**, *69*, 7926−7934.
(558) Wang, G.; Sun, W.; Luo, Y.; Fang, N. Resolving Rotational Motions of Nano-Objects in Engineered Environments and Live Cells with Gold Nanorods and Differential Interference Contrast Microscopy. *J. Am. Chem. Soc.* **2010**, *132*, 16417−16422.
(559) Jokerst, J. V.; Cole, A. J.; Van De Sompel, D.; Gambhir, S. S. Gold Nanorods for Ovarian Cancer Detection with Photoacoustic Imaging and Resection Guidance via Raman Imaging in Living Mice. *ACS Nano* **2012**, *6*, 10366−10377.
(560) Moon, H.; Kumar, D.; Kim, H.; Sim, C.; Chang, J.-H.; Kim, J.-M.; Kim, H.; Lim, D.-K. Amplified Photoacoustic Performance and Enhanced Photothermal Stability of Reduced Graphene Oxide Coated Gold Nanorods for Sensitive Photoacoustic Imaging. *ACS Nano* **2015**, *9*, 2711−2719.
(561) Wang, H.; Huff, T. B.; Zweifel, D. A.; He, W.; Low, P. S.; Wei, A.; Cheng, J.-X. In Vitro and in Vivo Two-Photon Luminescence Imaging of Single Gold Nanorods. *Proc. Natl. Acad. Sci. U. S. A.* **2005**, *102*, 15752−15756.
(562) Durr, N. J.; Larson, T.; Smith, D. K.; Korgel, B. A.; Sokolov, K.; Ben-Yakar, A. Two-Photon Luminescence Imaging of Cancer Cells Using Molecularly Targeted Gold Nanorods. *Nano Lett.* **2007**, *7*, 941−945.

DOI: 10.1021/acs.chemrev.8b00745
Chem. Rev. XXXX, XXX, XXX−XXX

(563) Huff, T. B.; Hansen, M. N.; Zhao, Y.; Cheng, J.-X.; Wei, A. Controlling the Cellular Uptake of Gold Nanorods. *Langmuir* **2007**, *23*, 1596−1599.
(564) Tong, L.; Zhao, Y.; Huff, T. B.; Hansen, M. N.; Wei, A.; Cheng, J.-X. Gold Nanorods Mediate Tumor Cell Death by Compromising Membrane Integrity. *Adv. Mater.* **2007**, *19*, 3136−3141.
(565) Tong, L.; He, W.; Zhang, Y.; Zheng, W.; Cheng, J.-X. Visualizing Systemic Clearance and Cellular Level Biodistribution of Gold Nanorods by Intrinsic Two-Photon Luminescence. *Langmuir* **2009**, *25*, 12454−12459.
(566) Li, J.-L.; Gu, M. Surface Plasmonic Gold Nanorods for Enhanced Two-Photon Microscopic Imaging and Apoptosis Induction of Cancer Cells. *Biomaterials* **2010**, *31*, 9492−9498.
(567) Motamedi, S.; Shilagard, T.; Edward, K.; Koong, L.; Qui, S.; Vargas, G. Gold Nanorods for Intravital Vascular Imaging of Preneoplastic Oral Mucosa. *Biomed. Opt. Express* **2011**, *2*, 1194−1203.
(568) Imura, K.; Nagahara, T.; Okamoto, H. Near-Field Two-Photon-Induced Photoluminescence from Single Gold Nanorods and Imaging of Plasmon Modes. *J. Phys. Chem. B* **2005**, *109*, 13214−13220.
(569) Dionne, J. A. Nanoplasmonics: Plasmons Rock in Metal Bands. *Nat. Mater.* **2013**, *12*, 380−381.
(570) Grobmyer, S. R., Moudgil, B. M. *Cancer Nanotechnology: Methods and Protocols*; Human Press, 2011; Vol. *624*.
(571) Huang, X.; El-Sayed, M. A. Gold Nanoparticles: Optical Properties and Implementations in Cancer Diagnosis and Photothermal Therapy. *J. Adv. Res.* **2010**, *1*, 13−28.
(572) Li, N.; Zhao, P.; Astruc, D. Anisotropic Gold Nanoparticles: Synthesis, Properties, Applications, and Toxicity. *Angew. Chem., Int. Ed.* **2014**, *53*, 1756−1789.
(573) MacKey, M. A.; Ali, M. R. K.; Austin, L. A.; Near, R. D.; El-Sayed, M. A. The Most Effective Gold Nanorod Size for Plasmonic Photothermal Therapy: Theory and in Vitro Experiments. *J. Phys. Chem. B* **2014**, *118*, 1319−1326.
(574) Vankayala, R.; Huang, Y.-K.; Kalluru, P.; Chiang, C.-S.; Hwang, K. C. First Demonstration of Gold Nanorods-Mediated Photodynamic Therapeutic Destruction of Tumors via near Infra-Red Light Activation. *Small* **2014**, *10*, 1612−1622.
(575) Wijaya, A.; Schaffer, S. B.; Pallares, I. G.; Hamad-Schifferli, K. Selective Release of Multiple DNA Oligonucleotides from Gold Nanorods. *ACS Nano* **2009**, *3*, 80−86.
(576) Alkilany, A. M.; Thompson, L. B.; Boulos, S. P.; Sisco, P. N.; Murphy, C. J. Gold Nanorods: Their Potential for Photothermal Therapeutics and Drug Delivery, Tempered by the Complexity of Their Biological Interactions. *Adv. Drug Delivery Rev.* **2012**, *64*, 190−199.
(577) Zhang, Z.; Wang, J.; Nie, X.; Wen, T.; Ji, Y.; Wu, X.; Zhao, Y.; Chen, C. Near Infrared Laser-Induced Targeted Cancer Therapy Using Thermoresponsive Polymer Encapsulated Gold Nanorods. *J. Am. Chem. Soc.* **2014**, *136*, 7317−7326.
(578) Tang, H.; Shen, S.; Guo, J.; Chang, B.; Jiang, X.; Yang, W. Gold Nanorods@mSiO_2 with a Smart Polymer Shell Responsive to Heat/Near-Infrared Light for Chemo-Photothermal Therapy. *J. Mater. Chem.* **2012**, *22*, 16095−16103.
(579) Niidome, Y.; Haine, A. T.; Niidome, T. Anisotropic Gold-Based Nanoparticles: Preparation, Properties, and Applications. *Chem. Lett.* **2016**, *45*, 488−498.
(580) Stone, J.; Jackson, S.; Wright, D. Biological Applications of Gold Nanorods. *Wiley Interdiscip Rev. Nanomed Nanobiotechnol* **2011**, *3*, 100−109.
(581) Agarwal, A.; MacKey, M. A.; El-Sayed, M. A.; Bellamkonda, R. V. Remote Triggered Release of Doxorubicin in Tumors by Synergistic Application of Thermosensitive Liposomes and Gold Nanorods. *ACS Nano* **2011**, *5*, 4919−4926.
(582) Ali, H. R.; Ali, M. R. K.; Wu, Y.; Selim, S. A.; Abdelaal, H. F. M.; Nasr, E. A.; El-Sayed, M. A. Gold Nanorods as Drug Delivery Vehicles for Rifampicin Greatly Improve the Efficacy of Combating Mycobacterium Tuberculosis with Good Biocompatibility with the Host Cells. *Bioconjugate Chem.* **2016**, *27*, 2486−2492.
(583) Lee, H.; Lee, Y.; Song, C.; Cho, H. R.; Ghaffari, R.; Choi, T. K.; Kim, K. H.; Lee, Y. B.; Ling, D.; Lee, H.; et al. An Endoscope with Integrated Transparent Bioelectronics and Theranostic Nanoparticles for Colon Cancer Treatment. *Nat. Commun.* **2015**, *6*, 10059.
(584) Pang, B.; Zhao, Y.; Luehmann, H.; Yang, X.; Detering, L.; You, M.; Zhang, C.; Zhang, L.; Li, Z. Y.; Ren, Q.; et al. ^{64}Cu-Doped PdCu@Au Tripods: A Multifunctional Nanomaterial for Positron Emission Tomography and Image-Guided Photothermal Cancer Treatment. *ACS Nano* **2016**, *10*, 3121−3131.
(585) Narang, P.; Sundararaman, R.; Atwater, H. A. Plasmonic Hot Carrier Dynamics in Solid-State and Chemical Systems for Energy Conversion. *Nanophotonics* **2016**, *5*, 96−111.
(586) Thrall, E. S.; Preska Steinberg, A. P.; Wu, X.; Brus, L. E. The Role of Photon Energy and Semiconductor Substrate in the Plasmon-Mediated Photooxidation of Citrate by Silver Nanoparticles. *J. Phys. Chem. C* **2013**, *117*, 26238−26247.
(587) Schlather, A. E.; Manjavacas, A.; Lauchner, A.; Marangoni, V. S.; DeSantis, C. J.; Nordlander, P.; Halas, N. J. Hot Hole Photoelectrochemistry on Au@SiO_2@Au Nanoparticles. *J. Phys. Chem. Lett.* **2017**, *8*, 2060−2067.
(588) Wang, F.; Li, C.; Chen, H.; Jiang, R.; Sun, L.-D.; Li, Q.; Wang, J.; Yu, J. C.; Yan, C.-H. Plasmonic Harvesting of Light Energy for Suzuki Coupling Reactions. *J. Am. Chem. Soc.* **2013**, *135*, 5588−5601.
(589) Wei, H.; Pan, D.; Zhang, S.; Li, Z.; Li, Q.; Liu, N.; Wang, W.; Xu, H. Plasmon Waveguiding in Nanowires. *Chem. Rev.* **2018**, *118*, 2882−2926.
(590) Sanders, A. W.; Routenberg, D. A.; Wiley, B. J.; Xia, Y.; Dufresne, E. R.; Reed, M. A. Observation of Plasmon Propagation, Redirection, and Fan-out in Silver Nanowires. *Nano Lett.* **2006**, *6*, 1822−1826.
(591) Fang, Y.; Li, Z.; Huang, Y.; Zhang, S.; Nordlander, P.; Halas, N. J.; Xu, H. Branched Silver Nanowires as Controllable Plasmon Routers. *Nano Lett.* **2010**, *10*, 1950−1954.
(592) Guo, X.; Qiu, M.; Bao, J.; Wiley, B. J.; Yang, Q.; Zhang, X.; Ma, Y.; Yu, H.; Tong, L. Direct Coupling of Plasmonic and Photonic Nanowires for Hybrid Nanophotonic Components and Circuits. *Nano Lett.* **2009**, *9*, 4515−4519.
(593) Li, Z.; Zhang, S.; Halas, N. J.; Nordlander, P.; Xu, H. Coherent Modulation of Propagating Plasmons in Silver-Nanowire-Based Structures. *Small* **2011**, *7*, 593−596.
(594) Wei, H.; Wang, Z.; Tian, X.; Käll, M.; Xu, H. Cascaded Logic Gates in Nanophotonic Plasmon Networks. *Nat. Commun.* **2011**, *2*, 387.
(595) Wei, H.; Li, Z.; Tian, X.; Wang, Z.; Cong, F.; Liu, N.; Zhang, S.; Nordlander, P.; Halas, N. J.; Xu, H. Quantum Dot-Based Local Field Imaging Reveals Plasmon-Based Interferometric Logic in Silver Nanowire Networks. *Nano Lett.* **2011**, *11*, 471−475.
(596) Wei, H.; Xu, H. Controlling Surface Plasmon Interference in Branched Silver Nanowire Structures. *Nanoscale* **2012**, *4*, 7149−7154.
(597) Pike, G. E.; Seager, C. H. Percolation and Conductivity: A Computer Study. I*. *Phys. Rev. B* **1974**, *10*, 1421−1434.
(598) Balberg, I.; Binenbaum, N. Computer Study Of the Percolation Threshold in a Two-Dimensional Anisotropic System Of Conducting Sticks. *Phys. Rev. B: Condens. Matter Mater. Phys.* **1983**, *28*, 3799−3812.
(599) Xu, W.; Su, X.; Jiao, Y. Continuum Percolation of Congruent Overlapping Spherocylinders. *Phys. Rev. E: Stat. Phys., Plasmas, Fluids, Relat. Interdiscip. Top.* **2016**, *94*, 32122.
(600) Balberg, I.; Binenbaum, N.; Wagner, N. Percolation Thresholds in the Three-Dimensional Sticks System. *Phys. Rev. Lett.* **1984**, *52*, 1465−1468.
(601) Balberg, I. Excluded-Volume Explanation of Archie's Law. *Phys. Rev. B: Condens. Matter Mater. Phys.* **1986**, *33*, 3618−3620.
(602) Lewis, J.; Grego, S.; Chalamala, B.; Vick, E.; Temple, D. Highly Flexible Transparent Electrodes for Organic Light-Emitting Diode-Based Displays. *Appl. Phys. Lett.* **2004**, *85*, 3450−3452.

DOI: 10.1021/acs.chemrev.8b00745
Chem. Rev. XXXX, XXX, XXX−XXX

(603) Chopra, K. L.; Major, S.; Pandya, D. K. Transparent Conductors-A Status Review. *Thin Solid Films* **1983**, *102*, 1−46.
(604) Sannicolo, T.; Lagrange, M.; Cabos, A.; Celle, C.; Simonato, J. P.; Bellet, D. Metallic Nanowire-Based Transparent Electrodes for Next Generation Flexible Devices: A Review. *Small* **2016**, *12*, 6052−6075.
(605) Granqvist, C. G.; Hultåker, A. Transparent and Conducting ITO Films: New Developments and Applications. *Thin Solid Films* **2002**, *411*, 1−5.
(606) Baetens, R.; Jelle, B. P.; Gustavsen, A. Properties, Requirements and Possibilities of Smart Windows for Dynamic Daylight and Solar Energy Control in Buildings: A State-of-the-Art Review. *Sol. Energy Mater. Sol. Cells* **2010**, *94*, 87−105.
(607) Wassei, J. K.; Kaner, R. B. Graphene, a Promising Transparent Conductor. *Mater. Today* **2010**, *13*, 52−59.
(608) Zhang, M.; Fang, S.; Zakhidov, A. A.; Lee, S. B.; Aliev, A. E.; Williams, C. D.; Atkinson, K. R.; Baughman, R. H. Strong, Transparent, Multifunctional, Carbon Nanotube Sheets. *Science* **2005**, *309*, 1215−1220.
(609) Rowell, M. W.; McGehee, M. D. Transparent Electrode Requirements for Thin Film Solar Cell Modules. *Energy Environ. Sci.* **2011**, *4*, 131−134.
(610) Zhu, H.; Fang, Z.; Preston, C.; Li, Y.; Hu, L. Transparent Paper: Fabrications, Properties, and Device Applications. *Energy Environ. Sci.* **2014**, *7*, 269−287.
(611) Hu, L.; Wu, H.; Cui, Y. Metal Nanogrids, Nanowires, and Nanofibers for Transparent Electrodes. *MRS Bull.* **2011**, *36*, 760−765.
(612) Maniyara, R. A.; Mkhitaryan, V. K.; Chen, T. L.; Ghosh, D. S.; Pruneri, V. An Antireflection Transparent Conductor with Ultralow Optical Loss (<2%) and Electrical Resistance (<6 Ω sq^{-1}). *Nat. Commun.* **2016**, *7*, 13771.
(613) Azzopardi, B.; Emmott, C. J. M.; Urbina, A.; Krebs, F. C.; Mutale, J.; Nelson, J. Economic Assessment of Solar Electricity Production from Organic-Based Photovoltaic Modules in a Domestic Environment. *Energy Environ. Sci.* **2011**, *4*, 3741−3753.
(614) Xia, Y.; Sun, K.; Ouyang, J. Solution-Processed Metallic Conducting Polymer Films as Transparent Electrode of Optoelectronic Devices. *Adv. Mater.* **2012**, *24*, 2436−2440.
(615) Vosgueritchian, M.; Lipomi, D. J.; Bao, Z. Highly Conductive and Transparent PEDOT:PSS Films with a Fluorosurfactant for Stretchable and Flexible Transparent Electrodes. *Adv. Funct. Mater.* **2012**, *22*, 421−428.
(616) Kim, Y. H.; Sachse, C.; MacHala, M. L.; May, C.; Müller-Meskamp, L.; Leo, K. Highly Conductive PEDOT:PSS Electrode with Optimized Solvent and Thermal Post-Treatment for ITO-Free Organic Solar Cells. *Adv. Funct. Mater.* **2011**, *21*, 1076−1081.
(617) Zhang, D.; Ryu, K.; Liu, X.; Polikarpov, E.; Ly, J.; Tompson, M. E.; Zhou, C. Transparent, Conductive, and Flexible Carbon Nanotube Films and Their Application in Organic Light-Emitting Diodes. *Nano Lett.* **2006**, *6*, 1880−1886.
(618) Geng, H.-Z.; Kim, K. K.; So, K. P.; Lee, Y. S.; Chang, Y.; Lee, Y. H. Effect of Acid Treatment on Carbon Nanotube-Based Flexible Transparent Conducting Films. *J. Am. Chem. Soc.* **2007**, *129*, 7758−7759.
(619) Wang, X.; Zhi, L.; Müllen, K. Transparent, Conductive Graphene Electrodes for Dye-Sensitized Solar Cells. *Nano Lett.* **2008**, *8*, 323−327.
(620) Becerril, H. A.; Mao, J.; Liu, Z.; Stoltenberg, R. M.; Bao, Z.; Chen, Y. Evaluation of Solution-Processed Reduced Graphene Oxide Films as Transparent Conductors. *ACS Nano* **2008**, *2*, 463−470.
(621) Li, X.; Zhu, Y.; Cai, W.; Borysiak, M.; Han, B.; Chen, D.; Piner, R. D.; Colombo, L.; Ruoff, R. S. Transfer of Large-Area Graphene Films for High-Performance Transparent Conductive Electrodes. *Nano Lett.* **2009**, *9*, 4359−4363.
(622) Wu, J.; Agrawal, M.; Becerril, H. A.; Bao, Z.; Liu, Z.; Chen, Y.; Peumans, P. Organic Light-Emitting Diodes on Solution-Processed Graphene Transparent Electrodes. *ACS Nano* **2010**, *4*, 43−48.
(623) Lee, J.-Y.; Connor, S. T.; Cui, Y.; Peumans, P. Solution-Processed Metal Nanowire Mesh Transparent Electrodes. *Nano Lett.* **2008**, *8*, 689−692.
(624) De, S.; Higgins, T. M.; Lyons, P. E.; Doherty, E. M.; Nirmalraj, P. N.; Blau, W. J.; Boland, J. J.; Coleman, J. N. Silver Nanowire Networks as Flexible, Transparent, Conducting Films: Extremely High DC to Optical Conductivity Ratios. *ACS Nano* **2009**, *3*, 1767−1774.
(625) Rathmell, A. R.; Wiley, B. J. The Synthesis and Coating of Long, Thin Copper Nanowires to Make Flexible, Transparent Conducting Films on Plastic Substrates. *Adv. Mater.* **2011**, *23*, 4798−4803.
(626) Kulkarni, G. U.; Kiruthika, S.; Gupta, R.; Rao, K. D. M. Towards Low Cost Materials and Methods for Transparent Electrodes. *Curr. Opin. Chem. Eng.* **2015**, *8*, 60−68.
(627) Khanarian, G.; Joo, J.; Liu, X.-Q.; Eastman, P.; Werner, D.; O'Connell, K.; Trefonas, P. The Optical and Electrical Properties of Silver Nanowire Mesh Films. *J. Appl. Phys.* **2013**, *114*, 024302.
(628) Bergin, S. M.; Chen, Y.-H.; Rathmell, A. R.; Charbonneau, P.; Li, Z. Y.; Wiley, B. J. The Effect of Nanowire Length and Diameter on the Properties of Transparent, Conducting Nanowire Films. *Nanoscale* **2012**, *4*, 1996−2004.
(629) Han, J.; Yuan, S.; Liu, L.; Qiu, X.; Gong, H.; Yang, X.; Li, C.; Hao, Y.; Cao, B. Fully Indium-Free Flexible Ag Nanowires/ZnO:F Composite Transparent Conductive Electrodes with High Haze. *J. Mater. Chem. A* **2015**, *3*, 5375−5384.
(630) Marus, M.; Hubarevich, A.; Fan, W. J.; Wang, H.; Smirnov, A.; Wang, K.; Huang, H.; Sun, X. W. Optical Haze of Randomly Arranged Silver Nanowire Transparent Conductive Films with Wide Range of Nanowire Diameters. *AIP Adv.* **2018**, *8*, 035201.
(631) Preston, C.; Xu, Y.; Han, X.; Munday, J. N.; Hu, L. Optical Haze of Transparent and Conductive Silver Nanowire Films. *Nano Res.* **2013**, *6*, 461−468.
(632) Van De Groep, J.; Spinelli, P.; Polman, A. Transparent Conducting Silver Nanowire Networks. *Nano Lett.* **2012**, *12*, 3138−3144.
(633) Stauffer, D.; Aharony, A. *Introduction to Percolation Theory*, 2nd ed.; Taylor & Francis: London, 2003.
(634) Li, J.; Zhang, S.-L. Conductivity Exponents in Stick Percolation. *Phys. Rev. E* **2010**, *81*, 21120.
(635) Zezelj, M.; Stanković, I. From Percolating to Dense Random Stick Networks: Conductivity Model Investigation. *Phys. Rev. B: Condens. Matter Mater. Phys.* **2012**, *86*, 134202.
(636) Xu, W.; Xu, Q.; Huang, Q.; Tan, R.; Shen, W.; Song, W. Fabrication of Flexible Transparent Conductive Films with Silver Nanowire by Vacuum Filtration and PET Mold Transfer. *J. Mater. Sci. Technol.* **2016**, *32*, 158−161.
(637) Large, M. J.; Cann, M.; Ogilvie, S. P.; King, A. A. K.; Jurewicz, I.; Dalton, A. B. Finite-Size Scaling in Silver Nanowire Films: Design Considerations for Practical Devices. *Nanoscale* **2016**, *8*, 13701−13707.
(638) Hu, L.; Hecht, D. S.; Gruner, G. Percolation in Transparent and Conducting Carbon Nanotube Networks. *Nano Lett.* **2004**, *4*, 2513−2517.
(639) Hecht, D.; Hu, L.; Grüner, G. Conductivity Scaling with Bundle Length and Diameter in Single Walled Carbon Nanotube Networks. *Appl. Phys. Lett.* **2006**, *89*, 133112.
(640) Unalan, H. E.; Fanchini, G.; Kanwal, A.; Du Pasquier, A.; Chhowalla, M. Design Criteria for Transparent Single-Wall Carbon Nanotube Thin-Film Transistors. *Nano Lett.* **2006**, *6*, 677−682.
(641) O'Callaghan, C.; Gomes Da Rocha, C.; Manning, H. G.; Boland, J. J.; Ferreira, M. S. Effective Medium Theory for the Conductivity of Disordered Metallic Nanowire Networks. *Phys. Chem. Chem. Phys.* **2016**, *18*, 27564−27571.
(642) Garnett, E. C.; Cai, W.; Cha, J. J.; Mahmood, F.; Connor, S. T.; Greyson Christoforo, M.; Cui, Y.; McGehee, M. D.; Brongersma, M. L. Self-Limited Plasmonic Welding of Silver Nanowire Junctions. *Nat. Mater.* **2012**, *11*, 241−249.

DOI: 10.1021/acs.chemrev.8b00745
Chem. Rev. XXXX, XXX, XXX−XXX

(643) Hu, L.; Kim, H. S.; Lee, J.-Y.; Peumans, P.; Cui, Y. Scalable Coating and Properties of Transparent Ag Nanowire Electrodes. *ACS Nano* **2010**, *4*, 2955−2963.
(644) Bellew, A. T.; Manning, H. G.; Gomes da Rocha, C.; Ferreira, M. S.; Boland, J. J. Resistance of Single Ag Nanowire Junctions and Their Role in the Conductivity of Nanowire Networks. *ACS Nano* **2015**, *9*, 11422−11429.
(645) Ahn, K.; Kim, D.; Kim, O.; Nam, J. Analysis of Transparent Conductive Silver Nanowire Films from Dip Coating Flow. *J. Coat. Technol. Res.* **2015**, *12*, 855−862.
(646) Gaynor, W.; Burkhard, G. F.; McGehee, M. D.; Peumans, P. Smooth Nanowire/Polymer Composite Transparent Electrodes. *Adv. Mater.* **2011**, *23*, 2905−2910.
(647) Lee, D.; Lee, H.; Ahn, Y.; Lee, Y. High-Performance Flexible Transparent Conductive Film Based on Graphene/AgNW/Graphene Sandwich Structure. *Carbon* **2015**, *81*, 439−446.
(648) Kim, A.; Lee, H.; Kwon, H.-C.; Jung, H. S.; Park, N.-G.; Jeong, S.; Moon, J. Fully Solution-Processed Transparent Electrodes Based on Silver Nanowire Composites for Perovskite Solar Cells. *Nanoscale* **2016**, *8*, 6308−6316.
(649) Ahn, Y.; Lee, D.; Jeong, Y.; Lee, H.; Lee, Y. Flexible Metal Nanowire-Parylene C Transparent Electrodes for next Generation Optoelectronic Devices. *J. Mater. Chem. C* **2017**, *5*, 2425−2431.
(650) Krantz, J.; Stubhan, T.; Richter, M.; Spallek, S.; Litzov, I.; Matt, G. J.; Spiecker, E.; Brabec, C. J. Spray-Coated Silver Nanowires as Top Electrode Layer in Semitransparent P3HT:PCBM-Based Organic Solar Cell Devices. *Adv. Funct. Mater.* **2013**, *23*, 1711−1717.
(651) Hwang, H.; Kim, A.; Zhong, Z.; Kwon, H.-C.; Jeong, S.; Moon, J. Reducible-Shell-Derived Pure-Copper-Nanowire Network and Its Application to Transparent Conducting Electrodes. *Adv. Funct. Mater.* **2016**, *26*, 6545−6554.
(652) Kim, T.; Canlier, A.; Kim, G. H.; Choi, J.; Park, M.; Han, S. M. Electrostatic Spray Deposition of Highly Transparent Silver Nanowire Electrode on Flexible Substrate. *ACS Appl. Mater. Interfaces* **2013**, *5*, 788−794.
(653) Lee, P.; Lee, J.; Lee, H.; Yeo, J.; Hong, S.; Nam, K. H.; Lee, D.; Lee, S. S.; Ko, S. H. Highly Stretchable and Highly Conductive Metal Electrode by Very Long Metal Nanowire Percolation Network. *Adv. Mater.* **2012**, *24*, 3326−3332.
(654) Kim, B. S.; Shin, K.-Y.; Pyo, J. B.; Lee, J.; Son, J. G.; Lee, S.-S.; Park, J. H. Reversibly Stretchable, Optically Transparent Radio-Frequency Antennas Based on Wavy Ag Nanowire Networks. *ACS Appl. Mater. Interfaces* **2016**, *8*, 2582−2590.
(655) Lee, H.; Hong, S.; Lee, J.; Suh, Y. D.; Kwon, J.; Moon, H.; Kim, H.; Yeo, J.; Ko, S. H. Highly Stretchable and Transparent Supercapacitor by Ag-Au Core-Shell Nanowire Network with High Electrochemical Stability. *ACS Appl. Mater. Interfaces* **2016**, *8*, 15449−15458.
(656) Lee, S. J.; Kim, Y.-H.; Kim, J. K.; Baik, H.; Park, J. H.; Lee, J.; Nam, J.; Park, J. H.; Lee, T.-W.; Yi, G.-R.; et al. A Roll-to-Roll Welding Process for Planarized Silver Nanowire Electrodes. *Nanoscale* **2014**, *6*, 11828−11834.
(657) Scheideler, W. J.; Smith, J.; Deckman, I.; Chung, S.; Arias, A. C.; Subramanian, V. A Robust, Gravure-Printed, Silver Nanowire/Metal Oxide Hybrid Electrode for High-Throughput Patterned Transparent Conductors. *J. Mater. Chem. C* **2016**, *4*, 3248−3255.
(658) Deng, B.; Hsu, P.-C.; Chen, G.; Chandrashekar, B. N.; Liao, L.; Ayitimuda, Z.; Wu, J.; Guo, Y.; Lin, L.; Zhou, Y.; et al. Roll-to-Roll Encapsulation of Metal Nanowires between Graphene and Plastic Substrate for High-Performance Flexible Transparent Electrodes. *Nano Lett.* **2015**, *15*, 4206−4213.
(659) Nian, Q.; Saei, M.; Xu, Y.; Sabyasachi, G.; Deng, B.; Chen, Y. P.; Cheng, G. J. Crystalline Nanojoining Silver Nanowire Percolated Networks on Flexible Substrate. *ACS Nano* **2015**, *9*, 10018−10031.
(660) Zhong, Z.; Woo, K.; Kim, I.; Hwang, H.; Kwon, S.; Choi, Y.-M.; Lee, Y.; Lee, T.-M.; Kim, K.; Moon, J. Roll-to-Roll-Compatible, Flexible, Transparent Electrodes Based on Self-Nanoembedded Cu Nanowires Using Intense Pulsed Light Irradiation. *Nanoscale* **2016**, *8*, 8995−9003.
(661) Zhong, Z.; Lee, H.; Kang, D.; Kwon, S.; Choi, Y.-M.; Kim, I.; Kim, K.-Y.; Lee, Y.; Woo, K.; Moon, J. Continuous Patterning of Copper Nanowire-Based Transparent Conducting Electrodes for Use in Flexible Electronic Applications. *ACS Nano* **2016**, *10*, 7847−7854.
(662) Kim, D.-J.; Shin, H.-I.; Ko, E.-H.; Kim, K.-H.; Kim, T.-W.; Kim, H.-K. Roll-to-Roll Slot-Die Coating of 400 mm Wide, Flexible, Transparent Ag Nanowire Films for Flexible Touch Screen Panels. *Sci. Rep.* **2016**, *6*, 34322.
(663) Kang, S.; Kim, T.; Cho, S.; Lee, Y.; Choe, A.; Walker, B.; Ko, S.-J.; Kim, J. Y.; Ko, H. Capillary Printing of Highly Aligned Silver Nanowire Transparent Electrodes for High-Performance Optoelectronic Devices. *Nano Lett.* **2015**, *15*, 7933−7942.
(664) Tokuno, T.; Nogi, M.; Karakawa, M.; Jiu, J.; Nge, T. T.; Aso, Y.; Suganuma, K. Fabrication of Silver Nanowire Transparent Electrodes at Room Temperature. *Nano Res.* **2011**, *4*, 1215−1222.
(665) Hauger, T. C.; Al-Rafia, S. M. I.; Buriak, J. M. Rolling Silver Nanowire Electrodes: Simultaneously Addressing Adhesion, Roughness, and Conductivity. *ACS Appl. Mater. Interfaces* **2013**, *5*, 12663−12671.
(666) Stewart, I. E.; Rathmell, A. R.; Yan, L.; Ye, S.; Flowers, P. F.; You, W.; Wiley, B. J. Solution-Processed Copper-Nickel Nanowire Anodes for Organic Solar Cells. *Nanoscale* **2014**, *6*, 5980−5988.
(667) Lee, J.; Lee, P.; Lee, H.; Lee, D.; Lee, S. S.; Ko, S. H. Very Long Ag Nanowire Synthesis and Its Application in a Highly Transparent, Conductive and Flexible Metal Electrode Touch Panel. *Nanoscale* **2012**, *4*, 6408−6414.
(668) Han, S.; Hong, S.; Ham, J.; Yeo, J.; Lee, J.; Kang, B.; Lee, P.; Kwon, J.; Lee, S. S.; Yang, M.-Y.; et al. Fast Plasmonic Laser Nanowelding for a Cu-Nanowire Percolation Network for Flexible Transparent Conductors and Stretchable Electronics. *Adv. Mater.* **2014**, *26*, 5808−5814.
(669) Chung, W.-H.; Kim, S.-H.; Kim, H.-S. Welding of Silver Nanowire Networks via Flash White Light and UV-C Irradiation for Highly Conductive and Reliable Transparent Electrodes. *Sci. Rep.* **2016**, *6*, 32086.
(670) Park, J. H.; Han, S.; Kim, D.; You, B. K.; Joe, D. J.; Hong, S.; Seo, J.; Kwon, J.; Jeong, C. K.; Park, H.-J.; et al. Plasmonic-Tuned Flash Cu Nanowelding with Ultrafast Photochemical-Reducing and Interlocking on Flexible Plastics. *Adv. Funct. Mater.* **2017**, *27*, 1701138.
(671) Lu, H.; Zhang, D.; Ren, X.; Liu, J.; Choy, W. C. H. Selective Growth and Integration of Silver Nanoparticles on Silver Nanowires at Room Conditions for Transparent Nano-Network Electrode. *ACS Nano* **2014**, *8*, 10980−10987.
(672) Liu, Y.; Zhang, J.; Gao, H.; Wang, Y.; Liu, Q.; Huang, S.; Guo, C. F.; Ren, Z. Capillary-Force-Induced Cold Welding in Silver-Nanowire-Based Flexible Transparent Electrodes. *Nano Lett.* **2017**, *17*, 1090−1096.
(673) Ge, Y.; Duan, X.; Zhang, M.; Mei, L.; Hu, J.; Hu, W.; Duan, X. Direct Room Temperature Welding and Chemical Protection of Silver Nanowire Thin Films for High Performance Transparent Conductors. *J. Am. Chem. Soc.* **2018**, *140*, 193−199.
(674) Liu, S.; Yue, J.; Gedanken, A. Synthesis of Long Silver Nanowires from AgBr Nanocrystals. *Adv. Mater.* **2001**, *13*, 656−658.
(675) Schuette, W. M.; Buhro, W. E. Silver Chloride as a Heterogeneous Nucleant for the Growth of Silver Nanowires. *ACS Nano* **2013**, *7*, 3844−3853.
(676) Xiang, H.; Guo, T.; Xu, M.; Lu, H.; Liu, S.; Yu, G. Ultrathin Copper Nanowire Synthesis with Tunable Morphology Using Organic Amines for Transparent Conductors. *ACS Appl. Nano Mater.* **2018**, *1*, 3754−3759.
(677) Zhang, Y.; Guo, J.; Xu, D.; Sun, Y.; Yan, F. Synthesis of Ultralong Copper Nanowires for High-Performance Flexible Transparent Conductive Electrodes: The Effects of Polyhydric Alcohols. *Langmuir* **2018**, *34*, 3884−3893.
(678) Bari, B.; Lee, J.; Jang, T.; Won, P.; Ko, S. H.; Alamgir, K.; Arshad, M.; Guo, L. J. Simple Hydrothermal Synthesis of Very-Long and Thin Silver Nanowires and Their Application in High Quality Transparent Electrodes. *J. Mater. Chem. A* **2016**, *4*, 11365−11371.

DOI: 10.1021/acs.chemrev.8b00745
Chem. Rev. XXXX, XXX, XXX−XXX

(679) Lee, J. H.; Lee, P.; Lee, D.; Lee, S. S.; Ko, S. H. Large-Scale Synthesis and Characterization of Very Long Silver Nanowires via Successive Multistep Growth. *Cryst. Growth Des.* **2012**, *12*, 5598−5605.
(680) Marus, M.; Hubarevich, A.; Lim, R. J. W.; Huang, H.; Smirnov, A.; Wang, H.; Fan, W.; Sun, X. W. Effect of Silver Nanowire Length in a Broad Range on Optical and Electrical Properties as a Transparent Conductive Film. *Opt. Mater. Express* **2017**, *7*, 1105−1112.
(681) Zhang, D.; Wang, R.; Wen, M.; Weng, D.; Cui, X.; Sun, J.; Li, H.; Lu, Y. Synthesis of Ultralong Copper Nanowires for High-Performance Transparent Electrodes. *J. Am. Chem. Soc.* **2012**, *134*, 14283−14286.
(682) Pradel, K. C.; Sohn, K.; Huang, J. Cross-Flow Purification of Nanowires. *Angew. Chem., Int. Ed.* **2011**, *50*, 3412−3416.
(683) Qian, F.; Lan, P. C.; Olson, T.; Zhu, C.; Duoss, E. B.; Spadaccini, C. M.; Han, T. Y.-J. Multiphase Separation of Copper Nanowires. *Chem. Commun.* **2016**, *52*, 11627−11630.
(684) Kang, C.; Yang, S.; Tan, M.; Wei, C.; Liu, Q.; Fang, J.; Liu, G. Purification of Copper Nanowires to Prepare Flexible Transparent Conductive Films with High Performance. *ACS Appl. Nano Mater.* **2018**, *1*, 3155−3163.
(685) Graedel, T. E.; Franey, J. P.; Gualtieri, G. J.; Kammlott, G. W.; Malm, D. L. On the Mechanism of Silver and Copper Sulfidation by Atmospheric H_2S and OCS. *Corros. Sci.* **1985**, *25*, 1163−1180.
(686) Mcmahon, M. D.; Lopez, R.; Meyer, H. M.; Feldman, L. C.; Haglund, R. F., Jr. Rapid Tarnishing of Silver Nanoparticles in Ambient Laboratory Air. *Appl. Phys. B: Lasers Opt.* **2005**, *80*, 915−921.
(687) Ahn, Y.; Jeong, Y.; Lee, Y. Improved Thermal Oxidation Stability of Solution-Processable Silver Nanowire Transparent Electrode by Reduced Graphene Oxide. *ACS Appl. Mater. Interfaces* **2012**, *4*, 6410−6414.
(688) Chen, Z.; Ye, S.; Stewart, I. E.; Wiley, B. J. Copper Nanowire Networks with Transparent Oxide Shells That Prevent Oxidation without Reducing Transmittance. *ACS Nano* **2014**, *8*, 9673−9679.
(689) Song, J.; Li, J.; Xu, J.; Zeng, H. Superstable Transparent Conductive Cu@Cu_4Ni Nanowire Elastomer Composites against Oxidation, Bending, Stretching, and Twisting for Flexible and Stretchable Optoelectronics. *Nano Lett.* **2014**, *14*, 6298−6305.
(690) Chu, C. R.; Lee, C.; Koo, J.; Lee, H. M. Fabrication of Sintering-Free Flexible Copper Nanowire/Polymer Composite Transparent Electrodes with Enhanced Chemical and Mechanical Stability. *Nano Res.* **2016**, *9*, 2162−2173.
(691) Dou, L.; Cui, F.; Yu, Y.; Khanarian, G.; Eaton, S. W.; Yang, Q.; Resasco, J.; Schildknecht, C.; Schierle-Arndt, K.; Yang, P. Solution-Processed Copper/Reduced-Graphene-Oxide Core/Shell Nanowire Transparent Conductors. *ACS Nano* **2016**, *10*, 2600−2606.
(692) Yang, C.; Gu, H.; Lin, W.; Yuen, M. M.; Wong, C. P.; Xiong, M.; Gao, B. Silver Nanowires: From Scalable Synthesis to Recyclable Foldable Electronics. *Adv. Mater.* **2011**, *23*, 3052−3056.
(693) Maurer, J. H. M.; González-García, L.; Reiser, B.; Kanelidis, I.; Kraus, T. Templated Self-Assembly of Ultrathin Gold Nanowires by Nanoimprinting for Transparent Flexible Electronics. *Nano Lett.* **2016**, *16*, 2921−2925.
(694) Yin, Z.; Song, S. K.; You, D.-J.; Ko, Y.; Cho, S.; Yoo, J.; Park, S. Y.; Piao, Y.; Chang, S. T.; Kim, Y. S. Novel Synthesis, Coating, and Networking of Curved Copper Nanowires for Flexible Transparent Conductive Electrodes. *Small* **2015**, *11*, 4576−4583.
(695) Won, Y.; Kim, A.; Yang, W.; Jeong, S.; Moon, J. A Highly Stretchable, Helical Copper Nanowire Conductor Exhibiting a Stretchability of 700%. *NPG Asia Mater.* **2014**, *6*, e132.
(696) Xu, F.; Zhu, Y. Highly Conductive and Stretchable Silver Nanowire Conductors. *Adv. Mater.* **2012**, *24*, 5117−5122.
(697) Yun, S.; Niu, X.; Yu, Z.; Hu, W.; Brochu, P.; Pei, Q. Compliant Silver Nanowire-Polymer Composite Electrodes for Bistable Large Strain Actuation. *Adv. Mater.* **2012**, *24*, 1321−1327.
(698) Zhu, Y.; Qin, Q.; Xu, F.; Fan, F.; Ding, Y.; Zhang, T.; Wiley, B. J.; Wang, Z. L. Size Effects on Elasticity, Yielding, and Fracture of Silver Nanowires: In Situ Experiments. *Phys. Rev. B: Condens. Matter Mater. Phys.* **2012**, *85*, 45443.
(699) Wu, J.; Zang, J.; Rathmell, A. R.; Zhao, X.; Wiley, B. J. Reversible Sliding in Networks of Nanowires. *Nano Lett.* **2013**, *13*, 2381−2386.
(700) Lim, G.-H.; Ahn, K.; Bok, S.; Nam, J.; Lim, B. Curving Silver Nanowires Using Liquid Droplets for Highly Stretchable and Durable Percolation Networks. *Nanoscale* **2017**, *9*, 8938−8944.
(701) Moon, H.; Won, P.; Lee, J.; Ko, S. H. Low-Haze, Annealing-Free, Very Long Ag Nanowire Synthesis and Its Application in a Flexible Transparent Touch Panel. *Nanotechnology* **2016**, *27*, 295201.
(702) Cho, S.; Kang, S.; Pandya, A.; Shanker, R.; Khan, Z.; Lee, Y.; Park, J.; Craig, S. L.; Ko, H. Large-Area Cross-Aligned Silver Nanowire Electrodes for Flexible, Transparent, and Force-Sensitive Mechanochromic Touch Screens. *ACS Nano* **2017**, *11*, 4346−4357.
(703) Yu, Z.; Li, L.; Zhang, Q.; Hu, W.; Pei, Q. Silver Nanowire-Polymer Composite Electrodes for Efficient Polymer Solar Cells. *Adv. Mater.* **2011**, *23*, 4453−4457.
(704) Kim, A.; Won, Y.; Woo, K.; Kim, C.-H.; Moon, J. Highly Transparent Low Resistance ZnO/Ag Nanowire/ZnO Composite Electrode for Thin Film Solar Cells. *ACS Nano* **2013**, *7*, 1081−1091.
(705) Yim, J. H.; Joe, S.; Pang, C.; Lee, K. M.; Jeong, H.; Park, J.-Y.; Ahn, Y. H.; De Mello, J. C.; Lee, S. Fully Solution-Processed Semitransparent Organic Solar Cells with a Silver Nanowire Cathode and a Conducting Polymer Anode. *ACS Nano* **2014**, *8*, 2857−2863.
(706) Hwang, H.; Ahn, J.; Lee, E.; Kim, K.; Kwon, H.-C.; Moon, J. Enhanced Compatibility between a Copper Nanowire-Based Transparent Electrode and a Hybrid Perovskite Absorber by Poly(ethylenimine). *Nanoscale* **2017**, *9*, 17207−17211.
(707) Ahn, J.; Hwang, H.; Jeong, S.; Moon, J. Metal-Nanowire-Electrode-Based Perovskite Solar Cells: Challenging Issues and New Opportunities. *Adv. Energy Mater.* **2017**, *7*, 1602751.
(708) Preston, C.; Fang, Z.; Murray, J.; Zhu, H.; Dai, J.; Munday, J. N.; Hu, L. Silver Nanowire Transparent Conducting Paper-Based Electrode with High Optical Haze. *J. Mater. Chem. C* **2014**, *2*, 1248−1254.
(709) Chen, T.-G.; Huang, B.-Y.; Liu, H.-W.; Huang, Y.-Y.; Pan, H.-T.; Meng, H.-F.; Yu, P. Flexible Silver Nanowire Meshes for High-Efficiency Microtextured Organic-Silicon Hybrid Photovoltaics. *ACS Appl. Mater. Interfaces* **2012**, *4*, 6857−6864.
(710) Krantz, J.; Richter, M.; Spallek, S.; Spiecker, E.; Brabec, C. J. Solution-Processed Metallic Nanowire Electrodes as Indium Tin Oxide Replacement for Thin-Film Solar Cells. *Adv. Funct. Mater.* **2011**, *21*, 4784−4787.
(711) Yang, L.; Zhang, T.; Zhou, H.; Price, S. C.; Wiley, B. J.; You, W. Solution-Processed Flexible Polymer Solar Cells with Silver Nanowire Electrodes. *ACS Appl. Mater. Interfaces* **2011**, *3*, 4075−4084.
(712) Li, L.; Yu, Z.; Hu, W.; Chang, C.-H.; Chen, Q.; Pei, Q. Efficient Flexible Phosphorescent Polymer Light-Emitting Diodes Based on Silver Nanowire-Polymer Composite Electrode. *Adv. Mater.* **2011**, *23*, 5563−5567.
(713) Yu, Z.; Zhang, Q.; Li, L.; Chen, Q.; Niu, X.; Liu, J.; Pei, Q. Highly Flexible Silver Nanowire Electrodes for Shape-Memory Polymer Light-Emitting Diodes. *Adv. Mater.* **2011**, *23*, 664−668.
(714) Liang, J.; Li, L.; Tong, K.; Ren, Z.; Hu, W.; Niu, X.; Chen, Y.; Pei, Q. Silver Nanowire Percolation Network Soldered with Graphene Oxide at Room Temperature and Its Application for Fully Stretchable Polymer Light-Emitting Diodes. *ACS Nano* **2014**, *8*, 1590−1600.
(715) Lee, J.; An, K.; Won, P.; Ka, Y.; Hwang, H.; Moon, H.; Kwon, Y.; Hong, S.; Kim, C.; Lee, C.; et al. A Dual-Scale Metal Nanowire Network Transparent Conductor for Highly Efficient and Flexible Organic Light Emitting Diodes. *Nanoscale* **2017**, *9*, 1978−1985.
(716) Sim, H.; Kim, C.; Bok, S.; Kim, M. K.; Oh, H.; Lim, G.-H.; Cho, S. M.; Lim, B. Five-Minute Synthesis of Silver Nanowires and Their Roll-to-Roll Processing for Large-Area Organic Light Emitting Diodes. *Nanoscale* **2018**, *10*, 12087−12092.

DOI: 10.1021/acs.chemrev.8b00745
Chem. Rev. XXXX, XXX, XXX−XXX

(717) Yun, T. G.; Kim, D.; Kim, Y. H.; Park, M.; Hyun, S.; Han, S. M. Photoresponsive Smart Coloration Electrochromic Supercapacitor. *Adv. Mater.* **2017**, *29*, 1606728.
(718) Moon, H.; Lee, H.; Kwon, J.; Suh, Y. D.; Kim, D. K.; Ha, I.; Yeo, J.; Hong, S.; Ko, S. H. Ag/Au/Polypyrrole Core-Shell Nanowire Network for Transparent, Stretchable and Flexible Supercapacitor in Wearable Energy Devices. *Sci. Rep.* **2017**, *7*, 41981.
(719) Jeong, S.; Cho, H.; Han, S.; Won, P.; Lee, H.; Hong, S.; Yeo, J.; Kwon, J.; Ko, S. H. High Efficiency, Transparent, Reusable, and Active PM2.5 Filters by Hierarchical Ag Nanowire Percolation Network. *Nano Lett.* **2017**, *17*, 4339−4346.
(720) Jung, J.; Lee, H.; Ha, I.; Cho, H.; Kim, K. K.; Kwon, J.; Won, P.; Hong, S.; Ko, S. H. Highly Stretchable and Transparent Electromagnetic Interference Shielding Film Based on Silver Nanowire Percolation Network for Wearable Electronics Applications. *ACS Appl. Mater. Interfaces* **2017**, *9*, 44609−44616.
(721) Hu, M.; Gao, J.; Dong, Y.; Li, K.; Shan, G.; Yang, S.; Li, R. K.-Y. Flexible Transparent PES/Silver Nanowires/PET Sandwich-Structured Film for High-Efficiency Electromagnetic Interference Shielding. *Langmuir* **2012**, *28*, 7101−7106.
(722) Kang, S.; Cho, S.; Shanker, R.; Lee, H.; Park, J.; Um, D.-S.; Lee, Y.; Ko, H. Transparent and Conductive Nanomembranes with Orthogonal Silver Nanowire Arrays for Skin-Attachable Loudspeakers and Microphones. *Sci. Adv.* **2018**, *4*, eaas8772.
(723) Zilberberg, K.; Gasse, F.; Pagui, R.; Polywka, A.; Behrendt, A.; Trost, S.; Heiderhoff, R.; Görrn, P.; Riedl, T. Highly Robust Indium-Free Transparent Conductive Electrodes Based on Composites of Silver Nanowires and Conductive Metal Oxides. *Adv. Funct. Mater.* **2014**, *24*, 1671−1678.
(724) Lu, H.; Sun, J.; Zhang, H.; Lu, S.; Choy, W. C. H. Room-Temperature Solution-Processed and Metal Oxide-Free Nano-Composite for the Flexible Transparent Bottom Electrode of Perovskite Solar Cells. *Nanoscale* **2016**, *8*, 5946−5953.
(725) Im, H.-G.; Jeong, S.; Jin, J.; Lee, J.; Youn, D.-Y.; Koo, W.-T.; Kang, S.-B.; Kim, H.-J.; Jang, J.; Lee, D.; et al. Hybrid Crystalline-ITO/Metal Nanowire Mesh Transparent Electrodes and Their Application for Highly Flexible Perovskite Solar Cells. *NPG Asia Mater.* **2016**, *8*, e282.
(726) Zeng, X.-Y.; Zhang, Q.-K.; Yu, R.-M.; Lu, C.-Z. A New Transparent Conductor: Silver Nanowire Film Buried at the Surface of a Transparent Polymer. *Adv. Mater.* **2010**, *22*, 4484−4488.
(727) Li, R.; Xiang, X.; Tong, X.; Zou, J.; Li, Q. Wearable Double-Twisted Fibrous Perovskite Solar Cell. *Adv. Mater.* **2015**, *27*, 3831−3835.
(728) Peng, C.; Zhan, Y.; Lou, J. Size-Dependent Fracture Mode Transition in Copper Nanowires. *Small* **2012**, *8*, 1889−1894.
(729) Filleter, T.; Ryu, S.; Kang, K.; Yin, J.; Bernal, R. A.; Sohn, K.; Li, S.; Huang, J.; Cai, W.; Espinosa, H. D. Nucleation-Controlled Distributed Plasticity in Penta-Twinned Silver Nanowires. *Small* **2012**, *8*, 2986−2993.
(730) Yue, Y.; Chen, N.; Li, X.; Zhang, S.; Zhang, Z.; Chen, M.; Han, X. Crystalline Liquid and Rubber-like Behavior in Cu Nanowires. *Nano Lett.* **2013**, *13*, 3812−3816.
(731) Narayanan, S.; Cheng, G.; Zeng, Z.; Zhu, Y.; Zhu, T. Strain Hardening and Size Effect in Five-Fold Twinned Ag Nanowires. *Nano Lett.* **2015**, *15*, 4037−4044.
(732) Catenacci, M. J.; Reyes, C.; Cruz, M. A.; Wiley, B. J. Stretchable Conductive Composites from Cu-Ag Nanowire Felt. *ACS Nano* **2018**, *12*, 3689−3698.
(733) Amjadi, M.; Pichitpajongkit, A.; Lee, S.; Ryu, S.; Park, I. Highly Stretchable and Sensitive Strain Sensor Based on Silver-Elastomer Nanocomposite. *ACS Nano* **2014**, *8*, 5154−5163.
(734) Yan, C.; Kang, W.; Wang, J.; Cui, M.; Wang, X.; Foo, C. Y.; Chee, K. J.; Lee, P. S. Stretchable and Wearable Electrochromic Devices. *ACS Nano* **2014**, *8*, 316−322.
(735) Chen, S.; Wei, Y.; Wei, S.; Lin, Y.; Liu, L. Ultrasensitive Cracking-Assisted Strain Sensors Based on Silver Nanowires/Graphene Hybrid Particles. *ACS Appl. Mater. Interfaces* **2016**, *8*, 25563−25570.
(736) Zhang, W.; Yin, Z.; Chun, A.; Yoo, J.; Kim, Y. S.; Piao, Y. Bridging Oriented Copper Nanowire-Graphene Composites for Solution-Processable, Annealing-Free, and Air-Stable Flexible Electrodes. *ACS Appl. Mater. Interfaces* **2016**, *8*, 1733−1741.
(737) Gong, S.; Schwalb, W.; Wang, Y.; Chen, Y.; Tang, Y.; Si, J.; Shirinzadeh, B.; Cheng, W. A Wearable and Highly Sensitive Pressure Sensor with Ultrathin Gold Nanowires. *Nat. Commun.* **2014**, *5*, 3132.
(738) Lee, T.-W.; Lee, S.-E.; Jeong, Y. G. Highly Effective Electromagnetic Interference Shielding Materials Based on Silver Nanowire/Cellulose Papers. *ACS Appl. Mater. Interfaces* **2016**, *8*, 13123−13132.
(739) Wu, C.; Fang, L.; Huang, X.; Jiang, P. Three-Dimensional Highly Conductive Graphene-Silver Nanowire Hybrid Foams for Flexible and Stretchable Conductors. *ACS Appl. Mater. Interfaces* **2014**, *6*, 21026−21034.
(740) Kim, A.; Ahn, J.; Hwang, H.; Lee, E.; Moon, J. A Pre-Strain Strategy for Developing a Highly Stretchable and Foldable One-Dimensional Conductive Cord Based on a Ag Nanowire Network. *Nanoscale* **2017**, *9*, 5773−5778.
(741) Lee, S.; Shin, S.; Lee, S.; Seo, J.; Lee, J.; Son, S.; Cho, H. J.; Algadi, H.; Al-Sayari, S.; Kim, D. E.; et al. Ag Nanowire Reinforced Highly Stretchable Conductive Fibers for Wearable Electronics. *Adv. Funct. Mater.* **2015**, *25*, 3114−3121.
(742) Lu, Y.; Jiang, J.; Yoon, S.; Kim, K.-S.; Kim, J.-H.; Park, S.; Kim, S.-H.; Piao, L. High-Performance Stretchable Conductive Composite Fibers from Surface-Modified Silver Nanowires and Thermoplastic Polyurethane by Wet Spinning. *ACS Appl. Mater. Interfaces* **2018**, *10*, 2093−2104.
(743) Tang, Y.; Gong, S.; Chen, Y.; Yap, L. W.; Cheng, W. Manufacturable Conducting Rubber Ambers and Stretchable Conductors from Copper Nanowire Aerogel Monoliths. *ACS Nano* **2014**, *8*, 5707−5714.
(744) Huang, G.-W.; Xiao, H.-M.; Fu, S.-Y. Paper-Based Silver-Nanowire Electronic Circuits with Outstanding Electrical Conductivity and Extreme Bending Stability. *Nanoscale* **2014**, *6*, 8495−8502.
(745) Li, R.-Z.; Hu, A.; Zhang, T.; Oakes, K. D. Direct Writing on Paper of Foldable Capacitive Touch Pads with Silver Nanowire Inks. *ACS Appl. Mater. Interfaces* **2014**, *6*, 21721−21729.
(746) Finn, D. J.; Lotya, M.; Coleman, J. N. Inkjet Printing of Silver Nanowire Networks. *ACS Appl. Mater. Interfaces* **2015**, *7*, 9254−9261.
(747) Wei, Y.; Chen, S.; Li, F.; Lin, Y.; Zhang, Y.; Liu, L. Highly Stable and Sensitive Paper-Based Bending Sensor Using Silver Nanowires/Layered Double Hydroxides Hybrids. *ACS Appl. Mater. Interfaces* **2015**, *7*, 14182−14191.
(748) Liang, J.; Tong, K.; Pei, Q. A Water-Based Silver-Nanowire Screen-Print Ink for the Fabrication of Stretchable Conductors and Wearable Thin-Film Transistors. *Adv. Mater.* **2016**, *28*, 5986−5996.
(749) Cui, Z.; Han, Y.; Huang, Q.; Dong, J.; Zhu, Y. Electrohydrodynamic Printing of Silver Nanowires for Flexible and Stretchable Electronics. *Nanoscale* **2018**, *10*, 6806−6811.
(750) Kim, K.-H.; Jeong, D.-W.; Jang, N.-S.; Ha, S.-H.; Kim, J.-M. Extremely Stretchable Conductors Based on Hierarchically-Structured Metal Nanowire Network. *RSC Adv.* **2016**, *6*, 56896−56902.
(751) Gong, S.; Lai, D. T. H.; Wang, Y.; Yap, L. W.; Si, K. J.; Shi, Q.; Jason, N. N.; Sridhar, T.; Uddin, H.; Cheng, W. Tattoolike Polyaniline Microparticle-Doped Gold Nanowire Patches as Highly Durable Wearable Sensors. *ACS Appl. Mater. Interfaces* **2015**, *7*, 19700−19708.
(752) Yao, S.; Zhu, Y. Wearable Multifunctional Sensors Using Printed Stretchable Conductors Made of Silver Nanowires. *Nanoscale* **2014**, *6*, 2345−2352.
(753) Wei, Y.; Chen, S.; Lin, Y.; Yang, Z.; Liu, L. Cu-Ag Core-Shell Nanowires for Electronic Skin with a Petal Molded Microstructure. *J. Mater. Chem. C* **2015**, *3*, 9594−9602.
(754) Al-Saleh, M. H.; Gelves, G. A.; Sundararaj, U. Copper Nanowire/Polystyrene Nanocomposites: Lower Percolation Threshold and Higher EMI Shielding. *Composites, Part A* **2011**, *42*, 92−97.

DOI: 10.1021/acs.chemrev.8b00745
Chem. Rev. XXXX, XXX, XXX−XXX

(755) Wang, Y.; Gu, F.-Q.; Ni, L.-J.; Liang, K.; Marcus, K.; Liu, S.; Yang, F.; Chen, J.; Feng, Z. Easily Fabricated and Lightweight PPy/PDA/AgNW Composites for Excellent Electromagnetic Interference Shielding. *Nanoscale* **2017**, *9*, 18318−18325.
(756) Yu, Y.-H.; Ma, C.-C. M.; Teng, C.-C.; Huang, Y.-L.; Lee, S.-H.; Wang, I.; Wei, M.-H. Electrical, Morphological, and Electromagnetic Interference Shielding Properties of Silver Nanowires and Nanoparticles Conductive Composites. *Mater. Chem. Phys.* **2012**, *136*, 334−340.
(757) Cruz, M. A.; Ye, S.; Kim, M. J.; Reyes, C.; Yang, F.; Flowers, P. F.; Wiley, B. J. Multigram Synthesis of Cu-Ag Core−Shell Nanowires Enables the Production of a Highly Conductive Polymer Filament for 3D Printing Electronics. *Part. Part. Syst. Charact.* **2018**, *35*, 1700385.
(758) Hwang, C.; Kim, T.-H.; Cho, Y.-G.; Kim, J.; Song, H.-K. All-in-One Assembly Based on 3D-Intertangled and Cross-Jointed Architectures of Si/Cu 1D-Nanowires for Lithium Ion Batteries. *Sci. Rep.* **2015**, *5*, 8623.
(759) Lu, L.-L.; Ge, J.; Yang, J.-N.; Chen, S.-M.; Yao, H.-B.; Zhou, F.; Yu, S.-H. Free-Standing Copper Nanowire Network Current Collector for Improving Lithium Anode Performance. *Nano Lett.* **2016**, *16*, 4431−4437.
(760) Chang, W.-C.; Kao, T.-L.; Lin, Y.; Tuan, H.-Y. A Flexible All Inorganic Nanowire Bilayer Mesh as a High-Performance Lithium-Ion Battery Anode. *J. Mater. Chem. A* **2017**, *5*, 22662−22671.
(761) Chu, H.-C.; Tuan, H.-Y. High-Performance Lithium-Ion Batteries with 1.5 μm Thin Copper Nanowire Foil as a Current Collector. *J. Power Sources* **2017**, *346*, 40−48.
(762) Yin, Z.; Cho, S.; You, D.-J.; Ahn, Y.; Yoo, J.; Kim, Y. S. Copper Nanowire/Multi-Walled Carbon Nanotube Composites as All-Nanowire Flexible Electrode for Fast-Charging/Discharging Lithium-Ion Battery. *Nano Res.* **2018**, *11*, 769−779.
(763) Choi, S.; Han, S. I.; Jung, D.; Hwang, H. J.; Lim, C.; Bae, S.; Park, O. K.; Tschabrunn, C. M.; Lee, M.; Bae, S. Y.; et al. Highly Conductive, Stretchable and Biocompatible Ag−Au Core−sheath Nanowire Composite for Wearable and Implantable Bioelectronics. *Nat. Nanotechnol.* **2018**, *13*, 1048−1056.
(764) Hansson, J.; Nilsson, T. M. J.; Ye, L.; Liu, J. Novel Nanostructured Thermal Interface Materials: A Review. *Int. Mater. Rev.* **2018**, *63*, 22−45.
(765) Bhanushali, S.; Ghosh, P. C.; Simon, G. P.; Cheng, W. Copper Nanowire-Filled Soft Elastomer Composites for Applications as Thermal Interface Materials. *Adv. Mater. Interfaces* **2017**, *4*, 1700387.
(766) Prasher, R. Thermal Interface Materials: Historical Perspective, Status, and Future Directions. *Proc. IEEE* **2006**, *94*, 1571−1586.
(767) Balachander, N.; Seshadri, I.; Mehta, R. J.; Schadler, L. S.; Borca-Tasciuc, T.; Keblinski, P.; Ramanath, G. Nanowire-Filled Polymer Composites with Ultrahigh Thermal Conductivity. *Appl. Phys. Lett.* **2013**, *102*, 093117.
(768) Chen, W.; Wang, Z.; Zhi, C.; Zhang, W. High Thermal Conductivity and Temperature Probing of Copper Nanowire/Upconversion Nanoparticles/Epoxy Composite. *Compos. Sci. Technol.* **2016**, *130*, 63−69.
(769) Rai, A.; Moore, A. L. Enhanced Thermal Conduction and Influence of Interfacial Resistance within Flexible High Aspect Ratio Copper Nanowire/Polymer Composites. *Compos. Sci. Technol.* **2017**, *144*, 70−78.
(770) Zhang, L.; Yin, J.; Yu, W.; Wang, M.; Xie, H. Great Thermal Conductivity Enhancement of Silicone Composite with Ultra-Long Copper Nanowires. *Nanoscale Res. Lett.* **2017**, *12*, 462.
(771) Hatta, H.; Taya, M. Thermal Conductivity of Coated Filler Composites. *J. Appl. Phys.* **1986**, *59*, 1851−1860.
(772) Nan, C.-W.; Birringer, R.; Clarke, D. R.; Gleiter, H. Effective Thermal Conductivity of Particulate Composites with Interfacial Thermal Resistance. *J. Appl. Phys.* **1997**, *81*, 6692−6699.
(773) Nan, C.-W.; Shi, Z.; Lin, Y. A Simple Model for Thermal Conductivity of Carbon Nanotube-Based Composites. *Chem. Phys. Lett.* **2003**, *375*, 666−669.
(774) Zhang, P.; Li, Q.; Xuan, Y. Thermal Contact Resistance of Epoxy Composites Incorporated with Nano-Copper Particles and the Multi-Walled Carbon Nanotubes. *Composites, Part A* **2014**, *57*, 1−7.
(775) Zhu, D.; Yu, W.; Du, H.; Chen, L.; Li, Y.; Xie, H. Thermal Conductivity of Composite Materials Containing Copper Nanowires. *J. Nanomater.* **2016**, *2016*, 1−6.
(776) Rivière, L.; Lonjon, A.; Dantras, E.; Lacabanne, C.; Olivier, P.; Gleizes, N. R. Silver Fillers Aspect Ratio Influence on Electrical and Thermal Conductivity in PEEK/Ag Nanocomposites. *Eur. Polym. J.* **2016**, *85*, 115−125.
(777) Wang, S.; Cheng, Y.; Wang, R.; Sun, J.; Gao, L. Highly Thermal Conductive Copper Nanowire Composites with Ultralow Loading: Toward Applications as Thermal Interface Materials. *ACS Appl. Mater. Interfaces* **2014**, *6*, 6481−6486.
(778) Chen, C.; Tang, Y.; Ye, Y. S.; Xue, Z.; Xue, Y.; Xie, X.; Mai, Y.-W. High-Performance Epoxy/Silica Coated Silver Nanowire Composites as Underfill Material for Electronic Packaging. *Compos. Sci. Technol.* **2014**, *105*, 80−85.
(779) Ahn, K.; Kim, K.; Kim, J. Thermal Conductivity and Electric Properties of Epoxy Composites Filled with TiO_2-Coated Copper Nanowire. *Polymer* **2015**, *76*, 313−320.
(780) Kim, K.; Ahn, K.; Ju, H.; Kim, J. Improvement of Insulating and Thermal Properties of SiO_2-Coated Copper Nanowire Composites. *Ind. Eng. Chem. Res.* **2016**, *55*, 2713−2720.
(781) Sorel, S.; Bellet, D.; Coleman, J. N. Relationship between Material Properties and Transparent Heater Performance for Both Bulk-like and Percolative Nanostructured Networks. *ACS Nano* **2014**, *8*, 4805−4814.
(782) Bobinger, M.; Mock, J.; La Torraca, P.; Becherer, M.; Lugli, P.; Larcher, L. Tailoring the Aqueous Synthesis and Deposition of Copper Nanowires for Transparent Electrodes and Heaters. *Adv. Mater. Interfaces* **2017**, *4*, 1700568.
(783) Lee, J.-G.; Lee, J.-H.; An, S.; Kim, D.-Y.; Kim, T.-G.; Al-Deyab, S. S.; Yarin, A. L.; Yoon, S. S. Highly Flexible, Stretchable, Wearable, Patternable and Transparent Heaters on Complex 3D Surfaces Formed from Supersonically Sprayed Silver Nanowires. *J. Mater. Chem. A* **2017**, *5*, 6677−6685.
(784) Li, J.; Liang, J.; Jian, X.; Hu, W.; Li, J.; Pei, Q. A Flexible and Transparent Thin Film Heater Based on a Silver Nanowire/Heat-Resistant Polymer Composite. *Macromol. Mater. Eng.* **2014**, *299*, 1403−1409.
(785) Hong, S.; Lee, H.; Lee, J.; Kwon, J.; Han, S.; Suh, Y. D.; Cho, H.; Shin, J.; Yeo, J.; Ko, S. H. Highly Stretchable and Transparent Metal Nanowire Heater for Wearable Electronics Applications. *Adv. Mater.* **2015**, *27*, 4744−4751.
(786) Choi, S.; Park, J.; Hyun, W.; Kim, J.; Kim, J.; Lee, Y. B.; Song, C.; Hwang, H. J.; Kim, J. H.; Hyeon, T.; et al. Stretchable Heater Using Ligand-Exchanged Silver Nanowire Nanocomposite for Wearable Articular Thermotherapy. *ACS Nano* **2015**, *9*, 6626−6633.
(787) Huang, Q.; Shen, W.; Fang, X.; Chen, G.; Guo, J.; Xu, W.; Tan, R.; Song, W. Highly Flexible and Transparent Film Heaters Based on Polyimide Films Embedded with Silver Nanowires. *RSC Adv.* **2015**, *5*, 45836−45842.
(788) Cheng, Y.; Zhang, H.; Wang, R.; Wang, X.; Zhai, H.; Wang, T.; Jin, Q.; Sun, J. Highly Stretchable and Conductive Copper Nanowire Based Fibers with Hierarchical Structure for Wearable Heaters. *ACS Appl. Mater. Interfaces* **2016**, *8*, 32925−32933.
(789) Doganay, D.; Coskun, S.; Genlik, S. P.; Unalan, H. E. Silver Nanowire Decorated Heatable Textiles. *Nanotechnology* **2016**, *27*, 435201.
(790) Yu, Z.; Gao, Y.; Di, X.; Luo, H. Cotton Modified with Silver-Nanowires/Polydopamine for a Wearable Thermal Management Device. *RSC Adv.* **2016**, *6*, 67771−67777.
(791) Celle, C.; Mayousse, C.; Moreau, E.; Basti, H.; Carella, A.; Simonato, J.-P. Highly Flexible Transparent Film Heaters Based on Random Networks of Silver Nanowires. *Nano Res.* **2012**, *5*, 427−433.
(792) He, X.; Liu, A.; Hu, X.; Song, M.; Duan, F.; Lan, Q.; Xiao, J.; Liu, J.; Zhang, M.; Chen, Y.; et al. Temperature-Controlled

DOI: 10.1021/acs.chemrev.8b00745
Chem. Rev. XXXX, XXX, XXX−XXX

Transparent-Film Heater Based on Silver Nanowire−PMMA Composite Film. *Nanotechnology* **2016**, *27*, 475709.
(793) Seh, Z. W.; Kibsgaard, J.; Dickens, C. F.; Chorkendorff, I.; Nørskov, J. K.; Jaramillo, T. F. Combining Theory and Experiment in Electrocatalysis: Insights into Materials Design. *Science* **2017**, *355*, eaad4998.
(794) Xia, Y.; Yang, X. Toward Cost-Effective and Sustainable Use of Precious Metals in Heterogeneous Catalysts. *Acc. Chem. Res.* **2017**, *50*, 450−454.
(795) Sun, S.; Jaouen, F.; Dodelet, J. P. Controlled Growth of Pt Nanowires on Carbon Nanospheres and Their Enhanced Performance as Electrocatalysts in PEM Fuel Cells. *Adv. Mater.* **2008**, *20*, 3900−3904.
(796) Jiang, K.; Zhao, D.; Guo, S.; Zhang, X.; Zhu, X.; Guo, J.; Lu, G.; Huang, X. Efficient Oxygen Reduction Catalysis by Subnanometer Pt Alloy Nanowires. *Sci. Adv.* **2017**, *3*, e1601705.
(797) Meng, H.; Sun, S.; Masse, J. P.; Dodelet, J. P. Electrosynthesis of Pd Single-Crystal Nanothorns and Their Application in the Oxidation of Formic Acid. *Chem. Mater.* **2008**, *20*, 6998−7002.
(798) Reier, T.; Oezaslan, M.; Strasser, P. Electrocatalytic Oxygen Evolution Reaction (OER) on Ru, Ir, and Pt Catalysts: A Comparative Study of Nanoparticles and Bulk Materials. *ACS Catal.* **2012**, *2*, 1765−1772.
(799) Oh, H. S.; Nong, H. N.; Reier, T.; Gliech, M.; Strasser, P. Oxide-Supported Ir Nanodendrites with High Activity and Durability for the Oxygen Evolution Reaction in Acid PEM Water Electrolyzers. *Chem. Sci.* **2015**, *6*, 3321−3328.
(800) Raciti, D.; Livi, K. J.; Wang, C. Highly Dense Cu Nanowires for Low-Overpotential CO_2 Reduction. *Nano Lett.* **2015**, *15*, 6829−6835.
(801) Wu, J.; Qi, L.; You, H.; Gross, A.; Li, J.; Yang, H. Icosahedral Platinum Alloy Nanocrystals with Enhanced Electrocatalytic Activities. *J. Am. Chem. Soc.* **2012**, *134*, 11880−11883.
(802) Hansen, T. W.; Delariva, A. T.; Challa, S. R.; Datye, A. K. Sintering of Catalytic Nanoparticles: Particle Migration or Ostwald Ripening? *Acc. Chem. Res.* **2013**, *46*, 1720−1730.
(803) Wang, X.; Choi, S.-I.; Roling, L. T.; Luo, M.; Ma, C.; Zhang, L.; Chi, M.; Liu, J.; Xie, Z.; Herron, J. A.; et al. Palladium−Platinum Core-Shell Icosahedra with Substantially Enhanced Activity and Durability towards Oxygen Reduction. *Nat. Commun.* **2015**, *6*, 7594.
(804) Li, K.; Li, X.; Huang, H.; Luo, L.; Li, X.; Yan, X.; Ma, C.; Si, R.; Yang, J.; Zeng, J. One-Nanometer-Thick PtNiRh Trimetallic Nanowires with Enhanced Oxygen Reduction Electrocatalysis in Acid Media: Integrating Multiple Advantages into One Catalyst. *J. Am. Chem. Soc.* **2018**, *140*, 16159−16167.
(805) Huang, H.; Li, K.; Chen, Z.; Luo, L.; Gu, Y.; Zhang, D.; Ma, C.; Si, R.; Yang, J.; Peng, Z.; Zeng, J. Achieving Remarkable Activity and Durability Toward Oxygen Reduction Reaction based on Ultrathin Rh-Doped Pt Nanowires. *J. Am. Chem. Soc.* **2017**, *139*, 8152−8159.
(806) Li, M.; Zhao, Z.; Cheng, T.; Fortunelli, A.; Chen, C. Y.; Yu, R.; Zhang, Q.; Gu, L.; Merinov, B. V.; Lin, Z.; et al. Ultrafine Jagged Platinum Nanowires Enable Ultrahigh Mass Activity for the Oxygen Reduction Reaction. *Science* **2016**, *354*, 1414.
(807) Wang, C.; Waje, M.; Wang, X.; Tang, J. M.; Haddon, R. C.; Yan, Y. Proton Exchange Membrane Fuel Cells with Carbon Nanotube Based Electrodes. *Nano Lett.* **2004**, *4*, 345−348.
(808) Strasser, P.; Koh, S.; Anniyev, T.; Greeley, J.; More, K.; Yu, C.; Liu, Z.; Kaya, S.; Nordlund, D.; Ogasawara, H.; et al. Lattice-Strain Control of the Activity in Dealloyed Core−shell Fuel Cell Catalysts. *Nat. Chem.* **2010**, *2*, 454.
(809) Wang, H.; Xu, S.; Tsai, C.; Li, Y.; Liu, C.; Zhao, J.; Liu, Y.; Yuan, H.; Abild-Pedersen, F.; Prinz, F. B.; et al. Direct and Continuous Strain Control of Catalysts with Tunable Battery Electrode Materials. *Science* **2016**, *354*, 1031−1036.
(810) Zhu, H.; Zhang, S.; Guo, S.; Su, D.; Sun, S. Synthetic Control of FePtM Nanorods (M = Cu, Ni) to Enhance the Oxygen Reduction Reaction. *J. Am. Chem. Soc.* **2013**, *135*, 7130−7133.
(811) Chen, H. S.; Liang, Y. T.; Chen, T. Y.; Tseng, Y. C.; Liu, C. W.; Chung, S. R.; Hsieh, C. T.; Lee, C. E.; Wang, K. W. Graphene-Supported Pt and PtPd Nanorods with Enhanced Electrocatalytic Performance for the Oxygen Reduction Reaction. *Chem. Commun.* **2014**, *50*, 11165−11168.
(812) Chou, S. W.; Shyue, J. J.; Chien, C. H.; Chen, C. C.; Chen, Y. Y.; Chou, P. T. Surfactant-Directed Synthesis of Ternary Nanostructures: Nanocubes, Polyhedrons, Octahedrons, and Nanowires of PtNiFe. Their Shape-Dependent Oxygen Reduction Activity. *Chem. Mater.* **2012**, *24*, 2527−2533.
(813) Guo, S.; Li, D.; Zhu, H.; Zhang, S.; Markovic, N. M.; Stamenkovic, V. R.; Sun, S. FePt and CoPt Nanowires as Efficient Catalysts for the Oxygen Reduction Reaction. *Angew. Chem.* **2013**, *125*, 3549−3552.
(814) Liu, L.; Samjeské, G.; Takao, S.; Nagasawa, K.; Iwasawa, Y. Fabrication of PtCu and PtNiCu Multi-Nanorods with Enhanced Catalytic Oxygen Reduction Activities. *J. Power Sources* **2014**, *253*, 1−8.
(815) Stamenkovic, V.; Mun, B. S.; Mayrhofer, K. J. J.; Ross, P. N.; Markovic, N. M.; Rossmeisl, J.; Greeley, J.; Nørskov, J. K. Changing the Activity of Electrocatalysts for Oxygen Reduction by Tuning the Surface Electronic Structure. *Angew. Chem., Int. Ed.* **2006**, *45*, 2897−2901.
(816) Lu, Y.; Jiang, Y.; Chen, W. PtPd Porous Nanorods with Enhanced Electrocatalytic Activity and Durability for Oxygen Reduction Reaction. *Nano Energy* **2013**, *2*, 836−844.
(817) Zhang, G.; Sun, S.; Cai, M.; Zhang, Y.; Li, R.; Sun, X. Porous Dendritic Platinum Nanotubes with Extremely High Activity and Stability for Oxygen Reduction Reaction. *Sci. Rep.* **2013**, *3*, 1526.
(818) Alia, S. M.; Zhang, G.; Kisailus, D.; Li, D.; Gu, S.; Jensen, K.; Yan, Y. Porous Platinum Nanotubes for Oxygen Reduction and Methanol Oxidation Reactions. *Adv. Funct. Mater.* **2010**, *20*, 3742−3746.
(819) Wittkopf, J. A.; Zheng, J.; Yan, Y. High-Performance Dealloyed PtCu/CuNW Oxygen Reduction Reaction Catalyst for Proton Exchange Membrane Fuel Cells. *ACS Catal.* **2014**, *4*, 3145−3151.
(820) Tong, X.; Zhang, J.; Zhang, G.; Wei, Q. L.; Chenitz, R.; Claverie, J. P.; Sun, S. Ultrathin Carbon-Coated Pt/Carbon Nanotubes: a Highly Durable Electrocatalyst for Oxygen Reduction. *Chem. Mater.* **2017**, *29*, 9579−9587.
(821) Wu, Z.; Lv, Y.; Xia, Y.; Webley, P. A.; Zhao, D. Ordered Mesoporous Platinum@Graphitic Carbon Embedded Nanophase as a Highly Active, Stable, and Methanol-Tolerant Oxygen Reduction Electrocatalyst. *J. Am. Chem. Soc.* **2012**, *134*, 2236−2245.
(822) Cheng, K.; Kou, Z.; Zhang, J.; Jiang, M.; Wu, H.; Hu, L.; Yang, X.; Pan, M.; Mu, S. Ultrathin Carbon Layer Stabilized Metal Catalysts Towards Oxygen Reduction. *J. Mater. Chem. A* **2015**, *3*, 14007−14014.
(823) Cao, X.; Wang, N.; Han, Y.; Gao, C.; Xu, Y.; Li, M.; Shao, Y. PtAg Bimetallic Nanowires: Facile Synthesis and Their Use as Excellent Electrocatalysts toward Low-Cost Fuel Cells. *Nano Energy* **2015**, *12*, 105−114.
(824) Zheng, J.; Cullen, D. A.; Forest, R. V.; Wittkopf, J. A.; Zhuang, Z.; Sheng, W.; Chen, J. G.; Yan, Y. Platinum-Ruthenium Nanotubes and Platinum-Ruthenium Coated Copper Nanowires as Efficient Catalysts for Electro-Oxidation of Methanol. *ACS Catal.* **2015**, *5*, 1468−1474.
(825) Lai, J.; Zhang, L.; Qi, W.; Zhao, J.; Xu, M.; Gao, W.; Xu, G. Facile Synthesis of Porous PtM (M = Cu, Ni) Nanowires and Their Application as Efficient Electrocatalysts for Methanol Electrooxidation. *ChemCatChem* **2014**, *6*, 2253−2257.
(826) Liao, Y.; Yu, G.; Zhang, Y.; Guo, T.; Chang, F.; Zhong, C. J. Composition-Tunable PtCu Alloy Nanowires and Electrocatalytic Synergy for Methanol Oxidation Reaction. *J. Phys. Chem. C* **2016**, *120*, 10476−10484.
(827) Xia, B. Y.; Wu, H. B.; Li, N.; Yan, Y.; Lou, X. W.; Wang, X. One-Pot Synthesis of Pt-Co Alloy Nanowire Assemblies with Tunable

DOI: 10.1021/acs.chemrev.8b00745
Chem. Rev. XXXX, XXX, XXX−XXX

Composition and Enhanced Electrocatalytic Properties. *Angew. Chem., Int. Ed.* **2015**, *54*, 3797−3801.
(828) Guo, S.; Zhang, S.; Sun, X.; Sun, S. Synthesis of Ultrathin FePtPd Nanowires and Their Use as Catalysts for Methanol Oxidation Reaction. *J. Am. Chem. Soc.* **2011**, *133*, 15354−15357.
(829) Wang, S.; Wang, X.; Jiang, S. P. Controllable Self-Assembly of Pd Nanowire Networks as Highly Active Electrocatalysts for Direct Formic Acid Fuel Cells. *Nanotechnology* **2008**, *19*, 455602.
(830) Jiang, X.; Fu, G.; Wu, X.; Liu, Y.; Zhang, M.; Sun, D.; Xu, L.; Tang, Y. Ultrathin AgPt Alloy Nanowires as a High-Performance Electrocatalyst for Formic Acid Oxidation. *Nano Res.* **2018**, *11*, 499−510.
(831) Liu, W.; Haubold, D.; Rutkowski, B.; Oschatz, M.; Hübner, R.; Werheid, M.; Ziegler, C.; Sonntag, L.; Liu, S.; Zheng, Z.; Herrmann, A. K.; et al. Self-Supporting Hierarchical Porous PtAg Alloy Nanotubular Aerogels as Highly Active and Durable Electrocatalysts. *Chem. Mater.* **2016**, *28*, 6477−6483.
(832) Wang, Y.; Liu, J.; Wang, Y.; Al-Enizi, A. M.; Zheng, G. Tuning of CO_2 Reduction Selectivity on Metal Electrocatalysts. *Small* **2017**, *13*, 1701809.
(833) Zhu, W.; Zhang, Y.-J.; Zhang, H.; Lv, H.; Li, Q.; Michalsky, R.; Peterson, A. A.; Sun, S. Active and Selective Conversion of CO_2 to CO on Ultrathin Au Nanowires. *J. Am. Chem. Soc.* **2014**, *136*, 16132−16135.
(834) Li, Y.; Cui, F.; Ross, M. B.; Kim, D.; Sun, Y.; Yang, P. Structure-Sensitive CO_2 Electroreduction to Hydrocarbons on Ultrathin 5-Fold Twinned Copper Nanowires. *Nano Lett.* **2017**, *17*, 1312−1317.
(835) Loiudice, A.; Lobaccaro, P.; Kamali, E. A.; Thao, T.; Huang, B. H.; Ager, J. W.; Buonsanti, R. Tailoring Copper Nanocrystals Towards C_2 Products in Electrochemical CO_2 Reduction. *Angew. Chem., Int. Ed.* **2016**, *55*, 5789−5792.
(836) Du, J.; Chen, Z.; Ye, S.; Wiley, B. J.; Meyer, T. J. Copper as a Robust and Transparent Electrocatalyst for Water Oxidation. *Angew. Chem., Int. Ed.* **2015**, *54*, 2073−2080.
(837) Chen, Z.; Ye, S.; Wilson, A. R.; Ha, Y. C.; Wiley, B. J. Optically Transparent Hydrogen Evolution Catalysts Made from Networks of Copper-Platinum Core-Shell Nanowires. *Energy Environ. Sci.* **2014**, *7*, 1461−1467.
(838) Chen, Z.; Rathmell, A. R.; Ye, S.; Wilson, A. R.; Wiley, B. J. Optically Transparent Water Oxidation Catalysts Based on Copper Nanowires. *Angew. Chem., Int. Ed.* **2013**, *52*, 13708−13711.
(839) Li, S.; Chen, Y.; Huang, L.; Pan, D. Large-Scale Synthesis of Well-Dispersed Copper Nanowires in an Electric Pressure Cooker and Their Application in Transparent and Conductive Networks. *Inorg. Chem.* **2014**, *53*, 4440−4444.
(840) Lin, L.; Wang, W.; Huang, J.; Li, Q.; Sun, D.; Yang, X.; Wang, H.; He, N.; Wang, Y. Nature Factory of Silver Nanowires: Plant-Mediated Synthesis Using Broth of Cassia Fistula Leaf. *Chem. Eng. J.* **2010**, *162*, 852−858.
(841) Varma, R. S. Greener and Sustainable Trends in Synthesis of Organics and Nanomaterials. *ACS Sustainable Chem. Eng.* **2016**, *4*, 5866−5878.
(842) Nadagouda, M. N.; Speth, T. F.; Varma, R. S. Microwave-Assisted Green Synthesis of Silver Nanostructures. *Acc. Chem. Res.* **2011**, *44*, 469−478.
(843) Saratale, R. G.; Saratale, G. D.; Shin, H. S.; Jacob, J. M.; Pugazhendhi, A.; Bhaisare, M.; Kumar, G. New Insights on the Green Synthesis of Metallic Nanoparticles Using Plant and Waste Biomaterials: Current Knowledge, Their Agricultural and Environmental Applications. *Environ. Sci. Pollut. Res.* **2018**, *25*, 10164−10183.
(844) Sambur, J. B.; Chen, P. Approaches to Single-Nanoparticle Catalysis. *Annu. Rev. Phys. Chem.* **2014**, *65*, 395−422.
(845) Niu, G.; Zhang, L.; Ruditskiy, A.; Wang, L.; Xia, Y. A Droplet-Reactor System Capable of Automation for the Continuous and Scalable Production of Noble-Metal Nanocrystals. *Nano Lett.* **2018**, *18*, 3879−3884.
(846) Holden, P. A.; Gardea-Torresdey, J. L.; Klaessig, F.; Turco, R. F.; Mortimer, M.; Hund-Rinke, K.; Cohen Hubal, E. A.; Avery, D.; Barceló, D.; Behra, R.; et al. Considerations of Environmentally Relevant Test Conditions for Improved Evaluation of Ecological Hazards of Engineered Nanomaterials. *Environ. Sci. Technol.* **2016**, *50*, 6124−6145.
(847) Holden, P. A.; Klaessig, F.; Turco, R. F.; Priester, J. H.; Rico, C. M.; Avila-Arias, H.; Mortimer, M.; Pacpaco, K.; Gardea-Torresdey, J. L. Evaluation of Exposure Concentrations Used in Assessing Manufactured Nanomaterial Environmental Hazards: Are They Relevant? *Environ. Sci. Technol.* **2014**, *48*, 10541−10551.
(848) Levard, C.; Hotze, E. M.; Lowry, G. V.; Brown, G. E. Environmental Transformations of Silver Nanoparticles: Impact on Stability and Toxicity. *Environ. Sci. Technol.* **2012**, *46*, 6900−6914.
(849) Kwak, J. I.; An, Y.-J. A Review of the Ecotoxicological Effects of Nanowires. *Int. J. Environ. Sci. Technol.* **2015**, *12*, 1163−1172.
(850) George, S.; Lin, S.; Ji, Z.; Thomas, C. R.; Li, L.; Mecklenburg, M.; Meng, H.; Wang, X.; Zhang, H.; Xia, T.; et al. Surface Defects on Plate-Shaped Silver Nanoparticles Contribute to Its Hazard Potential in a Fish Gill Cell Line and Zebrafish Embryos. *ACS Nano* **2012**, *6*, 3745−3759.
(851) Scanlan, L. D.; Reed, R. B.; Loguinov, A. V.; Antczak, P.; Tagmount, A.; Aloni, S.; Nowinski, D. T.; Luong, P.; Tran, C.; Karunaratne, N.; et al. Silver Nanowire Exposure Results in Internalization and Toxicity to Daphnia Magna. *ACS Nano* **2013**, *7*, 10681−10694.
(852) Kwak, J. Il; Park, J.-W.; An, Y.-J. Effects of Silver Nanowire Length and Exposure Route on Cytotoxicity to Earthworms. *Environ. Sci. Pollut. Res.* **2017**, *24*, 14516−14524.

DOI: 10.1021/acs.chemrev.8b00745
Chem. Rev. XXXX, XXX, XXX−XXX